POLITECNICO DI MILANO

School of Industrial and Information Engineering
Master of Science in Engineering Physics

Towards three-dimensional nanoscale imaging of spin-wave modes via X-Ray Laminography

Supervisor:
Dr. Edoardo ALBISETTI

Candidate:
Davide GIRARDI

ID number:
919257

Academic Year 2019-2020

Alla mia famiglia e a Federica.

Abstract

Recently, it has been proposed to employ spin waves-based devices as alternatives to the standard CMOS technology. Spin waves offer several advantages, such as the absence of Joule losses and the sub-μm wavelength in the GHz-THz range. While there are several well-established techniques that allow to study in two dimensions the magnetization dynamics, until now insights on the three-dimensional behavior of spin waves in thin films have only been possible through comparisons with simulations. In this context their direct three-dimensional visualization with nanoscale resolution would represent a huge step towards studying the physics of complex spin-wave modes and developing next generation computing architectures.

Here, we propose the innovative Soft X-ray Laminography technique for performing time-resolved imaging of spin-wave modes, aiming to directly probe all the magnetization components in 3D. To this purpose, we focused on synthetic antiferromagnetic structures, known for being efficient platforms for the emission and propagation of spin waves. First, micromagnetic simulations at several excitation frequencies and thicknesses were performed to identify the best conditions for visualizing the propagation of spin waves and their localization along the film thickness. Then, the samples were fabricated and magnetically characterized, after the optimization of the growth and nanofabrication parameters. In order to fabricate spin-wave emitters, either the samples were patterned via thermally assisted magnetic–Scanning Probe Lithography, or Landau domains were stabilized in nanopatterned geometric features. Spin waves have first been measured via standard 2D Scanning Transmission X-ray Microscopy, while later it was possible to visualize them at multiple angles with good magnetic contrast using time-resolved Laminography. Additionally, as a result of these measurements, it has also been possible to obtain a 3D topographic reconstruction of the investigated sample. This work represents a promising step towards obtaining for the first time a time-resolved three-dimensional reconstruction with nanoscale resolution of the spin-waves emission and propagation.

Sommario

Recentemente è stato proposto di utilizzare le onde di spin come alternativa alla tecnologia standard basata sui CMOS. Le onde di spin offrono numerosi vantaggi rispetto a quest'ultima, grazie all'assenza di dissipazione per effetto Joule e alle lunghezze d'onda nanometrica per frequenze fino ai THz. Sebbene ci siano diverse tecniche che permettono di studiare in due dimensioni la dinamica della magnetizzazione, fino ad ora le informazioni sul comportamento tridimensionale sono state ottenute solamente grazie alle simulazioni. A questo proposito, essere in grado di visualizzare tridimensionalmente le onde di spin rappresenterebbe un importante passo avanti per lo sviluppo dei computer di prossima generazione.

In questo lavoro, proponiamo l'innovativa Laminografia a raggi X come metodo per la visualizzazione dinamica dei modi delle onde di spin, con l'obiettivo di investigare direttamente tutte le componenti della magnetizzazione in 3D. Per questo motivo, ci siamo focalizzati sullo sviluppo di strutture antiferromagnetiche sintetiche, conosciute per essere delle efficienti piattaforme per l'emissione e la propagazione di onde di spin. Per prima cosa sono state condotte delle simulazioni micromagnetiche a diverse frequenze e spessori, per trovare le condizioni migliori per visualizzare la propagazione delle onde di spin e la loro localizzazione lungo lo spessore del film. I campioni sono stati poi cresciuti e caratterizzati magneticamente, dopo aver ottimizzato i parametri di crescita e nanofabbricazione. Per creare gli emettitori di onde di spin, i campioni sono stati litografati magneticamente attraverso la tecnica *thermally assisted magnetic–Scanning Probe Lithography*, oppure i domini di Landau sono stati stabilizzati in nanostrutture litografate. Le onde di spin sono prima state misurate con la tecnica standard 2D *Scanning Transmission X-ray Microscopy*, mentre successivamente è stato possibile visualizzarle a diversi angoli usando la Laminografia. In aggiunta, è stato possibile ottenere una ricostruzione topografica 3D del campione. Questo lavoro rappresenta uno step promettente verso l'ottenimento della ricostruzione 3D dinamica dell'emissione e propagazione delle onde di spin con risoluzione nanometrica.

Contents

List of Figures

Page

List of Tables

Chapter 1

Introduction

1.1 State of the art

In the recent years, a lot of attention has been focused on finding fast and efficient alternatives to standard CMOS electronics. The most pressing issues for the semiconductor industry are mainly related to the almost certain end of the historically famous Moore's law, which predicts the doubling of the number of transistors on a chip every two years. As a consequence, it will soon not be possible to sustain the increasing power requirements of modern high-performance computers. This has opened up the unique opportunity for studying novel interesting physical phenomena, and in this context spin-waves are one of the most promising candidates for the development of high-speed and low-power information carrier devices, as well as for systems for both digital and analog computing and signal processing.

Spin waves are defined as wave-like perturbations of the magnetic texture, where the magnetization precesses around its axis, while magnonics (from *magnons*, the associated quasi-particle) is the emerging field of magnetism that studies both their underlying physical phenomena and the potential applications through their control and manipulation. One of the most striking difference with respect to conventional electronics is related to the information transport mechanism: while the electrons motion is associated to a charge transfer, this is not true for spin-waves based devices, thus ohmic losses are avoided and power consumption is substantially reduced. This represents a huge benefit not only for the development of the next-generation supercomputers, but also on a wider societal scale would allow to significantly decrease the environmental impact of such devices [1]–[3]. Moreover, the associated spin-wave wavelength is considerably smaller with respect to its electromagnetic counterpart, up to five orders of magnitude: in the GHz-THz range, spin waves have sub-μm wavelength, which allows to develop miniaturized devices with large and controllable time delays, as well as a much wider frequency adjustability. This property, combined with the highly anisotropic dispersion relation caused by the long-range magnetostatic interaction, offers the potential for creating unconventional computing frameworks, such as neural networks and reservoir computing [1], [4], [5]. Additionally, the possibility of encoding the information with the spin orientation and the ability to propagate both in magnetic conductors and insulators further enhance the suitability of spin waves for nanoscale signal-processing devices.

The measurement of the dynamical behavior of magnetic structures with a three-dimensional resolution is a key point for the improvement of the comprehension and manipulation of spin waves, giving the possibility of a direct experimental visualization of the spin-waves complex spatial profile. This would have two fundamental benefits: first, from a fundamental point of view, it would allow to have a complete mapping of the internal structure and of the magnetization dynamics of magnetic materials, which so far has never been possible since the only insights on this matter are related to comparisons with simulations [6]. Secondly, from a technological point of view, harnessing the third dimension for the realization of innovative three-dimensional nanomagnonic devices with engineered bandstructure, long-range spin-waves emission and propagation inside complex heterostructures would represent a revolutionary breakthrough in the development of the next-generation computer architectures [3], [7], [8]. The three-dimensional time-resolved visualization of propagating spin-wave modes, however, has yet to be achieved. Only recently static 3D magnetic imaging has been realized: Kardjilov et al. [9]–[11] have successfully used neutrons to investigate magnetic domains inside solid materials, combining the high sensitivity of neutron to magnetic fields and the well-established tomographic imaging setup. A different technique called electron holographic VFET (Vector-field Electron tomography) that uses coherent wave interference has been employed by Tanigaki et al. [12] for visualizing three-dimensional magnetic vortices in stacked ferromagnetic discs by means of electrons. In this case, the Transmission Electron Microscope (TEM) instrumentation was customized for visualizing three-dimensionally the magnetic vector field. Magnetic vortexes have also been observed using hard x-ray vector nanotomography with high spatial resolution by Donnelly et al. [13]: the use of synchrotron radiation has several advantages, combining the high spatial resolution and high penetration depth of x-rays which allows the investigation of micrometer-sized samples. A similar approach was also reported by Suzuki et al. [14], that demonstrated the possibility of three-dimensionally reconstruct the magnetic domain structure by scanning a GdFeCo microdisc with hard x-rays using X-ray Magnetic Circular Dichroism (XMCD), tuning the photon energy to the Gd L_3 absorption edge. Of these methods, the ones employing synchrotron x-rays are the most promising given their high spatial resolution, the high degree of tunability and their pulsed time structure, that holds the promise of performing time-resolved measurements [6]. Nevertheless, two main criticalities have been identified, related to both the probe and the instrumental setup: for the former, since hard x-rays have photon energies above 5keV, they are only suitable for investigating bulk materials due to their high penetration depth, while they are disadvantageous for the study of thin films. For the latter, on the other hand, conventional x-ray computed tomography is best applicable to samples that are cylindrically shaped, since having the rotation axis perpendicular to the incident beam requires small changes on the x-rays transmission during the rotation scanning to work properly.

Within this framework, the newly developed Soft X-ray Laminography (SoXL) technique present at the PolLux beamline (X07DA) of the Swiss Synchrotron Light Source and described by Witte et al. in [15] offers the unique opportunity of combining time resolved imaging with soft x-rays, with the alternative Laminography geometry: soft x-rays are characterized by much smaller energies (smaller than 1 keV) respect to hard x-rays, making them more appropriate for studying thin samples. Additionally, their energy range is compatible with the L-absorption edges of magnetic materials, which shows very high magnetic contrast. To solve the problem connected with the tomographic setup, the more generalized method called Laminography has been proposed, where the rotation axis has been tilted in such a way that is no longer perpendicular to the incoming x-rays beam, reducing the associated errors and artefacts during the image reconstruction procedure for thin films. The new Laminography setup has been installed modifying the already existing time-resolved Scanning Transmission X-ray Microscope (STXM), giving for the first time also the concrete possibility of performing three-dimensional time-resolved measurements to study the spin-waves emission and propagation.

1.2 Thesis outline

The current work has been carried out under the supervision of Dr. Edoardo Albisetti, with the NanoBiotechnology and Spintronics (NaBiS) group, coordinated by Prof. Riccardo Bertacco. The exposed research activity has been mainly conducted in the laboratories of PoliFAB, the micro and nano-technology center of the Politecnico di Milano. I also collaborated at the measurements performed at the Swiss Light Source (SLS) synchrotron facility, hosted at the Paul Scherrer Institut (PSI) in Villigen, Switzerland.

This thesis work can be divided into two major topics: the first part aimed at optimizing the efficient spin-waves emission and propagation upon excitation of the magnetic configuration in Synthetic Antiferromagnetic (SAF) structures with varying thicknesses. The versatile thermally assisted magnetic – Scanning Probe Lithography (tam-SPL) technique have been used to magnetically pattern spin texture such as domain walls, since they have already been employed for the efficient generation and control of spin-wave wavefronts. Additionally, the possibility of stabilizing Landau domains by means of shape anisotropy for driving the emission and propagation of spin waves has also been investigated. Both static and time-resolved Scanning Transmission X-ray Microscopy experiments at the PolLux beamline of the SLS synchrotron facility have been performed, and the spin-wave dispersion relation has been derived as a function of the total thickness of the SAF multilayers.

In the second part of this work, the samples were investigated with the Soft X-ray Laminography technique. After the optimization of the Laminography rotational stage, multiple static images of the domain walls have been taken, and spin waves have been observed with time-resolved measurements at different angles. As a result of the experiments, a three-dimensional topographic reconstruction of the investigated region was possible. This work represents a promising step towards obtaining for the first time a time-resolved three-dimensional reconstruction with nanoscale resolution of the spin-waves emission and propagation, allowing to study the variation of the localization along the film thickness as a function of the excitation frequency.

The subsequent chapters are organized as follows:

- **Chapter 2 - Theoretical framework:** the fundamental theoretical background necessary to understand the discussed physical phenomena are provided.

- **Chapter 3 - Methods and techniques:** the working principle of the fabrication and characterization techniques employed in this work are presented, focusing in particular of the methods employed for studying the morphological and magnetic properties of the samples, and for the observation of the spin-wave emission and propagation.

- **Chapter 4 - Emission and propagation of spin waves in synthetic antiferromagnets:** first, the micromagnetic simulations performed to correctly design the optimal sample configuration for the investigation of the spin-waves emission and propagation inside synthetic antiferromagnetic structures are reported. Additionally, the sample preparation, magnetic characterization, and their subsequent nanofabrication processes are described. Finally, the final experimental investigation with the Scanning Transmission X-ray Microscopy technique is presented.

- **Chapter 5 - X-ray Laminography: towards three-dimensional nanoscale time-resolved imaging of spin-wave modes:** first, the micromagnetic simulations executed to analyze the three-dimensional profile of the spin waves are presented. Then, the procedures carried out for the optimization of the Soft X-ray Laminography instrumentation setup are reported. Finally, the obtained results for both the static and time-resolved three-dimensional SoXL experiments are presented.

- **Chapter 6 - Conclusions and perspectives:** summarizes the result achieved and outlines the future perspectives.

Chapter 2

Theoretical framework

2.1 Micromagnetism

In nature there is a wide class of materials that present very interesting magnetic properties, which arise from the very different types of magnetic interactions. Moreover, the magnetic moments that characterize the solids act in a cooperative way, leading to very peculiar behaviors respect to the isolated case [16], [17].

In order to describe the different states, the theoretical framework of *micromagnetism* can be introduced, which is a thermodynamical approach that consist in finding the most energetically stable state (i.e., ground state) minimizing a free energy functional. The expression of the free energy function includes all the competing magnetic interactions, such as the exchange interaction, the dipolar energy, the Zeeman interaction, the magnetic anisotropy terms, and the interfacial effects. To investigate the various ground states, the solid body is conveniently divided into very small volume elements ΔV, inside which the magnetization $\boldsymbol{M}$ (defined as the average dipole moment per unit volume) is considered as constant and with modulus equal to the saturation magnetization M_s. The size of this volume has to be chosen considering that it must be smaller than the length over which the magnetization changes inside the body, but big enough to allow to use statistics to investigate the solid. Moreover, the magnetization will be considered as a continuous function varying inside the body (*continuum approximation*).

The different possible ground states include *ferromagnets* (FMs), that are magnetic materials characterized by a macroscopic non-zero magnetization even in the absence of an applied field [16]. This zero-remanence magnetization is a consequence of the partial alignment of the magnetic moments at the atomic scale. When the FMs are heated above a certain temperature, called Curie temperature T_C, they experience a phase transition losing the ferromagnetic properties and obtaining the paramagnetic ones instead. Below T_C, on the other hand, the response of the magnetization $\boldsymbol{M}$ to an external field $\boldsymbol{H}$ is described by a hysteresis loop, highlighting the importance of the history of the material.

Another possible ground state consists in the *antiferromagnets* (AFs), that are magnetic materials in which the magnetic moments are aligned antiparallelly between each other. AFs are often seen as characterized by two sublattices, each one of them with the magnetic moments all aligned in the same direction, but with opposite orientation respect to each other: in these materials the net magnetization is zero. If the total magnetization is different from zero but the solid is still characterized by the presence of two oppositely oriented sublattices, the materials are called *ferrimagnets*.

2.1.1 Exchange interaction

Exchange interaction lies at the core of the phenomenon of long-range magnetic order. It can be explained with quantum mechanics, even though its true origin cannot still be fully understood. Exchange interactions arise from the simple electrostatic interactions between nearby charges, coupled with the Pauli exclusion principle, for which two or more identical fermions cannot occupy the same quantum state simultaneously [16], [18], [19].

To demonstrate the energetic term of the exchange interaction inside the free energy function, consider the simple case of two electrons a and b with spin $s = 1/2$ and whose coordinates are r_1 and r_2, respectively. Since the joint wavefunction must be invariant with respect to the exchange operator $\hat{\boldsymbol{P}}$, and since electrons are fermions, the Pauli exclusion principle must be respected, so the total wavefunction, which includes both the spatial and the spin part, must be antisymmetric:

$$\hat{\mathbf{P}}|\boldsymbol{r_1 r_2}> = -|\boldsymbol{r_2 r_1}> \tag{2.1}$$

There are two possible total wavefunctions, one with the spatial part symmetric while the spin part (called *spin singlet state* χ_S) is antisymmetric, and the other with the spatial part antisymmetric and the spin part (called *triplet spin state* χ_T) symmetric:

$$\Psi_S = \frac{1}{\sqrt{2}}[\psi_a(\boldsymbol{r}_1)\psi_b(\boldsymbol{r}_2) + \psi_a(\boldsymbol{r}_2)\psi_b(\boldsymbol{r}_1)]\chi_S$$

$$\Psi_T = \frac{1}{\sqrt{2}}[\psi_a(\boldsymbol{r}_1)\psi_b(\boldsymbol{r}_2) - \psi_a(\boldsymbol{r}_2)\psi_b(\boldsymbol{r}_1)]\chi_T$$

With the first one having a symmetric spatial component and the second one an antisymmetric spatial component. For the spin state, one possible configuration is identified for the singlet state and three possible configurations for the triplet state, as follows:

$$\chi_S = \frac{|\uparrow\downarrow> - |\downarrow\uparrow>}{\sqrt{2}} \qquad \chi_T = |\uparrow\uparrow>\,;\ |\downarrow\downarrow>\,;\ \frac{|\uparrow\downarrow> + |\downarrow\uparrow>}{\sqrt{2}}$$

where the spin part is completely normalized. Hence, if there is an energy difference between the singlet and the triplet functions this must come from the difference in the spatial part of the function, which is a consequence of the difference in probability of finding the electrons.

An effective Hamiltonian $\hat{\boldsymbol{H}}$ for the interaction can be introduced, in order to calculate the energy of the two states as:

$$E_S = \int \Psi_S^* \hat{H} \Psi_S d\boldsymbol{r}_1 d\boldsymbol{r}_2$$

$$E_T = \int \Psi_T^* \hat{H} \Psi_T d\boldsymbol{r}_1 d\boldsymbol{r}_2$$

The energy difference is then:

$$\Delta E = E_S - E_T = 2 \int \psi_a^* (\boldsymbol{r}_1)\psi_b^*(\boldsymbol{r}_2)\hat{H}\psi_a(\boldsymbol{r}_2)\psi_b(\boldsymbol{r}_1)d\boldsymbol{r}_1 d\boldsymbol{r}_2 \qquad (2.2)$$

Since it is known that the difference between singlet and triplet state can be parametrized using $\boldsymbol{S}_1 \cdot \boldsymbol{S}_2$ (for the singlet state $\boldsymbol{S}_1 \cdot \boldsymbol{S}_2 = -3/4$, for the triplet state $\boldsymbol{S}_1 \cdot \boldsymbol{S}_2 = 1/4$), the Hamiltonian can be written as an "effective Hamiltonian":

$$\hat{H} = \frac{1}{4}(E_s + 3E_T) - (E_s - E_T)\boldsymbol{S}_1 \cdot \boldsymbol{S}_2 \qquad (2.3)$$

which is the sum of a constant term and a term depending on the spin. The attention has then been moved from the distribution of the spatial wavefunction of the two electrons, which is the real responsible of the energy difference, to the spin part, which allows an easier treatment of the problem. Defining the *exchange integral* as

$$J = \frac{E_S - E_T}{2} = \int \psi_a^*(\boldsymbol{r}_1)\psi_b^*(r_2)\, \hat{H}\psi_a^*(\boldsymbol{r}_2)\psi_b^*(\boldsymbol{r}_1)d\boldsymbol{r}_1 d\boldsymbol{r}_2 \qquad (2.4)$$

The spin-dependent effective Hamiltonian then becomes:

$$\hat{H}_{eff} = -2J(\boldsymbol{S}_a \cdot \boldsymbol{S}_b) \qquad (2.5)$$

The sign of J determines which of the two states is energetically favorable: if J > 0, the energy of the singlet state is larger than the energy of the triplet state, so the spins tend to stay in the parallel configuration (χ_T). On the other hand, if J < 0, the energy of the triplet state will be higher respect to the one of the singlet state, so the spins tend to align antiparallelly respect to each other (χ_S).

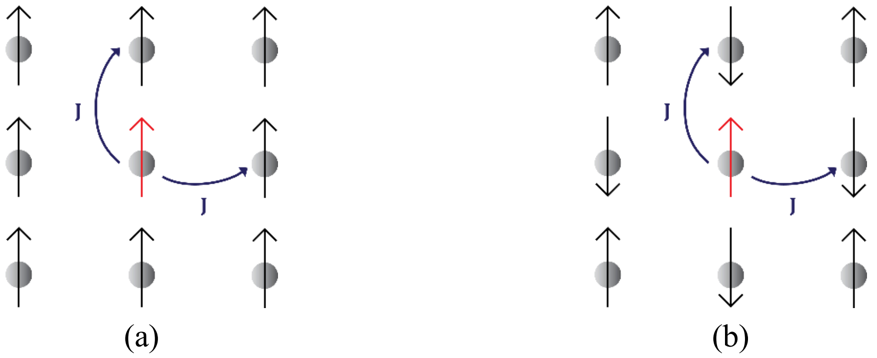

Figure 2.1: representation of the two possible spin configurations inside a simple 2D crystal, with (a) as the ferromagnetic configuration and (b) as the antiferromagnetic configuration.

As pointed out in Figure 2.1(b) if J < 0, the highlighted spin will be antiparallel respect to every one of its nearest neighbors giving an antiferromagnetic configuration, while if J > 0 as in Figure 2.1(a), the spin will be parallel giving a ferromagnetic configuration.

This model can be generalized considering the interaction between all the atoms inside a crystal. This motivates the Hamiltonian of the *Heisenberg model* [16], [18], [19]:

$$H = -\sum_{ij} J_{ij} \boldsymbol{S}_i \cdot \boldsymbol{S}_j \tag{2.6}$$

where J_{ij} is the exchange constant between the i$^{\text{th}}$ and j$^{\text{th}}$ spin. Since J_{ij} depends on the overlap between the electrons' wavefunction, generally the summation is taken over only the first nearest neighbors, and in some particular cases also over the next-nearest neighbors while neglecting the other long-range interactions.

The calculation of the exchange integral can be very complicated if considering all the contributions, but a very general comment can be made. If the two electrons belong to the same atom, J will be positive to stabilize the triplet configuration, so the spatial wavefunction will have an antisymmetric behavior, thus reducing the overlapping of the wavefunctions and minimizing the repulsive Coulomb interaction between the two electrons, which is consistent with Hund's first rule [16].

In the framework of micromagnetism this model cannot be applied because the problem is very different. The interest is shifted to a wider view of the system, where the single spins are not relevant anymore, and the attention is focused on the change in the magnetization between two different point of the solid. Inside the small volume ΔV the exchange interaction is so strong that locally all the spins are aligned, and the magnetization is then equal to the saturation magnetization $\boldsymbol{M_S}$, but from one point to the other it has a slightly different orientation. After a few calculations, the exchange energy can is modelled by:

$$E_{ex} = \frac{A}{2}\int\left[(\nabla m_x)^2 + \left(\nabla m_y\right)^2 + (\nabla m_z)^2\right]d\tau \qquad (2.7)$$

where m_i are the components of the reduced moment $\boldsymbol{m} = \boldsymbol{M}/M_S$and A [J/m] is the so-called *exchange stiffness* and is defined as:

$$A = 2JS^2\frac{Z}{a}$$

with Z as the number of sites on the unit cell, *a* as the lattice parameter and J as the exchange integral. The exchange stiffness gives then the strength of the exchange interaction inside the material and is very useful for comparing different materials. In general, for ferromagnets such as Co or Permalloy typical values are around tens of pJ/m (A_{Co} = 31 pJ/m, A_{Py} = 10pJ/m). The exchange energy is then different from zero only if there is a tilting in the magnetic moments, which is the case for non-uniform magnetizations, while is zero when all the moments are aligned in the same direction [16].

2.1.2 Magnetostatic energy and Zeeman interaction

As previously mentioned, in the framework of micromagnetism the magnetization of a body is seen as a continuous function $\boldsymbol{M}(r)$, as well as the *demagnetizing field* $\boldsymbol{H}_M(r)$*,* which is generated by the magnetic moments inside the body itself whenever they have a component normal to an internal or external surface ($\boldsymbol{M}\cdot\boldsymbol{n} \neq 0$) or when the magnetization is nonuniform ($\nabla\cdot\boldsymbol{M} \neq 0$) [18]. Inside the small volumes ΔV the modulus of the magnetization is equal to the saturation magnetization, and the only variation regards the local orientation. The *magnetostatic energy*, or *dipolar energy*, can be expressed then as:

$$E_M = -\frac{\mu_0}{2}\int_V \boldsymbol{H}_M\cdot\boldsymbol{M}d^3x = \frac{\mu_0}{2}\int_{a.s.}\boldsymbol{H}_M^2 d^3x \qquad (2.8)$$

with the first integral over the volume of the body, while the second one over all space. When considering an ellipsoid, a simple relationship between the internal field and the magnetization can be introduced: $\boldsymbol{H} = -\boldsymbol{N}\cdot\boldsymbol{M}$, with **N** called *demagnetizing tensor*, that is a second order tensor with unitary trace, and the value of its elements are determined by the shape of the solid. For example, for a sphere and a cylinder:

$$\boldsymbol{N}_{sphere} = \begin{bmatrix} 1/3 & 0 & 0 \\ 0 & 1/3 & 0 \\ 0 & 0 & 1/3 \end{bmatrix};\quad N_{cylinder} = \begin{bmatrix} 1/2 & 0 & 0 \\ 0 & 1/2 & 0 \\ 0 & 0 & 0 \end{bmatrix}$$

When the demagnetizing tensor can be used, the magnetostatic energy can be written as:

$$E_M = \frac{\mu_0}{2}\int_V \left(N_x M_x^2 + N_y M_y^2 + N_z M_z^2\right)dV \qquad (2.9)$$

Since the values of N depend on the shape of the body, this expression determines the so-called *shape anisotropy*. This means that the shape of the sample itself will strongly impact the orientation of the magnetization in order to reduce the total energy of the system.

The values of the demagnetizing tensor relate to the concept of *magnetic charges*, in analogy with the electric charges: $\nabla \cdot \boldsymbol{M}$ constitute the *volume magnetic charges*, while $\boldsymbol{M} \cdot \boldsymbol{n}$ acts as *surface magnetic charges*. Two simples but very important cases can then be analyzed: the prolate and oblate spheroids.

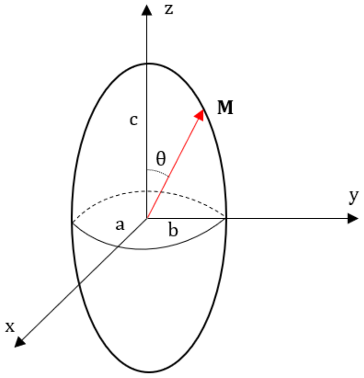

Figure 2.2: prolate spheroid.

In the case of the prolate spheroid (Figure 2.2), the *c*-axis is larger than the *a* and *b* axis, and since the larger the components, the lower the values of the demagnetizing tensor, $N_z < N_x = N_y$. After a few calculations, the energy can be written as:

$$E_M = \frac{\mu_0}{2} V(N_z - N_x) M_s^2 \cos^2\theta \tag{2.10}$$

with θ polar angle. Since the difference between N_z and N_x is negative, the minimum of the energy is for $\theta = 0, \pi$, with the magnetization aligned along the bigger axis in the *z* direction (*uniaxial anisotropy*).

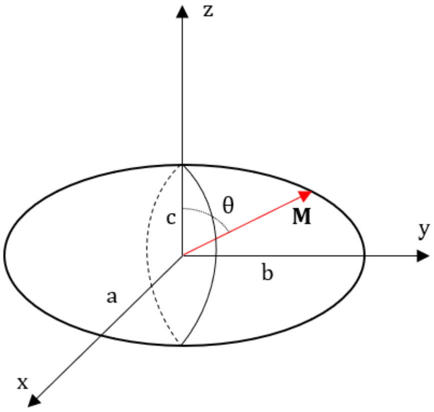

Figure 2.3: oblate spheroid.

On the other hand, for the case of the oblate spheroid (Figure 2.3), having the *c*-axis smaller than a and b, the difference between N_z and N_x in equation 2.10 is positive, which results in a minimum of the energy for $\theta = \pi/2$, with the magnetization in plane (*in plane anisotropy*). This last case is extremely important when considering thin films, where one axis is much smaller respect to the other two: because of the shape anisotropy term the magnetization will tend to stay in-plane rather than out of plane, if no other contributions are taken into consideration.

Another interesting approach can be taken into consideration if considering the thermodynamical point of view. Defining the *magnetic work* as the energy needed to magnetize the body, the work can be divided in three terms:

$$\delta L = \delta L' + \delta U_M + \delta L^* \tag{2.11}$$

where $\delta L'$ is the work done to set a given external field H_a in absence of the magnetic material, δU_M is the work corresponding to the energy stored in a given configuration $\boldsymbol{M}(\boldsymbol{r})$ and depends on the magnetostatic interaction between the local magnetic moments (without considering the origin on the magnetic moments) and δL^* is the work needed to magnetize the body to obtain the configuration $\boldsymbol{M}(\boldsymbol{r})$ considered when calculating δU_M. It is important to underline the difference between δU_M and δL^*: one is the energy associated to a given configuration, and the other is the energy needed to create that specific state.

The magnetostatic energy is then associated with the term δU_M. In a solid with a given magnetic configuration the magnetostatic energy will be calculated considering the interaction between each single magnetic moment with the overall field $\boldsymbol{h}$ produced by all the other dipoles. The energy associated to a magnetic moment in presence of a magnetic field is $E = -\boldsymbol{m} \cdot \boldsymbol{B}$, and $\boldsymbol{B}$ in vacuum can be written as $\mu_0 H$, so when calculating the magnetostatic energy for the system considering the interaction of all the dipoles with $\boldsymbol{h}$ it is possible to write:

$$U_M = -\frac{\mu_0}{2} \sum_i \boldsymbol{\mu}_i \cdot \boldsymbol{h}_i \tag{2.12}$$

with $\boldsymbol{\mu}_i$ as the i^{th} magnetic moment of the lattice and $\boldsymbol{h}_i$ as the overall field produced by all the other moments associated to it. To calculate the magnetostatic energy for the system, consider that the fine structure of the field will only depend on the nearest neighbors, while the rest of the body can be considered as in the continuous approximation, as depicted in Figure 2.4.

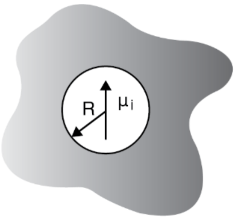

Figure 2.4: the nearest neighbors are considered as precise dipoles, while all the other dipoles for which $R >> a$ will be considered in the continuous approximation (with a lattice parameter).

It is possible to further simplify the problem to calculate the expression of $\boldsymbol{h}_i$ as the sum of three different contributions, as shown in Figure 2.5:

$$\boldsymbol{h}_i = \boldsymbol{H}_M - (-\boldsymbol{N} \cdot \boldsymbol{M}) + \boldsymbol{h}_i' \tag{2.13}$$

with $\boldsymbol{H}_M$ as the demagnetizing field, generated by the magnetic moments as continuous field varying smoothly inside the body, $\boldsymbol{H}_{sphere} = -1/3\,\boldsymbol{M}$ associated to the portion of the body seen with continuous magnetization and subtracted from the system, and $\boldsymbol{h}_i'$ as the field associated with the precise and discrete calculations of the dipole interaction of the sphere:

$$\boldsymbol{h}_i' = \frac{1}{4\pi} \sum_{|r_{ij}|<R} \left[-\frac{\boldsymbol{\mu}_j}{|r_{ij}|^3} + \frac{3(\boldsymbol{\mu}_j \cdot \boldsymbol{r}_{ij})\boldsymbol{r}_{ij}}{|r_{ij}|^5} \right] \tag{2.14}$$

with $\boldsymbol{\mu}_j$ indicating the dipole contributing to the field and $\boldsymbol{r}_{ij}$ as the distance between the dipole and the point. More in general, it is possible to write $\boldsymbol{h}_i' = -\boldsymbol{\Lambda} \cdot \mathbf{M}$ with $\boldsymbol{\Lambda}$ a tensor that describes the relationship with the magnetization.

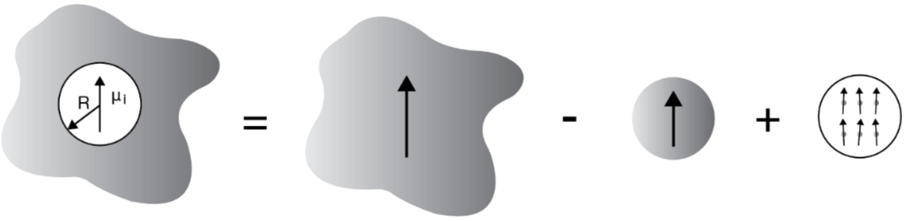

Figure 2.5: the system under consideration is seen as the sum of three contributions.

The expression of the magnetostatic energy then becomes:

$$U_M = -\frac{\mu_0}{2} \sum_i \boldsymbol{\mu}_i \cdot \left(\boldsymbol{H}_M + \frac{1}{3} \cdot \boldsymbol{M} - \boldsymbol{\Lambda} \cdot \mathbf{M} \right) \tag{2.15}$$

Replacing $\boldsymbol{\mu}_i = \boldsymbol{M} d^3 x$ and integrating:

$$U_M = -\frac{\mu_0}{2}\int \boldsymbol{M}\cdot\left(\boldsymbol{H}_M + \frac{1}{3}\cdot\boldsymbol{M} - \boldsymbol{\Lambda}\cdot\mathbf{M}\right)d^3x$$
$$= -\frac{\mu_0}{2}\int \boldsymbol{M}\cdot\boldsymbol{H}_M d^3x - \frac{\mu_0}{6}\int \boldsymbol{M}^2 d^3x - \frac{\mu_0}{2}\int \boldsymbol{M}\cdot\boldsymbol{\Lambda}\cdot\mathbf{M}d^3x$$

the second term clearly minimizes the energy when the magnetization is maximum so equal to the saturation magnetization, in the same way the exchange interaction does. It has a similar expression as in the mean field approximation of the Weiss theory of ferromagnetism, but a factor of λ (>1) is missing, making this term negligible. The third term takes into consideration the anisotropic behavior of the system and will be included into another energetic term. The only term left is the first one, which is the already presented expression of the magnetostatic energy of Equation 2.8:

$$E_M = -\frac{\mu_0}{2}\int_V \boldsymbol{H}_M\cdot\boldsymbol{M}d^3x$$

When an external field $\boldsymbol{H}_a$ is present another contribution must be considered, describing the tendency of the magnetization to align towards the direction of the external applied field. This contribution is called *Zeeman coupling* and can be written as:

$$E_Z = -\mu_0\int_V \boldsymbol{H}_a\cdot\boldsymbol{M}d^3x$$

2.1.3 Magnetic anisotropy terms

In real materials the Heisenberg Hamiltonian that describes the system is rarely isotropic, and the anisotropic behavior of the system must be taken into account, introducing the dependency of the total energy of the system on the orientation of the magnetization respect to some preferential axis. The preferential orientation of the magnetization $\boldsymbol{M}(\boldsymbol{r})$ is a consequence of broken symmetries in the lattice and can be explained by the so-called *magnetocrystalline anisotropy*, that considers the action of both the crystal field and the spin-orbit coupling. In this framework, after the definition of the *anisotropic surface energy*, that is a curve that describes the energy of the system in space depending on the position of each point A respect to the origin, two specific directions are identified: the *easy axis*, that is a local minimum of the anisotropic surface energy, and the *hard axis*, that is a local maximum of the anisotropic surface energy.

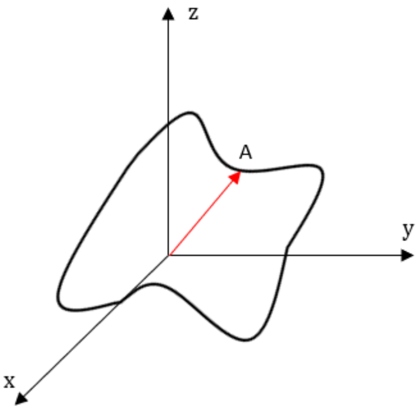

Figure 2.6: anisotropic surface energy.

Generally, the model of this problem is obtained through parametrization. Introducing the anisotropy energy term *$F_{AN}(\boldsymbol{m})$* present in the free energy function and normalize it respect to the small volume ΔV as $f_{AN}(\boldsymbol{m}) = F_{AN}(\boldsymbol{m})/\Delta V$, and considering that $f_{AN}(\boldsymbol{m})$ must be unchanged upon rotation around the anisotropy axis, a good variable to use for the expansion of $f_{AN}(\boldsymbol{m})$ is $\sin^2\theta$ with θ the polar angle between the magnetization and the anisotropy axis. The trigonometric expansion used is then:

$$f_{AN} = k_0 + k_1 \sin^2\theta + k_2 \sin^4\theta + k_3 \sin^6\theta + \cdots \tag{2.16}$$

where the coefficients k_0, k_1 and so on depends on the characteristics of the material and on the temperature. Usually, the expansion is used for practical uses just considering the first two terms. In this case then, the sign of k_1 determines the final configuration: if $k_1 > 0$ then there is a minimum in the function for $\theta = 0, \pi$ and thus the magnetization lies along the z-direction (*easy axis anisotropy*), while if $k_1 < 0$ then the minimum is for $\theta = \pi/2$ and then the magnetization lies in the (*x,y*) plane (*easy plane anisotropy*).

For many practical applications it becomes extremely important to calculate the *anisotropy field* $\boldsymbol{H}_{an}$, that is the applied field necessary to drive the magnetization in the direction perpendicular to the easy axis. Consider as an example the case of a body with uniform magnetization: the energy per unit volume can be written as a function of the azimuthal angle θ, considering the contribution of both the anisotropy energy and of the Zeeman interaction, having a system with an applied external field:

$$g_L = k_1 sin^2\theta - \mu_0 \boldsymbol{M} \cdot \boldsymbol{H}_{an} = k_1 sin^2\theta - \mu_0 M_{\boldsymbol{s}} H_{\boldsymbol{an}} sin\theta \tag{2.17}$$

The calculations of the minimum of (2.18) and of its stability leads to the following result for the modulus of the anisotropy field:

$$|H_{an}| = \frac{2k_1}{\mu_0 M_s} \tag{2.18}$$

The anisotropy field is often used to express the strength of the anisotropy of a material [16], [18], [20].

Finally, the origin of the magnetocrystalline anisotropy can be introduced. Generally, two causes are identified, namely the *single ion anisotropy* and the *two ions anisotropy*. The single ion anisotropy is connected to the crystal field and to the spin-orbit interaction. The crystal field tends to stabilize particular orbitals due to the electrostatic interaction, so the angular momentum **L** is fixed. Since the spin-orbit interaction Hamiltonian is proportional to $\boldsymbol{L}\cdot\boldsymbol{S}$, when applying an external field to tilt the spin, changing the angle between the fixed **L** and **S**, the energy changes. The easy axis will then be identified as the direction along which the spin-orbit interaction energy is minimized. The two ions anisotropy on the other hand is associated with the dipolar interaction. There are two possible dipole configurations, the *parallel* and the *head-to-tail* configuration.

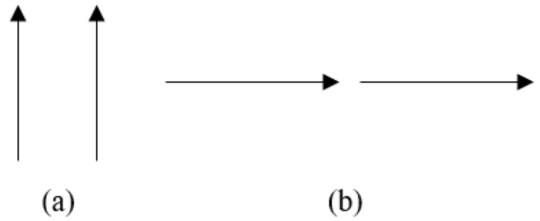

Figure 2.7: schematic representation of the spins in (a) parallel configuration and (b) head-to-tail configuration

The difference of energy for the two configurations is calculated with (2.14) and is equal to:

$$E_P - E_{HT} = \frac{3\mu_0 m^2}{4\pi r^3} \tag{2.19}$$

showing a lower energy for the head-to-tail configuration.

2.1.4 Total energy

All these competing terms introduced in the paragraphs before are summed up to obtain the expression of the total energy of the system:

$$G_L = \int_V \frac{A}{2}[(\nabla m_x)^2 + \left(\nabla m_y\right)^2 + (\nabla m_z)^2 + f_{AN}(\boldsymbol{m},\boldsymbol{n}) - \frac{\mu_0}{2}\boldsymbol{M}\cdot\boldsymbol{H}_M - \mu_0\boldsymbol{M}\cdot\boldsymbol{H}_a]dV \tag{2.20}$$

with $\boldsymbol{m} = \boldsymbol{M}/M_s$ as the reduced magnetization and $\boldsymbol{n}$ as the anisotropy axis. In the framework of micromagnetism, the solid is divided in small volumes dV, inside which the magnetization is equal to the saturation magnetization, and ***M(r)*** changes continuously from one point to the other, varying its orientation. The equilibrium configuration is found through the non-trivial minimization of the functional. Equation (2.20) can be rewritten using dimensionless quantities dividing G_L by $\mu_0 M_s^2 V$:

$$g_L = g_{ex} + g_{an} + g_m + g_z = \\ = \frac{1}{V}\int_V \left\{ \frac{{l_{ex}}^2}{2}\left[(\nabla m_x)^2 + \left(\nabla m_y\right)^2 + (\nabla m_z)^2\right] + Kf(\boldsymbol{m}) - \frac{1}{2}h_M \cdot \boldsymbol{m} - h_a \cdot \boldsymbol{m} \right\} dV$$

where $K = 2k_1/\mu_0 M_s^2 = \boldsymbol{H}_{an}/M_s$ is the *escape factor* and $l_{ex} = \sqrt{A/\mu_0 M_s^2}$ is the *exchange length*, which is the shorter length scale over which the magnetization can be tilted to minimize the energy if only the exchange and dipolar interaction are considered.

Magnetic materials can be classified according to their value of K: if $K \ll 1$ they are called *soft materials* (for example Nickel and Permalloy), which correspond to having a small anisotropy field, while if $K \gg 1$ they are referred to as *hard materials* (for example Cobalt) and have a high coercive field. As an example, if considering a small sphere of radius R, the free energy function of soft and hard materials can be used to understand the possible stable configuration as a function of R/l_{ex}.

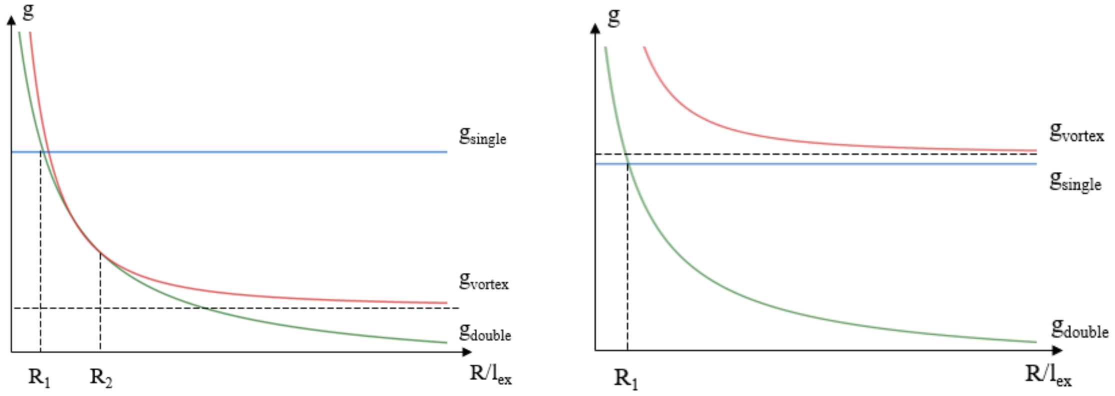

(a) (b)

Figure 2.8: (a) free energy function for single domain, double domains, and vortex configuration for soft materials; (b) free energy function for single domain, double domain and vortex configuration for hard materials

The possible configurations under investigation are the *single domain* configuration, the *two domains* configuration, and the presence of *vortexes* inside the sphere. In the case of soft materials, as shown in Figure 2.8(a), for smaller radius the most favorable configuration is the single domain one, while increasing R the system changes into a two domains system. There is a radius R_2 however where the energies of the single domain and of the two domains configurations are equal: in this case, there is *instability* and vortexes can be present.

In the case of hard materials (Figure 2.8(b)), on the other hand, having $K \gg 1$, the two energy functions of single domain and two domains configuration are never equal: in this case then, the vortexes are not allowed, and only single or two domains will be present.

2.1.5 Brown equation

The problem of finding the equilibrium configuration of the magnetization for equation (2.20) is extremely complex since ***m(r)*** is varying inside the solid. The solution for finding the stable configuration of the magnetization was first introduced in 1940 by Brown [21] using a variational minimization procedure. Starting from the equilibrium configuration $\boldsymbol{m}^{(0)}$ and considering small variations of it such that:

$$\begin{cases} m_x = m_x^{(0)} + \varepsilon \cdot u(\boldsymbol{r}) \\ m_y = m_y^{(0)} + \varepsilon \cdot v(\boldsymbol{r}) \\ m_z = \sqrt{1 - m_x^2 - m_y^2} \end{cases}$$

where $u(\boldsymbol{r})$ and $v(\boldsymbol{r})$ are functions varying in space, ε is much smaller than 1 and the boundary condition of $|\boldsymbol{m}(\boldsymbol{r})| = 1$ was imposed. The conditions for the magnetic configuration that minimizes the free energy function are:

$$\begin{cases} \boldsymbol{m} \times \boldsymbol{H}_{eff} = 0 \\ \dfrac{\partial \boldsymbol{m}}{\partial \boldsymbol{n}} = 0 \end{cases} \tag{2.21}$$

being ***n*** the unitary vector normal to the surface of the magnetic body and $\boldsymbol{H}_{eff}$ an effective magnetic field written as:

$$\boldsymbol{H}_{eff} = \frac{A}{\mu_0 M_s} \nabla^2 \boldsymbol{m} + \boldsymbol{H}_M + \boldsymbol{H}_a - \frac{1}{\mu_0 M_s} \frac{\partial f_{an}}{\partial n} \tag{2.22}$$

Equation (2.21) and (2.22) are named *Brown equations* and according to them the equilibrium magnetic configuration lies parallel to $\boldsymbol{H}_{eff}$ everywhere, and no torque is experienced by the magnetization.

2.1.6 Landau-Lifshitz-Gilbert equation

The Brown equations not only show the equilibrium configuration of the system, but also represent the starting point for the analysis of the dynamic evolution of the magnetization inside a magnetic body. Knowing that the magnetic moment $\boldsymbol{\mu}$ can be related to the intrinsic angular momentum **S** through the gyromagnetic ratio γ ($\boldsymbol{\mu} = \gamma \boldsymbol{S}$, $\gamma = -g \cdot e/2m_e$) and that the temporal variation of the angular momentum is equal to the torque applied (*angular momentum theorem*), it is possible to write:

$$\frac{d\boldsymbol{\mu}}{dt} = \gamma \boldsymbol{\mu} \times \boldsymbol{B} \rightarrow \frac{d\boldsymbol{m}}{dt} = \gamma_0 \boldsymbol{m} \times \boldsymbol{H}_{eff} = -\frac{g \cdot e}{2m_e} \boldsymbol{m} \times \boldsymbol{H}_{eff} \tag{2.23}$$

having $\boldsymbol{B} = \mu_0 \boldsymbol{H}_{eff}$ and $\gamma_0 = \gamma\mu_0 < 0$. The general solution of equation (2.23) is an undamped precession of the magnetization $\boldsymbol{m}(\boldsymbol{r})$ around the effective field $\boldsymbol{H}_{eff}$ without ever reaching the equilibrium configuration of $\boldsymbol{m}(\boldsymbol{r})$ parallel to $\boldsymbol{H}_{eff}$. To account for the possibility for the magnetization to reach the equilibrium configuration in a finite time, a phenomenological damping term is introduced describing the dissipation events present in real systems. This is done adding a component to the torque pointing toward $\boldsymbol{H}_{eff}$ to be able to reach alignment, as shown in Figure 2.9. Equation (2.23) is then modified into:

$$\frac{d\boldsymbol{M}}{dt} = \gamma_0 \boldsymbol{M} \times \left(\boldsymbol{H}_{eff} - \eta \frac{d\boldsymbol{M}}{dt}\right) = \gamma_0 \boldsymbol{M} \times \left(\boldsymbol{H}_{eff} - \frac{\alpha}{\gamma\mu_0 M} \frac{d\boldsymbol{M}}{dt}\right) \tag{2.24}$$

with η, α as a fitting damping parameter. The parameter α is a dimensionless number, and it is the most used one between the two: the larger α, the faster the equilibrium configuration is reached. Equation (2.24) is called *Landau-Lifshitz-Gilbert equation*, or LLG equation and describes the precessional damped mode of the magnetization [22], [23].

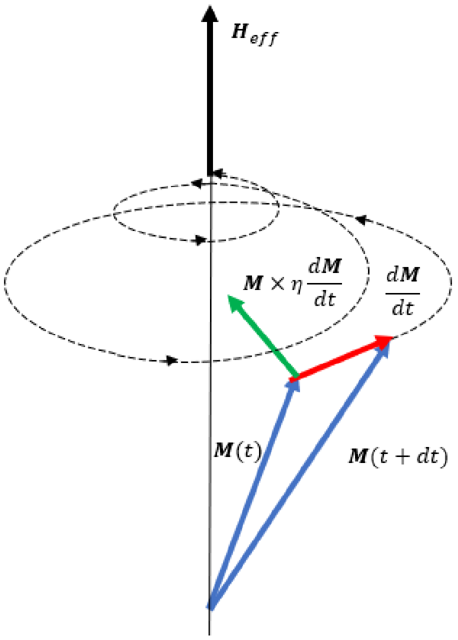

Figure 2.9: vectorial representation of the terms of equation (2.24). Due to the damping term, shown with the green arrow, the magnetization can align to the effective field in a finite time.

There is an alternative expression for the LLG equation as:

$$\frac{d\boldsymbol{M}}{dt} = \gamma_0'(\boldsymbol{M} \times \boldsymbol{H}_{eff}) + 4\pi\lambda \left[\boldsymbol{H}_{eff} - \frac{(\boldsymbol{M} \cdot \boldsymbol{H}_{eff})\boldsymbol{M}}{\boldsymbol{M}^2}\right]$$

with $\gamma_0' = \gamma_0/(1+\gamma_0^2\eta^2 M_s^2)$ and $\lambda = \eta\gamma_0^2/(1+\gamma_0^2\eta^2 M_s^2)$ and with the term on the squared bracket representing only the component of $\boldsymbol{H_{eff}}$ perpendicular to $\boldsymbol{M}$, highlighting the behavior of the damping term to align the magnetization with the effective field.

When solving equation (2.24) a few important variables and parameters can be identified to describe the precessional motion of $\boldsymbol{M}$. The radiant frequency of the precession of the magnetic moment without damping ω_0 is related to $\boldsymbol{H_{eff}}$ by the relationship $\omega_0^2 = \gamma_0^2 H_{eff}^2$, while the precession frequency influenced by the damping is $\omega = \omega_0/(1+\alpha^2)$. Defining $\tau_0 = 1/\alpha\omega_0$ and $\tau = \tau_0(1+\alpha^2)$, the behavior of the azimuthal angle θ (considering $\boldsymbol{H_{eff}}$ pointing towards the negative z-axis) can be described as:

$$\tan\frac{\theta}{2} = \left(\tan\frac{\theta_0}{2}\right)e^{t/\tau}$$

with θ_0 as the initial angle; the azimuthal angle θ tends to change its value in time showing the alignment of the magnetization to the effective field (in this example $\theta = \pi$ correspond to the equilibrium configuration). From the values of α, τ, ω two different situations can be identified: if $\alpha^2 \ll 1$ then $\tau \cong \tau_0$ and $1/\omega \ll \tau$, which is the case of *small damping*, that allows an oscillating behavior with many precessional circulations. On the other hand, if $\alpha^2 \gg 1$, then $\tau \cong \tau_0\alpha^2 = \alpha/\omega_0$ and $1/\omega \gg \tau$, a *large damping* can be identified, with a creep behavior leading to less than one circulation.

2.2 Magnetic domains and hysteresis cycle

Exchange interaction, magnetostatic energy and magnetocrystalline anisotropy are all competing terms that define the magnetic structure of a magnetic body. As highlighted in equation (2.20) to describe the behavior of a real body an integration over its volume is required.

In the next paragraphs, different scenarios will be identified, starting from the simplest case of a uniformly magnetized particle depicted in the *Stoner-Wohlfarth model*, to the symmetry breaking leading to the formation of *domains*, regions of the body uniformly magnetized but with different directions with respect to each other because of the minimization of the magnetostatic self-energy.

2.2.1 Stoner-Wohlfarth model

The Stoner-Wohlfarth model is the simplest analytical model that depicts the presence of a hysteretic behavior and consists in calculating the magnetization curve for a uniformly magnetized ellipsoid with uniaxial anisotropy and with an applied field $\boldsymbol{H_a}$ at an angle α respect to the easy axis, as depicted in Figure 2.10 [16], [18].

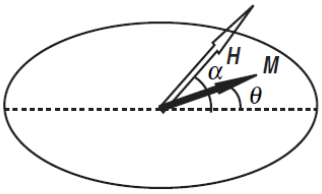

Figure 2.10: uniformly magnetized ellipsoid with magnetization at an angle θ respect to the easy axis and with an applied field $\boldsymbol{H}_a$ at an angle α respect to the easy axis [18].

In general, the energy should be written considering all the terms previously introduced. However, being the particle uniformly magnetized, a few simplifications occur: since all the spins are parallel, the contribution of the exchange interaction is zero. Moreover, the change of the magnetostatic energy during rotation caused by the anisotropic shape of the body is accounted by the anisotropy terms, so the actual dipolar energy term can be considered constant and can be neglected. The general expression of the energy density can be written as:

$$G_L = k_u sin^2\theta - \mu_0 M_s cos(\alpha - \theta) \tag{2.25}$$

with k_u as the uniaxial anisotropy constant. Introducing the dimensionless parameters $g_L = G_L/2k_uV$ and $\boldsymbol{h}_a = \boldsymbol{H}_a/\boldsymbol{H}_{an}$ with $H_{an} = 2k_u/\mu_0 M_s$ the equation becomes:

$$g_L = \frac{1}{2} sin^2\alpha - \boldsymbol{h}_a cos(\alpha - \theta) = \frac{1}{2} sin^2\alpha - \boldsymbol{h}_{a,\parallel} \cos\alpha - \boldsymbol{h}_{a,\perp} \sin\alpha \tag{2.26}$$

having defined $\boldsymbol{h}_{a,\parallel} = \boldsymbol{h}_a \cos\theta$ and $\boldsymbol{h}_{a,\perp} = \boldsymbol{h}_a \sin\theta$, explicitly showing the parallel and perpendicular contributions of the applied field.

The analytical solutions of this problem can be easily found in the two opposite cases of an applied field parallel to the easy axis ($\boldsymbol{h}_{a,\perp} = 0$) and perpendicular to the easy axis ($\boldsymbol{h}_{a,\parallel} = 0$) through the minimization of the energy. For the case of an applied field parallel to the easy axis equation (2.26) becomes:

$$g_L = \frac{1}{2} sin^2\alpha - \boldsymbol{h}_{a,\parallel} \cos\alpha$$

From which the calculated minima and the stability ranges are:

$$\begin{cases} \alpha = 0 \; stable\ for \;\; H_a > -H_{an} \\ \alpha = \pi \; stable\ for \;\; H_a < H_{an} \end{cases}$$

This behavior is depicted in Figure 2.12, which shows the presence of a *hysteresis cycle*. For the same value of H_a the magnetization can have two different magnetization states, which depends on the history of the sample. When the applied field is larger than the coercive field (i.e., anisotropy field) an abrupt change of the direction of the magnetization is observed, aligning $\boldsymbol{M}$ to the external field. This can be understood from an energetic point of view, as shown in Figure 2.11: when the applied field is zero, the two minima are energetically perfectly equivalent and separated by an energy barrier. Switching on the field, the energy of one minimum increases respect to the other, but as long as the intensity of the external field is lower than the coercive one, the system still has to overcome an energy barrier to change its configuration, so it remains in the initial state. Finally, when H_a is larger than the coercive field, the system can shift to the only remaining energy minimum of the system, which correspond to tilting the magnetization in the opposite direction.

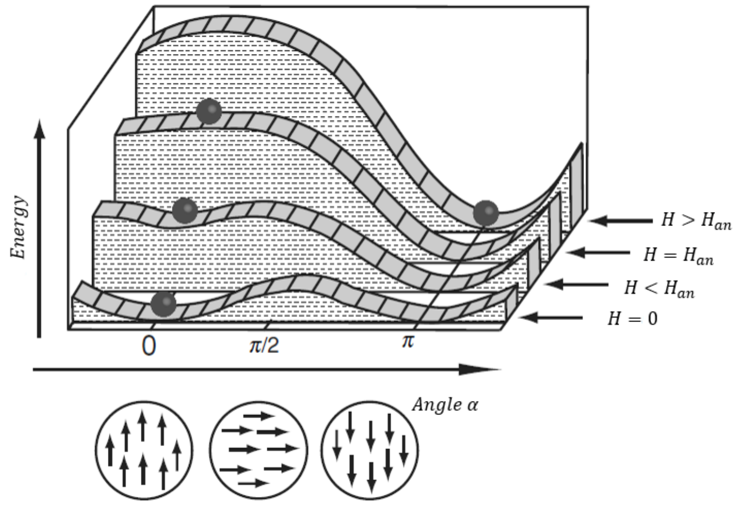

Figure 2.11: energy landscape describing the direction of the magnetization according to the intensity of the applied field [18].

For the case of an applied field perpendicular to the easy axis instead, the energy is expressed as:

$$g_L = \frac{1}{2} sin^2 \alpha - \boldsymbol{h}_{a,\perp} \sin \alpha$$

whose minima are:

$$\begin{cases} \alpha = \frac{\pi}{2} \ \ stable\ for \quad H_a > H_{an} \\ \alpha = -\frac{\pi}{2} \ \ stable\ for \quad H_a < -H_{an} \\ \sin \alpha = \frac{H_a}{H_{an}} \ \ stable\ for \quad |H_a| < H_{an} \end{cases}$$

This means that applying a filed perpendicular to the direction of the easy axis induces a gradual tilting of the magnetic moments of the body, until the coercive field is large enough to drive the magnetization perfectly aligned to it and with modulus equal to the saturation magnetization. In this case then no hysteresis cycle is present, and as soon as the applied field is set to zero, the magnetization immediately realigns with the direction of the easy axis, as shown in Figure 2.12.

Of course, when the angle is neither 0 nor 90° respect to the easy axis, the obtained result is a hysteresis cycle that is not anymore perfectly squared, and will more and more resemble a straight line passing from the origin the more α moves towards $\pi/2$.

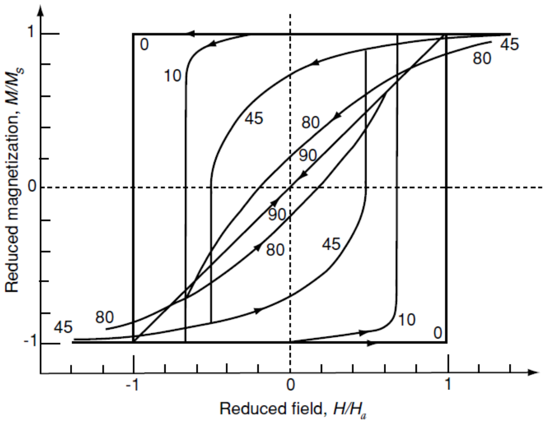

Figure 2.12: magnetization curves for the Stoner-Wohlfarth model for various angles α between the direction of the applied field and of the easy axis. Note the square loop for $\alpha = 0$ and the lack of hysteresis cycle for $\alpha = \pi/2$ [18].

2.2.2 Domains formation and domain walls

In real magnetic bodies the equilibrium magnetic configuration is generally much more complicated than the uniform case, due to the competition of the exchange interaction, magnetic anisotropy and of magnetostatic energy. In 1906 Weiss proposed that a ferromagnetic material is characterized by the presence of a number of small regions, called *domains*, where all the atomic magnetic moments are aligned parallelly [24]. In this way, the local magnetization of the single domain is equal to the saturation value. The direction of the different domains, however, does not need to be parallel, and the direction of the alignment changes almost randomly from domain to domain [16]. The formation of domains can be related to the minimization of the magnetostatic energy of the body. As previously mentioned, the demagnetizing field is created in presence of *surface magnetic charges*, that are given by a system with a component of the magnetization perpendicular to an external or internal surface, and by *volume magnetic charges*, that originates from a non-uniform magnetization inside the body. The presence of domains then tends to create regions where the magnetization is parallel to the surface and going from one domain to the other the rotation of the magnetic moments is gradual: in this way the magnetostatic energy contribution is minimized. If only this term is considered, the magnetization of the body would be characterized by a *flux closure state*, being always parallel to the surface and slowly tilting from one point to the other. However, the exchange interaction is minimized when the magnetic moments are parallel to each other, with their direction governed by the magnetocrystalline anisotropy, so a compromise has to be found between the contributions: inside domains the magnetization is uniform and equal to the saturation magnetization, but the orientation changes between them to allow a minimization of the demagnetizing field [18].

The region of the body over which the magnetization tilts to accommodate the change in orientation from one domain to the other is called *domain wall*. As a matter of fact, a complete flip of the magnetization from one plane of atoms to the next one would be energetically too expensive, so $\boldsymbol{M}$ slowly rotates over many interatomic distances under the combined influence of exchange and anisotropy [18]: this distance is called *domain wall width* and can be calculated from the minimization of the total energy cost for the formation of a domain wall, considering both the exchange and the anisotropy contribution. For the exchange interaction between two spins with different orientation the energy variation is $\Delta E = -2JS^2 \cos\theta = J\,S^2\theta^2$ having considered that $\theta \rightarrow 0$. Considering the spin rotation by π over N states, the energy per unit area becomes:

$$\sigma_{ex} = \frac{JS^2\pi^2}{Na^2}$$

The $1/N$ dependence is consistent with what has been said so far about exchange interaction: when $N \rightarrow \infty$ then $\sigma_{ex} \rightarrow 0$ because the angle between consecutive spins decreases, and so does the exchange interaction contribution. Consider now the anisotropy contribution in the case of uniaxial anisotropy: supposing that the magnetization of the two domains is along the easy axis, the initial and final orientations of the magnetic moments of the domain wall are in the most energetically favorable condition. However, during the rotation, an increase of the energy is present since the magnetic moments are not aligned with the easy axis. This can be modelled as:

$$\Delta E_{an} = \sum_{i}^{N} k_u sin^2\theta_i \cong \frac{N}{\pi}\int_0^{\pi} k_u sin^2\theta d\theta = \frac{Nk_u}{2}$$

that in terms of energy per unit area is:

$$\sigma_{an} = \frac{Nk_u a}{2}$$

showing a linear dependence with N.

The total energy cost for the formation of the domain wall considering both contributions becomes:

$$\sigma_{DW} = \frac{JS^2\pi^2}{Na^2} + \frac{Nk_u a}{2} \tag{2.27}$$

Equation (2.27) highlights the competition between the exchange interaction, that promotes the creation of large domain, and of the anisotropy that favors small domains. The equilibrium configuration is found minimizing the energy respect to N, which leads to an analytic expression of the domain wall width in terms of the exchange integral J and of the uniaxial anisotropy constant k_u:

$$\delta = N \cdot a = \pi S \sqrt{\frac{2J}{k_u a}} = \pi \sqrt{\frac{A}{k_u}} \tag{2.28}$$

where the exchange stiffness introduced in paragraph 2.1.1 has been used. Typical values of δ are of the order of 10-100 nm, explaining why very small particles are in a single domain configuration, since there is no room for the formation of the domain wall [16].

Two common types of domain wall are illustrated in Figure 2.13, namely the *Bloch wall* and the *Néel wall*. In Bloch walls the magnetization rotation is in the plane of the wall, and the divergence of the magnetization is zero. This leads to the absence of volume magnetic charges, meaning that there is no source of demagnetizing field in the wall. In Néel wall, on the other hand, the magnetization rotates within the plane of the domain, giving a higher energy contribution respect to the Bloch wall, as a consequence of the stray field created by the non-zero divergence of the magnetization. In this case, however, the magnetization is always parallel to the surface, so there are no surface charges and no stray field associated to them [18].

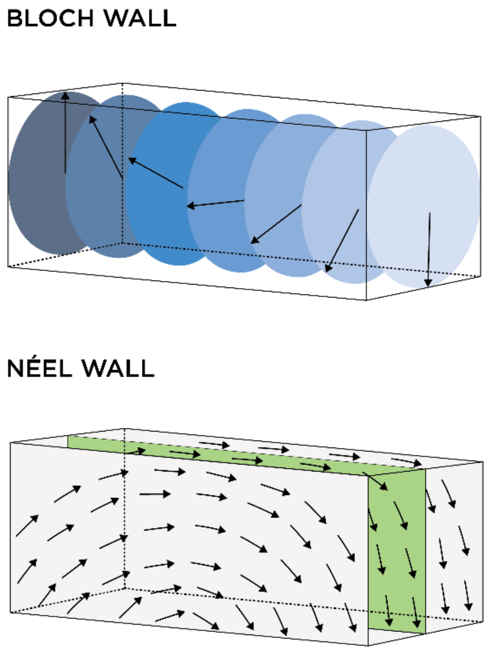

Figure 2.13: schematic representation of the spin rotation in Bloch wall and Néel wall.

2.2.3 Hysteresis loop

The hysteresis loop is not an intrinsic property of a material, but depends on the field, on the shape of the body, on the multidomain composition, and shows features of *coherent rotation* and *domain wall motion*, that are two possible mechanisms for the reversal of the magnetization [18]. Coherent rotation is a mode in which the magnetization remains uniform everywhere and it rotates all together: this leads to an increase of the stray field for the configurations in which $\boldsymbol{M}$ is perpendicular to the easy axis. Domain wall motion, on the other hand, is a slower mechanism that involves the expansion of the domain with the same direction of the external applied field. These two modes are used to describe the behavior of hysteresis loops for high and low applied fields, respectively. Real hysteresis loops are often characterized by the present of jumps and plateaus, in particular around $\boldsymbol{H}_a = 0$. This is known as the *Barkhausen effect*, corresponding to the physical noise of the system, and can be explained by the domain wall motion mechanism in presence of defects: when the domain is expanding under the application of an external field, it may encounter a defect inside the material that stops its expansion. To overcome it, an increase on the field is needed, that is translated in the presence of jumps in the cycle [16], [18].

2.3 Interfacial phenomena

Sor far only the properties and interactions regarding bulk materials and isolated ferromagnets interacting with an external field have been considered. It is also possible, however, to directly engineer very peculiar magnetic systems by growing thin films of magnetic materials [16]. Thin films are extremely interesting because their magnetic properties may differ greatly from the ones of the respective bulk material [16], [18]. Moreover, interesting new phenomena arise as it often happens with systems with broken symmetries, such as *surface phenomena* and *interfacial phenomena*, that characterize two layers that are interacting with each other. The change in behavior is a consequence of the very different environment of surfaces and interfaces respect to bulk systems. Atoms are characterized by fewer nearest neighbors, thus having different band structures with an increase in the density of states at the Fermi level.

As previously introduced, the exchange length is a very important parameter in magnetic systems since it determines the characteristic length over which the magnetization can be twisted, reflecting the balance of exchange and magnetostatic interaction. For typical ferromagnetic systems, the exchange length l_{ex} is of the order of 2-5 nm. For systems with a dimension of the order of the exchange length, the configuration of the surface will propagate all along that direction, without having enough space to change, meaning that the system will be dominated by the interfacial phenomena. As it often happens with surface phenomena, their intensity scales with the inverse of the thickness of the film t, or more in general as $\sim t^{-\alpha}$ with $\alpha > 1$, showing a decrease in their effect on the system when moving from the nanoscopic to the bulk dimension.

2.3.1 Exchange bias interaction

Exchange bias interaction was the first phenomenon that allowed to use antiferromagnets for practical uses. In particular, when a ferromagnetic and an antiferromagnetic film are put in contact a shift in the hysteresis loop is observed, leading to some interesting possibilities for the creation of useful devices. This effect was first observed in 1956 by Meiklejohn and Bean [18], [20] in Co nanoparticles (FM, $T_C = 1390\ K$) coated with CoO (AF, $T_N = 291\ K$). After a cooling procedure below T_N, a shift in the hysteresis loop was observed and the effect identified as a new type of magnetic anisotropy due to the interaction between the ferromagnetic and antiferromagnetic films. Some years later, Néel described a similar effect in coupled thin films [25], [26].

Exchange bias in ferromagnetic-antiferromagnetic coupled bilayers represent a fundamental effect for the development of the devices discussed in this work. In order to have exchange bias, the characteristic disordering temperature of the antiferromagnetic material, called Néel temperature T_N, must be significantly lower than the one of the ferromagnetic material, called Curie temperature T_C. The antiferromagnet has total magnetization $\boldsymbol{M} = 0$ and is characterized by a low magnetic susceptibility and can be hardly oriented by the presence of an external magnetic field. To create exchange bias, a particular process called *field cooling* must be followed: the system is first heated up at the initial temperature T_i such that $T_N < T_i < T_C$. In this way, the ferromagnetic layer is still ordered, while the antiferromagnetic one is in a disordered state and the magnetic moments are randomly oriented. An external field is then applied to set the preferential orientation of the magnetization of the ferromagnetic layers, whose magnetic moments will align parallelly to H_{ext} (Figure 2.14(a)). The system is then cooled down at a final temperature $T_f < T_N$, keeping the applied field: the antiferromagnetic layer will start orienting the magnetic moments in such a way that is influenced by the exchange interaction at the interface with the FM layer. The system will be characterized by an alignment of magnetic moments at the interface between the FM and AF materials, driven by exchange interaction, as shown in Figure 2.14(b) [25]–[27].

(a) (b)

Figure 2.14: To obtain exchange bias in a system with coupled layers of ferromagnet and antiferromagnet a field cooling process must be performed. (a) Initially, while applying an external field, the temperature is raised above the T_N of the AF, which then results disordered, while the FM is ordered and oriented parallel to H_{ext} (being the temperature lower than T_C). (b) The system is then cooled down at a temperature below T_N, with H_{ext} still applied. The AF will order and the magnetic moments at the interface will orient parallelly to the FM layer, due to exchange interaction.

The presence of this additional energetic term has a huge impact in the shape of the hysteresis loop, leading to its shift. Consider the bilayer investigated so far and start with a situation of a large applied field (Figure 2.15(a)): the ferromagnetic layer will be aligned with the external field, and the first layer of the antiferromagnet at the interface will have the same direction, due to exchange interaction. Decreasing the intensity and moving towards negative fields, the ferromagnetic layer starts to tilt its magnetization, while the field has no effect on the antiferromagnet, due to its low magnetic susceptibility. However, due to the presence of the exchange interaction between FM and AF at the interface, in order to shift the magnetization of the FM in the opposite direction (parallel to the external field) the system has to overcome an additional energy cost, which results in a delay of the transition towards the antiparallel configuration at the interface and a shift of the hysteresis cycle (Figure 2.15(b)). Finally, for very large negative field, the system will be characterized by an antiparallel configuration of the magnetizations of FM and AF in contact at the interface (Figure 2.15(c)). Note that the magnetic configuration of the AF has been unchanged throughout the process since the applied field influences only the ferromagnetic layer. If the cycle is performed in the opposite direction starting at negative fields, the system will switch the FM magnetization to a configuration parallel to the one of the AF at the interface even before reaching positive values of the applied field, due to the minimization of the exchange interaction (back to Figure 2.15(a)).

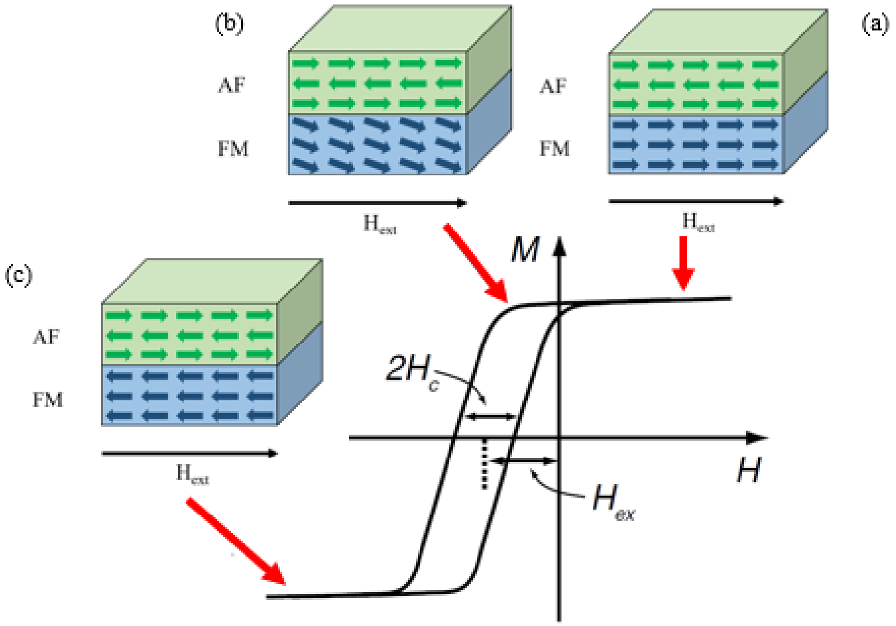

Figure 2.15: typical hysteresis cycle of an exchanged biased system. (a) After the field cooling process, the magnetic moments of the antiferromagnet at the interface are parallel to the magnetization of the ferromagnetic layer, which is oriented according to the external field. (b) When decreasing the intensity of the external filed, the magnetic moments of the FM start to tilt, but the system must overcome an additional energy contribution given by the exchange interaction with the AF layer, resulting in a delay of the reversal of the magnetization and on a shift of the cycle. (c) As soon as the field is large enough, the magnetization of the FM is reversed. H_{ex} is the exchange field corresponding to the shift of the hysteresis loop, while H_c correspond to the coercive field giving half of the width of the loop [18].

From the energetic point of view, this additional term can be modelled as a *unidirectional anisotropy* contribution, which sets a preferential direction of the magnetization due to the exchange interaction with the antiferromagnet at the interface. The energy of the bilayer system when the magnetization lies at an angle ϕ respect to the field applied along the x axis becomes:

$$G_L = -\mu_0 M_p H_x \cos\phi - K_{ex} \cos\phi \tag{2.29}$$

with M_p as the magnetization of the pinned layer. The additional anisotropic term has a linear dependence with $\cos\phi$ and not quadratic as in the case of uniaxial anisotropy, to underline the unidirectionality of the anisotropic behavior. The minimum of the energy is found only for $\phi = 0$ which correspond to the magnetization pointing towards the positive direction and parallel to AFM magnetization in contact at the interface. The unidirectional anisotropy constant K_{ex} can be modelled considering a dependence with the thickness of the ferromagnetic layer and in terms of surface energy, being the exchange interaction an interfacial interaction, such that $K_{ex} = \sigma_{ex}/t_p$. The *exchange bias field* obtained minimizing equation (2.29) is:

$$\boldsymbol{H}_{ex} = \frac{K_{ex}}{\mu_0 M_P} = \frac{\sigma_{ex}}{\mu_0 M_P t_P} \tag{2.30}$$

that correspond to the amount of the shift of the hysteresis loop shown in Figure 2.15. Typical values of σ_{ex} are of the order of $0.1 - 0.2\ mJ/m^2$.

The effectiveness of the exchange bias clearly depends on the thickness of the ferromagnetic layer, but also on the thickness of the antiferromagnetic layers: as a matter of fact, there is a threshold thickness t_{AF}^C necessary to have exchange bias. The exchange surface energy constant σ_{ex} can be related also to the volume anisotropy of the antiferromagnet ($\sigma_{ex} \approx K_{AF} t_{AF}^C$) so that typical values for the threshold AF thickness are of about 10 nm [18], [28].

Despite being one of the most important and practically used interfacial phenomena, exchange bias is still imperfectly understood. One possible explanation comes from the exchange interaction at the interface between the ferromagnetic and antiferromagnetic layers. Considering in this case a perfectly flat interface and typical values of exchange stiffness and interlayer distance, the resulting σ_{ex} would be of about $\sim 100\, mJ/m^2$, which is three order of magnitude higher than the real value. The reason behind this is the fact than only a small fraction of atoms in the interface actually participate effectively in the exchange bias interaction [18]. This may be caused by the imperfect interface between FM and AF, that is characterized by a certain roughness and by the presence of disordered grain boundaries. These grains have uncompensated magnetic moments that are the only ones that actually play a role in the exchange bias interaction. Another possible explanation is related to the anisotropic behavior of the magnetic susceptibility of the antiferromagnet, which means that its response to an applied filed strongly depends on the direction of $\boldsymbol{H}_{ext}$, and has its maximum value for the axis perpendicular to the applied field. Since the magnetization of the ferromagnetic layer will align in the direction of the external field, there is an energetic cost related to the rotation of the magnetic moments of the AF.

The most common way of exploiting the exchange bias interaction is to shift the hysteresis cycle such that at $\boldsymbol{H}_{ext} = 0$ there is only one possible value of the magnetization for the FM layer, which is called *pinned* layer. These systems are often used as magnetic sensor, due to the fact that the pinned layer acts as a reference layer [29].

2.3.2 Néel “orange-peel” coupling

In real devices for everyday use the impact of the surface roughness and corrugation is extremely relevant, leading to a change in the energy of the system due to an interfacial phenomenon called *Néel “orange-peel” coupling* [30]. Consider two ferromagnetic layers, one of which is pinned, separated by a non-magnetic layer, and model the roughness of the layers in the simplest possible way, as a sinusoidal function. If the two layers were perfectly flat, the magnetization would be parallel to the surfaces everywhere, giving $\boldsymbol{M} \cdot \boldsymbol{n} = 0$ and no surface magnetic charges. As depicted in Figure 2.16, however, the roughness causes the formation of surface magnetic charges where the normal to the surface is not parallel to the magnetization, such that the magnetic charge density is $\sigma_M = \boldsymbol{M} \cdot \boldsymbol{n} \neq 0$, which can be either positive or negative according to the direction of the normal of the surface. If the magnetization of the pinned layer and of the free layer are the same, the charges facing each other have opposite signs, leading to a decrease of the total energy of the system, in analogy with the electrostatic case. If the two layers have opposite direction of the magnetization instead, the system will be characterized by same sign charges facing each other, giving an increase in the total energy.

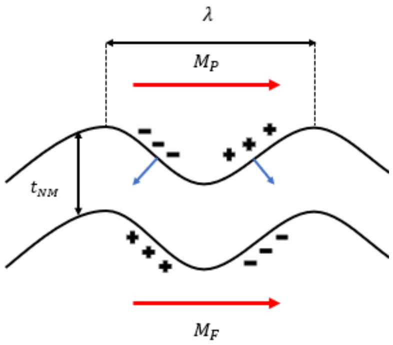

Figure 2.16: The Néel “orange-peel” coupling introduces an additional energetic term due to the roughness of the layers, which leads to the formation of surface magnetic charges. If the magnetization of the pinned layer and of the free layer are parallel, the charges facing each other have opposite sign, leading to a decrease of the total energy of the system. If on the contrary the magnetizations are antiparallel, the charges are of the same sign and the energy increases.

To model this problem, an energy density term can be introduced as $E_{OP} = -J_{OP}\boldsymbol{m}_{pinned} \cdot \boldsymbol{m}_{free}$ with J_{OP} related to the difference in energy between the layers and written as:

$$J_{OP} = \frac{1}{\sqrt{2}\,\lambda}\pi^2 h^2 \mu_0 M_{free} M_{pinned} \exp\left(-\frac{2\pi\sqrt{2}t_{NM}}{\lambda}\right) \tag{2.31}$$

Typical values of J_{OP} can be of the order of $\sim 10^{-4} - 10^{-5}\,J/m^2$. The impact of this effect of the hysteresis loop is similar to the case of the exchange bias, leading to a shift of the cycle. The energy term is added as a contribution for the unidirectional anisotropy as:

$$\begin{aligned} G_L &= -\mu_0 M_F H \cos\theta - J_{OP}\cos\theta \cdot \frac{1}{t_{FM}} \\ &= -\mu_0 M_F \cos\theta \left(H + \frac{J_{OP}}{\mu_0 M_F t_{FM}}\right) \end{aligned} \tag{2.32}$$

where θ is the angle between the magnetization of the pinned layer and of the free layer. Equation (2.32) has been factorized to highlight the presence of a bias field responsible of a shift in the hysteresis cycle, called *Néel field* $H_N = J_{OP}/\mu_0 M_F t_{FM}$. For typical values of the thickness of the FM layer ($\sim 2 - 5$ nm) the intensity of the field can be of the order of 10^2 Oe, that is relevant and need to be considered for any possible application [30].

2.3.3 Interlayer exchange coupling

Interlayer exchange coupling or *bilinear coupling* is an extremely interesting phenomenon and consist in the coupling of two ferromagnetic layers separated by a non-ferromagnetic one, whose thickness is the key parameter leading to different possible magnetic configurations for the system. It was first discovered in 1986 by Grünberg *et al.* [31] when studying Fe/Cr/Fe or Fe/Au/Fe multilayers, where it was shown that with proper thicknesses of the spacer interlayer it was possible to have antiferromagnetic coupling between the two Fe layers. Later in 1991, Unguris *et al.* [32], [33] demonstrated an oscillating behavior of ferromagnetic to antiferromagnetic exchange coupling between the two Fe layers when properly tuning the thickness of the interlayer, as shown in Figure 2.17. It was possible to identify at least two different frequencies of oscillation for the spatial component: a fast oscillation and a slow oscillation [32]–[34].

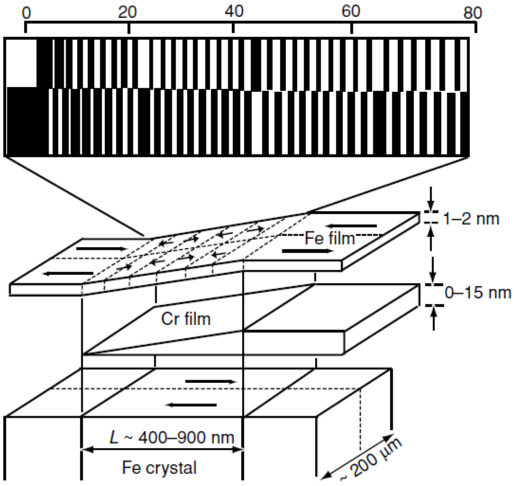

Figure 2.17: Two Fe whiskers are grown with a longitudinal domain wall and are separated by a wedge-shaped Cr spacer. The system shows an oscillating behavior of the exchange coupling for the magnetization of the Fe layers depending on the thickness of the Cr layer [18].

In the past decades, several approaches have been introduced to explain the interlayer exchange coupling [35], [36]. One possible detailed theoretical treatment consists in predicting the oscillation periods for electronic band structures by considering the Fermi surface of the non-magnetic material. As a matter of fact, it is found a relationship with the so-called critical spanning vector $\boldsymbol{Q}$ in reciprocal space. A *spanning vector* is defined as a vector perpendicular to the interface between layers connecting two points on the Fermi surface with opposite velocity; the *critical spanning vector* is then defined as the spanning vector that connects two portions of the Fermi surface that are locally parallel. An example for the Au Fermi surface is shown in Figure 2.18, where $\boldsymbol{Q}_1$ and $\boldsymbol{Q}_2$ are two critical spanning vectors [37].

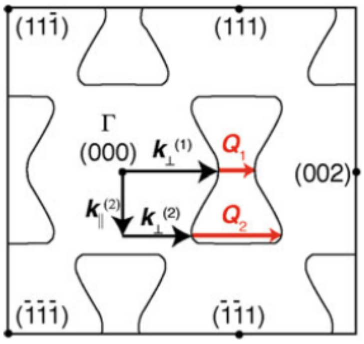

Figure 2.18: Cross section of the Fermi surface of Au with highlighted the critical spanning vectors $\boldsymbol{Q}_1$ and $\boldsymbol{Q}_2$ in the [001] direction [18].

For each critical spanning vector an oscillation period can be associated as $2\pi/\boldsymbol{Q}$ and in the case of multiple critical spanning vectors $\boldsymbol{Q}_i$ the experimentally measured oscillation in the superposition of all the oscillation corresponding to the different $\boldsymbol{Q}_i$. A relationship between the oscillations related to the critical spanning vectors and the periodicity of the coupling can be found with very good agreement. In the case of Au in the [001] direction for example, the experimentally measured periodicity is $1{,}72\ nm$ (having $d_2 = 8.6\ ML$ and $a_{Au} = 0{,}407\ nm$). Considering $\boldsymbol{Q}_2 = 28\ nm^{-1}$ and remembering that the periodic function must be sampled only where the atomic planes are present (correction for the *aliasing,* as shown in Figure 2.19) the corresponding oscillation is $\sin(|Q_2 - g_2|z) = 1{,}87\ nm$ with $g_2 = 2\pi/d_2$, showing good agreement with the experimental data.

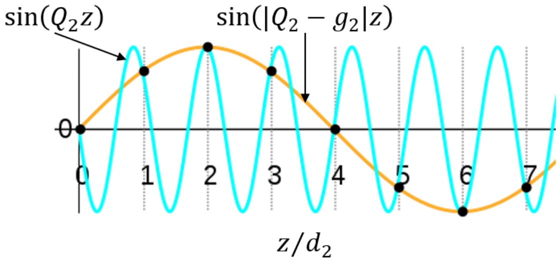

Figure 2.19: The aliasing effect.

There is then a connection between the interlayer coupling and the periodicity associated with the critical spanning vectors of the non-magnetic material, due to the arrangement of the electronic states of the interlayer [37].

Another possible explanation of bilinear coupling involves *magnetic quantum well states* (QWs) forming in the interlayer. To calculate the energy difference of the system in terms of parallel and antiparallel magnetization of the two FM layers, the exchange integral can be written as:

$$J = \frac{1}{2A}(E_{AP} - E_P)$$

where the contribution of both bulk states and quantum wells is considered. According to the *force theorem*, the difference between energies calculated as sum of single particle energies can be approximated as the difference of energies calculated in a self-consistent way, so it is possible to write $\Delta(\sum E_i) \sim \Delta E_{tot}$. It is possible to demonstrate that the presence of QWs is strongly influenced by the orientation of the magnetization of the two FM layers, due to a spin dependent reflection probability for the electrons inside the non-magnetic layer. This can be explained through a simple model involving the analysis of the interface between a noble metal and a 3d-transition metal. While in a noble metal the d-bands are completely filled and are below the Fermi level, in a FM transition metal the 3d-bands are across E_F and characterized by a non-symmetric behavior respect to the spin of the electrons. In this case the electrons whose magnetic moment is parallel to the magnetization of the layer (i.e., spin antiparallel) are called *majority electrons* and they are characterized by an energy decrease of the correspondent d-band. On the other hand, electrons with opposite magnetic moments respect to the magnetization of the FM layer (i.e., spin parallel) are called *minority electrons* and experience and energy increase of the d-band. For this reason, electrons that are crossing the interface between the non-magnetic layer and the ferromagnetic one will experience a different behavior based on their spin. Majority electrons having their d-band at the same height of the noble metal's one are characterized by a high transmission coefficient and low reflection coefficient, while the opposite is true for minority electrons, since no energetic states are available when moving towards the transition metal. This situation is depicted in Figure 2.20.

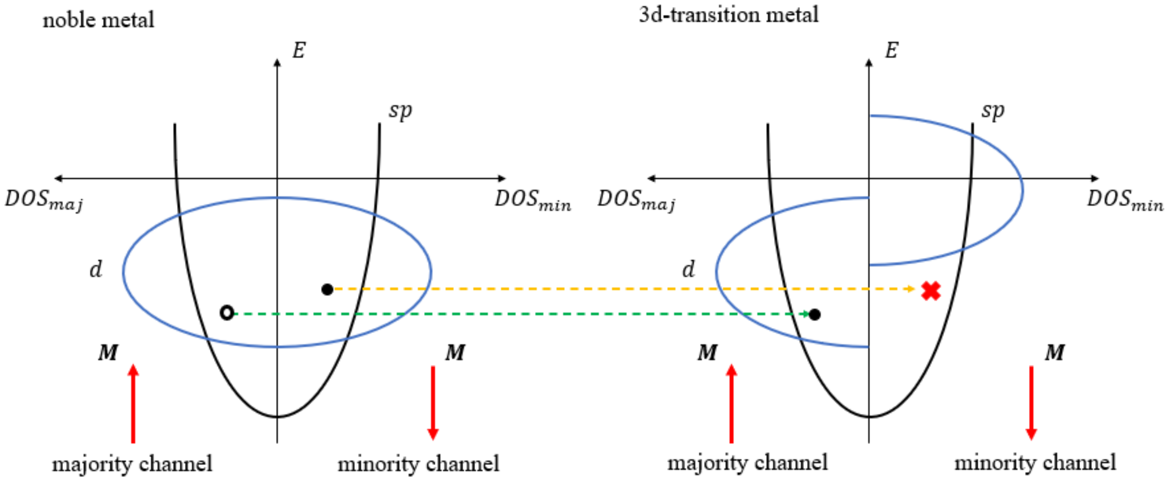

Figure 2.20: schematic of the spin density of states for a noble metal and a 3d-transition metal representing the non-magnetic layer and ferromagnetic layers, respectively. The possible transition between the layers for the majority channel is highlighted in green, while the same it is not possible for the minority channel (orange line).

The creation of quantum wells is then possible only in case of high reflection between the layers since it allows the confinement of the electrons. Considering the parallel and antiparallel configuration of the magnetization of the FM layers it becomes clear that QWs are present only in case of parallel alignment, as shown in Figure 2.21. As a matter of fact, for the antiparallel case, the character of the electrons changes from majority to minority when going from one FM layer to the other since it depends on the relative orientation of the magnetic moment respect to the magnetization. This change is reflected in the transmission coefficient, and confinement is not possible.

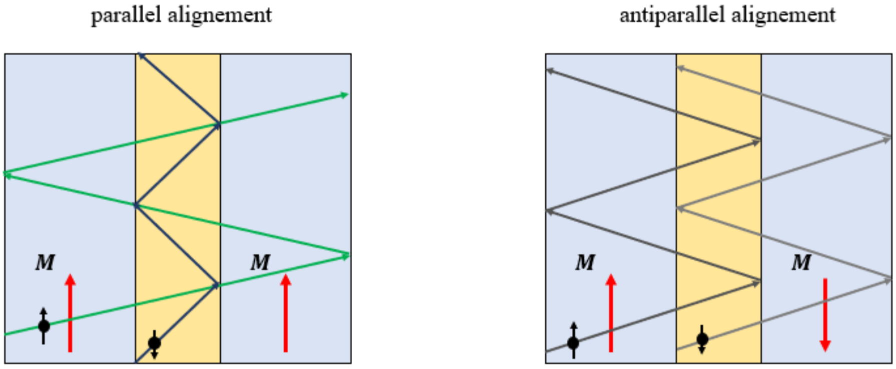

Figure 2.21: Behavior of electrons according to the orientation of the magnetic moments respect to the magnetization of the FM layers. In the case of parallel alignment, the majority electrons have high transmission coefficient, while minority electrons have high reflection coefficient, leading to their confinement and formation of QWs. In the case of antiparallel alignment, since electrons change character from one FM layer to the other, high reflection is present only on one side, so QWs are not allowed.

The presence of QWs is then responsible for the change in energy between the parallel and antiparallel configuration. To calculate it, it is possible to use the so-called *phase accumulation model*. Electrons being confined inside the QWs and bouncing back and forth accumulate a phase shift. Having A_0 as the initial amplitude and A_∞ as the final one, and considering the addition of a phase shift term $R_{R,L}\exp(ikD)$ with $R_{R,L}$ the reflection coefficient of the right (left) layer and D the thickness of the non-magnetic layer, it is possible to write:

$$A_\infty = A_0 \sum_{n=0}^{\infty} [R_R R_L \exp(2ikD)]^n = \frac{[R_R R_L \exp(2ikD)]}{1 - R_R R_L \exp(2ikD)} A_0 \qquad (2.33)$$

In order to have a non-negligible amplitude the denominator must be minimized. In a simple 1D-model the reflection coefficients can be written as $R_{R,L} = \alpha_{R,L}\exp(i\phi_{R,L})$, and the following *phase matching condition* is obtained:

$$2k_F D + \phi_R + \phi_L = 2n\pi$$

which corresponds to constructive interference and a resonance condition. When increasing the thickness of the interlayer, the energy of the resonances for QWs decreases, and each time a level crosses E_F it is immediately populated, and the overall energy of the system increases. When the level moves below E_F, the energy of the system decreases again until the next one approaches E_F. This behavior is depicted in Figure 2.22. The oscillating behavior depending on the thickness of the non-magnetic layer has a period of

$2\pi/2k_F = 2\pi/spanning\ vector$ and correspond to the origin of the oscillations in the interlayer exchange coupling parameter J [38].

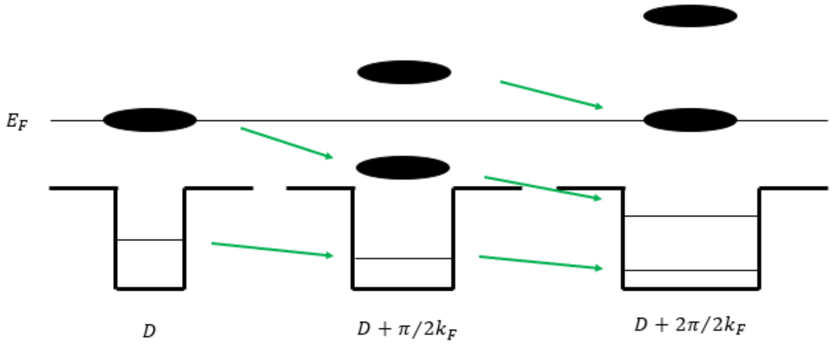

Figure 2.22: Evolution of the quantum well resonances depending on the thickness of the magnetic interlayer. The lines represent the bound states while the ellipses represent the resonances. The arrows show how each resonance change in energy as the thickness increases [38].

For large D, the exchange integral can be written as:

$$\lim_{D\to\infty} J = \frac{\hbar v_F}{4\pi D}\mathbb{R}[(R_\uparrow - R_\downarrow)^2 \exp{(i2k_F D)}]$$

in which the oscillating behavior with period $2k_F$ is present and the difference between the reflection coefficient for spin-up and spin-down is highlighted.

So far, a 1D-model of the Fermi surface has been used. If considering a more appropriate 3D-model of the system (Figure 2.23(a)) it becomes clear that the parallel component of **k** is conserved, while the phase matching condition applies only to the perpendicular component. For each $k_\parallel$ it is possible to associate the correspondent $k_\perp$ that determines the oscillating behavior accordingly. The exchange parameter can be rewritten as:

$$\lim_{D\to\infty} J \cong \frac{\hbar v_F}{4\pi D}\int_{1BZ} \frac{d^2k_\parallel}{(2\pi)^2}\mathbb{R}\{[R_\uparrow(k_\parallel) - R_\downarrow(k_\parallel)]^2 \exp{(i2k_{F,\perp}D)}\} \tag{2.34}$$

The integrand oscillates rapidly, and all the oscillations tend to cancel out except for one dominant term (cut-off) equal to the vector $2k_F$, that correspond to the critical spanning vector. This situation is depicted in Figure 2.23 (b, c) and demonstrate the dependence of the oscillating behavior of J to the critical spanning vector $2k_F$ [38].

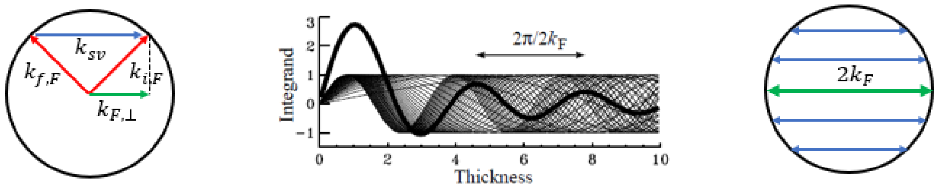

(a) (b) (c)

Figure 2.23: (a) section of the Fermi sphere with highlighted a possible incident k-vector and its correspondent reflected k-vector. For this couple, also the spanning vector k_{sv} is represented, as well as the perpendicular component $k_{F,\perp}$ which determines the oscillation of the exchange integral. (b) Oscillating functions for each possible spanning vector (light curve) and the integral over all of them (heavy curve); (c) section of the Fermi sphere with highlighted in green the critical spanning vector $2k_F$, that gives the only dominant contribution to the exchange [38].

In the past years, other interesting approaches have been developed to explain interlayer exchange coupling. A detailed description of all of them is beyond the scope of this work, but a final comment can be made about the Ruderman-Kittel-Kasuya-Yosida (RKKY) interaction [39]–[42]. In this approach the magnetic susceptibility of a magnetic material described with the free electron gas model is calculated in response to a δ-like perturbation, that can be written as:

$$\boldsymbol{H}(\boldsymbol{r}) = \delta(\boldsymbol{r})H = \frac{1}{(2\pi)^3}\int H\,[\exp{(i\boldsymbol{q}\cdot\boldsymbol{r})}]d^3q$$

The susceptibility obtained in this framework is then:

$$\chi(r) = \frac{2k_F^3\chi_P}{\pi}F(2k_F r) \quad with \quad F(x) = \frac{\sin x - x\cos x}{x^4} \tag{2.35}$$

The shape of the function $F(x)$ is depicted in Figure 2.24. It has been demonstrated that the magnetization changes its sign moving further away from the δ-like perturbation positioned at $x = 0$. The periodicity of the oscillation is equal to $2k_F$, the same as the oscillation of the exchange integral for the interlayer exchange coupling. Moreover, a strong dependency on the position is present, similarly to the relation of J with the thickness of the interlayer demonstrated before.

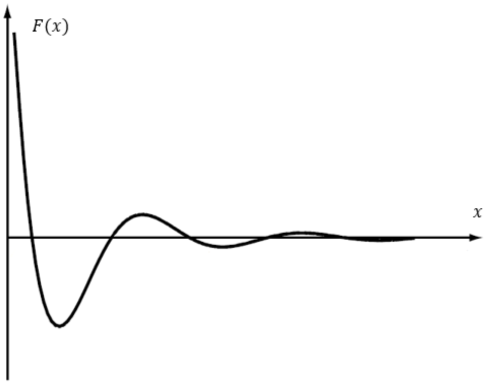

Figure 2.24: qualitative plot of the RKKY function F(x) introduced in equation (2.35) [18].

2.4 Synthetic antiferromagnets

Since the discoveries of the interfacial phenomena described in the paragraphs before and thanks to the advances in the nanofabrication techniques for magnetic materials, the research has focused its efforts on engineering stack of thin nanometric layers of both magnetic and non-magnetic materials [43], which has led to the discovery of many interesting potential applications.

One of the most interesting examples in this context is the creation of the so-called *synthetic antiferromagnets* (SAF), that are the structures studied in this work. Synthetic antiferromagnets consists of two ferromagnetic layers separated by a non-magnetic spacer, whose magnetization at remanence is in the antiparallel configuration. In these systems, an antiferromagnetic layer is often added to the structure in contact with one of the two ferromagnetic layers. The key ingredients for the stabilization of this system are the interlayer exchange coupling and the exchange bias interaction. As already mentioned, the critical parameter for the interlayer exchange coupling is the thickness of the non-magnetic spacer, which determines the relative orientation of the two ferromagnetic coupled layers. In this case, the thickness of the non-magnetic layer is tuned in such a way that an antiferromagnetic configuration between the two is established at zero applied field. On the other hand, the exchange bias interaction between an antiferromagnets and one of the two ferromagnetic layers is established to pin the magnetization of the FM in one direction by inducing uniaxial anisotropy. The presence of EB is extremely important as it is the *only* effect that determines the in-plane orientation of the magnetization of the exchange-biased FM layer at remanence, which in turns sets the direction of the magnetization of the other FM due to the interlayer exchange coupling [1], [43]. As an example, in Figure 2.25 the experimental hysteresis loop of a SAF developed in this work is represented, where the exchange bias sets the magnetization of the topmost layer towards the positive y-direction. For strong, negative fields the magnetization of both FM layers is saturated parallelly along the negative y-direction. By decreasing the field, the interlayer exchange coupling forces the tilting of the magnetic moments establishing an antiparallel coupling between the two FM layers, while at the same time the exchange bias drives the magnetization of the top layer towards the positive y-axis. Finally, applying a strong positive field the antiferromagnetic coupling is overcome and the magnetization of both layers is saturated along the positive y-direction [1].

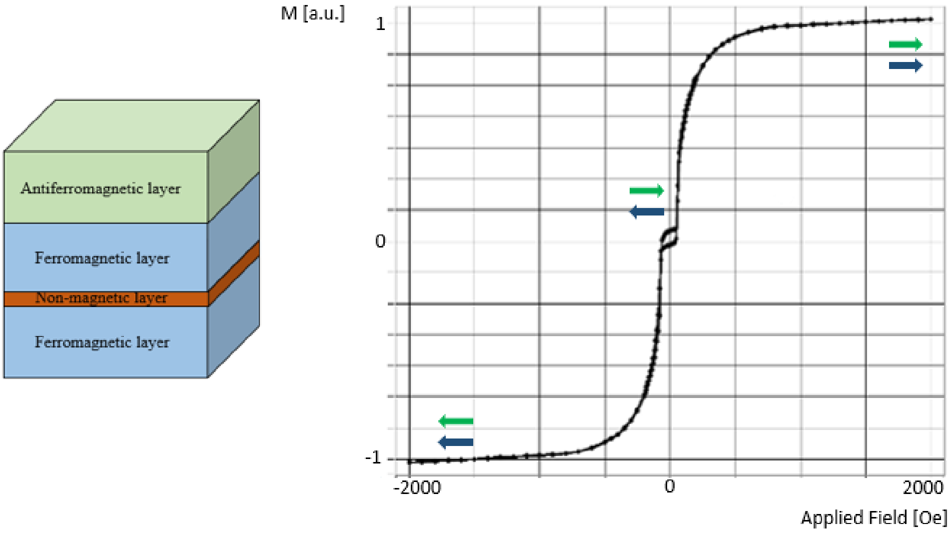

Figure 2.25: Normalized in-plane hysteresis loop of a synthetic antiferromagnetic sample developed in this work. The blue and green arrows show the direction of the magnetization of the bottom and top layer, respectively.

Historically speaking, the antiferromagnetic system was crucial for the discovery of the dependency of the resistance of metallic magnetic multilayers on the relative orientation of the FM layers, with two fundamental phenomena called *giant magnetoresistance* (GMR) and *tunneling magnetoresistance* (TMR), which kick-started the fields of nanomagnetism and spintronics [43]. In this work, SAF systems are used for the generation of nanoscale spin textures as functional elements for the propagation of spin waves, as it will be described in more details in the next chapters.

It is important to underline the key differences between synthetic and natural crystal antiferromagnets. First of all, since interlayer exchange coupling is much weaker respect to the interaction governing the antiferromagnetic order, the manipulation of the magnetic structure is much easier in SAFs. Moreover, the spin texture in SAF is more easily detectable through magneto-optical Kerr effect microscopy, so the dynamics in SAF can be studied using the conventional methods used for ferromagnets [43]. Another very important difference is related to the typical distances of the magnetic order: in natural AF it varies over atomic length scales, while for SAF it is of several nanometers.

2.5 Spin waves: theory and applications

2.5.1 Spin waves theory

As already mentioned in paragraph 2.1.1, the ground state of a ferromagnetic system described with Heisenberg model (equation (2.6)) correspond to a situation where all the spins are lined up parallelly towards a given direction, and their interaction is governed by the exchange interaction. In the Dirac notation, the ground state can be represented as $|0\rangle$. Consider now a perturbation of this system, such as the flip of a single spin in the j-th position on the lattice: the state described as $\left|\downarrow_j\right\rangle$ is *not* an eigenstate of the Heisenberg Hamiltonian, and the true excited state must be represented as a linear combination of all the possible single spin inversions for all the lattice points, such as:

$$|k\rangle = \sum_{j=1}^{N} e^{i\boldsymbol{k}\cdot\boldsymbol{r}_j}\left|\downarrow_j\right\rangle \tag{2.36}$$

Since equation (2.36 presents a phase term, the excited state can be seen as a system where each spin precesses around its axis with a phase shift respect to each other, which correspond to a wave-like perturbation of the system. This simplistic view of the problem, however, does *not* correspond to the description of spin waves inside a magnetic material, but it is a helpful tool to visualize qualitatively the dynamical behavior of the system.

To correctly describe the problem, once again the micromagnetic description of the system must be considered, as already done in the previous paragraphs, where the whole magnetic body is divided into small volumes ΔV with uniform magnetization. The magnetostatic spin waves are then described as wave-like propagating perturbations of the magnetic texture where the magnetization precesses around the axis (Figure 2.26).

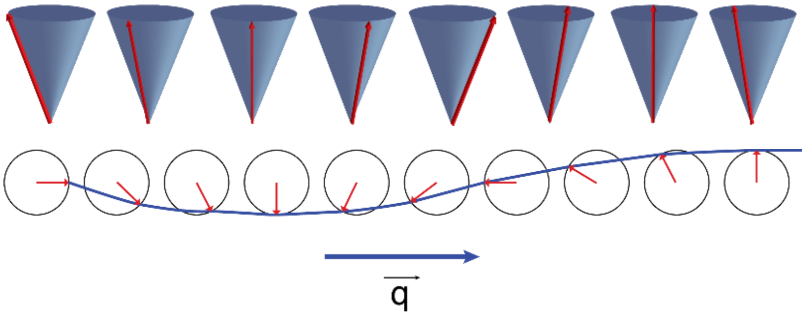

Figure 2.26: schematic representation of the propagation of the spin wave inside the material

In general, in presence of an external applied field $\boldsymbol{H}$, the magnetization $\boldsymbol{M}$ is described as:

$$\boldsymbol{M} = \boldsymbol{M_0} + \overline{\chi}\cdot\boldsymbol{H}$$

Where $\boldsymbol{M_0}$ is the initial equilibrium magnetization and $\overline{\chi}$ is the susceptibility tensor. To correctly describe the evolution of the magnetization in the system, the goal is to obtain the expression of a small-signal susceptibility that can be used in presence of RF and microwave fields associated with the propagation of magnetostatic spin waves. Firstly, consider the problem as described by the lossless dynamic equation (2.23):

$$\frac{d\boldsymbol{m}}{dt} = \gamma_0\boldsymbol{m}\times\boldsymbol{H}_{eff}$$

Where $\boldsymbol{H}_{eff} = \boldsymbol{H}_a + \boldsymbol{H}_{ex} + \boldsymbol{H}_k$ with $\boldsymbol{H}_a$, $\boldsymbol{H}_{ex}$, $\boldsymbol{H}_k$ the applied field, exchange field and anisotropy field, respectively. In a first approximation, only the effect of the applied field will be considered, while the exchange and anisotropy fields will be neglected [44].

Consider now a medium with an applied static field $\boldsymbol{H}_0$ and the equilibrium magnetization $\boldsymbol{M}_0$ is parallel to it and apply a small time-dependent perturbation **h** along a different direction, as represented in Figure 2.27.

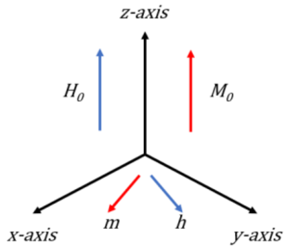

Figure 2.27: schematic representation of a system with an applied field $\boldsymbol{H}_0$ and a small external perturbation $\boldsymbol{h}$ along a different direction, with the correspondent components of the resulting magnetization.

In general, the applied field and the magnetization can be divided into static and time-varying parts as:

$$\begin{cases}\boldsymbol{M} = \boldsymbol{M}_0 + \boldsymbol{m}(t)\\ \boldsymbol{H} = \boldsymbol{H}_0 + \boldsymbol{h}(t)\end{cases}$$

and the resulting lossless dynamic equation becomes:

$$\frac{d\boldsymbol{m}}{dt} = \gamma\mu_0[\cancel{\boldsymbol{M_0}\times\boldsymbol{H_0}} + \boldsymbol{M_o}\times\boldsymbol{h} + \boldsymbol{m}\times\boldsymbol{H_0} + \cancel{\boldsymbol{m}\times\boldsymbol{h}}]$$

in which the first term has been cancelled out since the magnetization is parallel to the external static field due to the saturation of single domain materials ($M_0{\sim}M_S$, with M_S saturation magnetization), while the last one has been neglected being a second order term [44]. Considering a time-dependence with the form of exp $(-i\omega t)$, the linearized dynamic equation becomes:

$$-i\omega\boldsymbol{m} = \boldsymbol{z}\times[-\omega_M\boldsymbol{h}+\omega_0\boldsymbol{m}] \tag{2.37}$$

where $\omega_M = -\gamma\mu_0 M_s$ and $\omega_0 = -\gamma\mu_0 H_0$ which corresponds to the *ferromagnetic resonance frequency*. Solving this equation for the components of $\boldsymbol{h}$ and inverting the equation to have an expression with the form $\boldsymbol{m} = \overline{\boldsymbol{\chi}}\cdot\boldsymbol{h}$, it is possible to obtain the so-called *Polder susceptibility tensor* in the form:

$$\overline{\boldsymbol{\chi}} = \begin{bmatrix}\chi & -i\kappa\\ i\kappa & \chi\end{bmatrix}\ with \begin{cases}\chi = \dfrac{\omega_0\omega_M}{\omega_0^2-\omega^2}\\ \kappa = \dfrac{\omega\omega_M}{\omega_0^2-\omega^2}\end{cases}$$

This relationship highlights a different phase and direction for $\boldsymbol{m}$ and $\boldsymbol{h}$; moreover, in the lossless limit if the frequency approaches the ferromagnetic resonance frequency the elements of the Polder susceptibility tensor diverge.

Consider now the more general case where also the presence of the exchange and anisotropy field is considered, decomposing their contribution in a static and time-dependent component as well. Assuming that the equilibrium magnetization $\boldsymbol{M}_0$ is still parallel to the external applied field $\boldsymbol{H}_0$, and that the static fields are all aligned along the z-direction, the linearized dynamic equation becomes:

$$i\Omega\boldsymbol{m} = \hat{\boldsymbol{z}}\times[h+\lambda_{ex}\nabla^2 m+\overline{\boldsymbol{N}}^a\cdot\boldsymbol{m}-(Z_0+Z_k)\boldsymbol{m}] \tag{2.38}$$

Where:

$$\begin{cases}\Omega = \omega/\omega_M\\ Z_0 = \boldsymbol{H_0}/\boldsymbol{M_S}\\ Z_k = \boldsymbol{H}_{0k}\cdot z/\boldsymbol{M_S}\\ h_k = \overline{\boldsymbol{N}}^a\cdot\boldsymbol{m}\end{cases}$$

With $\overline{\boldsymbol{N}}^a$ as the anisotropy tensor. It is important to underline that only the z-component of the anisotropy field has a contribution, giving rise to a precession in the (x,y)-plane, while the other components are considered as a second order perturbation. It is possible to solve this problem for $\boldsymbol{h}$ such that $\boldsymbol{h} = \overline{\boldsymbol{A_{op}}}\cdot\boldsymbol{m}$ where $\overline{\boldsymbol{A_{op}}}$ is an operator corresponding to:

$$\overline{\boldsymbol{A_{op}}} = \begin{bmatrix}Z_0+Z_k-N_{xx}^a-\lambda_{ex}\nabla^2 & i\Omega-N_{xy}^a\\ -i\Omega-N_{yx}^a & Z_0+Z_k-N_{yy}^a-\lambda_{ex}\nabla^2\end{bmatrix} \tag{2.39}$$

Due to the presence of the exchange operator, it is difficult to invert $\overline{\boldsymbol{A_{op}}}$ and calculate the susceptibility. If the exchange contribution is neglected, it is possible to obtain the so-called *generalized Polder susceptibility tensor* as:

$$\overline{\boldsymbol{\chi}} = \frac{1}{D}\begin{bmatrix}Z_0+Z_k-N_{yy}^a & -i\Omega+N_{xy}^a\\ i\Omega+N_{yx}^a & Z_0+Z_k-N_{xx}^a\end{bmatrix}$$

with

$$D = \left[Z_0 + Z_k - N_{yy}^a\right]\left[Z_0 + Z_k - N_{xx}^a\right] - \left[i\Omega + N_{yx}^a\right]\left[i\Omega + N_{yx}^a\right]$$

For which we have a *resonant magnetic precession* when $D = 0$ [44].

From the theoretical point of view, to the precessional motion of the magnetization there is associated a variation of the magnetic field, which leads to the formation of an electric field as well. It is then possible to study the evolution of the magnetization in the system *as electromagnetic waves in a magnetic media*, for which the following constitutive equations in the frequency domain can be introduced:

$$\begin{cases} \boldsymbol{P}(\omega) = \varepsilon_0 \overline{\boldsymbol{\chi}_e}(\omega) \cdot \boldsymbol{E}(\omega) \\ \boldsymbol{M}(\omega) = \overline{\boldsymbol{\chi}_m}(\omega) \cdot \boldsymbol{H}(\omega) \end{cases} with \begin{cases} \boldsymbol{D} = \bar{\boldsymbol{\varepsilon}} \cdot \boldsymbol{E} \\ \boldsymbol{B} = \bar{\boldsymbol{\mu}} \cdot \boldsymbol{H} \end{cases}$$

Where $\bar{\boldsymbol{\varepsilon}} = \varepsilon_0(\bar{\boldsymbol{I}} + \overline{\boldsymbol{\chi}_e})$ and $\bar{\boldsymbol{\mu}} = \mu_{\boldsymbol{0}}(\bar{\boldsymbol{I}} + \overline{\boldsymbol{\chi}_m})$ are the susceptibility and permeability tensor, respectively. Considering the Maxwell equations for plane-wave solutions in the case of source-free and non-conductive media, two complex wave equations for the fields $\boldsymbol{H}$ and $\boldsymbol{E}$ are derived:

$$\begin{gathered} \left[\bar{\boldsymbol{k}} \cdot \bar{\boldsymbol{\varepsilon}}^{-1} \cdot \bar{\boldsymbol{k}} + \omega^2 \bar{\boldsymbol{\mu}}\right] \cdot \boldsymbol{H} = 0 \\ \left[\bar{\boldsymbol{k}} \cdot \bar{\boldsymbol{\mu}}^{-1} \cdot \bar{\boldsymbol{k}} + \omega^2 \bar{\boldsymbol{\varepsilon}}\right] \cdot \boldsymbol{E} = 0 \end{gathered} \tag{2.40}$$

where an antisymmetric matrix $\bar{\boldsymbol{k}} = \boldsymbol{k} \times \bar{\boldsymbol{I}}$ has been introduced.

It is possible to solve equations (2.40) and obtain an expression for the dispersion relation for some simplified cases. First, for an isotropic media the expected dispersion relation for plane-waves simply becomes: $k^2 = \omega^2 \mu \varepsilon$. Considering then the case of magnetize ferrite, which is an electrically isotropy medium, such that $\bar{\boldsymbol{\varepsilon}}^{-1} = (1/\varepsilon)\bar{\boldsymbol{I}}$, with the permeability tensor written as:

$$\bar{\boldsymbol{\mu}} = \mu_0 \begin{bmatrix} 1+\chi & -i\kappa & 0 \\ i\kappa & 1+\chi & 0 \\ 0 & 0 & 1 \end{bmatrix}$$

non-trivial solutions can be found for $\det[\mathbf{k}\,\mathbf{k} - k^2 \bar{\boldsymbol{I}} + \omega^2 \bar{\boldsymbol{\mu}} \varepsilon] = 0$.

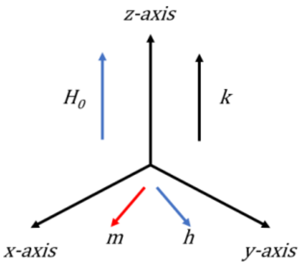

Figure 2.28: schematic of a system with waves propagating in the direction parallel to the applied field

For waves propagating parallel to the applied field, as represented in Figure 2.28, the resulting dispersion relation is:

$$
\begin{aligned}
k_+^2 &= k_0^2\left[\frac{\omega_0+\omega_M-\omega}{\omega_0-\omega}\right] \\
k_-^2 &= k_0^2\left[\frac{\omega_0+\omega_M+\omega}{\omega_0+\omega}\right]
\end{aligned}
\tag{2.41}
$$

The dispersion relation for $\omega_0/\omega_M = 1$ is represented in Figure 2.29, where the wave number has been normalized considering $k_M = \omega_M\sqrt{\mu_0\varepsilon}$ and $k_0^2 = \omega^2\mu_0\varepsilon$. It becomes clear than two differently polarized waves are present in the system, one with the same polarization of the precessional motion (k_+^2) and strongly interacting with it giving rise to a resonant condition, while the other with opposite chirality (k_-^2) has a negligible interaction with the precession of the magnetization [44].

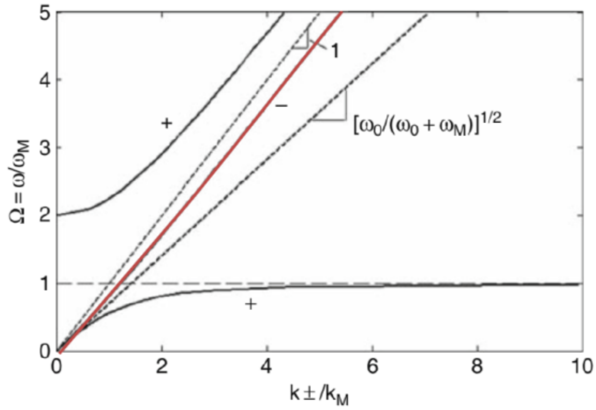

Figure 2.29: dispersion relations for $\omega_0/\omega_M = 1$ [44].

The relative components of the $\boldsymbol{h}$ field are right circularly polarized and left circularly polarized for k_+ and k_-, respectively. To find the expression of the spin waves, the *magnetostatic approximation* is often introduced, corresponding to sufficiently large wave vectors. In this context, the expression $\nabla\times\boldsymbol{h} = 0$ can be demonstrated. Introducing a suitable potential ψ such that $\boldsymbol{h} = -\nabla\psi$ and considering a medium uniformly magnetized along the z-direction, it is possible to obtain the so-called *Walker equation*:

$$(1+\chi)\left[\frac{\partial^2\psi}{\partial^2 x}+\frac{\partial^2\psi}{\partial^2 y}\right]+\frac{\partial^2\psi}{\partial^2 z}=0 \tag{2.42}$$

For a plane wave propagating in an infinite medium with an angle θ respect to the z-direction, the dispersion relation becomes:

$$\omega = [\omega_0(\omega_0+\omega_M sin^2\theta)]^{1/2} \tag{2.43}$$

that is independent from the wavevector. The magnetostatic solution then approximates the low branch of k_+ of the dispersion presented in Figure 2.29. To remove the frequency degeneracy in the magnetostatic approximation, the exchange interaction or some physical interfaces with the corresponding boundary conditions must be added [44]. Considering the exchange interaction and solving for plane waves, an additional term $\omega_M\lambda_{ex}k^2$ is present, such that the more general dispersion relation becomes:

$$\omega = [(\omega_0+\omega_M\lambda_{ex}k^2)(\omega_0+\omega_M(\omega_M\lambda_{ex}k^2+sin^2\theta)]^{1/2} \tag{2.44}$$

2.5.2 Spin waves in thin films: an overview

The solution of the Walker equation presented in the paragraph before, while being useful to understand the behavior of spin waves inside a magnetic body, does not consider the more interesting and technologically relevant case of spin waves in thin films. Considering a thin ferromagnetic film (thickness *d*), three primary types of spin waves can be identified. For all these cases, the appropriate boundary conditions must be set, taking into consideration the discontinuity at the interface and the reflection that the spin waves will experience [45].

In the case of a normally magnetized film along the z-direction as represented in Figure 2.30, a trial solution is often used in the following form:

$$\psi_{film}=\psi_0 e^{ik_t\cdot r}\left[\frac{e^{ik_z\cdot r}+e^{-ik_z\cdot r}}{2}\right]=\psi_0 e^{ik_t\cdot r}\cos(k_z\cdot r)$$

with $\boldsymbol{k_t}$ the wave vector tangent to the propagation direction.

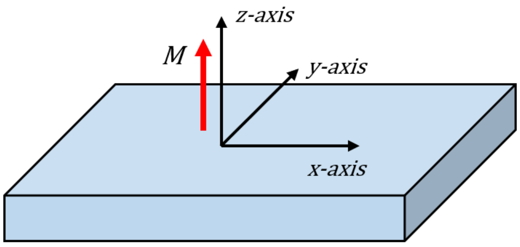

Figure 2.30: schematic representation of a ferromagnetic thin film normally magnetized along the z-direction.

Introducing as boundary conditions for the field that the tangential $\boldsymbol{h}$ field and the normal $\boldsymbol{b}$ fields must be continuous, and assuming that $k_t = k_x$, the solution of the problem $\boldsymbol{h} = -\nabla\psi$ considering the relationship $\boldsymbol{m} = \overline{\boldsymbol{\chi}} \cdot \boldsymbol{h}$ leads to the following equations:

$$\begin{cases} m_x = (-ik_x\chi)\psi_0 \cos(k_z z)\, e^{i(k_x x - \omega t)} \\ m_y = (k_x\kappa)\psi_0 \cos(k_z z)\, e^{i(k_x x - \omega t)} \end{cases} \tag{2.45}$$

while $m_z = 0$ for $z = 0$, and in general just a small perturbation to M_z that it can be neglected. Equation (2.45) demonstrates that $\boldsymbol{m}$ locally precesses around $\boldsymbol{H}$ and that the phase varies linearly along the x-direction of propagation, and the wave amplitude is distributed sinusoidally through the film volume. The spin waves in this case are characterized by the following dispersion relation, represented in Figure 2.31:

$$\omega^2 = \omega_0' \left[\omega_0' + \omega_M \left(1 - \frac{1 - e^{-k_t d}}{k_t d}\right)\right] = -\gamma\mu_0(H_a - M_s) \tag{2.46}$$
$$with\ \ \omega_0' = \omega_{FMR}$$

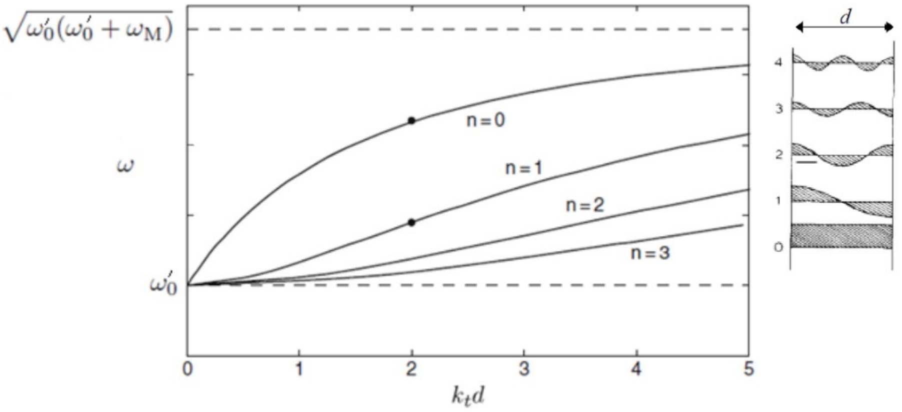

Figure 2.31: dispersion relation for the Forward Volume Magnetostatic Spin Waves in the case of normally magnetized ferromagnetic thin film [44].

It is important to notice that the dispersion relation depends on the magnitude of $\boldsymbol{k}_t$, but not on its direction: unless magnetocrystalline anisotropy is considered, the wave propagation is isotropic in the plane of the film. The group velocity for $kd = 0$ is $\left(v_g\right)^{-1} = 4/\omega_M d,$ and it always has a positive value. For this reason, they are called *Forward Volume Magnetostatic Spin* Waves (FWVMSW). As an example, assuming a typical value for the saturation magnetization $M_s = 140\, kA/m$ and an applied field $H_a = 240\ kA/m$, the resulting value of the ferromagnetic resonance frequency f_{FMR} is of about 7 GHz. Considering a thin film with thickness $d = 1\ \mu m$ and a realistic value from the plot of $k_t d = 2$, the corresponding wavelength is $\lambda_{film} = 2\pi/k_t = 2\pi/(2/d) \cong 3\ \mu m$, that is much smaller than the free-space wavelength at the same frequency $\lambda_{free} \cong 4\ cm$. This result is extremely interesting and technologically relevant: since this mode has a positive group velocity, FVMSW can be used to carry information in the same direction of the wave propagation, but differently from the free-space case, the wavelength is of the order of the μm, which allows the possibility of miniaturization of microwave processing with spin waves. Moreover, unlike other examples of guided electromagnetic waves, all modes have the same cutoff frequency, thus there is no frequency range where only a single mode can propagate. This degeneracy can be lifted if the effect of exchange interaction is added to the system.

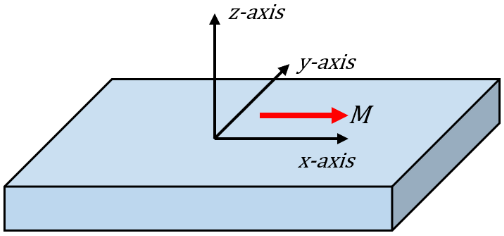

Figure 2.32: schematic representation of a ferromagnetic thin film with in-plane magnetization and propagation direction parallel to the magnetization.

With a similar approach, it is possible to demonstrate the dispersion relation in the case of $\boldsymbol{k_t}$ parallel to the magnetization $\boldsymbol{M}$ (Figure 2.32):

$$\omega^2 = \omega_0 \left[\omega_0 + \omega_M \left(\frac{1 - e^{-k_t d}}{k_t d}\right)\right] \tag{2.47}$$

whose plot is represented in Figure 2.33. In this case, the group velocity is:

$$\left.\frac{1}{v_g}\right|_{kd=0} = -\frac{4}{\omega_M d}\frac{\sqrt{\omega_0(\omega_0 + \omega_M)}}{\omega_0}$$

that always has a negative value. For this reason, the spin waves in this mode are called *Backward Volume Magnetostatic Spin Waves* (BWVMSW). The value of the ferromagnetic resonance frequency is $\omega_{FMR} = \sqrt{\omega_0(\omega_0 + \omega_M)}$, while ω_0 represents the magnetostatic limit for bulk materials with $\boldsymbol{k_t}$ parallel to $\boldsymbol{M}$. Similarly to the FVMSW case, the cutoff frequency is the same for all modes and the amplitude is sinusoidally distributed across the film thickness; however, in this case the propagation is anisotropic in the plane of the film.

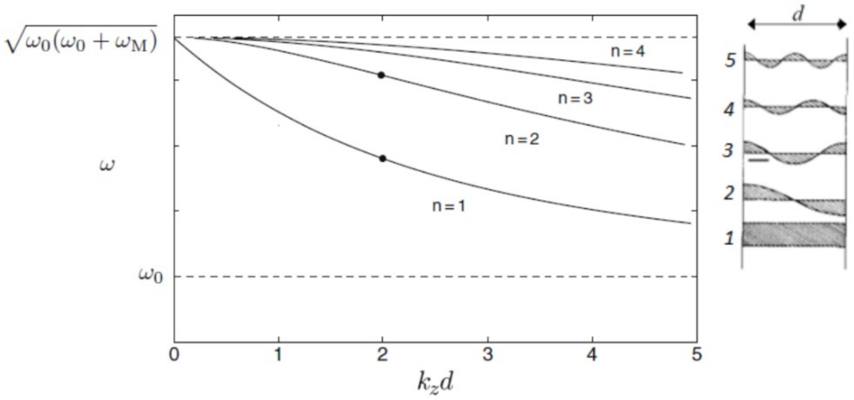

Figure 2.33: dispersion relation for the Backward Volume Magnetostatic Spin Waves in the case of k_t parallel to the in-plane magnetization $\boldsymbol{M}$ [44].

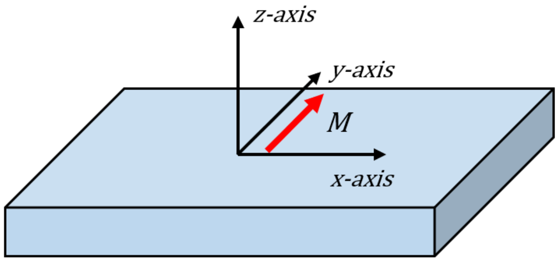

Figure 2.34: schematic representation of a ferromagnetic thin film with in-plane magnetization and propagation direction perpendicular to the magnetization.

Finally, the case of in-plane magnetized thin film with propagation perpendicular to the magnetization ($\boldsymbol{k_t} \perp \boldsymbol{M}$, Figure 2.34). The dispersion relation (plotted in Figure 2.35) is:

$$\omega^2 = \omega_0(\omega_0 + \omega_M) + \frac{\omega_M^2}{4}[1 - e^{-2kd}] \tag{2.48}$$

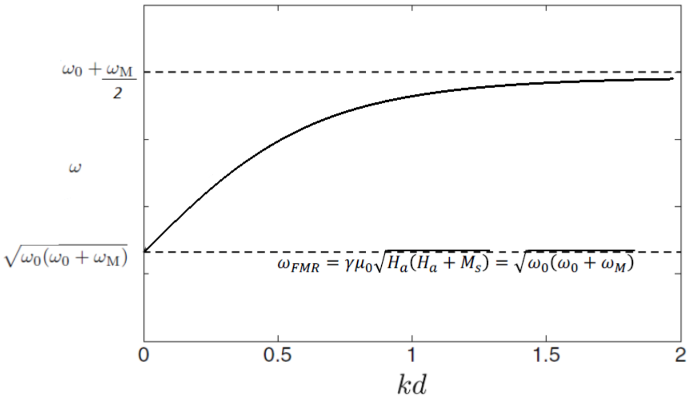

Figure 2.35: dispersion relation for the Magnetostatic Surface Spin Waves in the case of k_t perpendicular to the in-plane magnetization $\boldsymbol{M}$ [31].

The group velocity in this mode is:

$$\left.\frac{1}{v_g}\right|_{kd=0} = \frac{4}{\omega_M d}\frac{\sqrt{\omega_0(\omega_0+\omega_M)}}{\omega_M}$$

which is always positive. The spin waves for this configuration are characterized by the peculiar property of an exponentially decreasing amplitude along the thickness of the film, as shown in Figure 2.36: for this reason, they are called *Magnetostatic Surface Spin Waves* (MSSW) or *Damon-Eshbach* Spin Waves (DE) [46], [47].

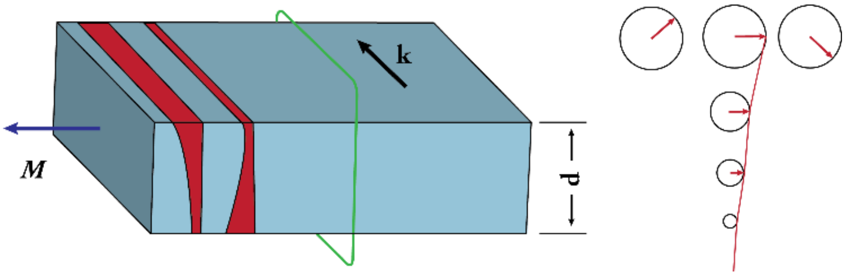

Figure 2.36 schematic representation of the variation of the amplitude of the MSSW along the thickness of the film.

It is important to underline that the Damon-Eshbach spin waves are characterized by an anisotropic propagation, with direction perpendicular to the in-plane magnetization, and by a non-reciprocal propagation on the same interface, such that $\boldsymbol{k} = \boldsymbol{H} \times \hat{\boldsymbol{n}}$.

To summarize, three different spin-wave modes have been identified for a ferromagnetic thin film, according to the relationship between the direction of the propagation and of the magnetization, and the corresponding dispersion relations are plotted in Figure 2.37, together with the corresponding precessional motion of the magnetization inside the film [44], [46], [48], [49]. During this thesis work, the attention will be focuses on the investigation of Damon-Eshbach modes in synthetic antiferromagnetic structures, as it will be presented in Chapter 4 and Chapter 5.

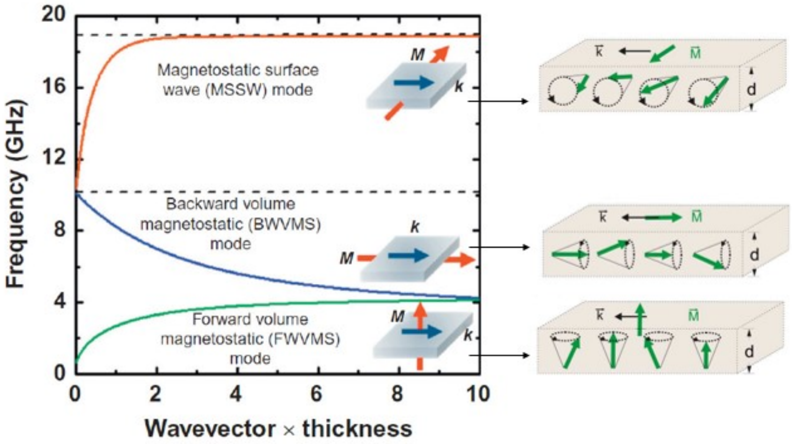

Figure 2.37: dispersion relation for the three possible configurations of FVMWS, BVMWS and MSSW in a ferromagnetic thin film [48] and corresponding precessional motion of the magnetization [49].

Chapter 3

Methods and techniques

In the following chapter, the micro- and nanofabrication techniques and characterization methods adopted in this thesis work will be described. In particular, the focus will be on the techniques employed for studying the morphological and magnetic properties of the samples, and for the observation of the spin-wave emission and propagation. Finally, the micromagnetic simulation methods will be presented.

3.1 Growth and sample preparation

3.1.1 Magnetron sputtering

The magnetron sputtering technique is a Physical Vapor Deposition (PVD) process used for the growth of high-quality thin films of a large variety of materials, even with high melting points (i.e. refractory materials) and alloys, using the erosive action of a self-sustained plasma. This method allows to have excellent adhesion of the film to the substrate, to have high density and to finely control the thickness (down to fraction of nm) and composition of the materials. A schematic representation of the magnetron sputtering working principle is reported in Figure 3.1.

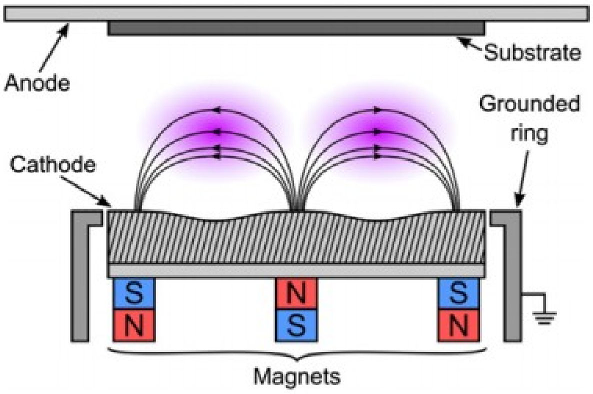

Figure 3.1: schematic representation of the magnetron sputtering process [50].

As illustrated above, a magnetically confined Argon plasma is first ignited inside a vacuum chamber applying a negative potential difference between the target and the substrate. The applied voltage is slowly increased until it reaches a threshold value, called *breakdown voltage*, at which the free electrons present inside the chamber ionize the Ar atoms. The positively charged ions will then be accelerated towards the source material, while the electrons travel towards the substrate establishing a net current. The Ar^+ ions will strike the surface of the target, releasing source material such as atoms, clusters of atoms or molecules via energy transfer and causing the emission of more free electrons. This released material will travel across the chamber towards the substrate, where they may deposit contributing to the thickness of the film. By further increasing the applied bias, a cascade of collisions between the Ar gas and the new electrons travelling towards the anode is obtained, in such a way that the ensemble of charged particles self-sustains (self-sustained plasma).

To increase the efficiency of the initial ionization process and creating a plasma at lower pressure, magnetron sputtering uses an extra magnetic field to trap the free electrons close to the surface of the target, confining the plasma. This confinement has two positive consequences: first, the free electrons, that are rejected from the negatively charged target, cannot move towards the substrate, avoiding its overheating and the damaging of the structure. In addition to this, the electrons will travel across the magnetic field lines in closed circular orbits, enhancing the probability of colliding with the Argon gas by several orders of magnitude, which in turns increases the deposition rate of the target materials onto the substrate [50]. In order to create the extra magnetic field that allows the confinement of the plasma, two permanent magnets are placed behind the target, and this configuration (also depicted in Figure 3.1) is called *planar magnetron sputtering*.

With the magnetron sputtering method both metallic and insulating materials can be deposited: in the first case, corresponding to the easier one, DC configuration is used, since the target itself can directly conducts the electricity. For insulators, the situation is more complicated but can be overcome applying a high frequency RF excitation to the system. This leads to the creation of a DC sheath potential on the surface of the target, that then allows the ion bombardments as before.

Figure 3.2: The AJA Orion 8 Sputtering System.

The instruments employed in this present work for the growth of the magnetic film is an AJA Orion 8 Sputtering System, developed by AJA International Inc (Figure 3.2). It is equipped by 7 2” magnetron sputtering sources with flip-top shutter and 3 1” magnetron sputtering sources with sliding shutter arranged in a confocal sputtering-up configuration (meaning that the source material travels from the bottom to the top). The targets include $Co_{40}Fe_{40}B_{20}$, $Ir_{22}Mn_{78}$, Ru, Ta, MgO, Al_2O_3, Au, Ti, Pt, SiO_2. With this configuration it is possible to deposit thin films with a uniformity for the thickness of ±2% over 3” wafers. The substrate can be heated up to 800°C, and if required it can be mounted on a magnetic sample holder; it also has an automatic closed-loop pressure control. A Cryo Vacuum Pumping in the main chamber maintains the pressure between $10^{-8}/10^{-9}$ Torr, while a load-lock system with a turbo-pump decouples the main chamber from the outside during the loading/unloading procedure of the sample. It allows the possibility to operate both in manual or in fully automated mode: in this last case, the recipes can be created and are remotely executed by the Phase II LabVIEW software. This option is particularly useful when creating complicated multilayers systems, where the thickness of the layers must be precisely controlled.

3.1.2 Electron-beam lithography

Historically speaking the origins of the word *lithography* (from ancient Greek, *lithos* ‘stone’ and *graphein* ‘to write’) can be dated back to the 17th century, when Alois Senefelder discovered that through an accurate chemical process it was possible to transfer the imprinted ink from a limestone to paper as a new printing method. Nowadays, the concept of lithography has evolved and diversified, but the basic idea behind this process is the same: lithography is a process to transfer a pattern from one media to another [51], and is one of the most important procedure in semiconductor industry. There are several different lithographic methods, ranging from the more common photolithography to the high-resolution electron beam lithography. In general, a lithographic process comprises of three steps: first, a polymeric layer called *resist* (priorly deposited over the surface of the substrate) is exposed with a proper excitation. This leads to a change in the solubility properties of the resist, creating a contrast between the irradiated and non-irradiated regions. The resist is then properly developed in a solvent, which selectively wipes out upon chemical reaction the soluble zones, finally allowing to transfer the desired pattern onto the surface. During the lithographic process there are several critical operations that must be carefully performed. For example, the deposition of the resist over the sample surface, since it determines the thickness of the resist film, has a great influence on the efficacy of both the exposition and the development [52]. This step is performed using the *spin coating* technique, consisting of depositing the resist dissolved into a proper solvent over the surface of the sample, which is then put into fast rotation inside a vacuum chamber. Manipulating the rotation speed and the spinning time it is possible to change the resulting resist thickness (of the order of hundreds on nm for electron beam lithography). After the spin coating, a *thermal soft baking* is performed to remove the solvent in excess and stabilize the adhesion of the resist with the surface of the substrate. In particular, two types of resists can be used: if the exposed resist becomes more sensitive to the solvent, they are called *positive resists*, whereas if they become less soluble to the solvent, they are called *negative resists.* Another extremely important step consists in the development of the resist: as a matter of fact, the nature of the resist-developer interaction and the developing time have a great influence on the final shape of the resist profile, and if not properly determined can lead to either un *under*- or *overdevelopment*.

After the lithographic process, the sample is available for either an additive or a subtractive process. For the former, a new layer of material (often a metal) is deposited over the sample: in the regions where the resist is no longer present the metal will be in direct contact with the substrate, while in the other areas it will be over the resist layer. After that, a final *lift-off* procedure is employed, aiming at removing all the resist left on the sample. In this way the final film will be characterized by a metal patterning only in selected regions, corresponding to the ones that have been initially exposed by the beam. The second case, on the other hand, consists in an etching process, that can be performed either in dry or wet environment.

Among all the different lithographic methods, electron beam lithography (EBL) is an innovative process introduced in the 60s in which a focused electron beam is used for changing the solubility of a resist. Figure 3.3 shows a schematic representation of an EBL process, followed by an additive procedure, where a metal layer has been deposited over the surface of the sample, and the subsequent lift-off step is used to remove the remaining resist. Differently from the standard photolithographic methods, which use a mask to selectively pattern the regions of the resist, the EBL is a maskless lithographic technique, in which the patterns are directly written onto the substrate by scanning a highly focused electron beam. Several parameters and factors within the different phases of the process contribute to the quality results, such as the energy and intensity of the electron beam, the molecular structure of the resist and its interaction with the incident electron and the chemistry of the developer. The major advantage of the EBL respect to a photolithographic technique is the fact that the electrons De Broglie wavelengths (for the range of energies used in this method) is of the orders of few nanometers, allowing to produce sub-10 nm features. The only limit in this context is actually related to the scattering of electrons in the resist and by imperfections in the electron optics. Despite not being suitable for large scale productions, it is widely used in nanoelectronics and low-dimensional physics thanks to the extremely high resolution and flexibility.

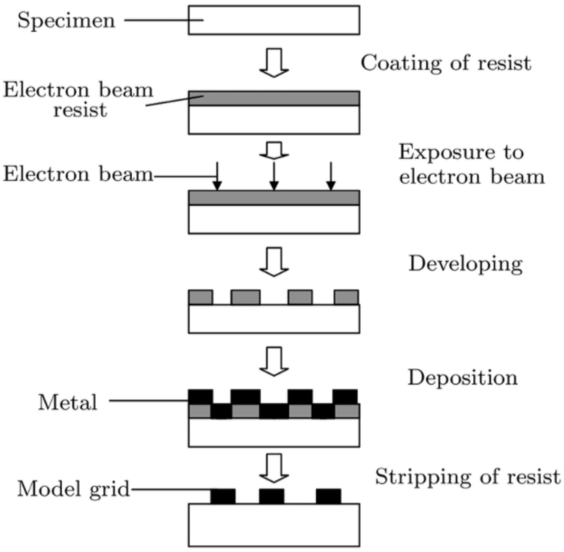

Figure 3.3: schematic representation of the electron-beam lithography, followed by an additive process of a metal layer and the lift-off of the resist [53].

The patterning of the nanostructures presented in detail in paragraph 4.4.2 has been performed with a Vistec EBPG 5000PlusES available at the Swiss Light Source synchrotron facility of the Paul Scherrer Institut, hosted in Villigen. It is a vector-scan direct write tool with a Gaussian shaped beam, characterized by a maximum writing size of 512 x 512 μm^2; the beam has a frequency up to 50 MHz and can be focused on a spot with less than 5 nm in diameter. The operating acceleration voltage is 100 keV, allowing to expose with high precision layers that are several micrometers thick.

3.1.3 Thermal annealing and field cooling

Thermal annealing is a widely used process to modify and improve the magnetic properties of the material. It consists in slowly heating and then slowly cooling down the sample above a certain threshold temperature typical of the system. This allows the atoms to change their configuration, rearranging inside the solid and stabilizing the energetically most convenient state, thus reducing the number of defects and imperfections. In addition to this, if an external magnetic field is present, also the magnetic properties of the material may be changed: in this case, the process is called *magnetic thermal annealing*. This helps to stabilize the magnetic anisotropies inside a ferromagnetic material, allowing for example to set its easy axis along the direction of the external field.

The process of *field cooling*, on the other hand, is a slightly different procedure respect to the magnetic thermal annealing: while the magnetic thermal annealing is defined as the process where the heating of the sample is performed under the presence of an external field, in field cooling the magnetic field is applied during the cooling down of the system. This is particularly important for setting the direction of the exchange bias interaction in systems where a FM-AF interface is present, as described in detail in paragraph 2.3.1: in order to set the EB direction, the systems must be cooled down below the blocking temperature *while* the external field is applied.

In this work, thermal annealing was employed in a vacuum annealing system: the samples were positioned onto a ceramic sample holder in contact with a resistive filament. A turbopump connected to the system allows to reach a pressure lower than 10^{-4} mbar inside the vacuum chamber, avoiding as much as possible any contamination of the sample. The resistive filament raises the temperature of the chamber by Joule heating, which is controlled by a PID controller, which also sets the heating rate. The sample was heated at 250°C for 5 minutes, while an external in plane field of 4000 Oe was present. To set the direction of the exchange bias of the developed samples, the process of field cooling was also performed, and then the system was cooled down while the external field was still present, “freezing” the EB along its direction.

3.1.4 tam-SPL

The fabrication of magnetic devices through the nanopatterning of magnetic materials is mainly performed via conventional lithography, where the chemical or physical changes induced on the sample are irreversible, and it is not possible to finely tune and manipulate the magnetic properties of the material. In this context, the *thermally-assisted magnetic Scanning Probe Lithography* (tam-SPL) is a versatile technique that allows to create reconfigurable magnetic nanopatterns in continuous exchange biased films [54], such as domain walls for the manipulation of the emission and propagation of spin waves. Similarly to the most advanced SPL-based techniques used nowadays, tam-SPL employs the tip of a Scanning Probe Microscope (SPM) to induce local changes of the properties of the surface of the sample and relies on the use of an Atomic Force Microscope (AFM) to control the patterning process. It has several advantages respect to the standard lithographic techniques (i.e. optical lithography and electron-beam lithography): first of all, tam-SPL allows to modify only the magnetic properties of the materials, leaving unaltered the morphology of the sample, opening up the opportunity of creating reconfigurable magnetic devices. In addition to this, it is characterized by a single-step approach, rather than performing multiple subsequent processes. Finally, common instruments already available in most research facilities, such as atomic force or tunneling microscopes, can be modified to implement this technique. The working principle of tam-SPL is the local heating and cooling of an exchange biased system using a hot tip of a SPM in contact with the sample, in presence of an external magnetic field [54]. This basically consists in a local field cooling process described in the paragraph before, where the external magnetic field sets the orientation of the unidirectional magnetic anisotropy of the ferromagnet exchange-coupled with the antiferromagnetic material. Figure 3.4 shows a schematic representation of the process: (a) an exchange biased FM-AF system, which has been initialized upon field cooling setting the magnetization of the FM layer along a preferential direction, is (b) locally heated by a hot tip above the blocking temperature, while an external field is applied to the system in opposite direction respect to the one set during the thermal annealing. The tip is moved with a certain velocity over the surface of the sample, (c) and the previously heated region undergoes a “local field cooling”, in which the spins are fixed in the position set by the external field, leading to a shift of the hysteresis loop in the opposite direction only for the patterned area. In this way, the spins of the patterned area are antiparallelly oriented respect to the ones of the rest of the film. The nanopatterned features are extremely field-resisting, meaning that they cannot be erased or permanently modified only by using an external field: this makes the devices patterned via tam-SPL extremely interesting for magnonic and spintronics applications.

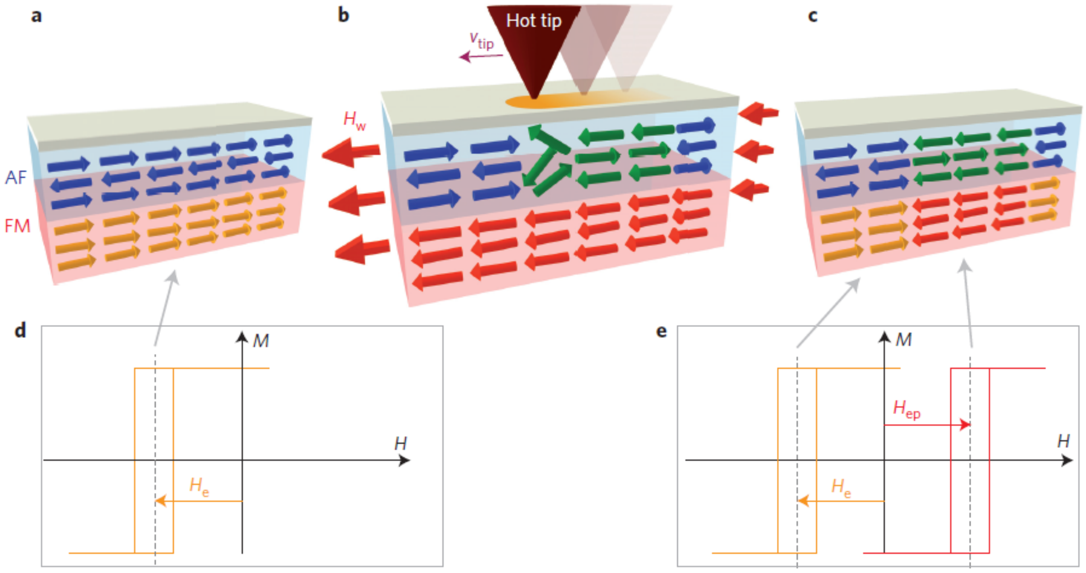

Figure 3.4: working principle of tam-SPL. (a), (d) first, the exchange-biased system undergoes a magnetic thermal annealing procedure, to set the direction of the exchange bias along a preferential direction (initialization field); (b) scanning the hot tip over the surface of the sample with an external applied field in opposite direction to the initialization field produces a local field cooling in that region; (c), (e) upon the removing of the external field, the patterned area fixes the magnetization in the opposite direction respect to rest of the film [54].

One of the most critical parameter during the tam-SPL pattering process is the temperature at the tip-sample interface (T_{int}), since it must be above the blocking temperature to correctly perform the local field cooling. This temperature, however, can be particularly difficult to determine, due to the complex nature of the nanoscale heat transport from the tip to the multilayer [54]. Figure 3.5 shows a scheme that is used to estimate the heating efficiency parameter *c* of the tip, from which the value of the temperature at the tip-sample interface can be derived. In particular, the thermal resistance at the tip-surface contact is modelled as the sum of three contributions, namely the resistance of the tip, the resistance of the interface and the spreading resistance of the sample, such that: $R_{ts} = R_{tip} + R_{int} + R_{spread}$.

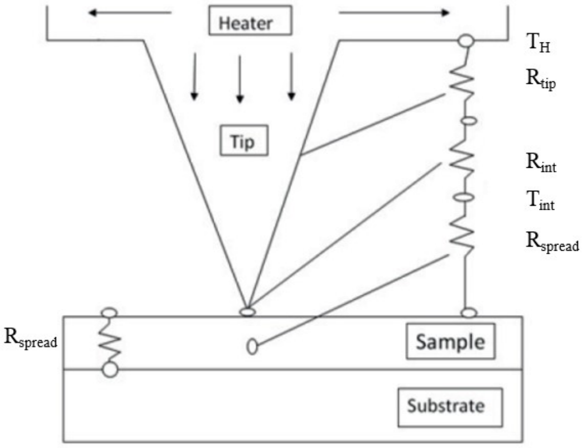

Figure 3.5: schematic representation of the tip in contact with the sample surface, highlighting the different contributions to the resistance at the tip-surface contact [54].

Considering the equivalent thermal circuit of the system, the heating efficiency parameter becomes:

$$c = \frac{R_{spread}}{R_{tip} + R_{int} + R_{spread}} = \frac{T_{int} - RT}{T_H - RT}$$

with RT as the room temperature. With this model it is then possible to derive the value of the temperature at the tip-surface interface with good precision.

To magnetically pattern the samples described in Chapter 4 via tam-SPL, the customized experimental setup of the AFM System Keysight 5600LS (available at the PoliFAB facility, the micro and nanofabrication center of Politecnico di Milano) was used.

3.2 Characterization techniques

3.2.1 Vibrating sample magnetometry

The Vibrating Sample Magnetometer (VSM) is a standard instrument used to characterize the magnetic properties of the sample. The sample is put inside a uniform magnetic field, whose magnitude can range up to a few Tesla. A sinusoidal vibration along the z-axis is induced by the sample holder, as depicted by Figure 3.6: the magnetic moments of the sample will then produce a stray field that oscillates in time. As a consequence of the Faraday-Neumann-Lentz effect, for which $f = -d\phi/dt$ (i.e. electromotive force f depends on the variation of the magnetic flux ϕ in time) it is possible to convert the magnetic flux oscillations in an electric signal thanks to two pickup coils arranged around the system. The resulting electromotive force will then be proportional to the magnetization of the sample, and to the amplitude and the frequency of the vibration. A lock-in amplifier measures the resulting signal, which uses the same reference signal as the one that is triggering the oscillations. In this way it is possible to recover the hysteresis loop of the sample and study its magnetic properties as a function of the temperature and the angle of the magnetization of the sample with respect to the external uniform field.

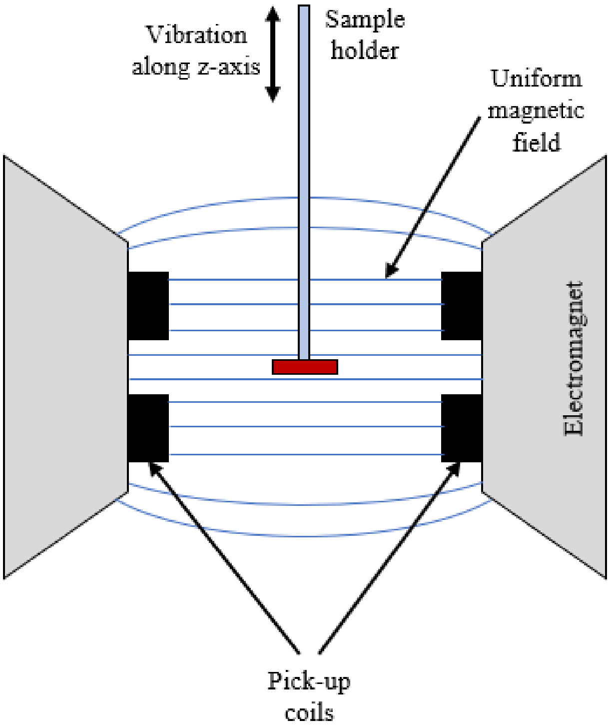

Figure 3.6: schematic representation of a Vibrating Sample Magnetometer.

To characterize the magnetic properties of the samples developed throughout this thesis work a commercial Microsense, LLC. Easy VSM model EZ-9 was employed (Figure 3.7). A maximum field of 2.25 T can be applied, and it can measure magnetic moments down to μemu. In addition to this, it allows a fully automated rotation of the sample of 360° and it is possible to support operations with a temperature ranging from 100 K to 1000 K and a temperature rate up to 60-100 K/min.

Figure 3.7: the Microsense, LLC. Easy VSM model EZ-9.

3.2.2 Atomic force microscopy

The ability to observe individual atoms was an elusive goal until the introduction of the Scanning Tunnelling Microscope (STM) in 1981 [55]. The introduction of this revolutionary instruments represented an extraordinary breakthrough in material science, allowing for the first time to observe the individual surface atoms of flat samples. Despite its incredible success in the past decades, however, the STM presents important limitations, mainly related to the nature of the investigated sample, which must be conductive since the investigation is carried out through the measurement of the tunneling current flowing from the STM-tip to the sample. Moreover, the use of STM is mainly restricted to ultrahigh vacuum conditions, since in ambient conditions the conductive properties of the surface of the investigates sample is constantly changing due to the adsorption and desorption of atoms present in the surrounding atmosphere. In this context, the invention of the *Atomic Force Microscope* (AFM) in 1986 allowed to overcome this problems: because the electrical conductivity of the sample is not required, the AFM can virtually image any flat solid surface, investigating metals, insulators, semiconductors, hard and soft materials, either in air, liquid or vacuum, achieving a resolution down to the atomic level [55], [56]. In addition to this, it also allows to manipulate the matter, as already explained in paragraph 3.1.4. The AFM belongs to the wide family of Scanning Probe Microscopes (SPM), for which the surface of the sample is raster scanned with a peculiar probe (constituted by a cantilever made of silicon or silicon nitride with a very sharp tip at the end), and through an active feedback loop it is possible to determine in different ways the morphology of the sample and some of its properties. In the case of the AFM, the probe measures the Van der Waals forces between the tip and the surface of the sample, which can be either attractive or repulsive according to the relative distance between the two. This will lead to the deflection of the cantilever, which depends on its stiffness and can be expressed in terms of the elastic constant. The bending of the cantilever can be detected with several methods: among these, the most common one consists in using a laser beam pointed on the backside of the cantilever, and the reflected beam is measured with a partitioned photodiode which allows to record both its vertical and lateral deflections. These movements are then analyzed by a computer, which through a controller drives the piezoactuator that controls the raster scanning of the sample. A schematic representation of the described working principle of an AFM is shown in Figure 3.8.

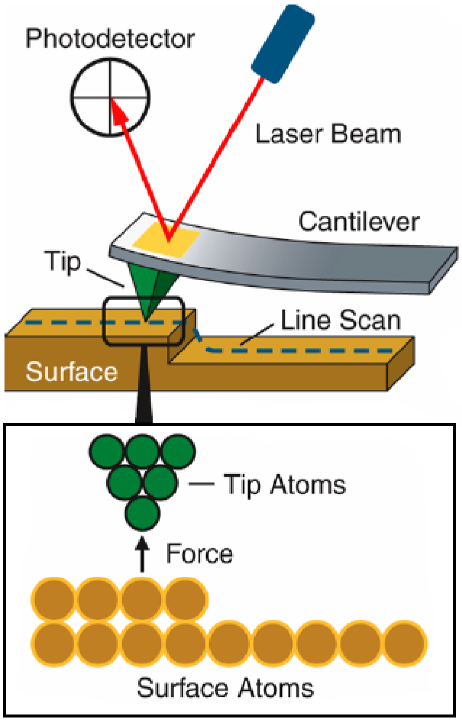

Figure 3.8: schematic representation of the working principle of an Atomic Force Microscope [57].

The morphology of the sample can be investigated in two different ways, either keeping constant the force acting between the tip and the sample or the distance between the two. In the first case, a reference set point is arbitrarily decided by the user, depending on the relative height of the tip respect to the surface. When changing the position of the probe, the cantilever will experience a deflection, depending on the variation of the morphology. This change is recorded and compared through a negative feedback loop to the reference set point, and their difference triggers the signal to the piezoelectric actuator which will restore the force to the set point on the next scanner movement. In the second case, on the other hand, the negative feedback loop is switched off and the bending of the cantilever is simply recorded without comparing it to a reference set point. In this case, the surface of the sample must be particularly flat, otherwise it may happen that in presence of extreme variations on the morphology the tip scratches the surface, deteriorating its shape and disabling further investigations of the sample.

It is also possible to define two different operation modes for the AFM, depending on the type of tip-sample interactions that is acting on the system. According to the Lennard-Jones model, the potential describing the Van der Waals forces can be represented with the curve shown in Figure 3.9. If the tip and the sample are very close to each other, the probe will experience a repulsive force (the slope of the potential is negative), while as the tips moves away from the surface the attractive forces will become dominant. Based on this model, the AFM can work in *tapping mode* (dynamic) or *contact mode* (static). For the former, which is based on the attractive interaction between tip and sample, the cantilever is put into vibration at a certain frequency, close to the resonance frequency of the system. When moving along the surface of the sample, the variation in the strength of the interaction will lead to a shift in the resonance frequency: this change will result in a change of the amplitude and on the phase of the oscillations, which is measured by the detector and that will contain information about the morphology and the properties of the sample, respectively. Moreover, thanks to the negative feedback loop, the relative height of the tip is restored to its reference value and the same process is repeated for each scanning point. In the second case, on the other hand, the tip is put into close contact with the surface of the sample, where the repulsive forces are dominant. This mode is extremely sensitive to the morphology of the sample, and it is possible to achieve very high resolutions.

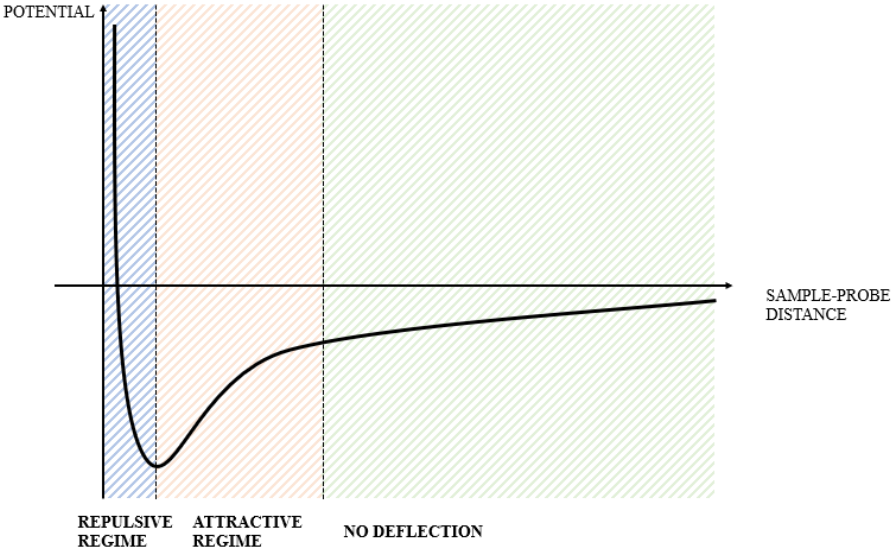

Figure 3.9: general shape of the Lennard-Jones potential describing the Van der Waals forces acting between the tip of the AFM and the surface of the sample. If the two are very close, the repulsive force will dominate the interaction, while when moving further away from the surface the tip will experience an attraction towards it.

The AFM can be modified and customized in several ways, in order to measure different types of interactions. In the context of this thesis work, it is important to mention the *Magnetic Force Microscope* (MFM), which allows to characterize magnetically the surface of the sample using a properly magnetized tip. The working principle of the MFM is based on the detection of the force $F = -\nabla U = \mu_0 \nabla(\boldsymbol{m} \cdot \boldsymbol{H})$, corresponding to the interaction with the dipole of the magnetic tip $\boldsymbol{m}$ with the stray field $\boldsymbol{H}$ generated by the surface of the sample. Of course this is not the only force acting on the system: the Van der Walls forces described before still influence the interaction with the probe. For this reason, to magnetically characterize the sample, the MFM is used is the so-called "*lift-off*" mode. The sample is first morphologically investigated in contact mode, where the Van der Waals forces are dominant respect to the magnetic ones. Once the morphology is known, the tip is put further away from the sample (at about 100-200 nm), where the Van der Waals forces are negligible, while the magnetic ones are dominant. With a second scanning of the sample then the magnetic forces are recorded and comparing the results with the morphology template obtained before it is possible to derive its magnetic configuration.

During this thesis work the topographic and magnetic configuration of the sample were investigated using a Keysight 5600LS AFM system, available at the PoliFAB facility of Politecnico di Milano.

3.2.3 Magneto-optic Kerr effect microscopy

The ability to directly observe the magnetic configuration of the materials, visualizing for example the shape and dimension of its domains is extremely important in the development of novel devices in the field of spintronics and magnonics. As described in the paragraph before, the MFM is able to convert the information about the magnetic forces acting between the tip and the sample in an image representing the magnetic stray field arising from regions with non-uniform magnetization. Using a MFM, however, is not always convenient due to its high measurement time and impossibility to apply an external field in our setup. For this reason, the *Magneto-Optical Kerr Effect* (MOKE) Microscope is extremely useful, being characterized, despite a lower spatial resolution by a larger flexibility and easiness to use in terms of measurement conditions, and by a lower measurement time.

The magneto-optical Kerr effect is a particular phenomenon belonging to the wider family of magneto-optical effects, for which the light changes some of its properties upon interaction with a magnetic material. The Faraday effect discovered in 1845, for example, is related to the rotation of the polarization of linearly polarized light transmitted through a glass immersed in a magnetic field. In 1877 Kerr observed a similar phenomenon, where linearly polarized light reflected by a magnetic medium showed a change in its polarity and the acquisition of a small ellipticity [58]. For the magneto-optical Kerr effect three different configurations can be distinguished, arising from different changes in the light properties respect to the direction of the magnetization of the sample (Figure 3.10). In particular, if the magnetization is perpendicular to the reflecting surface and parallel to the incidence plane (Figure 3.10(a)) the reflected beam will change from linearly polarized light to elliptically polarized light; this configuration is called Polar-MOKE. Similarly, if the magnetization lies in the surface of the sample and is parallel to the incidence plane, the reflected light will experience the same change, from linearly to elliptically polarized light. This configuration is called Longitudinal-MOKE. Historically speaking, these two cases are recognized separately, but the MOKE signal that involves the polarization analysis comes from $\boldsymbol{k} \cdot \boldsymbol{M}$ in both cases, and there is thus no intrinsic difference between the two geometries [59]. In the final configuration, on the other hand, the magnetization is in the plane of the sample but perpendicular with respect to the plane of incidence: for this reason, no rotation of the polarization is observed. This configuration is called Transverse-MOKE (Figure 3.10(c)). Since the change in the ellipticity is generally small, it is often neglected, and the reflected beams are considered as circularly polarized.

Polar **Longitudinal** **Transverse**

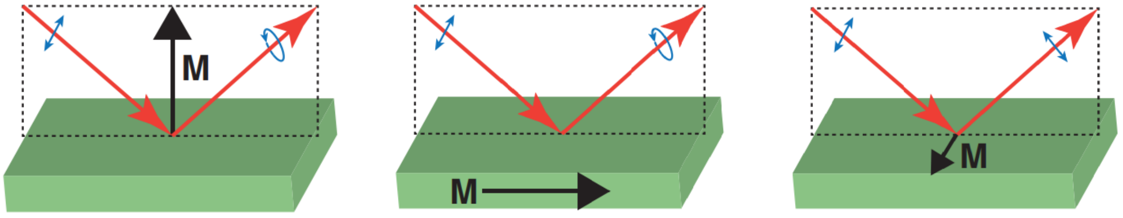

(a) (b) (c)

Figure 3.10: schematic representation of the three configurations of the magneto-optical Kerr effect: (a) polar-MOKE: if the magnetization is out-of-plane and lies in the incidence plane, the reflected linearly polarized light is changed in elliptically polarized light; (b) longitudinal-MOKE: if the magnetization is in-plane and lies in the incidence plane, the reflected linearly polarized light is changed in elliptically polarized light; (c) transverse-MOKE: if the magnetization is in-plane and lies perpendicular to the incidence plane, the reflected linearly polarized light is not changed [59].

Being based on a simple change of the polarization properties of light, the MOKE has attracted a lot of interest for performing the magnetic characterization of materials: the reflected beam contains all the needed information on the magnetic configuration of the materials, both quantitatively and qualitatively. Modifying a simple optical microscope, implementing the so called MOKE microscope, it is then possible to derive the magnetic configuration of the system, analyzing the polarization angle of the reflected beam. The only limitation in this case is given by the penetration depth of the light itself, which limits the analysis on the surface of the sample.

The MOKE microscope employed in this work is a custom made instrument, characterized by a five basic elements: a light source, a polarizer, an analyzer, an electromagnet and a photodetector [60]. A LED lamp is used for the lighting apparatus, and the emitted light is collected, focused, and polarized before hitting the surface of the sample. Of particular importance are the slit placed along the transmission path: since the MOKE microscope setup must be able to perform both polar and longitudinal configurations, the slits allow to select the angle of incidence of the light on the surface of the sample (normal incidence for longitudinal-MOKE, wider angles for polar-MOKE). The reflected beam will be characterized by a rotation of its polarization, which is proportional to the magnetization vector of the illuminated region. Using a second polarizer, which is called analyzer, it is possible to convert the angle of rotation into the information on the sample magnetic configuration. Finally, a CMOS camera acquires the 2D image, which is then processed via a dedicated MATLAB software in order to reduce the noise. Managing the noise of the images is one of the most crucial aspects of this instrument: first, the background noise must be cancelled, since it is much bigger than the MOKE intensity. To do so, two images at opposite saturation are taken, averaged, and subtracted from each obtained frame. This results in black/white images, and the different grayscale represent different orientation of the magnetization. In addition to this, also the distortion of the images as a consequence of the Faraday effect must be taken into consideration, so during the post-processing of the image a second-order fitting is performed. Finally, several frames for each image are taken and averaged together, to reduce the electrical noise coming from the instrumentation. The objectives used in this work corresponded to 10x, 20x and 50x magnification. In Figure 3.11 a schematic representation of the instrument is reported.

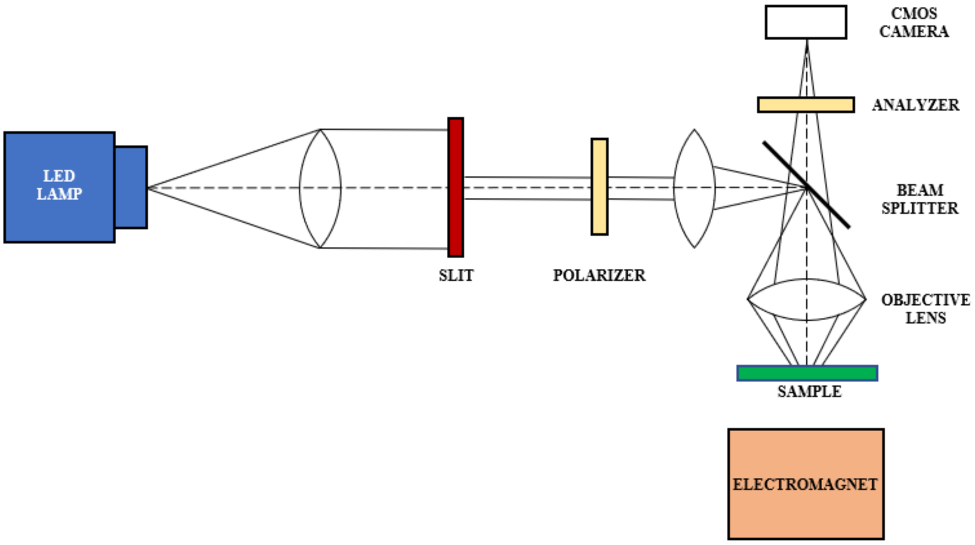

Figure 3.11: schematic representation of the structure of a MOKE microscope.

3.2.4 Scanning Transmission X-ray Microscopy

The *Scanning Transmission X-ray Microscopy* (STXM) is a synchrotron-based technique that is able to produce high resolution images and to map out several properties of the investigated sample, such as elemental and chemical composition, molecular orientation, oxidation state and, noticeably for the scope of this work, magnetic domains [61]. To study the spin texture and the magnetization dynamics of the samples presented in Chapter 4, static and time-resolved STXM experiments were performed at the Swiss Light Source (SLS) synchrotron facility hosted in the Paul Scherrer Institut (PSI) at Villigen, which is a third-generation synchrotron light source able to accelerate electrons along a 288 m ring up to 2.4 GeV. The emitted photons have a frequency ranging from hard x-rays to the infrared region. The STXM setup at PSI, in particular, allows to achieve a spatial resolution better than 50 nm and uses soft x-rays to investigate the magnetic properties of thin films. One of the most critical element of the STXM instrument is the Fresnel Zone plate (FZP) shown in Figure

3.12(a), which focuses the monochromatic x-ray beam onto the sample, selecting only the first order of diffraction and blocking all the others. Importantly, the sample must be thin enough to be semi-transparent at the appropriate x-ray wavelength. The transmitted photon flux is then measured by the detector placed behind the sample. In Figure 3.12(b) a photo of the STXM setup at the PolLux beamline is reported.

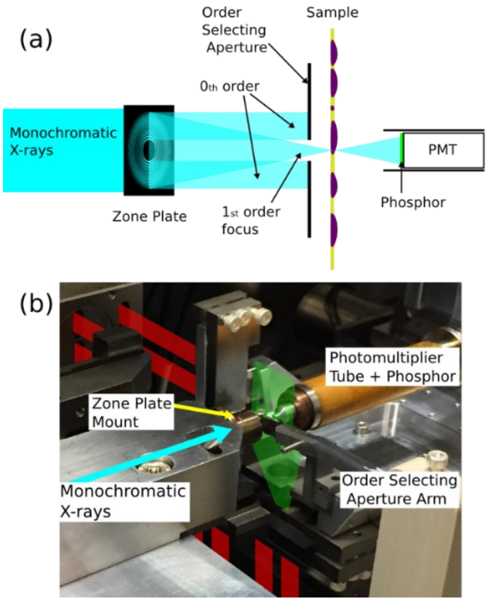

Figure 3.12: (a) Schematic representation of the STXM technique; (b) Photograph of the major components of the PolLux STXM. The position and shape of the plate over which the samples are mounted is indicated in green, while the interferometer beams are indicated in red [61].

To be able to study the magnetic properties of materials, the *X-Ray Magnetic Circular Dichroism* (XMCD) is exploited, which consist in obtaining two different spectra when investigating the sample with right and left circularly polarized light, since they behave differently according to the orientation of the spins inside the system. This is translated in a change in the magnetic contrast, which is proportional to the relative orientation of the magnetization with the direction of the x-ray beam. For this reason, it is possible to probe different components of the magnetization choosing the angle of incidence of the x-rays: if they are normal to the surface, only the out-of-plane component of the magnetization is measured, while if they are tilted it is possible to gain information also on the in-plane components. In order to perform correctly a XMCD measure, the energy must be properly tuned at the resonant absorption edges of the element to investigate. In the case of transition metals, for example, it corresponds to the excitation energy of 2p electrons to 3d states. In this thesis work, the energy was tuned at the Co L_2 and L_3 absorption edges, corresponding to 796 eV and 781 eV, respectively.

One of the main strength of the STXM is the ability to perform time-resolved imaging, thanks to the use of an avalanche photodiode detector (APD). At the PolLux endstation a pump-probe technique is used for this purpose. The pump signal is used to excite the dynamical process, while the probe is necessary to monitor the status of the sample at a given instant of time. By varying the delay time between the pump and the probe signal, a complete picture of the dynamical processes occurring in the sample can be obtained [62]. The SLS synchrotron facility operates on a multibunch filling pattern tuned at 500 MHz, meaning that an x-ray pulse is expected every 2 ns. Since the APD detector is characterized by a bandwidth larger than 500 MHz, it is possible to perform the time-resolved imaging using the entire filling pattern of the synchrotron light source, allowing to acquire time-resolved images in a much more efficient way. In general, as the excitation is frequency locked to the synchrotron, this means that its frequency f (or an integer multiple of it) must be an integer multiple of the synchrotron frequency, such that:

$$N \cdot f = M \cdot 500\ [MHz]$$

where M indicated the number of times the excitation signal is repeated within a period of $N \cdot 2$ [ns]. There are two possible methods for the acquisition of time-resolved images: in the first case, the excitation is synchronized with the 500 MHz master clock of the synchrotron facility, and it is sampled at different intervals by the x-ray pulses belonging to different bunches. Since the system illuminates the sample every 2 ns, the sampling of the state will occur every 2 ns, and it will be possible to identify the points in the excitation that will get sampled, as shown in Figure 3.13, representing the case of N = 7 and M = 7 [62]. To have a sufficiently meaningful statistic, the excitation process is repeated several number of times (of the order or 10^8-10^{10}).

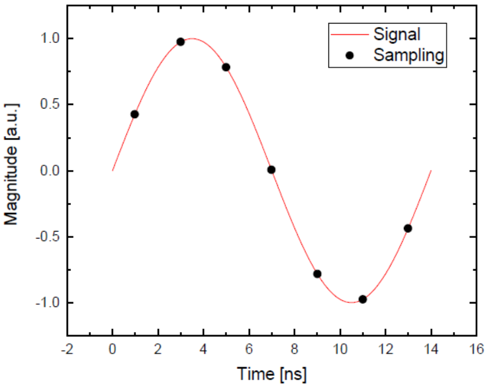

Figure 3.13: example of a time-resolved sampling with N = 7 and M = 7. Note that the sampling points are every 2 ns [62].

In the case of the asynchronous measurements, to obtain the final time-resolved image the collected data is processed one more time through a Field Programmable Gate Array

(FPGA), which is used to recognize to which sampling each of the x-ray bunches is contributing and allows to correctly sort the detection events. In this case, the sampling does not occur over one period of time, but over M periods, as shown by the example in Figure 3.14(a). For this reason, to reconstruct correctly the final time-resolved image, the sampling points need to be reshuffled to obtain a time series over one single excitation period [62]: this is done by calculating the phase at each sampling point, and ordering them respect to their phase (Figure 3.14(b)), leading to the correct reconstructed time-resolved image. Noticeably, this also allows to reconstruct images with a time step smaller than 2 ns and equal to 2/M [ns], further improving the quality of the image.

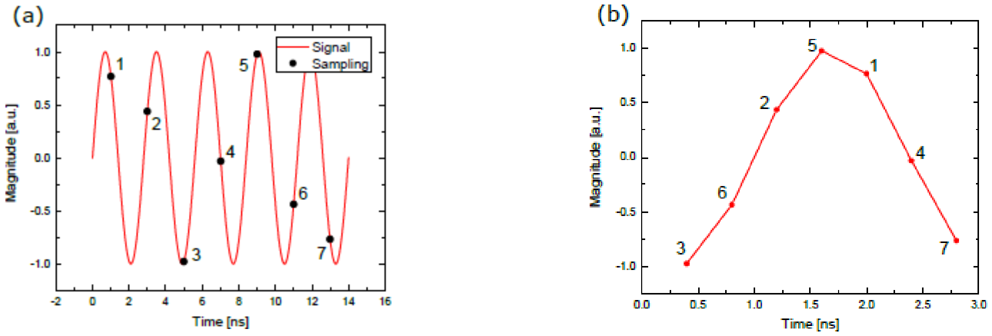

Figure 3.14: (a) example of a time-resolved sampling with N = 7 and M = 5; (b) reconstructed signal after having reordered the sampling points according to their local phase. Note that the final time step is smaller than 2 ns [62].

3.2.5 X-Ray Laminography

X-ray Computed Tomography represents the most established technique for 3D imagining, and it is best applicable to samples whose x-ray transmission does not change exceedingly during the rotational scanning, meaning samples that are ideally cylindrically shaped [15], [63]. However, one problem arises with this method: since in the tomography setup the axis of rotation is perpendicular to the direction of the incident x-ray beam, it is extremely suited for the three-dimensional investigation of bulk samples, but becomes restricted in the case of extended planar sample, due to the fact that they are characterized by an increasing thickness during the sample rotation [6], [15], [63], [64]. This leads to the formation of the so called “missing-wedge” artifact (Figure 3.15(a)), for which it is impossible to access the corresponding information in the Fourier space [15], [63]. For this reason, the reconstruction process of the obtained data becomes particularly complicated, and much information is missing from the final image.

(a) (b)

Figure 3.15: (a) Schematic representation of the filling of the Fourier space with the computed tomography setup ($\theta = 90^\circ$) with the corresponding “missing-wedge” artifact: (b) schematic representation of the filling of the Fourier space with the Laminography setup ($\theta < 90^\circ$) with the corresponding “missing-cone” artifact [63].

A possible solution for this problem corresponds to tilting the rotation axis in such a way that it is no longer perpendicular to the incoming x-ray beam: in this way the associated inaccessible information in the Fourier space is localized within a cone rather than a wedge, as reported in Figure 3.15(b). This generalized method called *Laminography* offers several advantages respect to the tomography setup. First, it allows a much easier analysis of flat objects: since the angle between the incoming x-rays and the surface is constant, the effective sample thickness remains constant as well. For this reason, for the laminography setup it is not required to prepare the sample with a cylindrical shape. In addition to this, it has a much higher degree of flexibility for the selection of the measurement position [15], [63]. Figure 3.16 shows the described difference between the two configurations, with (a) representing the X-ray Computed Tomography setup and (b) the innovative X-ray Laminography instrumentation.

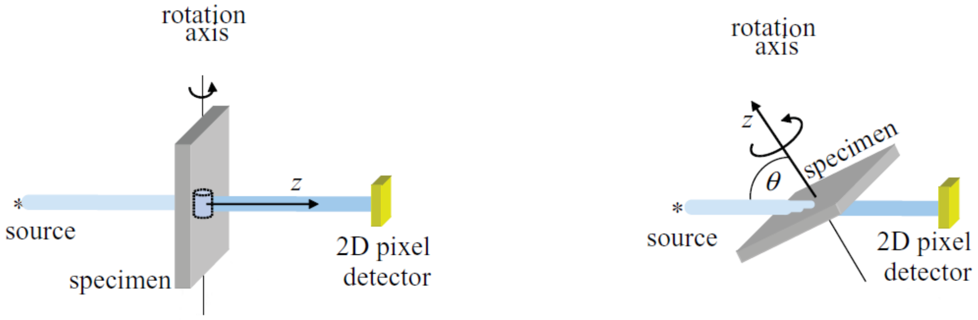

(a) (b)

Figure 3.16: schematic representation of (a) the x-ray computed tomography setup, characterized by a perpendicular rotation axis respect to the direction of the x-ray beam and

(b) the laminography setup, which present a tilted axis of rotation respect to the incoming beam, allowing to analyze flat objects sensibly reducing the reconstruction artefacts [64].

The conventional tomographic techniques mentioned above are generally performed with synchrotron radiation, in particular with hard x-rays with a photon energy above 5 keV. The use of hard x-rays, however, is disadvantageous for the study of thin films, due to their high penetration depth. In contrast, using the less energetic soft x-rays (E < 1 keV) has been recently demonstrated to be particularly favorable for the investigation of thin specimens, with thickness in the µm and nm range, given the strong decrease of the penetration depth. Moreover, the soft x-rays energy range is compatible for the investigation of the magnetic properties of materials, due to the fact that it can be tuned to the L-absorption edges which exhibits magnetic contrast up to *30%* thanks to the X-ray Magnetic Circular Dichroism (XMCD) effect [15]. For these reasons, the combination of soft x-rays with the generalized three-dimensional laminography setup offers extremely promising possibilities for the three-dimensional investigation of the magnetic configuration of thin samples.

In this context, one of the main challenges is also related to the development of the reconstruction algorithm able to recover all three components of the magnetization. So far, this have been possible considering additional constraints to the system or with the addition of priorly known information about the system's magnetic configuration. Recently in [65] it has been proposed a new iterative algorithm for the three-dimensional reconstruction of the magnetic configuration of structures probed using x-ray magnetic circular dichroism (XMCD) without the need of prior informations, applicable to both the tomography and laminography setup. The object is investigated with different orientations, and for each one of them a lot of projections are taken. All the information contained in the projections are combined in a single iterative method for the three-dimensional reconstruction of the magnetic configuration of the sample. Specifically, the reconstruction method is built on a gradient-based optimization: at first, an estimate of the projections dataset $\widehat{P_n}(x,y)$ is derived from an estimation of the magnetic configuration of the object (based for example on magnetic simulations). These projections are later compared to the actual measured projections $P_n(x,y)$, and the error is calculated as the difference between the two:

$$\epsilon = \sum_{n}\sum_{x,y}\left[\widehat{P_n}(x,y) - P_n(x,y)\right]^2 \tag{3.1}$$

where (x,y,z) are the laboratory coordinates. The error is then iteratively reduced calculating its gradient, which gives information about how the object in each pixel should be changed [65]: every new estimate of the projection gives a smaller error respect to the one before, until convergence or a pre-defined maximum number of iterations is reached. The gradient of the error respect to the magnetization is given by:

$$\frac{\partial \epsilon}{\partial m(\boldsymbol{R}^{(n)}\boldsymbol{r})} = 2\sum_{n}\left[\widehat{P_n}(x,y) - P_n(x,y)\right]\boldsymbol{R}^{(n)}\begin{bmatrix}0\\0\\1\end{bmatrix} \tag{3.2}$$

where $\boldsymbol{R}^{(n)}$ is the matrix that describe the rotation around the axis, $\boldsymbol{R}^{(n)}\boldsymbol{r}$ are the objects coordinate and multiplying by $[0 \quad 0 \quad 1]^T$ it is possible to select the sensitivity in the direction parallel to the propagating x-ray beam (which in this case is along the z-direction). With this powerful method it is possible to obtain the three components of the magnetization $\boldsymbol{m}(\boldsymbol{r})$ [65].

The magnetic configuration of the samples developed in this thesis work have been three-dimensionally investigated using the newly developed S*oft X-ray Laminography* (SoXL) technique present at the PolLux beamline (X07DA) of the Swiss Synchrotron Light Source, Paul Scherrer Institut, Switzerland [15].

3.3 Micromagnetic simulations

Mumax^3 is an open-source GPU-accelerated micromagnetic simulation software developed at the Dynamics of Functional Nano Materials Group at Ghent University, and allows to calculate the space-and time-dependent magnetization dynamics in nano- and micro-sized ferromagnets using a finite-difference discretization [66]. Since GPUs have the ability to perform calculations in parallel, differently from CPUs that work in series, this software allows to improve considerably the speed of calculations respect to other software, even with low-performance GPUs. In addition to this, the software is optimized for low memory use. To study the evolution of the magnetization dynamics inside magnetic systems, Mumax^3 solves the Landau-Lifshitz-Gilbert (LLG) equation, also considering the presence of the damping parameter (see paragraph 2.1.6 for more details):

$$\frac{d\boldsymbol{M}}{dt} = \gamma_0 \boldsymbol{M} \times \left(\boldsymbol{H}_{eff} - \eta \frac{d\boldsymbol{M}}{dt}\right) = \gamma_0 \boldsymbol{M} \times \left(\boldsymbol{H}_{eff} - \frac{\alpha}{\gamma \mu_0 M}\frac{d\boldsymbol{M}}{dt}\right)$$

where $\boldsymbol{H}_{eff}$ is an effective magnetic field that groups together all the total energy terms as:

$$\boldsymbol{H}_{eff} = \frac{A}{\mu_0 M_s}\nabla^2 \boldsymbol{m} + \boldsymbol{H}_M + \boldsymbol{H}_a - \frac{1}{\mu_0 M_s}\frac{\partial f_{an}}{\partial n}$$

while α is the dimensionless Gilbert parameter, which describes the damping of the magnetization, accounting the presence of dissipation events present in real systems. The damping term adds a torque component pointing towards $\boldsymbol{H}_{eff}$ and allows to reach the alignment of the magnetization with it, as depicted in Figure 3.17.

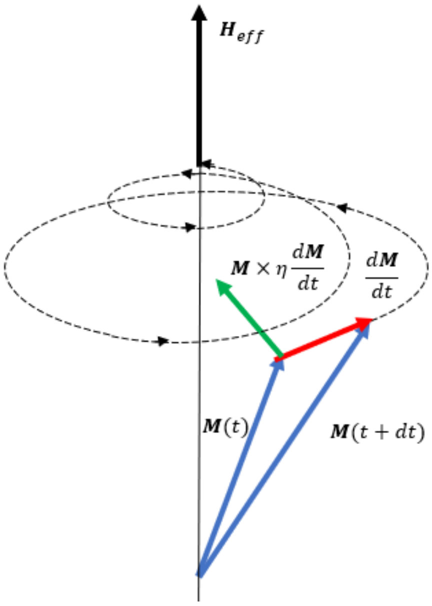

Figure 3.17: vectorial representation of the terms of the LLG equation. As a consequence of the presence of the damping term, represented with the green arrow, the magnetization aligns with the effective field in a finite time.

After having defined the dimension of the volume to be simulated and its parameters, Mumax^3 divides its magnetization $\boldsymbol{M}(\boldsymbol{r}, t)$ in small cells, employing a finite difference discretization of space using a 2D or 3D grid of orthorhombic cells. The magnetization is treated at the center of each cell, while the coupling quantities, such as the exchange strength are considered on the faces of the cells [66]. The external excitation can be set both region- and time-wise, similarly to the way the material parameters are assigned. To define the shapes of the magnet and the material regions inside it, the software uses Constructive Solid Geometry, in which any shape is described by a function $f(x, y, z)$ that returns true when (x, y, z) lies inside the shape or false otherwise [66]. The shapes can also be rotated, combined, scaled allowing to represent complex geometries in a rather easy way. After having discretized the magnetic volume and stored the material properties, it solves the LLG equation for each one cells. The problems are defined through file text with the extension .ovf and they are solved using the Fast Fourier Transform (FFT) method. The number of operations performed are of the order of $NlogN$, with N as the total number of cells if it is a power of two. If it is not a power of two, the number of operations increases drastically as N^2. To integrate the equations, numerical methods for the solution of differential equations are employed (Runge-Kutta methods). The parameters and data used for simulations were obtained from direct measurements when possible, otherwise the data from literature were used.

The visualization of the magnetic configuration solved with the Mumax^3 software was possible thanks to the Object Oriented MicroMagnetic Framework (OOMMF), an open-source software developed by the Applied and Computational Mathematics Division of ITL/NIST. This program is also capable of performing micromagnetic simulations of different magnetic configurations and is characterized by multiple tools, for visualization, analysis, and execution of simulations. It was not directly used for solving the LLG equation, since being a CPU-based software is considerably slower in solving problems for large volumes respect to Mumax^3, but it was nevertheless extremely useful for visualizing the obtained results.

Chapter 4

Emission and propagation of spin waves in synthetic antiferromagnets

4.1 Overview

In the last decade, spin waves have been intensively studied in various systems, since they represent an extremely interesting route for the development of information carrier devices, as well as for both analog and digital computation and signal processing. One of the most pressing issues of present-day high-performance computing is the high power requirements: the absence of Joule losses in spin wave-based devices would allow to substantially reduce the power consumption, with the additional benefit of an extended lifetime for the device and an improvement in the environmental sustainability [1]–[3], [67]. Moreover, they are characterized by much smaller wavelengths (up to five orders of magnitudes) for the same frequency range. For example, as demonstrated in paragraph 2.5.2, spin waves have a sub-μm wavelength at the GHz-THz frequency range: this opens up the possibility of developing miniaturized devices, with large and easily controllable time delays, as well as a much wider frequency adjustability [1]–[3]. In this context, synthetic antiferromagnetic structures are promising for the development of different types of magnonic devices given their large tunability, which allows to optimize almost at will the magnetic properties of the multilayer. From the physical point of view, the possibility of tuning the stray field improving the stability is a consequence of the coupling between the two ferromagnetic layers, which adds an extra degree of freedom to the system [43]. Synthetic antiferromagnets have been proven to be very versatile and are currently studied for several different applications, such as for magnetic-field sensing and magnetic random-access memory (MRAM) [68], for the development of spin-torque oscillators [69], for the control of current-driven domain wall motion [70] and of skyrmions dynamics [71], and for the manipulation of spin waves [1]. In particular, focusing on spin waves-based devices, the nonreciprocity of spin waves in SAFs arising from the dipolar coupling between the two magnetic layers leads to a resilience from back-scattering at defects [1], which allows to maintain high quality spin-wave wavefronts. This allows the development of optically inspired nanomagnonic devices for the generation, control, and engineering of spatially coherent propagating spin waves inside the spin texture with a high degree of tunability. In addition to this, having sub-µm wavelengths at relatively low frequencies (below GHz) makes synthetic antiferromagnets the perfect candidates for the time-resolved investigation of spin-waves modes via STXM technique, which is limited to operational frequencies below 5 GHz at the synchrotron facility where the experiments have been performed. Finally, the propagating Demon-Eschbach spin-wave modes in SAF are extremely localized along the z-direction, which allows to demonstrate the feasibility of Soft X-ray Laminography for the three-dimensional visualization of the magnetization dynamics, as presented in detail in Chapter 5.

This thesis work aimed at the realization and investigation of synthetic antiferromagnetic structures similar to the one proposed by Albisetti et al. in [1], with increased thicknesses of the ferromagnetic layers. Micromagnetic simulations at several excitation frequencies and thicknesses were initially performed to derive the optimal conditions for the visualization of spin-waves emission and propagation inside a SAF and of their localization along the z-direction. Subsequently, the designed structures were fabricated and magnetically characterized; the attention in this case was focused on the optimization of the growth and nanofabrication parameters. In particular, since domain walls have been previously efficiently employed to generate and control spin-wave wavefronts, tam-SPL was performed to magnetically pattern them on the multilayer structure. Moreover, the possibility to use shape anisotropy on e-beam lithography nanopatterned structures to drive the formation of Landau domains has been investigated. Finally, the spin-wave dynamics was directly visualized via the well-established static and time-resolved *Scanning Transmission X-ray Microscopy* (STXM) technique (described in detail in paragraph 3.2.4) available at the Swiss Light Source (SLS) synchrotron facility of the Paul Scherrer Institut, hosted in Villigen. The goal of these measurements was to verify the efficiency of the spin waves emission and propagation from the spin texture inside thicker synthetic antiferromagnetic structures compared to the previously investigated system [1], and to study their dispersion relation, identifying the best samples for the three-dimensional visualization of the magnetization dynamics via Laminography technique, presented in Chapter 5.

My work was directly related to the micromagnetic simulations, performed with the software Mumax^3 and OOMMF, and to the growth and magnetic characterization of the samples, which were performed within the cleanroom facility available at PoliFAB, the micro and nanofabrication center of Politecnico di Milano; I also assisted with the magnetic patterning via tam-SPL process, and I collaborated to the STXM experiments performed at the PolLux beamline at the SLS synchrotron facility hosted in Villigen.

4.2 Micromagnetic simulations: spin waves in SAF

A Synthetic Antiferromagnet (SAF) consists in a magnetic multilayer structure of two ferromagnetic films, separated by a non-magnetic spacer, whose magnetization at remanence, i.e. when no external magnetic field is applied, points in the opposite direction (Paragraph 2.4). The key physical ingredient of this structure is the interlayer exchange coupling (IEC) (explained in detail in Section 2.3.3), and in this context the thickness of the non-magnetic layer is a critical parameter for setting the relative orientation of the magnetization of the two FM layers. An antiferromagnetic layer is often introduced in contact with one of the two ferromagnetic layers, pinning its magnetization and setting the direction at remanence through the exchange bias interaction. Synthetic antiferromagnetic structures are particularly interesting from the technological point of view, since the possibility of tuning the thickness of the different layers and their composition allows to obtain very peculiar magnetic properties.

Micromagnetic simulations with the Mumax^3 software [66] were realized to correctly design the synthetic antiferromagnetic structures for the investigation of the spin waves emission and propagation. Specifically, an exchange-biased SAF consisting of a CoFeB / Ru / CoFeB / IrMn multilayer and a SAF designed as a CoFeB / Ru / CoFeB (lacking the antiferromagnetic layer that induces the exchange bias coupling) have been studied. In both cases, the structure was designed as perfectly compensated, meaning that the thickness of the two ferromagnetic layer is equal. In the first case, several micromagnetic simulations have been performed at different excitation frequencies ranging from 1 to 7 GHz, and the dynamic behavior of the system was studied with respect to the variation of the total thickness of the multilayer equal to 90 nm, 140 nm, and 200 nm, respectively. In the second one, on the other hand, the goal was to explore the magnetic configuration of different nanostructures (rectangles, squares, ellipses) stabilized by shape anisotropy and the emission of spin waves from their spin texture at a 2 GHz excitation frequency applied to the system with total thickness equal to 200 nm.

Before presenting the results of the simulated dynamical behavior of the magnetization for the two configurations, some general comments can be made. First, Figure 4.1 shows a static micromagnetic simulation of the spin texture in proximity of a domain wall established in a perfectly compensated exchange-biased synthetic antiferromagnetic structure with total thickness of 200 nm (the detailed description of the simulation parameters for the structure will be presented in the next paragraph). As expected, the two ferromagnetic layers are antiparallelly coupled everywhere on the structure, thanks to the interlayer exchange coupling, as shown by the black arrows. The red and blue colors represent the out-of-plane component of the magnetization, in the positive and negative directions, respectively. Noticeably, moving closer to the domain wall the magnetization experiences an out-of-plane tilting in the same direction for both the top and bottom layers, and a change from red to blue contrast is present across the domain wall. This breaking of the SAF perfect compensation in the z-direction is a consequence of the magnetostatic energy minimization, allowing to reach a *flux closure state*, while the direction of the z-component of the magnetization is determined by the chirality of the wall [1].

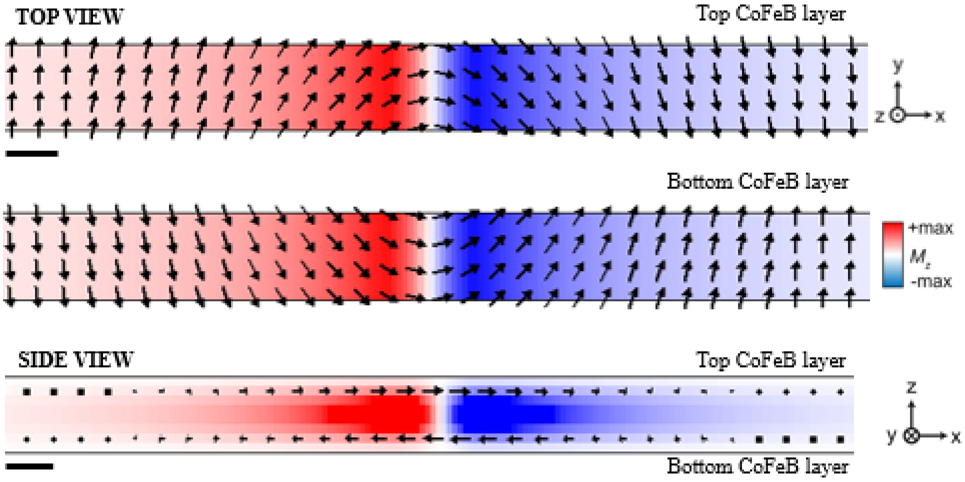

Figure 4.1: static micromagnetic simulation of the magnetic configuration near a domain wall of the synthetic antiferromagnetic structure investigated. Both the top and side view are shown, highlighting the spin texture of the two ferromagnetic layers. Scale bar (top view) = 100 nm, scale bar (side view) = 50 nm.

Secondly, the spin-waves excitation mechanism employed during the STXM experiments consists in injecting RF currents inside micrometric striplines, generating an Oersted magnetic field that couples with the domain walls. To investigate this phenomenon, a perfectly compensated exchange-biased SAF with total thickness of 200 nm with a DW stabilized in the center of the film was simulated. The system was studied in four different conditions, with no applied field along the z direction, with a static out-of-plane field equal to +5 mT and -5mT and with a RF out-of-plane field of 1 mT, respectively. The obtained results are shown in Figure 4.2: the images have been taken in the same position along the x-direction. The black dashed line represents the position of the domain wall in the condition of zero applied field, the black arrows the in-plane direction while the red and blue colors represent the out-of-plane component of the magnetization, in the positive and negative directions. Importantly, a sizeable displacement is observed according to the static field direction: this behavior can be explained by the fact that the coupling of the external field with the domain wall is mediated by the orientation of the spins in the proximity of the domain wall itself. The magnetization in that region is characterized by an out-of-plane component m_z, as explained before. On one side of the DW, m_z is parallel to the external field, while on the other one m_z is antiparallel. Depending on the direction of the external field, the domain wall will move towards the domain with the out-of-plane component of the magnetization in the opposite direction. Noticeably, if considering the behavior under an external RF field in the z-direction, the coupling with the domain wall leads to its oscillation and to the efficient emission of spin waves, even in case of a perfectly compensated SAF [1].

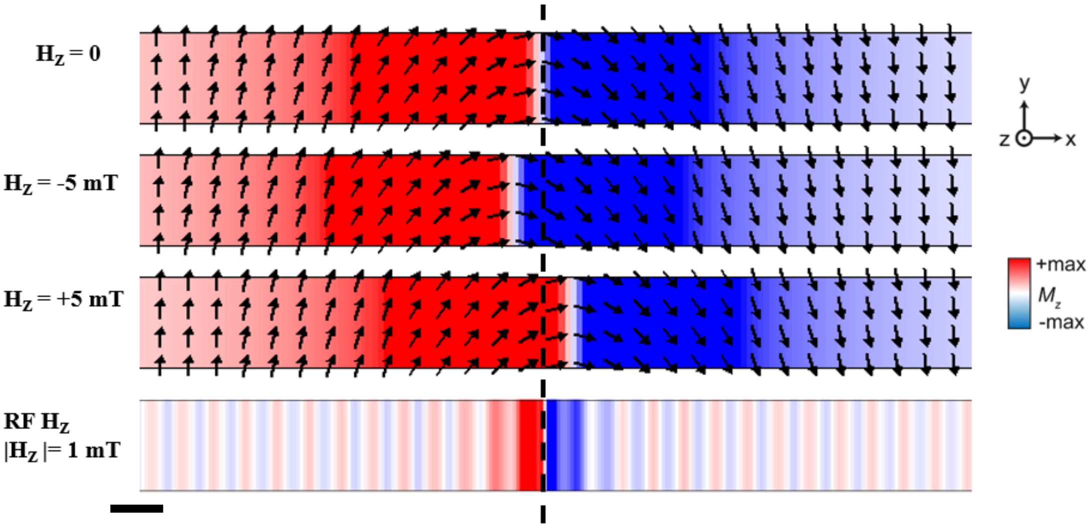

Figure 4.2: coupling on an external field with the nanoscale spin texture. From top to bottom, the applied field is equal to zero, +5 mT (static), -5 mT (static), 1 mT (RF). The domain wall is indicated with a black dashed line, the black arrows show the direction of the magnetization in-plane, while the red-blue contrast its out-of-plane component in the positive and negative directions, respectively. For the static fields, a displacement of the domain wall is observed, coherently to the direction of the external field; for the RF field, on the other hand, the spin-waves emission from the domain wall is visible. Scale bar = 100 nm.

Finally, another important property of spin waves is their characteristic non-reciprocity, which refers to the fact that spin waves propagate differently with respect to the direction of their wavevector. Consider for example the dispersion relation presented in [1] and shown in Figure 4.3, where the colored lines show the simulated spin-wave dispersion in the investigated SAF multilayer, as a function of the angle φ between the wavevector and the magnetization of the top ferromagnetic layer, while the black dots are the experimental points. The strong nonreciprocity causes the two branches ($\pm k$) describing the dispersion relation are significantly different. Additionally, below the threshold frequency corresponding to the crossing point of the different curves at k = 0 (f = 1.57 GHz), the only spin-wave modes available are the one with positive wavevector.

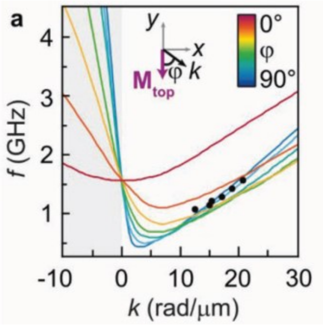

Figure 4.3: Simulated and experimental dispersion relations presented in [1]. The colored lines show the results of the simulations for the investigated SAF multilayer, as a function of the angle φ between the wavevector and the magnetization of the top ferromagnetic layer, while the black dots report the obtained experimental points.

This is a consequence of the breaking of the time-reversal symmetry [72], and in general arises from the classical dipole-dipole interaction. In synthetic antiferromagnets, this behavior is further enhanced, thanks to the synthetic antiferromagnetic coupling [1], [2], [72]. For positive wavevector it is possible to understand the direction of the spin-waves propagation in a simple way, applying the right-hand rule as depicted in Figure 4.4. Starting with the open hand and closing the fingers towards the palm, following the flux closure of the magnetization of top and bottom layers (see circular arrow in the picture), the thumb indicates the direction of the propagation of the spin waves.

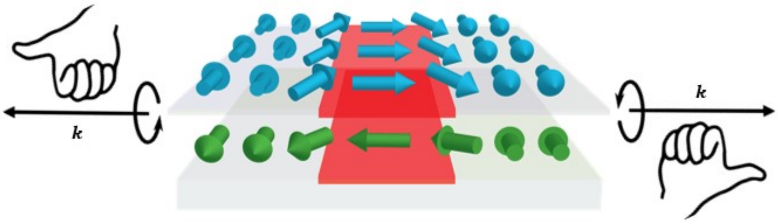

Figure 4.4: application of the right-hand rule to understand the direction of propagation of the spin waves from the orientation of the magnetization of the two sides of the domain wall.

In what follows, the results of the micromagnetic simulation on the exchange-biased SAF consisting of a CoFeB / Ru / CoFeB / IrMn / Ru multilayer and on the SAF designed as a CoFeB / Ru / CoFeB / Ru (lacking the antiferromagnetic layer that induces the exchange bias coupling) will be reported.

4.2.1 Spin-waves emission from a domain wall in an exchanged-biased SAF

To simulate the exchange biased synthetic antiferromagnetic structure consisting of a perfectly compensated CoFeB / Ru / CoFeB / IrMn multilayer with varying thickness for the ferromagnetic layers, the total volume was discretized into 1024 x 128 x 8 cells, whose dimensions d_i in the x, y and z direction is summarized in Table 4.1:

Total thickness	d_x	d_y	d_z
90 nm	10 nm	10 nm	11.25 nm
140 nm	10 nm	10 nm	17.5 nm
200 nm	10 nm	10 nm	25 nm

Table 4.1: dimensions of a single cell in the discretized volume respect to the total thickness of the simulated film.

The micromagnetic parameters set to simulate the SAF structure summarized in Table 4.2 where chosen from direct measurements when possible, and coherently to what is present in literature [73]:

Exchange anisotropy constant	$A_{ex} = 1.2 \cdot 10^{-11}\, J/m$
Exchange bias field	$H_{EB} = 10^{-3}\, A/m$
Saturation magnetization	$M_{sat} = 10^{6}\, A/m$
Gilbert damping parameter	$\alpha = 0.005$
Unidirectional anisotropy constant	$K_u = 10^{3}\, J/m^3$
RKKY strength	$RKKY = -1.2 \cdot 10^{-3}\, mJ/m^2$

Table 4.2: micromagnetic parameters used to simulate the CoFeB / Ru / CoFeB / IrMn / Ru SAF structure.

After the relaxation of the system and the identification of the ground state stabilizing the spin texture, the magnetization was excited applying to the whole system a time-varying sinusoidal magnetic field in the z-direction with amplitude of 1 mT at different frequencies. Figure 4.5 presents as an example the extracted frames for the simulated system with total thickness of 200 nm, showing the emission and propagation of the excited spin waves. For each image, the position of the domain wall has been highlighted with a red line. Moreover, as an example, in the first image the direction of the in-plane magnetization is shown with the white arrows, while the black arrows show the direction of the spin-wave propagation: they are emitted from the domain wall and propagate outwards, and their motion is visible due to the oscillation of the out-of-plane component of the magnetization, represented by the black/white contrast. Finally, the green lines show how the spin-wave wavelength has been extracted from each frame: this procedure has been repeated for all the simulated values of frequencies and thicknesses, allowing to obtain the dispersion relations for the three simulated configurations.

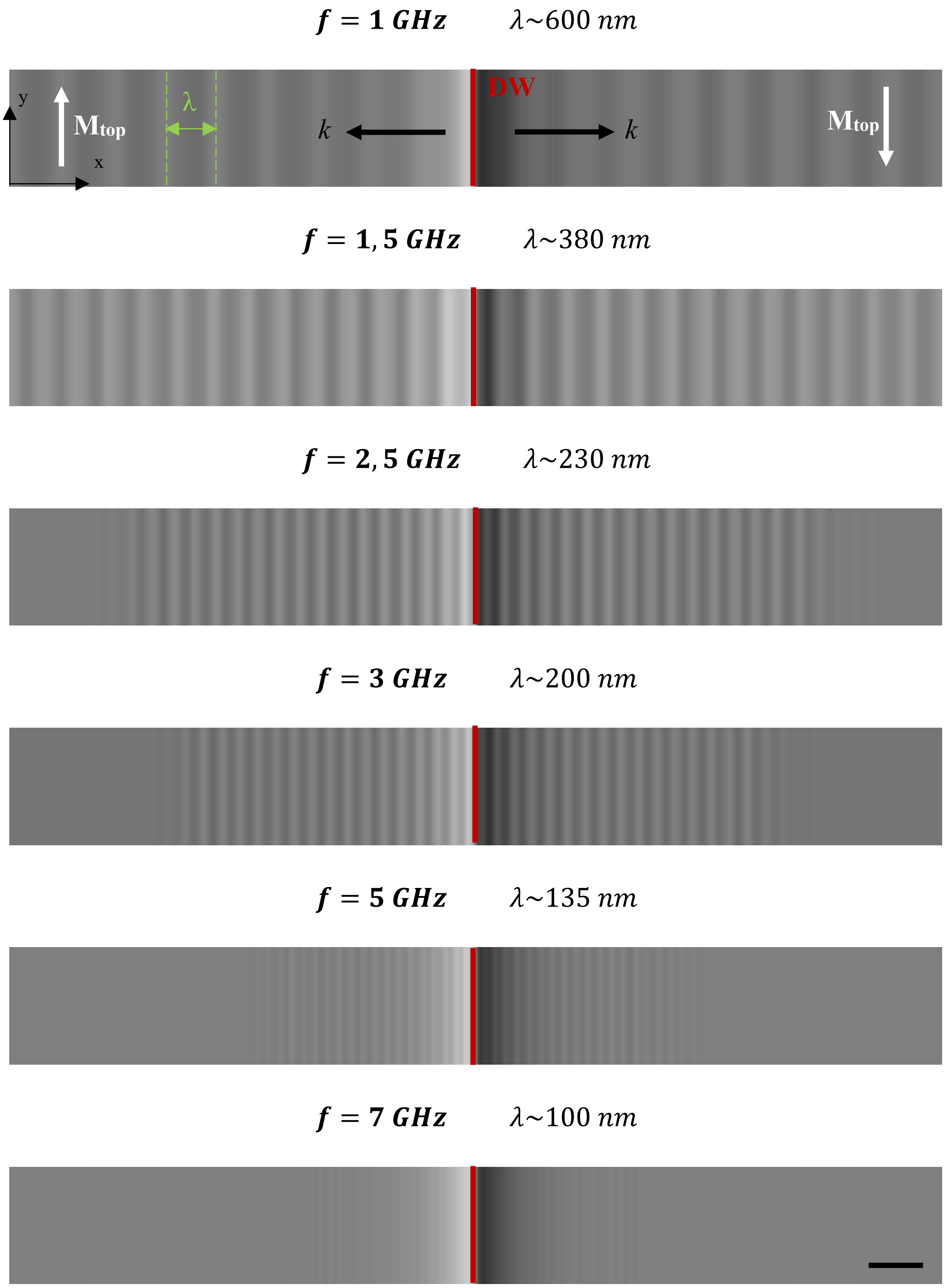

$\boldsymbol{f = 1\ GHz}$ $\lambda \sim 600\ nm$

$\boldsymbol{f = 1,5\ GHz}$ $\lambda \sim 380\ nm$

$\boldsymbol{f = 2,5\ GHz}$ $\lambda \sim 230\ nm$

$\boldsymbol{f = 3\ GHz}$ $\lambda \sim 200\ nm$

$\boldsymbol{f = 5\ GHz}$ $\lambda \sim 135\ nm$

$\boldsymbol{f = 7\ GHz}$ $\lambda \sim 100\ nm$

Figure 4.5: extracted frames of the time-varying simulations of the synthetic antiferromagnetic system with total thickness of 200 nm for different frequencies. The red line shows the position of the domain wall, the white arrows the direction of the

magnetization in the plane of the film, while the black arrows the direction of propagation of the spin waves. Scale bar = 1 μm.

Figure 4.6 reports the obtained dispersion relations for the three systems, both in terms of wavevector and wavelength. At low frequencies, the corresponding spin-wave wavelengths for $t_{tot} = 90, 140, 200\ nm$ are exactly the same: for $f = 1\ GHz, 1.5\ GHz, 2.5\ GHz, 3\ GHz$ the wavelengths are $\lambda \sim 600\ nm$,$380\ nm$,$235\ nm$, $200\ nm$, respectively. At higher frequencies, on the other hand, a small difference is observed for the three configurations: for the thicker sample, at 5 GHz and 7 GHz, the resulting wavelength is 135 and 105 nm, respectively. For the intermediate system, with thickness equal to 140 nm, at 5 GHz and 7 GHz the resulting wavelength is 130 and 100 nm, while for the SAF with $t_{tot} = 90\ nm$, λ is 120 and 100 nm for $f = 5\ GHz$ and $f = 7\ GHz$. In general then, it is possible to conclude that the spin-wave dispersion relation is basically independent on the thickness of the synthetic antiferromagnetic structure at low frequencies, while a minor and often negligible difference is observed when increasing the excitation frequency. This may be explained by the fact that at high frequencies the domain wall is not able anymore to sustain such fast oscillations, so it behaves in a slightly different way depending on the thickness of the system.

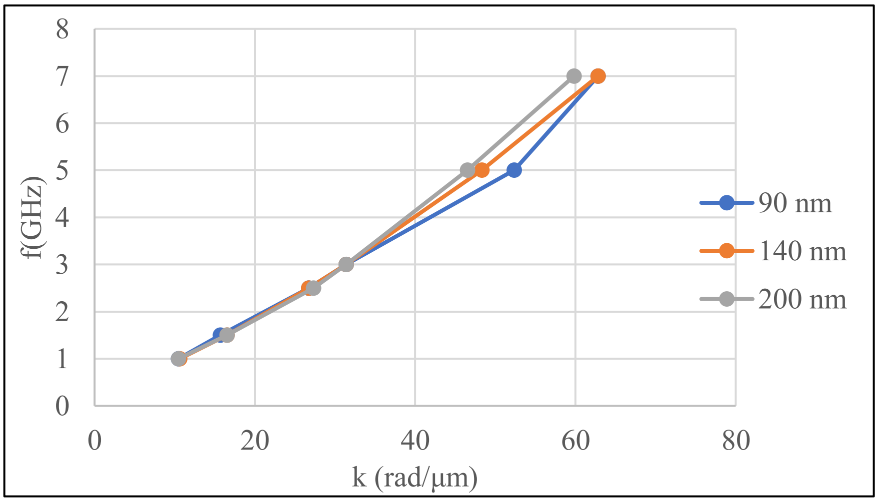

(a)

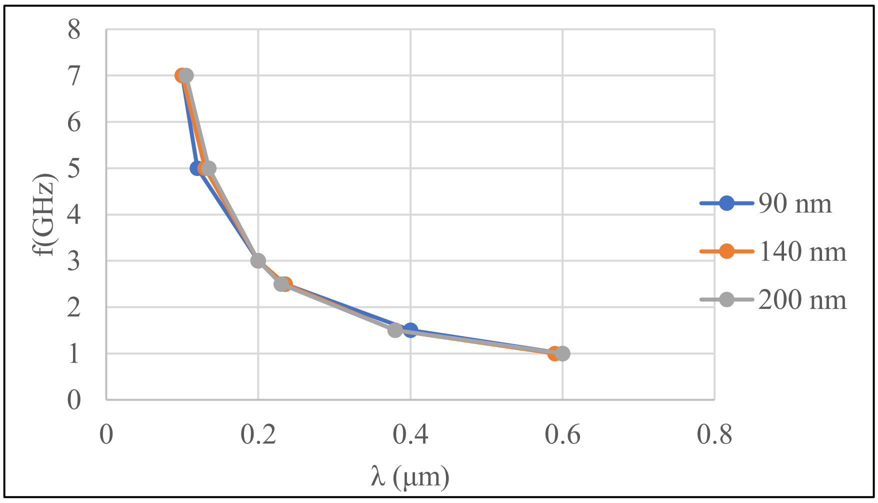

(b)

Figure 4.6: simulated spin-waves dispersion relation for the three simulated SAF with $t_{tot} = 90, 140, 200\ nm$ for (a) frequency vs wavevector and (b) frequency vs wavelength.

4.2.2 Spin-waves emission inside nanostructures in a SAF

For the synthetic antiferromagnetic structure consisting of a perfectly compensated CoFeB / Ru / CoFeB / Ru multilayer with total thickness of 200 nm, the goal was to investigate the magnetic configuration and the spin-wave dynamics induced at $f = 2\ GHz$ in different types of nanostructures, such as squares, rectangles, and ellipses. For each structure, the volume was discretized into cells, and the total simulated volume for each system is summarized in Table 4.3:

Nanostructure	Simulated volume
Square	2560 nm x 2560 nm
Rectangle	5120 nm x 1280 nm
Ellipse	5000 nm x 1200 nm

Table 4.3: total simulated volume for each simulated nanostructure for the CoFeB / Ru / CoFeB / Ru multilayer systems.

The micromagnetic parameters used to simulate the systems are consistent to what has been reported in Table 4.2, but in this case no exchange bias was added to the structures, since no antiferromagnetic film is present in the multilayer. To obtain the ground state magnetic configuration, the initial system was relaxed exploiting shape anisotropy, stabilizing the formation of the so-called Landau domains, corresponding to a magnetization ground state of a flux-closing, planar vortex-like system with the center core characterized by a perpendicular magnetization [2]. As an example, in Figure 4.7 a possible magnetic configuration of a Landau domain in a square is reported, where the white arrows show the direction of the magnetization inside the domain. The domain walls have also been highlighted.

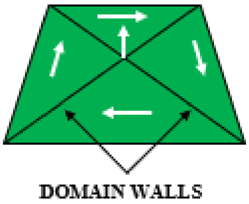

Figure 4.7: schematic representation of a possible ground state configuration of a Landau domain stabilized in a nanostructured square. The white arrows represent the direction of the magnetization inside the domain.

These states, however, are characterized by a non-trivial topological structure: they possess a binary *core polarity*, indicated as $p = \pm 1$ ($p = +1$ magnetization in the core pointing upwards, $p = -1$ magnetization in the core pointing downwards), and by a *circulation polarity*, represented by the parameter $c = \pm 1$ ($c = +1$ anticlockwise rotation, $c = -1$ clockwise rotation). Inside a synthetic antiferromagnetic structure, considering for both FM layers a core polarity of $p = +1$, two possible configurations can be stabilized in terms of the circulation polarity of the flux-closure state for the FM films: either the bottom layer has $c_{bottom} = +1$ and the top layer $c_{top} = -1$, or vice versa. This situation is shown as an example in Figure 4.8 for a squared nanostructure. Note that the antiferromagnetic coupling between the two ferromagnetic layers fixes the product between the two circulation parameters as $c_{top} \cdot c_{bottom} = -1$. The two configurations presented exhibit two different relative handedness, defined by the right-hand rule which follows the circulation polarity of the flux-closure state (as indicated by the sketches in Figure 4.8). The circulations can either point towards each other (defined by $\mathrm{C}^{+}\text{: } \mathrm{c}_{\mathrm{bottom}} = +1, \mathrm{c}_{\mathrm{top}} = -1$, picture on the left) or away from each other (defined by $\mathrm{C}^{-}\text{: } \mathrm{c}_{\mathrm{bottom}} = -1, \mathrm{c}_{\mathrm{top}} = +1$, picture on the right) [2].

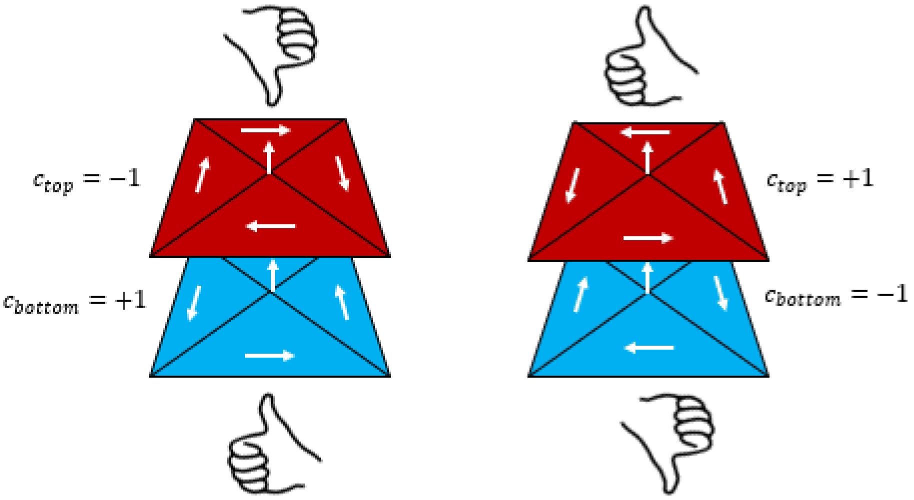

Figure 4.8: schematic representation of the two possible configuration in terms of circulation polarity stabilized inside squared nanostructure for a synthetic antiferromagnetic system. For both FM layers, the core polarity has been fixed as $p = +1$, with the magnetization pointing upwards. On the left, the top layer exhibits a clockwise circulation ($c_{bottom} = +1$), while the bottom layer shows an anticlockwise circulation ($c_{top} = -1$); in this case, the circulations point towards each other (as shown by the right-hand rule) and are indicated with C^+. On the right, the opposite situation is depicted, with $c_{bottom} = -1$ and $c_{top} = +1$, corresponding to the case of circulations pointing towards the opposite direction (C^-).

When the system is excited with an oscillating RF magnetic field in the z-direction, the direction of propagation of the emitted spin waves *only* depends on the relative circulation handedness: for C^+ the spin waves propagate outwards, while for C^- they propagate inwards, as shown by the example in Figure 4.9. This is because in both cases in every point of the nanostructure the right-hand rule (explained in detail in Figure 4.4) is fulfilled [2].

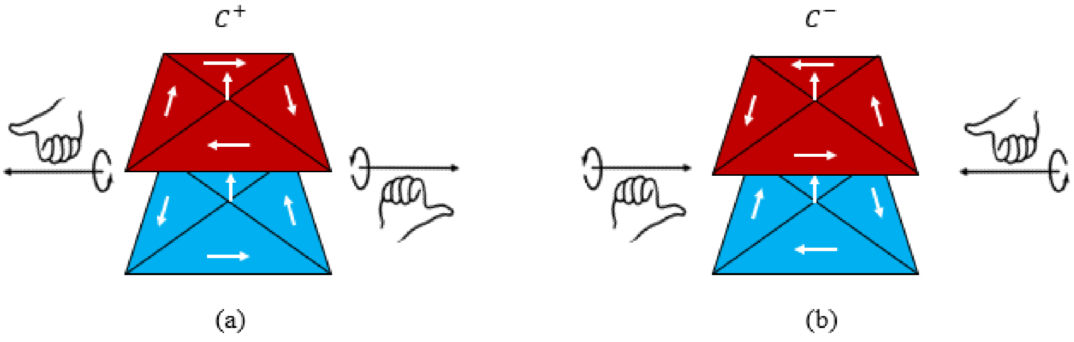

Figure 4.9: schematic representation of the possible direction of the spin waves propagation inside a nanostructured square for the two possible configuration with relative handedness C^+ (left) and C^- (right). The direction of propagation is determined by the right-hand rule.

The results of the micromagnetic simulations performed on the three different types of nanostructures, namely squares, rectangles, and ellipses, are reported below in Figure 4.10, Figure 4.11, and Figure 4.12, respectively. For each structure, the spin-waves emission and propagation as a consequence of the excitation with an out-of-plane RF magnetic field with $f = 2\ GHz$ has been investigated for both types of relative handedness configurations (C^+ and C^-). The black arrows show the direction of the magnetization and the circulation polarity of the top ferromagnetic layer, while the white arrows report the direction of the propagation of the emitted spin waves; the domain walls have also been highlighted as an example in the first image. Figure 4.10(a) represent the C^+ configuration of a squared nanostructures: the spin waves are emitted outwards from the vortex in the center of the structure. Moreover, the emission of planar wavefronts from the domain walls of the Landau domains is also visible, as well as the interference between the SWs emitted from the different sources. A similar situation is present also in Figure 4.11(a) and Figure 4.12(b), for the rectangle and the ellipses in the C^+ configuration, respectively. In these cases, the emission from the domain walls is even more clear, thanks to the longer horizontal domain wall, leading to the creation of multiple interference patterns with the spin waves emitted from the vortex core. The opposite configuration C^- is presented on the other hand in Figure 4.10(b), Figure 4.11(b), and Figure 4.12(b) for the square, rectangle, and ellipses, respectively. In this case, the spin waves propagate inwards towards the center of the structure, as shown by the white arrows.

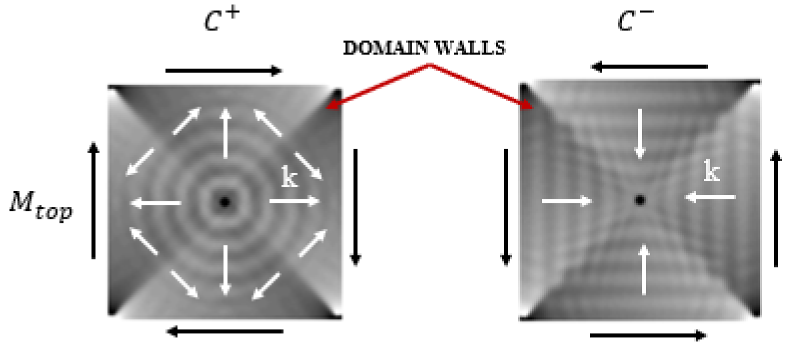

(a) (b)

Figure 4.10: micromagnetic simulation on the Landau domains stabilized by shape anisotropy inside a squared feature with size 2560 nm x 2560 nm at $f = 2\ GHz$ with (a) clockwise and (b) counterclockwise flux closure state for the top FM layer. The spin waves are emitted outwards and inwards, respectively.

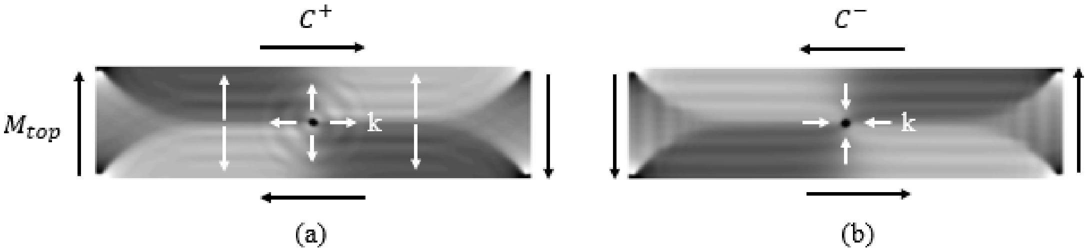

Figure 4.11: micromagnetic simulation on the Landau domains stabilized by shape anisotropy inside a rectangular feature with size 5120 nm x 1280 nm at $f = 2\ GHz$ with (a) clockwise and (b) counterclockwise flux closure state for the top FM layer. The spin waves are emitted outwards and inwards, respectively.

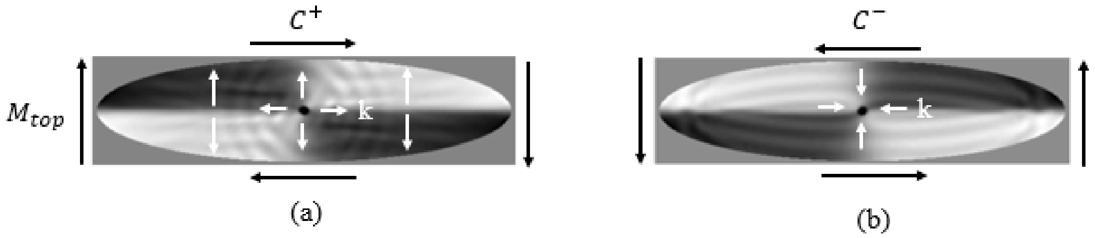

Figure 4.12: micromagnetic simulation on the Landau domains stabilized by shape anisotropy inside an elliptic feature with size 5000 nm x 1200 nm at $f = 2\ GHz$ with (a) clockwise and (b) counterclockwise flux closure state for the top FM layer. The spin waves are emitted outwards and inwards, respectively.

4.3 Samples growth, characterization, and optimization

In this work, two types of synthetic antiferromagnetic structures have been developed: an exchange-biased SAF consisting of a CoFeB / Ru / CoFeB / IrMn / Ru stack (Figure 4.13(a)) and a SAF without the antiferromagnetic film, consisting of a CoFeB / Ru / CoFeB / Ru multilayer (Figure 4.13(b)). In the first case, the presence of the AF layer was needed to set the exchange bias interaction with the top FM layer, pinning its magnetization and allowing via tam-SPL the magnetic patterning of the spin texture with the formation of domain walls used as emitting sources of spin waves. On the other hand, not adding the AF layer to the structure allows the stabilization of Landau domains due to shape anisotropy in previously nanopatterned features with different geometries. All the details regarding the creation and stabilization of domain walls for the emission and propagation of spin waves will be presented in the next paragraphs. For what this research thesis is concerned, the designed systems presented a symmetric structure, with equal thicknesses for the top and bottom CoFeB layers. Among all the possible ferromagnetic materials that can be used for developing a synthetic antiferromagnetic structure, $Co_{40}Fe_{40}B_{20}$ was chosen thanks to its small Gilbert damping parameter ($\alpha \approx 0.005$), which makes it particularly suitable for the operations involving spin waves [73]. Regarding the non-magnetic material interlayer, Ru was identified as the ideal choice since it induces a strong antiferromagnetic coupling between the two ferromagnetic layers, and it is particularly stable at high temperatures [74] that are needed to magnetically pattern the structure. The design of the samples had to face several constrains when tuning the optimal thicknesses of the different layers involved. First, both the interlayer exchange coupling and the exchange bias, being interfacial interactions, are inversely proportional to the thickness of the films. Moreover, since the experimental observation of spin waves via STXM requires the x-rays to go *through* the multilayer, that needs to be thin enough to allow an investigation of the complete heterostructure. On the other hand, however, the XMCD contrast is strongly related to the amount of ferromagnetic material present on the sample, so the two ferromagnetic layers cannot be too thin, and the three-dimensional Laminography experiments presented in the next chapter are more suited for larger thicknesses, since a better resolution on the z-direction can be achieved. Finally, increasing the thickness of these layers allow to reduce the effect of defects and impurities presents on the samples, increasing the spin-waves travelling path. Due to the competing nature of these different phenomena, several samples with different thicknesses of ferromagnetic layers were growth, allowing to find the optimal conditions for the visualization of the propagating spin waves.

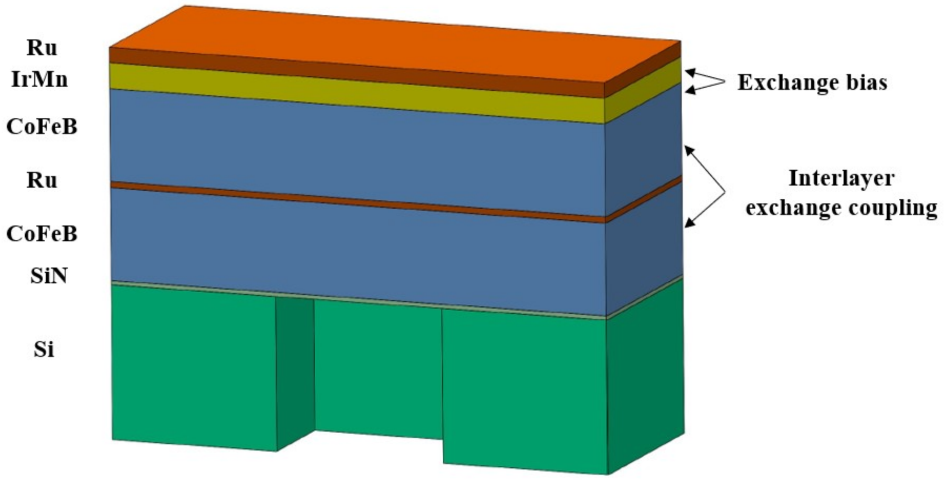

(a)

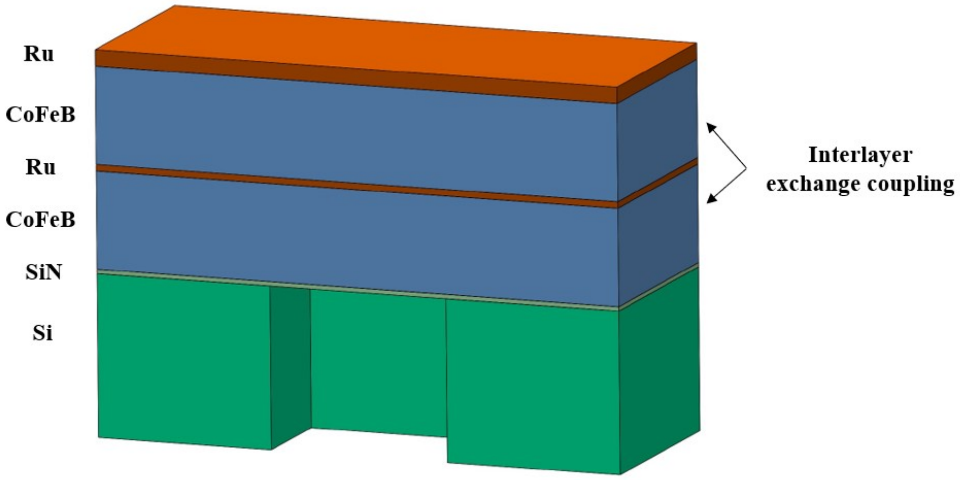

(b)

Figure 4.13: sketch of the two different types of synthetic antiferromagnetic samples developed: (a) exchange biased SAF CoFeB / Ru / CoFeB / IrMn / Ru; (b) SAF without the antiferromagnetic layer establishing the exchange bias interaction CoFeB / Ru / CoFeB / Ru. The major magnetic interactions governing its behavior are highlighted.

As represented in Figure 4.13, the magnetic multilayers investigated consist of an exchange-biased SAF with the structure CoFeB (x)/Ru (0.5 nm)/CoFeB (x)/IrMn (10 nm)/Ru (2 nm), and a SAF designed as CoFeB (y)/Ru (0.5 nm)/CoFeB (y) /Ru (2 nm). Starting from the reference value for the thickness of the ferromagnetic layers studied in [1], and aiming at improving the time-resolved STXM contrast, the chosen values of x and y corresponded to 45-70-100 nm and 45-75-100 nm, respectively. Coherently with the previous works on CoFeB/IrMn exchange-coupled systems [1], [52], [75], the IrMn layer was designed as 10 nm thick. The reasoning behind this choice resides on two important physical phenomena strongly depending on the thickness of the antiferromagnetic layer. As a matter of fact, raising the thickness of the polycrystalline IrMn leads to an increase on the average dimension of its crystals, which in turns has a strong influence on the blocking temperature T_b of the exchange biased structure. In particular, having a larger grain size results in requiring a higher thermal energy to induce fluctuations of the spin orientation inside the grain, which macroscopically translates in an increase of the blocking temperature [76]. For thicknesses larger than 4-5 nm, the corresponding T_b is above room temperature, which is a fundamental requirement for the development of properly working devices. On the other hand, however, larger values lead first to a saturation of the exchange bias interaction, and then to its decrease approximately as $1/t_{AF}$ [77]; the optimal value for this structure has been demonstrated to be of 10 nm. In the investigated structures, the IrMn layer is always positioned in contact with the top-CoFeB layer, closer to the surface of the system. This design choice is dictated by the fact that before reaching the necessary temperature to set the exchange bias with the FM layer, atomic interdiffusion is present at the interface, damaging it and restraining the exchange bias. Being closer to the surface, and consequently to the hot tip, allows the AF layer to reach the critical temperature faster and more homogenously during the magnetic patterning via tam-SPL. Finally, as previously mentioned, the thickness of the Ru interlayer is the most critical parameter of the structure since it is responsible for the antiferromagnetic coupling between the two ferromagnetic layers. The optimal value identified granting a stable antiparallel orientation of the two FM layers at zero applied field corresponds to 0,5 nm.

All samples were grown via magnetron sputtering, and the growth conditions are listed in Table 4.4. Despite not being present in the structure, the working conditions of Ta are present as well, since it has been used to favor the plasma strike of CoFeB, allowing a more stable deposition. The exchange biased SAF has been grown with an in-plane applied magnetic field during the deposition of each layer, to set a favorable direction for the EB (easy axis) at the top-CoFeB/IrMn interface, while no in-plane field was present during the growth of the SAF samples without the antiferromagnetic layer. During the deposition process, a test sample was positioned on the sample-holder, which was later used to record the hysteresis loop by Vibrating Sample Magnetometry (VSM). The hysteresis cycles were analyzed both immediately after the deposition and following a thermal annealing process at 250°C for 5 min in an in-plane magnetic field of 4 kOe ($\boldsymbol{H}_{in}$) oriented in the same direction of the one present during the growth, to strongly set the direction of the exchange bias. The thermal annealing was performed *only* on the exchange-biased samples.

Material	**Mode**	**Ar pressure**		**Power**		**Rate**
		strike	**deposition**	**strike**	**deposition**	
CoFeB	RF	40 mTorr	3 mTorr	60 W	100 W	10,1 A/min
Ru	DC	no strike	5 mTorr	no strike	50 W	17,9 A/min

IrMn	DC	no strike	3 mTorr	no strike	50 W	28,9 A/min
Ta	DC	no strike	3 mTorr	no strike	100 W	not dep.

Table 4.4: magnetron sputtering deposition condition for synthetic antiferromagnetic structures

In Table 4.5 are summarized the different samples that have been developed during this work, with the associated names that will be used from now on.

Sample	**Thickness (nm)**		
	CoFeB	**Ru**	**IrMn**
SAF20b_5	45	0,5	10
SAF20b_6	70	0,5	10
SAF20b_7	100	0,5	10
SAF21_3	45	0,5	-
SAF21_4	75	0,5	-
SAF21_5	100	0,5	-

Table 4.5: samples designed with the corresponded values for the thicknesses of the layers.

In what follows, the complete study of the hysteresis cycles of all the developed samples is presented, starting with the loops after the deposition of SAF20b_5 (Figure 4.14) along both the easy axis and hard axis (parallel and perpendicular to the direction of the field applied during the deposition process, respectively). It is important to observe the behavior along the easy axis (Figure 4.14(a)): the cycle can be seen as the sum of the loops for the two CoFeB layers taken separately. For the first loop, a shift from the origin is visible, and is a consequence of the pinning of the magnetization of the top CoFeB layer; the second curve, on the other hand, describes the rotation of the magnetization of the second layer. Moreover, if the hysteresis loop is considered as a whole, the presence of the antiferromagnetic coupling becomes clear observing the central plateau. This means that even before the thermal annealing process, the antiferromagnetic coupling at zero applied field is present, confirming the strength of the established IEC.

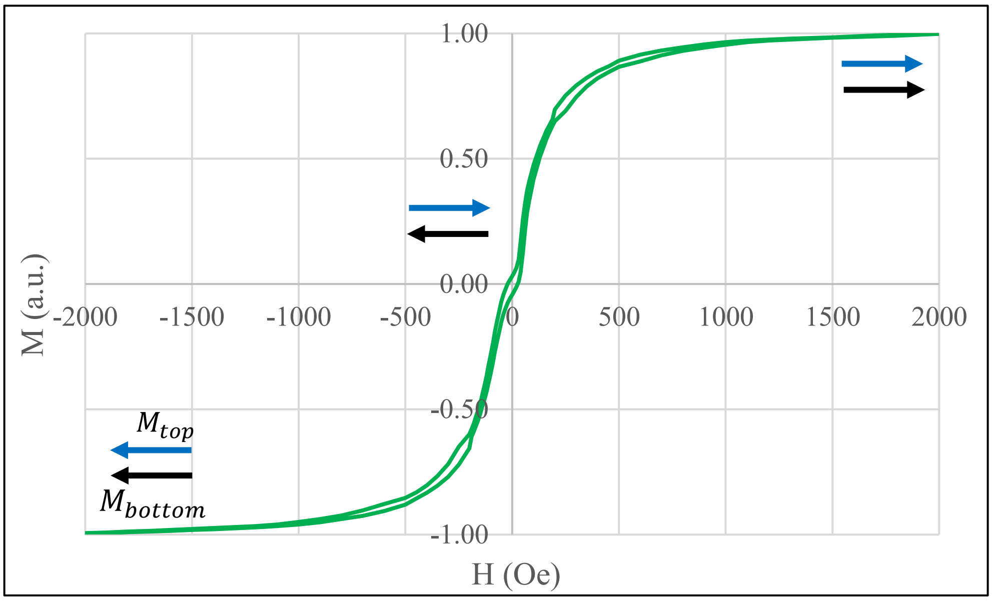

(a)

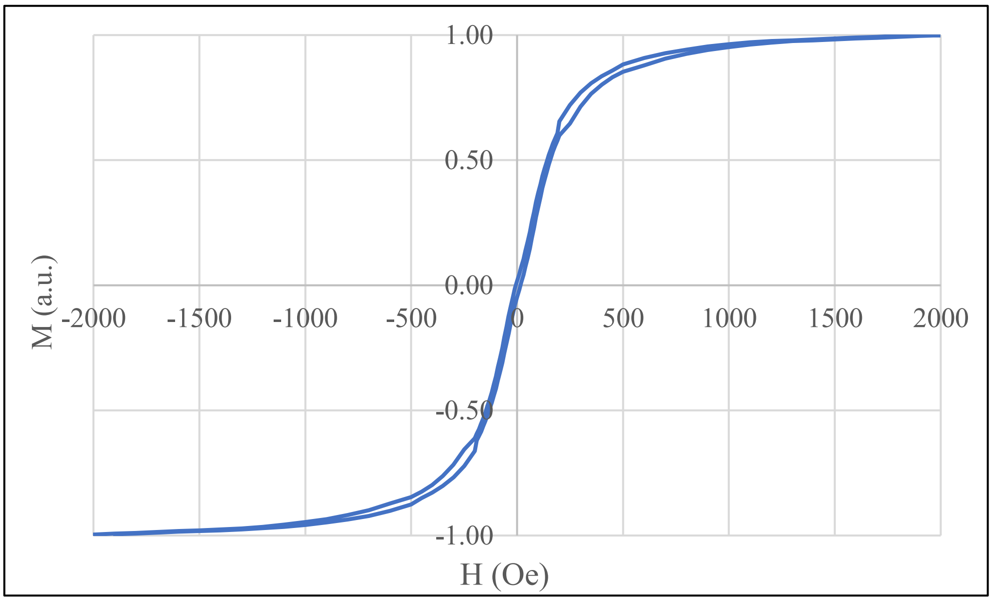

(b)

Figure 4.14: Hysteresis loop after the deposition for SAF20b_5 along (a) easy axis and (b) hard axis.

A similar behavior has been verified also for SAF20b_6 and SAF20b_7. Later, the thermal annealing process at 250°C with an in-plane applied field of 4 kOe along the preferential direction set during the deposition for 5 minutes has been carried out, and the results for SAF20b_5, SAF20b_6 and SAF20b_7 are shown in Figure 4.15, Figure 4.16 and Figure 4.17

for both the easy axis and hard axis, respectively. Noticeably, two important information can be extracted from the loops relative to the easy axis: first of all, the role of $\boldsymbol{H}_{in}$ during the annealing process for setting the exchange bias becomes clear, leading to a small shift towards the negative direction of the cycles. Moreover, the intensity of the interlayer exchange coupling $\boldsymbol{H}_{ex}$ can be estimated, as shown by the black lines: a quantitative analysis has led to $\boldsymbol{H}_{ex}{\sim}130\,Oe$, $\boldsymbol{H}_{ex}{\sim}55\,Oe$ and $\boldsymbol{H}_{ex}\,{\sim}35\,Oe$ for $t_{CoFeB} = 45\,nm$, $t_{CoFeB} = 70\,nm$ and $t_{CoFeB} = 100\,nm$, respectively. Despite a decrease of the strength of the interlayer exchange coupling when increasing the thickness of the ferromagnetic layer, consistently with the interfacial origin of the interlayer exchange coupling, our findings suggest it to be large enough to allow a good stability and robustness for the antiferromagnetic coupling between the two CoFeB layer, as confirmed by the characteristic plateau around $\boldsymbol{H} = 0$, while improving at the same time the STXM contrast and allowing a better resolution along the z-direction for the Laminography measurements. In addition to this, another valuable information can be extracted from the cycles along the hard axis. In particular, the slope of the curves is inversely proportional to the interlayer coupling strength. It was possible to estimate the IEC strength in terms of normalized susceptibility, calculating the slope of the curve in percentage respect to the applied field. The quantitative analysis has led to ${\chi_{IEC}}^{-1} \propto 0.6\%/Oe$, ${\chi_{IEC}}^{-1} \propto 1\%/Oe$, and ${\chi_{IEC}}^{-1} \propto 1.5\%/Oe$, for $t_{CoFeB} = 45\,nm$, $t_{CoFeB} = 70\,nm$ and $t_{CoFeB} = 100\,nm$, respectively. This confirms the trend observed for the extrapolation of $\boldsymbol{H}_{ex}$ from the easy axis loops: increasing the thickness of the ferromagnetic layer leads to a decrease of the IEC strength, which is translated in an increase of the slope of the curve for the hard axis.

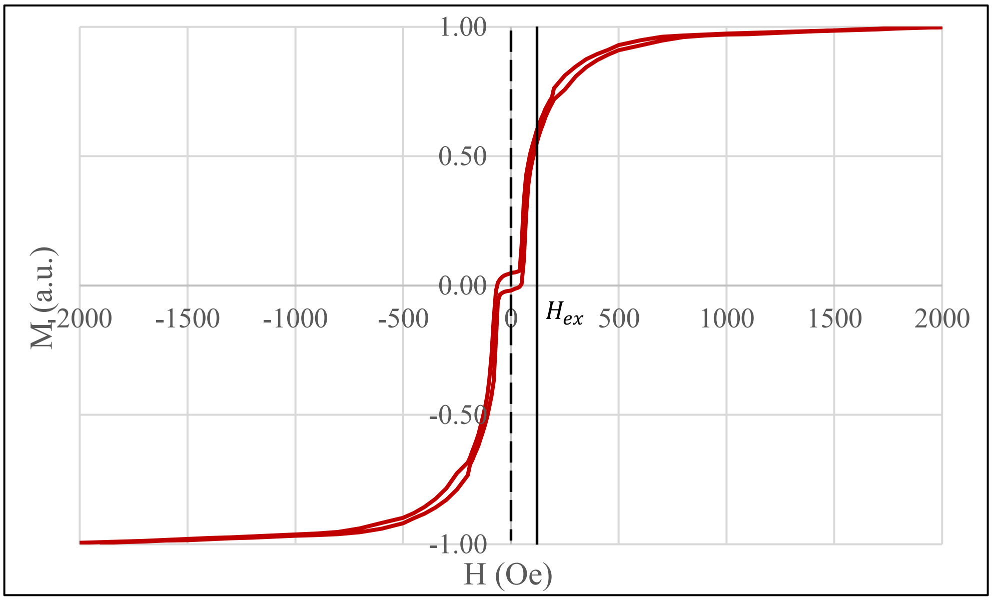

(a)

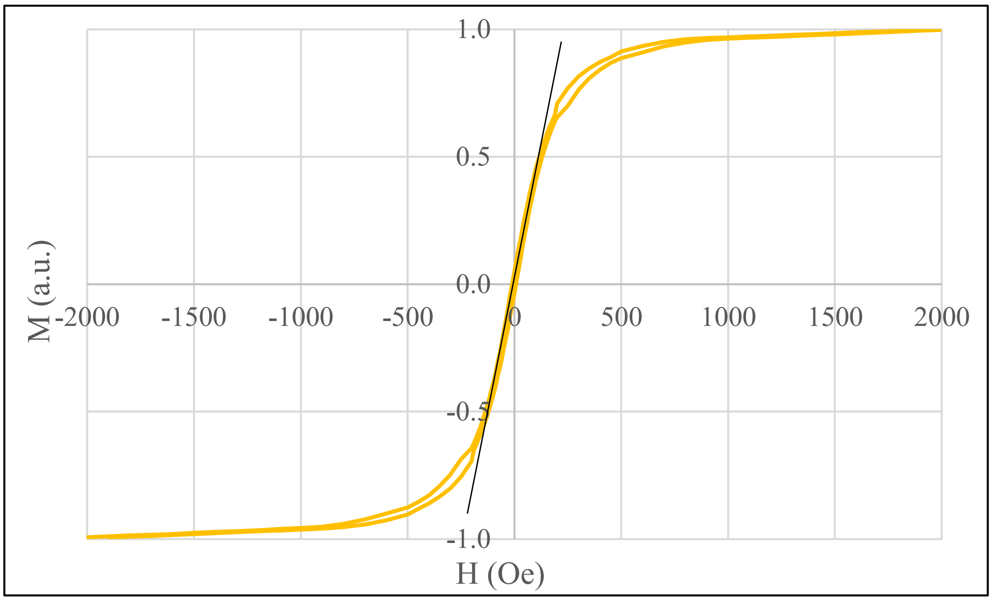

(b)

Figure 4.15: Hysteresis loop after thermal annealing at 250°C at 4 kOe for 5 min SAF20b_5 along (a) easy axis and (b) hard axis

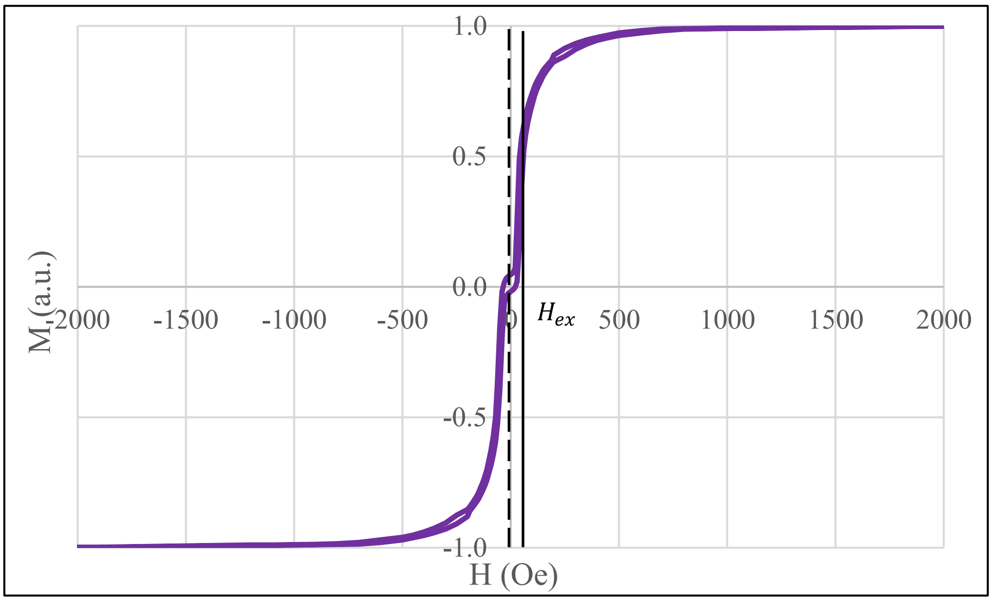

(a)

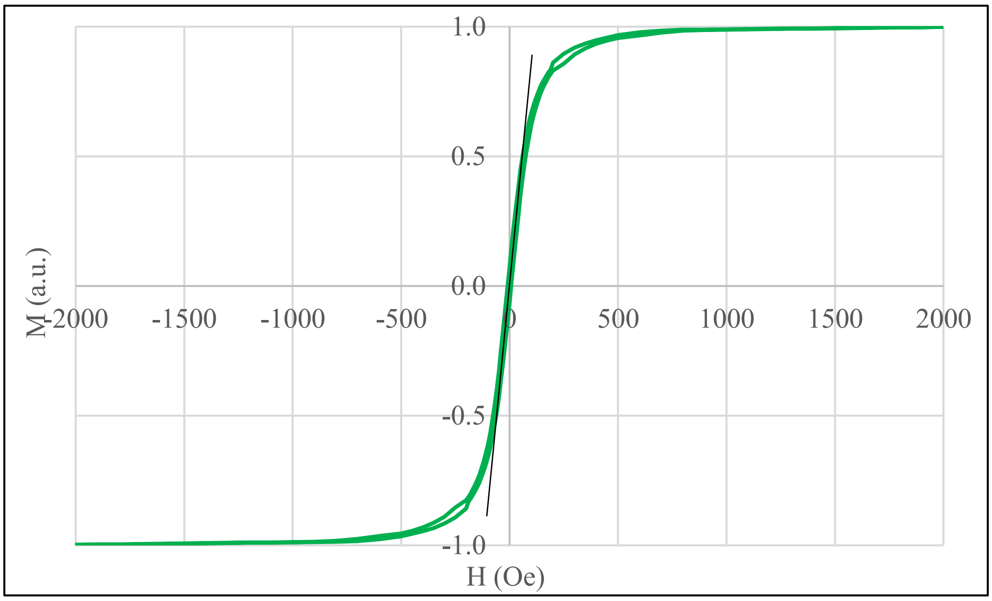

(b)

Figure 4.16: Hysteresis loop after thermal annealing at 250°C at 4 kOe for 5 min SAF20b_6 along (a) easy axis and (b) hard axis

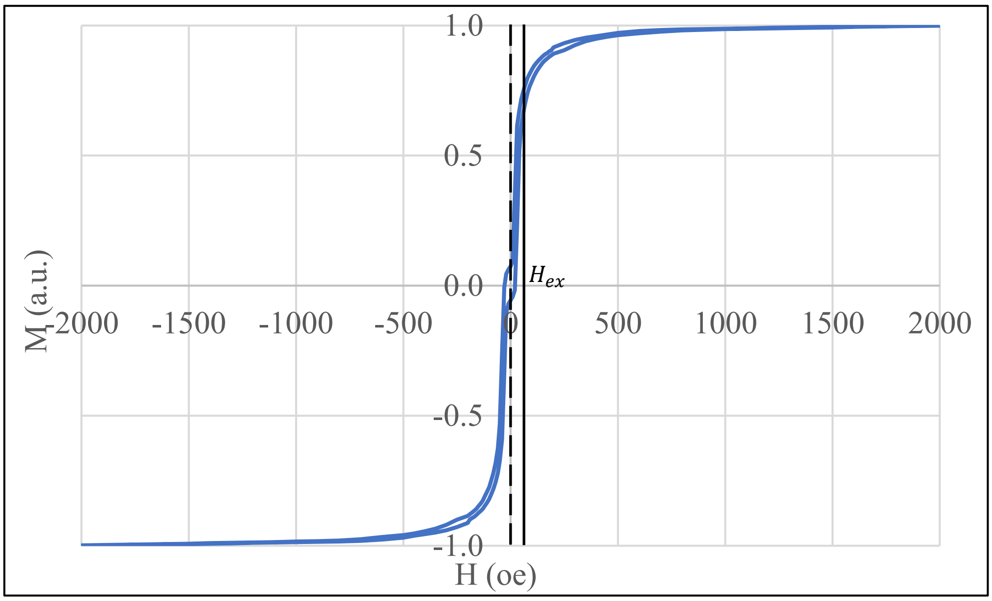

(a)

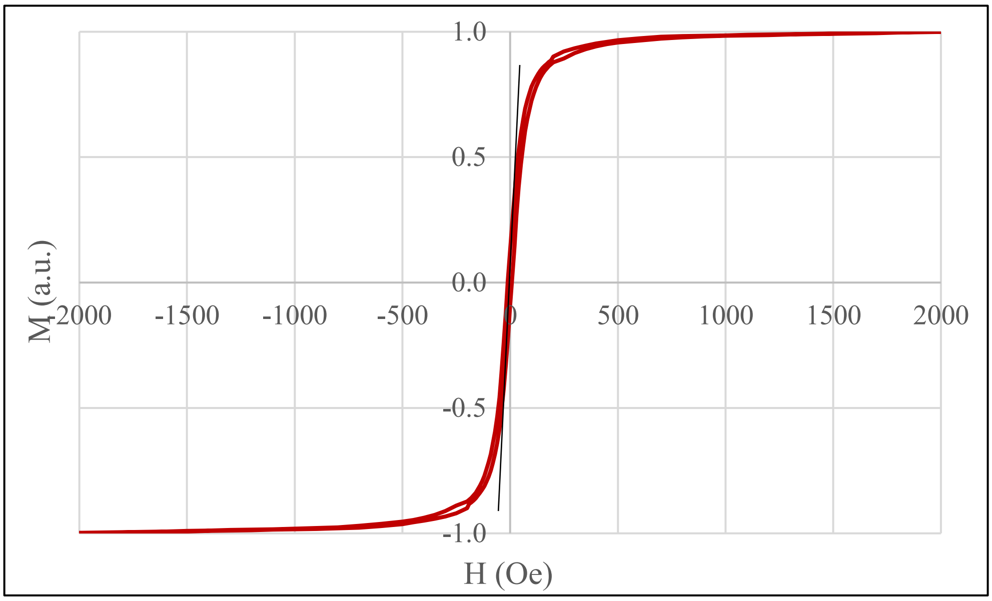

(b)

Figure 4.17: Hysteresis loop after thermal annealing at 250°C at 4 kOe for 5 min for SAF20b_7 along (a) easy axis and (b) hard axis.

The quantitative results obtained are summarized in Figure 4.18, where both the values of $\boldsymbol{H}_{ex}$ extracted from the hysteresis loops along the easy axis and of the slope derived from the hard axis are reported. For the former, a decrease of the intensity of $\boldsymbol{H}_{ex}$ is observed when increasing the thickness of the ferromagnetic layer, while for the latter increasing the thickness the slope of the magnetization curve taken along the hard axis increases as well (i.e. the susceptibility χ_{IEC} decreases). This is consistent to what is expected: due to the fact that the IEC is an interfacial interaction, increasing the thickness of the structure leads to a decrease of its strength.

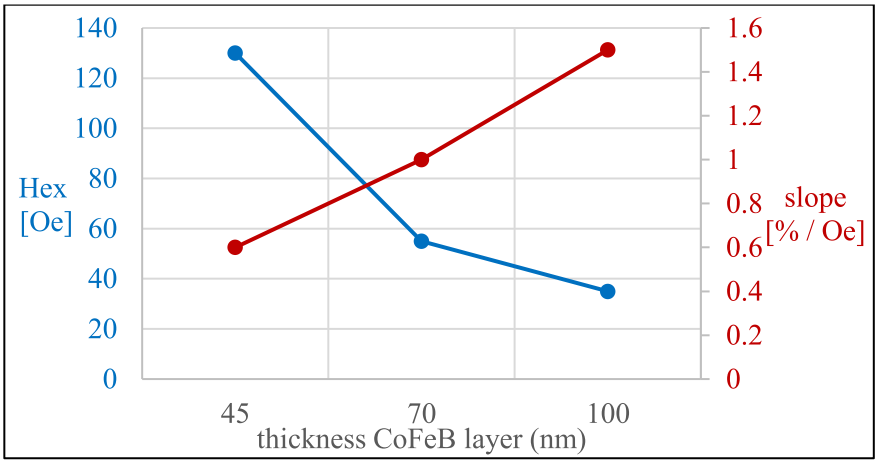

Figure 4.18: obtained results for the strength of the interlayer exchange coupling in terms of IEC field $\boldsymbol{H}_{ex}$, obtained from the hysteresis loop along the easy axis (blue curve) and in terms of the normalized slope from the hard axis (red curve), which is related to the inverse of the IEC susceptibility.

For the SAF samples without the antiferromagnetic layer, since no exchange bias is present, the thermal annealing process has not been performed. For this reason, the hysteresis cycles have been measured only after the deposition, and because no in-plane field was present during the growth process, the direction of the easy axis was not known. Therefore, the resulting hysteresis loops measured along two arbitrarily chosen axis (called here 0° and 90°) both resemble the shape of a hard-axis cycle (Figure 4.19 for SAF21_3). Nevertheless, the lack of a clear jump around $\boldsymbol{H} = 0$ as would happen in the case of a ferromagnetic alignement, but rather the presence of a smooth transition from negative to positive magnetization when moving from negative to positive applied fields, and the presence of the typical inflection point for the curve around zero applied field, proves indirectly the correct antiferromagnetic coupling of the CoFeB layers. A similar behavior has been confirmed also for SAF21_4 and SA21_5.

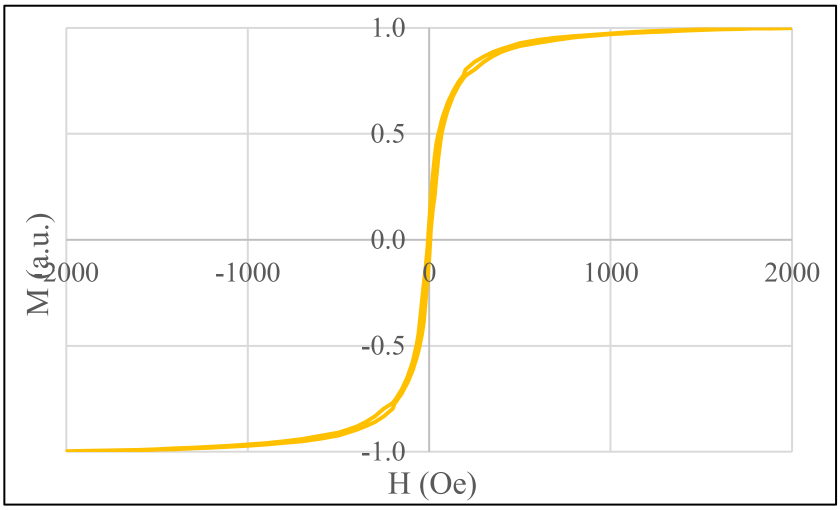

(a)

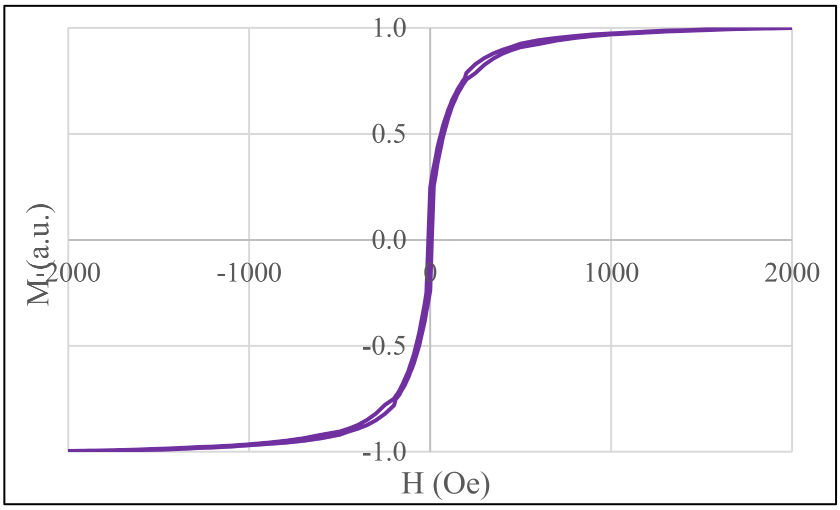

(b)

Figure 4.19: In-plane hysteresis cycle after deposition of SAF21_3 along two arbitrarily chosen directions, called here (a) 0° and (b) 90°. Since no exchange bias is present, no thermal annealing has been performed on the sample and the direction of the easy axis is not known. Despite that, the antiferromagnetic coupling between the two ferromagnetic layers can be indirectly deduced from the smooth transition from negative to positive values of the magnetization when going from negative to positive applied field and from the typical inflection point present around $\boldsymbol{H} = 0$.

4.4 Samples nanofabrication

After the identification of the optimal growth conditions and of the thicknesses of the CoFeB layers for the fulfillment of the requirements mentioned in the last paragraph, the next step was the fabrication of the actual samples for the investigation of the emission and propagation of the spin waves. Thus, the magnetic heterostructures were deposited by magnetron sputtering on suitable supports purchased from Silson Ltd, consisting of silicon nitride SiN membranes 200 nm thick fabricated on a silicon substrate using anisotropic etching, with variable size between 0,5 mm x 0,5 mm and 1,0 mm x 1,0 mm. As previously mentioned, the deposition of SAF20b_5, SAF20b_6 and SAF20b_7 was performed on an in-plane magnetized sample-holder to drive the orientation of the exchange bias at the CoFeB/IrMn interface, while a non-magnetized sample-holder was used for SAF21_3, SAF21_4 and SAF21_5. For the exchange-biased SAF a field cooling in a chamber with pressure below 10^{-4} mbar was later performed to set the direction of the exchange bias while at the same time allowing a higher control of the temperature and preserving the sample from contaminations. The annealing was set at 250°C for 5 minutes, with a 4 kOe in-plane applied field, in the same direction of the field present during the deposition. The temperature was increased with a controlled rate of 5°C/min.

What follows is a detailed description of the different nanofabrication processes needed to either magnetically pattern the domain walls via tam-SPL or to nanopattern different geometries on the membranes for the stabilization of Landau domains in the structure.

4.4.1 Patterning magnetic domain walls via tam-SPL

At this point the exchange biased SAF samples were ready to be patterned via tam-SPL with the aim of writing the domain walls to be exploited for the emission of spin waves. The magnetic patterning was performed by means of the AFM available at the PoliFAB facility at the Politecnico di Milano. As described in detail in paragraph 3.1.4, a highly localized field cooling is performed via tam-SPL, using the hot tip of a Scanning Probe Microscopy (SPM), while an in-plane applied field is present. To pattern the spin texture, the tip was swept above the surface in a raster-scan fashion. For the purpose of this work, the applied field was set with opposite direction with respect to the exchange bias field set during the thermal annealing process, with an intensity of 500 Oe. This allowed to spatially control the magnetization of the top-CoFeB layer and to orient its magnetization at remanence parallelly to the external field. Importantly, since the interlayer exchange coupling is present, the magnetization of the bottom-CoFeB layer is point-to-point antiferromagnetically oriented respect to the top layer. A voltage is applied to the tip, which increases its temperature by Joule heating. The calibration curve of the tip is presented in Figure 4.20, relating the applied voltage to the tip temperature. To magnetically pattern the samples successfully, the tip must be heated above the blocking temperature of the exchange bias system, roughly corresponding to 300°C. A range of voltages was applied in different positions of the patterned membranes, aiming at creating domains with different dimensions: to higher tip temperatures a larger patterning area is associated, leading to the formation of bigger domains. This can be explained by the fact that the membrane has a low thermal conductivity, and therefore the thermal profile associated to the patterning is much larger with respect to the tip dimensions. For this reason, temperatures higher than the blocking temperature are reached much further away (tens of μm) with respect to the position of the hot tip. In Table 4.6 the applied voltages during the magnetic patterning and the corresponding tip temperatures and domain dimensions (corresponding to the length of the red arrow in Figure 4.21) are reported.

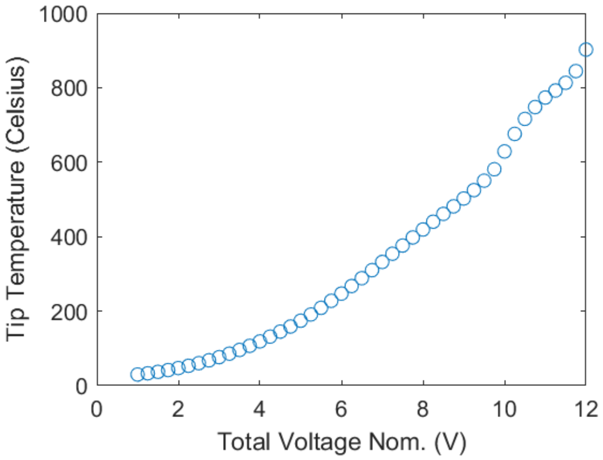

Figure 4.20: tam-SPL tip calibration curve. The applied voltage is converted in the tip temperature. To obtain this curve, the variation of the resistance vs the applied voltage is measured during the calibration, from which the dissipated power is derived and so the temperature of the tip can be obtained.

Voltage	Tip Temperature	Domain dimension
7,5 V	376 °C	15 μm
7,75 V	398°C	22 μm
8 V	419°C	25 μm
8,25 V	440°C	40 μm
8,5 V	481°C	43 μm

Table 4.6: applied voltages during tam-SPL and corresponding tip temperature and domain dimension.

Since the setting and monitoring of the temperature during the patterning process are performed indirectly (controlling the voltage and measuring the resistance, respectively), some uncertainty may be present. For this reason, to avoid having inhomogeneities and not correctly reaching the blocking temperature to set the exchange bias, all the voltages used corresponds to temperature well above T_b.

Some examples of the domains patterned with the different applied voltages **(a)** 7,5 V **(b)** 7,75 V **(c)** 8 V **(d)** 8,25 V and **(e)** 8,5 V are show in Figure 4.21. The images were taken with the Magneto-Optic Kerr Effect Microscope (µMOKE), and the difference in contrast represents the different orientation of the in-plane component of the magnetization of the top CoFeB layer. As an example, in the first image on the left the direction of the magnetization of the top-CoFeB layer is represented with a white arrow, while the direction of the magnetization along the patterned domain is shown with the blue arrow. Further details on the magnetic characterization via µMOKE will be presented in paragraph 4.5. The panel below reports in detail a simulation of the magnetization of the two CoFeB layers: on the left, a tridimensional visualization of the rotation of the magnetization alongside the domain wall is represented, while on the right the result of a Mumax^3 simulation for an exchange biased SAF is shown, where the black arrows mark the direction of the magnetization, while the colors represent the out-of-plane component of the magnetization. As expected, the magnetic moments are pointing in opposite direction everywhere. Moreover, as already mentioned in paragraph 4.2, moving towards the DW a partial out-of-plane canting of the magnetization is present (which is shown on the image on the right with an increased contrast of the colors), as a consequence of the magnetostatic energy minimization in proximity of the domain wall (flux closure state).

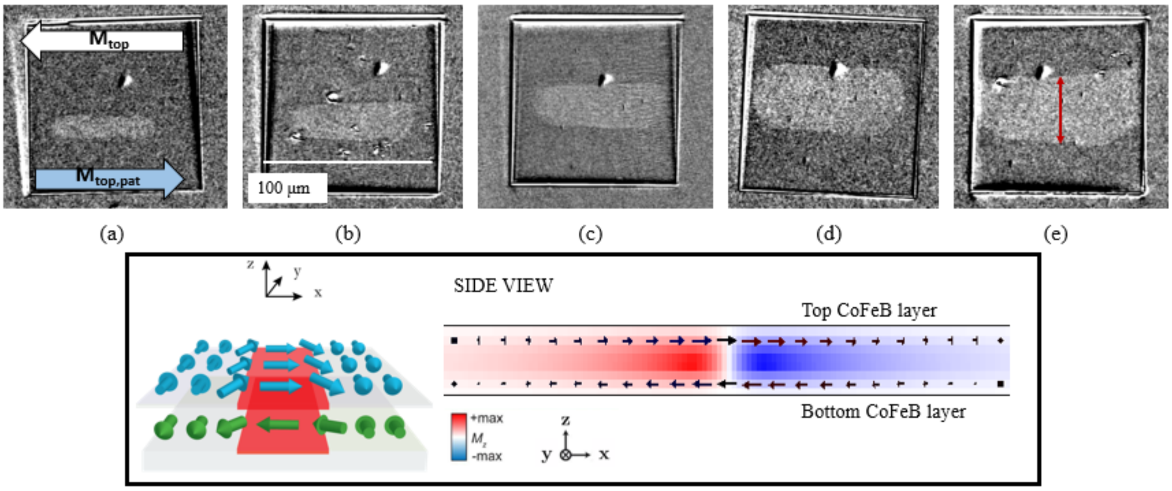

Figure 4.21: µMOKE images at 50x of the domains patterned via tam-SPL with different voltages applied: (a) 7,5 V (b) 7,75 V (c) 8 V (d) 8,25 V and (e) 8,5 V. The white arrow shows the orientation of the magnetization of the top-CoFeB layer, while the blue arrows point in the direction of the magnetization written during tam-SPL. In the panel a simulation of the magnetic configuration of the multilayer is shown, highlighting the orientation of the

magnetization of the two CoFeB layers. The simulation on the right has been carried out via the Mumax^3 software, while the visualization of the magnetic configuration with OOMMF. The black arrows show the direction of the magnetization, while the colors represent the out-of-plane component of the magnetization.

To summarize, in Figure 4.22 the optical microscopy images of the patterned membranes for the three exchange-biased SAF are reported, and the squared features have been numerated. In Table 4.7 the applied voltages for the patterning via tam-SPL of each square are summed up.

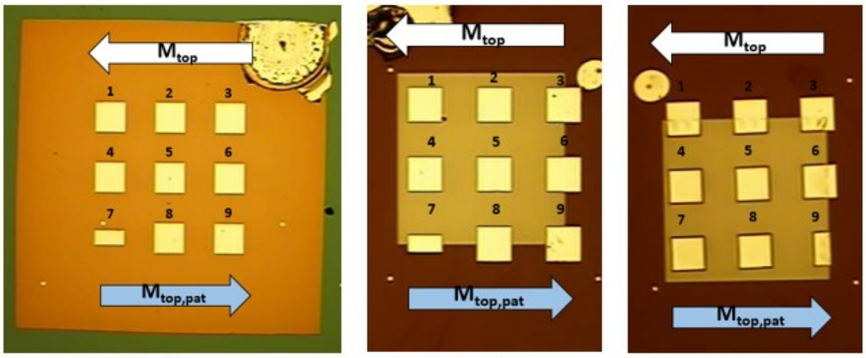

SAF20b_5 1000 µm   SAF20b_6 500 µm   SAF20b_7 500 µm

Figure 4.22: Optical microscopy images taken at 20x with the numerate features (100 µm x 100 µm) that were patterned via tam-SPL for each of the three exchange biased samples.

Voltage (V)	SAF20b_5 1000 µm	SAF20b_6 500 µm	SAF20b_7 500 µm
Square 1	7,5	8	-
Square 2	8	8	-
Square 3	8,5	-	-
Square 4	7,75	7,75	8
Square 5	8	8	8
Square 6	8,25	-	-
Square 7	-	-	8,5
Square 8	8	-	8
Square 9	8	-	-

Table 4.7: applied voltages during tam-SPL for each squared feature on the membranes for each of the exchange-biased SAF

4.4.2 Fabrication of magnetic nanostructures via e-beam lithography

The nanopatterning of the different nanostructures on the membranes was performed via electron-beam lithography *before* the deposition process. The complete patterning process was carried out by Dr. Simone Finizio at the Paul Scherrer Institut (PSI) facility using a 100kV Vistec EBPG 5000Plus, which allows to write customed shapes on a large area with sub-10 nm spatial resolution without using a mask (maskless lithography). The detailed description of the e-beam lithography working principle has been presented in Section 3.1.2. This method was first used to pattern the nanostructures reported in Figure 4.23 on the membranes. In particular, nine 100 x 100 μm^2 squares (Figure 4.23(a)) were designed on the exchange biased SAF sample for performing the tam-SPL method for magnetically writing the domains, while the different small geometric features (Figure 4.23(b)) were fabricated on the SAF samples for stabilizing the formation of Landau domains induced by shape anisotropy.

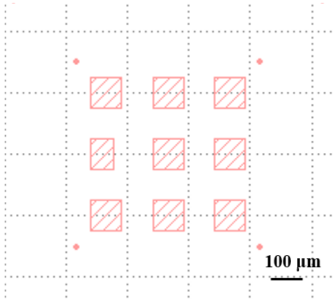

(a)

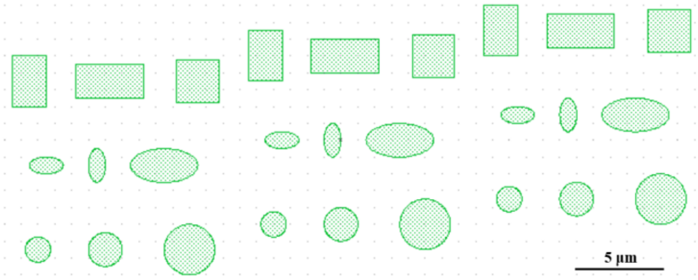

(b)

Figure 4.23: nanopatterned features on the SiN membranes (a) 100 x 100 μm^2 squares patterned via tam-SPL and (b) small geometric shapes for the stabilization via shape anisotropy of Landau domains.

4.4.3 Fabrication of the striplines

After the deposition process and magnetic patterning, the striplines needed for the generation of the Oersted field for the excitation of the spin waves have been fabricated on top of the structures. For the fabrication process, a bi-layer of MMA and PMMA was spin-coated on top of the sample and exposed with electron-beam lithography with electron energy of 100 keV. After the development of the resist, a Cr film of 10 nm was deposited as adhesion layer, followed by a Cu film of 300 nm. The deposition process was performed using a Balzers BAE250 thermal evaporator, available at the PSI facility. Finally, the unexposed resin has been removed by immersion on pure acetone. Copper was chosen instead of Au, which is often used to fabricate electrical contacts, because it has a higher transparency to X-rays radiation. The striplines have been designed aiming at crossing the written spin texture or the stabilized Landau domains, in order to efficiently excite the propagation of spin waves. The length of each stripline is 40 µm, while the width is 5 µm. Each stripline is characterized by two pads, one for the signal and one for ground, respectively. The width of the stripline is a critical factor since it must be large enough to reduce local Joule heating, but thin enough to allow the generation of the Oersted field. As an example, in Figure 4.24 the stripline patterned above one of the SAF samples is reported.

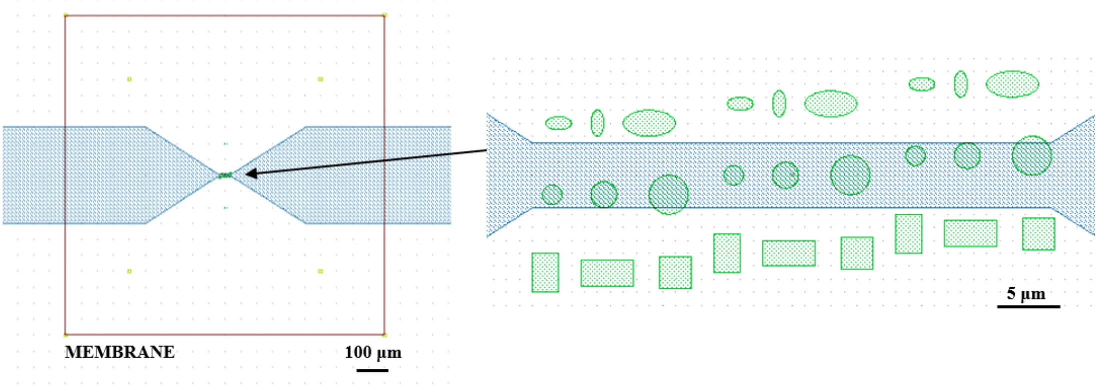

Figure 4.24: schematics of the stripline patterned via e-beam lithography above the membrane.

4.5 Characterization of the magnetic domain structure via MOKE microscopy

The Magneto-Optical-Kerr Effect (MOKE) microscope was employed to complete the first step of the magnetic characterization of the samples, verifying the correct magnetic behavior induced by the patterning via tam-SPL or by shape anisotropy, respectively. Despite having a lower spatial resolution with respect to the Magnetic Force Microscopy (MFM), the MOKE microscopy is particularly useful thanks to its larger flexibility in terms of measurement conditions, the lower measurement time, and its relative easiness of use.

The MOKE microscope employed in this work is a custom-made instrument and can obtain information about the magnetization state of the sample illuminating it with a polarized light and analyzing the information contained in the reflected beam, while applying on the sample a controlled magnetic field. The quantitative and qualitative information about the magnetization is limited by the penetration depth of the light beam, which is of the order of few tens of nm, so only the surface magnetic properties of the sample are obtained. This allows to observe the presence of the magnetic domains on the developed structures, even though the SAFs are perfectly compensated. The detailed description of the MOKE instrumentation is present in paragraph 3.2.3.

In Figure 4.25 the resulting hysteresis loop images taken with the MOKE microscope on square number 6 of SAF20b_5 (1 mm x 1 mm membrane) with different applied in-plane field highlights the presence of the magnetic patterning via tam-SPL. The external field was applied between -1450 Oe and 1450 Oe (1450, 800, 150, 125, 100, 75, 50, 25, 0 for the modulus of the field). Several interesting observations can be made: first of all, comparing the images taken at the same value of the external field equal to -75 Oe but on different branches of the loop, it becomes immediately clear that the situation is very different. This confirms the presence of the exchange bias on the structure, which shifts the hysteresis cycle of the system. In addition to this, the images taken at zero applied field show an intense contrast between the patterned area and the background, once again proving the robustness of the exchange bias, which is strong enough to permanently impose the magnetization of the patterned domain in the opposite direction respect to the background, independently on the sample history. This measurement has been carried out for every patterned square for all three exchange-biased samples (Table 4.7), and the presence of the patterned domains have been confirmed for each one of them.

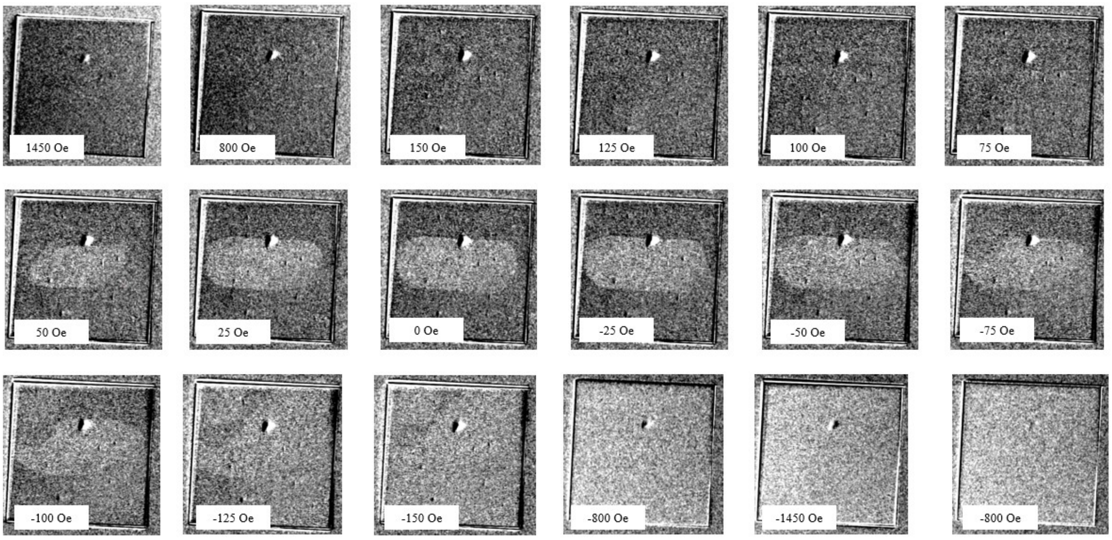

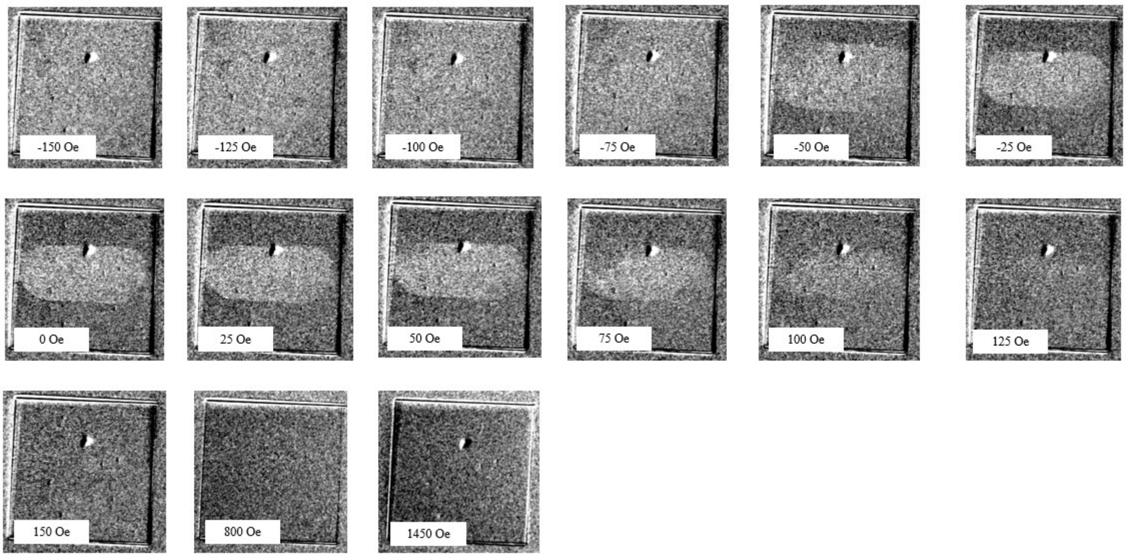

Figure 4.25: Resulting MOKE images of the hysteresis loop performed on the structures (size 100 μm x 100 μm) patterned via tam-SPL under different values of external in-plane applied field.

In Figure 4.26 the MOKE frames obtained during the measurement have been organized to highlight the hysteresis loop of SAF20b_5 and the displacement given by the exchange bias, which in this case corresponds to about 90 Oe.

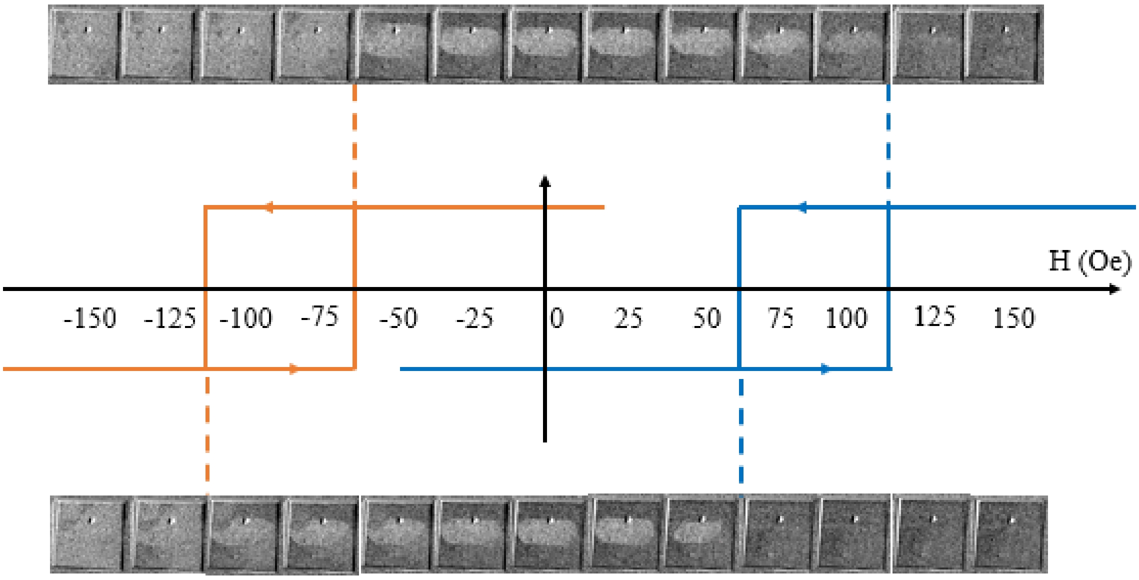

Figure 4.26: MOKE frames organized to show the hysteresis loop of the system, highlighting the displacement given by the exchange bias induced by the presence of the antiferromagnetic IrMn layer. The top sequence shows the evolution of the system from -150 to 150 Oe, while the bottom sequence from 150 to -150 Oe. The EB is strong enough to permanently set the

magnetization of the domain along the direction imposed during tam-SPL, regardless of the sample history. The domain appears to be stable for a good interval of external field.

A similar analysis was performed on samples SAF21_3, SAF21_4 and SAF21_5 which are not characterized by the presence on exchange bias. In this case, the aim of the measurement was to discriminate whether the Landau domains had been stabilized by shape anisotropy. In Figure 4.27 is shown the result of a complete hysteresis loop on sample SAF21_3, with the in-plane applied field sweeping from 200 Oe to -200 Oe. Despite a magnification at 50x, it was not possible to distinguish clearly the different geometries patterned on the sample (present on the bottom of the images) due to their small size, while for the images at higher magnification the noise was too high. Nevertheless, the presence of the triangle on top, which was originally designed as a feature to be used for helping to locate the nanostructures, confirms the presence of the antiferromagnetic coupling between the ferromagnetic layers and the domain evolution as a function of the external field.

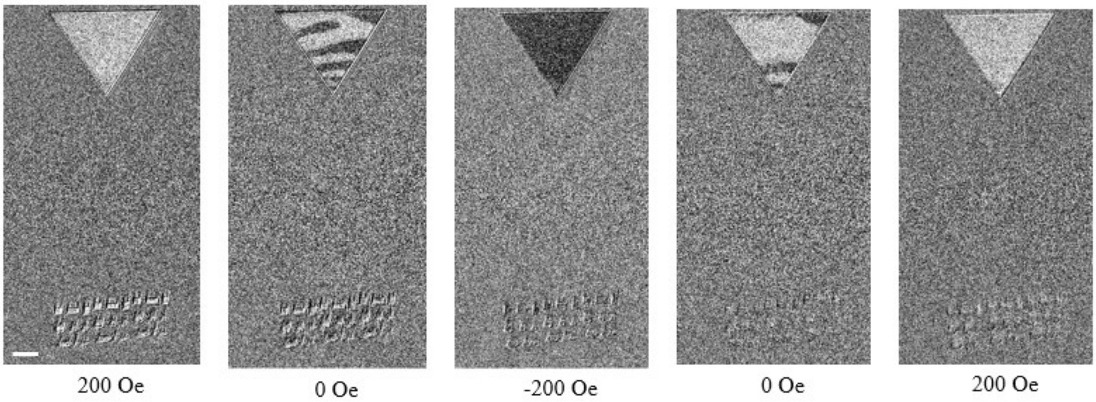

Figure 4.27: Resulting MOKE images of the hysteresis loop performed on the structures patterned via e-beam lithography and stabilized via shape anisotropy under different values of external in-plane applied field. Scale bar = 10 μm.

4.6 Static and time-resolved imaging of spin waves via STXM technique

After the fabrication and characterization processes, the attention was focused on studying the excitation and propagation of spin waves via the conventional static and time-resolved Scanning Transmission X-ray Microscopy (STXM) technique. These experiments were carried out at the PolLux endstation of the Swiss Light Source, at the Paul Scherrer Institut (PSI). Tuning the monochromatic x-rays at the Co L_3 absorption edge (with photon energy of 781 eV) and focusing them using an Au Fresnel zone plated (outermost width of 25 nm) onto a spot on the sample, the transmitted photons were recorded through an avalanche photodiode used as detector behind the sample. To obtain the images, both static and time-resolved, the sample was raster-scanned using a piezoelectric stage. For each pixel of the image, with point resolution between 50 and 100 nm, the transmitted x-rays were measured, while to improve the signal-to-noise ratio for each pixel the signal was integrated over time. During the measurements, a variable in-plane magnet was also mounted, with values of the applied field ranging between 0 and 2 mT. For static images, magnetic contrast was achieved taking advantage of the X-ray Magnetic Circular Dichroism (XMCD) effect, illuminating the sample with circularly polarized x-rays. For XMCD-STXM images the transmitted signal was first recorded separately for the left and right circularly polarized light, and then the two were subtracted to obtain the image, while for normalized images only one photon helicity was sensed (circular negative), and the average value of the intensity measured over one period of oscillation of the pump signal was subtracted pixel-to-pixel. To probe the out-of-plane component of the magnetization, the samples were mounted such that the surface was perpendicular respect to the x-ray beam. For the time resolved-images on the other hand, where the temporal resolution is the result of a stroboscopic detection, a pump-probe technique was employed. A RF magnetic field that was generated injecting a RF current in the patterned striplines and was used as the pumping signal, while the x-rays generated by the synchrotron light source corresponded to the probing signal. To correctly perform the time-resolved measurement, the pumping signal needs to be synchronized by a field programmable gate array (FPGA) to the master clock of the synchrotron light source (500 MHz). Given the specific requirements of the FPGA and of the pump-probe setup available at the PolLux endstation, the accessible RF frequencies corresponds to $f_{ex} = 500 \times M/N\ [MHz]$, where N is a prime number (selected equal to 7, meaning that each video was composed by 7 frames) and M is a positive integer. The corresponding phase resolution for this setup was equal to 50°, while the temporal resolution depending on the value of M was given by $2/M\ [ns]$ with a lower limit equal to 70 ps FWHM (from the width of the x-ray pulse generated by the synchrotron light source).

First, it is important to mention why it is possible to observe spin-wave dynamics inside a synthetic ferromagnetic structure with the STXM technique. This is a consequence of the way spin waves propagates in the two ferromagnetic layers. In particular, the oscillation is in-phase for the z-component of the magnetization, thus summing up and allowing its measurement, while it is out-of-phase for the x- and y-components, giving a total magnetization equal to zero in the x-y plane. This situation is qualitatively depicted in Figure 4.28.

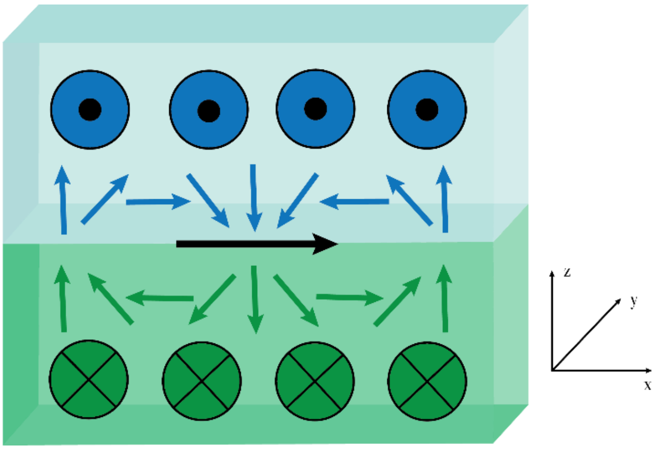

Figure 4.28: schematic representation of the precessional motion of the magnetization inside a SAF. The projection of the magnetization in the z-direction for the two layers is in-phase, allowing the measurement of the spin-waves signal, while for the x- and y-direction the magnetization of the two layers is out-of-phase, giving a total in-plane component of the magnetization equal to zero.

Another important consideration regards the direction of the propagation of spin waves inside the designed structures: as already mentioned in paragraph 4.2, the right-hand rule easily allows to understand the direction of the spin-wave wavevector (Figure 4.4). In the case of the patterned domains via tam-SPL described in 4.4.1, the spin waves are expected to propagate from the bottom domain walls of the spin texture shown in Figure 4.21. For the Landau domains stabilized by shape anisotropy, on the other hand, the emission and direction of the spin waves depends on the circularity of the magnetization inside the domains, as already shown in paragraph 4.2.2. For these structures, during the experiments the attention was focused on studying the propagation of spin waves outwards respect to the center of the nanostructures (i.e. structures with C^+ relative circulation polarity). In the next sections, the results of all the STXM measurements performed will be presented for both types of synthetic antiferromagnetic structures developed.

4.6.1 Spin-wave modes in exchange-biased SAF

Considering first the exchange-biased SAF (SAF20b_5, SAF20b_6 and SAF20b_7), all samples were analyzed at different frequencies, allowing a systematic study of the dispersion relation of the spin waves inside an exchange-biased synthetic antiferromagnet respect to the thickness of the layer. As shown for example by the single frame extracted from a time-resolved STXM video in Figure 4.29 (top panel), the synthetic antiferromagnetic structures developed present an extremely rich and interesting environment for the emission and propagation of spin waves. The presence of the patterned domain wall is extremely clear and the tilting in opposite out-of-plane directions of the magnetization on the two sides of the

DW is given by the black/white contrast. Similarly, the contrast corresponds to oscillations of the out-of-plane magnetization with respect to the average value of the *z*-component and is associated to the propagation of spin waves. Three different propagation modes have been highlighted: emission from a vortex (blue dot) with radial wavefronts, emission from the domain wall (red line) with linear wavefronts, and propagation inside the domain wall itself (green arrow). Moreover, interference figures are formed on the top right and bottom left of the center of the figure.

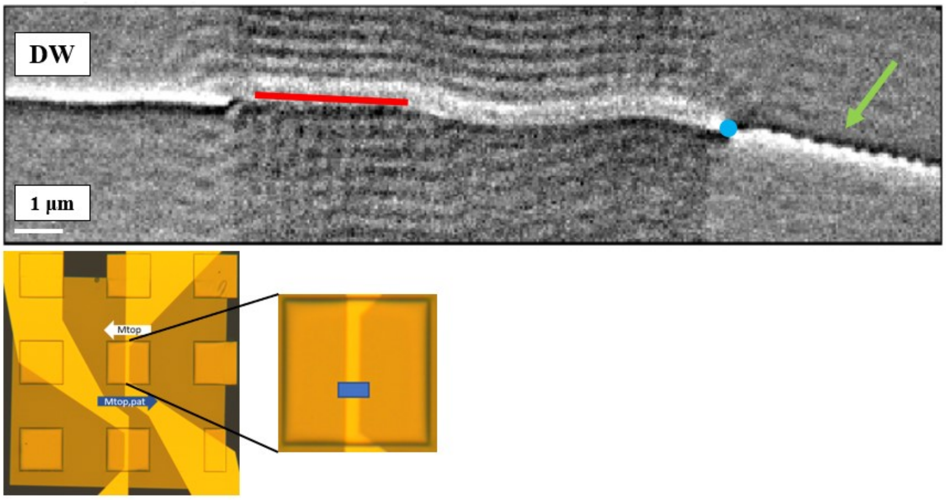

Figure 4.29: (top panel) static XMCD-STXM image of the domain wall across the stripline of SAF20b_7. The system was excited at 0,5 MHz and the spatial resolution is 50 nm, while the amplitude of the voltage injected in the stripline is 1,5 V peak-to-peak. The contrast arising from the XMCD distinguishes the magnitude of the out-of-plane component of the magnetization. Three different propagation modes have been highlighted: the blue dot shows a radial wavefront from a vortex inside the domain wall, the red line correspond to a linear wavefront of spin waves propagating outwards and the green arrow points to the propagation of spin waves inside the domain wall itself. (bottom panel) on the left, optical microscope image of the patterned membrane (size 0.5 mm x 0.5 mm). The white arrow shows the direction of the magnetization of the top layer, while the blue arrow shows the direction of the magnetization of the patterned domain. On the right, the zoomed optical microscope image of the investigated patterned square (size 100 µm x 100 µm) with highlighted in blue the region investigated with the STXM technique and referring to the top panel.

The first step corresponded to taking static XMCD images at different frequencies to locate the presence of the domain walls and to detect the emitted spin waves. After the identification of the ideal positions for studying the propagation of spin waves, time-resolved measurements were performed at different frequencies for acquiring videos of the propagating spin waves. In what follows, a comprehensive analysis of the relationship between the spin-wave wavelength and the frequencies for each sample will be presented. As a matter of fact, a change in behavior of the resulting spin-wave wavelength with the frequency of the Oersted field generated by the current injected into the striplines is expected. Moreover, the goal of the measurement was also to assess whether the thickness of the ferromagnetic layers and/or the dimension of the membranes had an influence on the dispersion relation of the spin waves. To better study the magnetization dynamics, a magnet was added to the STXM setup ($H_{st} < 2\, mT$). The reasoning behind this choice was to use the emitted static in-plane field as an additional knob to tune the spin-textures for maximizing the emission of spin waves. Starting from the exchange-biased SAF20b_5 ($t_{CoFeB} = 45\, nm$) and exciting the systems at $f = 1{,}14\, GHz$ and $f = 1{,}42\, GHz$, the resulting wavelength calculated along the dashed lines are $\lambda{\sim}350\, nm$ and $\lambda{\sim}300\, nm$, respectively (Figure 4.30). Coherently to what it was expected, an increase in the excitation frequency leads to a decrease of the wavelength of the spin waves.

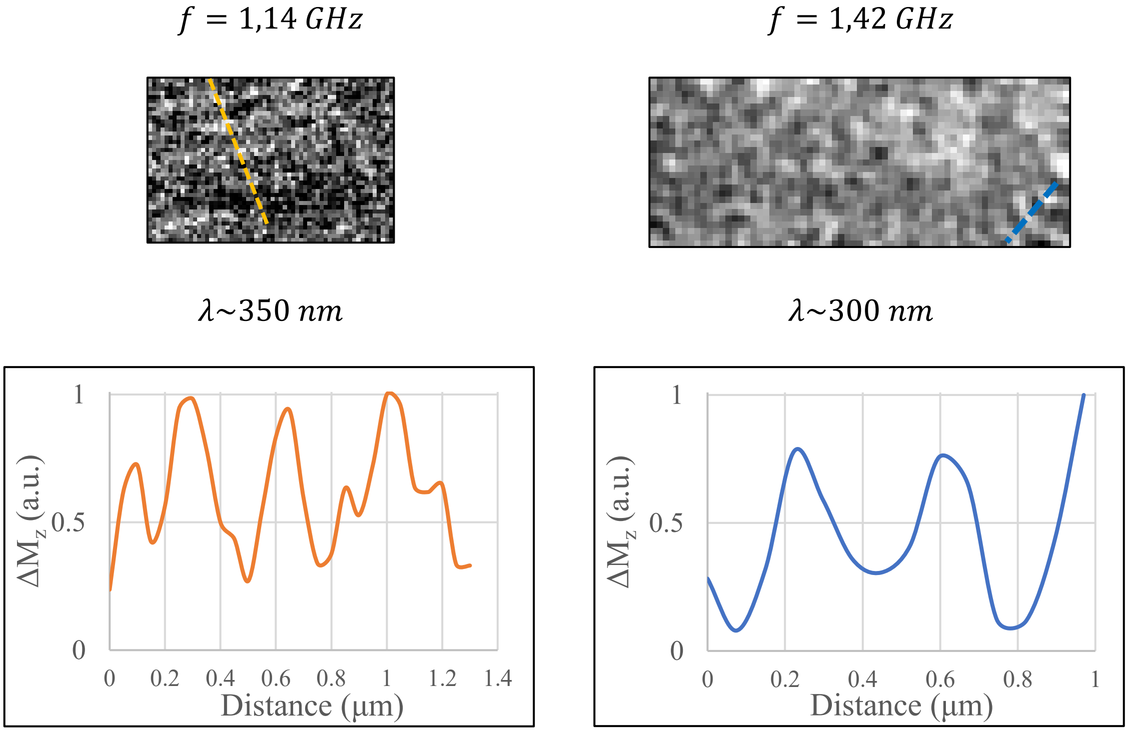

(a) (b)

Figure 4.30: STXM frames of emitted spin waves and intensity profile for the out-of-plane component of the magnetization as a function of the excitation frequency. (a) size 3x2 µm^2; (b) size 5x2 µm^2.

A similar behavior but at lower frequency has been observed for SAF20b_6 ($t_{CoFeB} = 70\, nm$), for which the radiofrequency used for the spin waves investigation was $f = 0{,}43\, GHz$, $f = 0{,}57\, GHz$ and $f = 0{,}64\, GHz$, with an associated wavelength of $\lambda{\sim}830\, nm$,

$\lambda \sim 530\ nm$ and $\lambda \sim 450\ nm$, respectively. The corresponding frames and intensity profiles are shown in Figure 4.31.

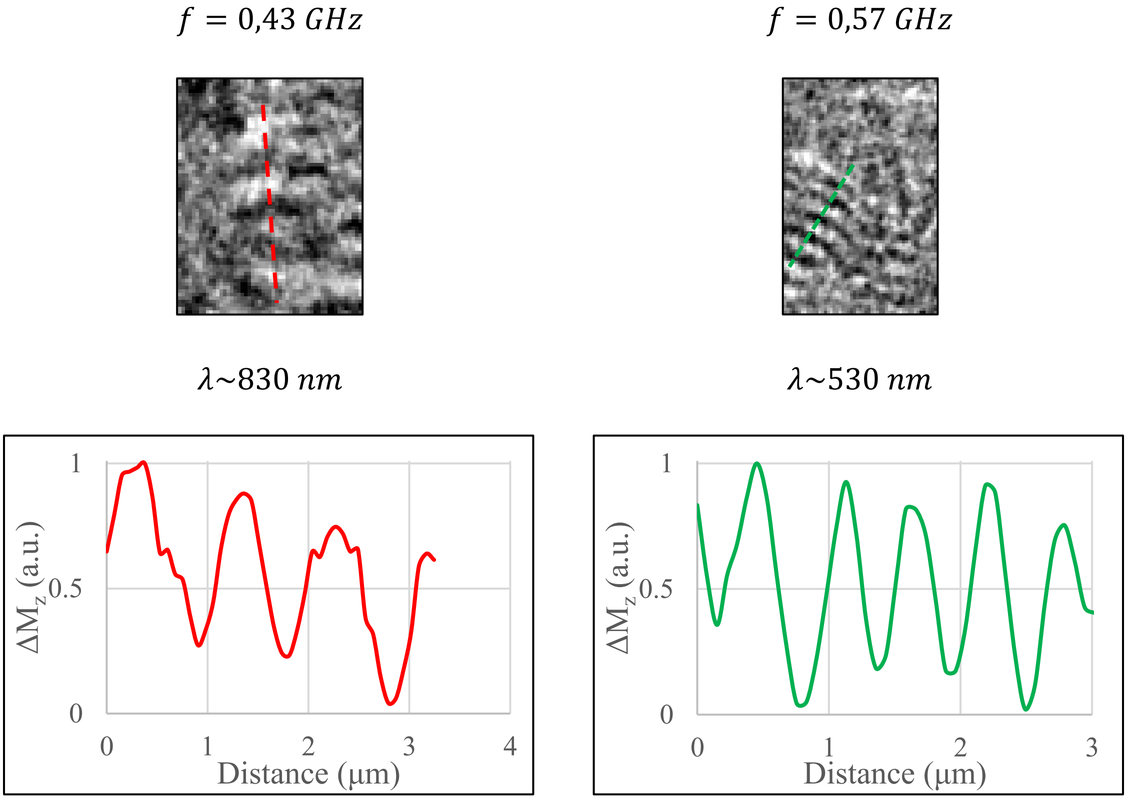

(a)

(b)

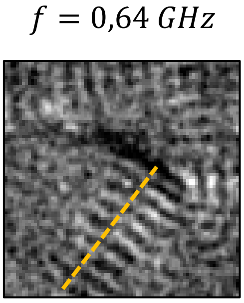

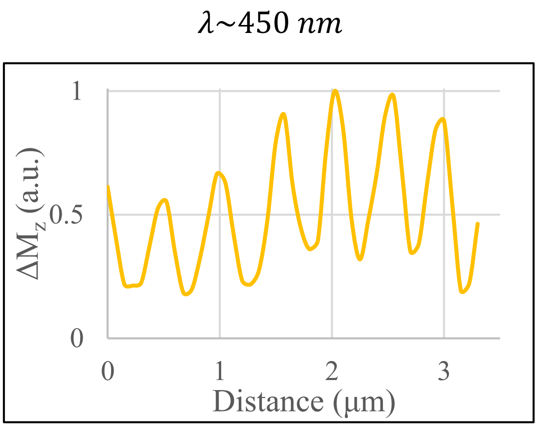

(c)

Figure 4.31: STXM frames of emitted spin waves and intensity profile for the out-of-plane component of the magnetization as a function of the excitation frequency. (a) size 4x5 µm^2; (b) size 4x6 µm^2; (c) size 6x6 µm^2.

For SAF20b_7, which is the sample with larger thickness of the CoFeB layer ($t_{CoFeB} = 100\ nm$), the excitation frequencies at which spin waves are observable are comparable with those of SAF20b_6, but the associated wavelength are smaller (Figure 4.32). Specifically, the investigated frequencies were $f = 0{,}43\ GHz$, $f = 0{,}57\ GHz$, $f = 0{,}64\ GHz$ and $f = 0{,}79\ GHz$, corresponding to $\lambda\sim 600\ nm$, $\lambda\sim 410\ nm$, $\lambda\sim 400\ nm$ and $\lambda\sim 350\ nm$, respectively.

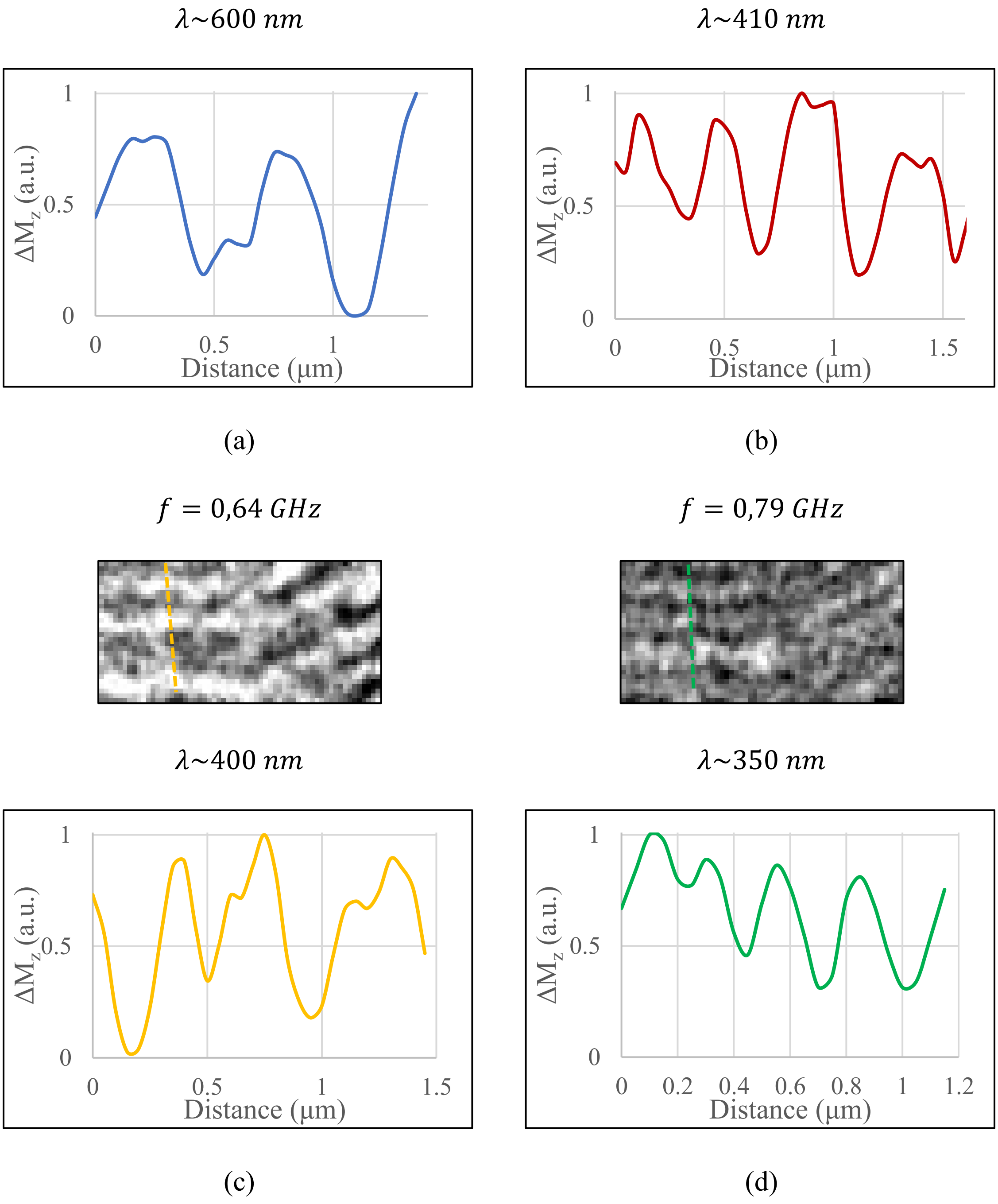

Figure 4.32: STXM frames of emitted spin waves and intensity profile for the out-of-plane component of the magnetization as a function of the excitation frequency. (a) size 3x1,5 μm^2; (b) size 3x4 μm^2; (c) size 3x1,5 μm^2; (d) size 3x1,5 μm^2.

Noticeably, the emission of spin waves was observed also after removing the magnet, as highlighted in the example in Figure 4.33, where a large area across the whole stripline has been investigated. Spin waves have been observed all over the analyzed area, propagating from multiples spin-wave emitters, below the stripline and from its borders. The wavelengths of the emitted spin waves are evidently different one respect to the other in different positions of the investigated region: identifying the cause of this behavior is not trivial, however it is possible that there is a slight variation of the orientation of the in-plane magnetization respect to the propagation direction due to the influence of the stripline, which causes a change in the dispersion relation.

In general, despite the lower tunability of the spin waves given by the absence of the external field from the magnet, the magnetization dynamic was still strongly distinguishable in the system. However, the domains and spin-wave emitters in this case were not very stable in time: the system evolved during the measurements shifting the position of the DWs. A possible explanation for this behavior could be given by the influence of a too high RF current injected through the striplines, which leads to the Joule heating of the system and a consequent change of the spin texture.

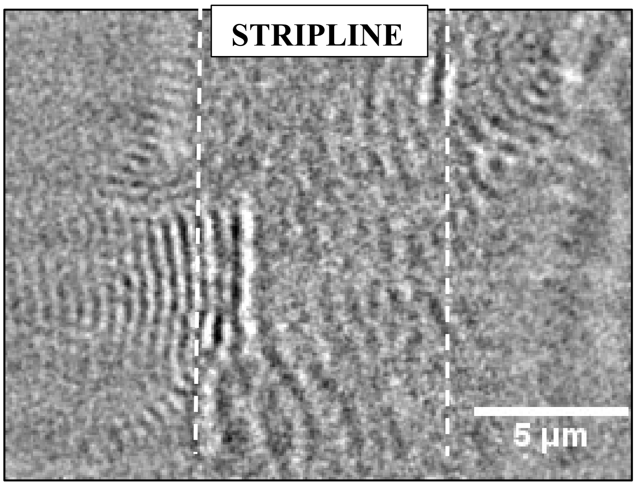

Figure 4.33: time-resolved STXM overview above the stripline of SAF20b_6 at $f = 0{,}64\ GHz$. The size of the analyzed area is 20x15 µm^2. Spin waves are visible across the whole area, emitted both from multiple spin-wave emitters and from the borders of the stripline (white dashed line).

The information obtained for the exchange-biased SAF samples developed in this work were confronted with the data acquired during the previous experiences of the group at the SLS synchrotron facility described in [1] and relative to an exchange-biased SAF CoFeB (45 nm) / Ru (0,6 nm) / CoFeB (45 nm) / IrMn (10 nm) / Ru (2 nm) deposited on a 200 nm thick Si_3N_4 membrane. In this regard, Figure 4.34 reports the calculated dispersion relations for the all the samples (where the label “ADV MAT” refers to the mentioned article), both in terms of wavevectors and wavelengths. For the samples reported in [1], the excitation frequency ranges between 1.14 and 2.14 GHz, with the corresponding wavelength between 500 and 300 nm. The SAF20b_5 was excited at 1.14 and 1.42 GHz, and showed a wavelength of 350 and 300 nm, respectively; increasing the thickness of the ferromagnetic layers at 140 nm, SAF20b_6 showed a wavelength in the range between 830 and 450 nm when excited with a frequency between 0.43 and 0.64 GHz. Finally, for the thicker sample, the system was excited at 0.43-0.93 GHz, and the propagating spin waves showed a wavelength in the range of 600 and 300 nm. In general, a strong shift towards lower frequencies is clearly visible for thicker samples: this behavior could be explained if the effect of strain is considered. As a matter of fact, the deposition of material over the membrane adds a strain component to the system that influences the magnetic properties of the structure. For small thicknesses, the strain effect may be negligible, but it can become visible for larger ones. This hypothesis is consistent to what has been observed in [78], where the vortex gyration eigenfrequency in a 2,5 μm diameter CoFeB disc decreased as the applied isotropic strain increased. Parallelly, if considering two samples at the same frequency (for example SAF20b_6 vs SAF20b_7) the resulting wavelength is shorter for thicker samples (Figure 4.34(b)). The presence of strain in the system can also explain the evolution of domain walls and magnetic features over time mentioned before, making the emitters less stable to very long measurements.

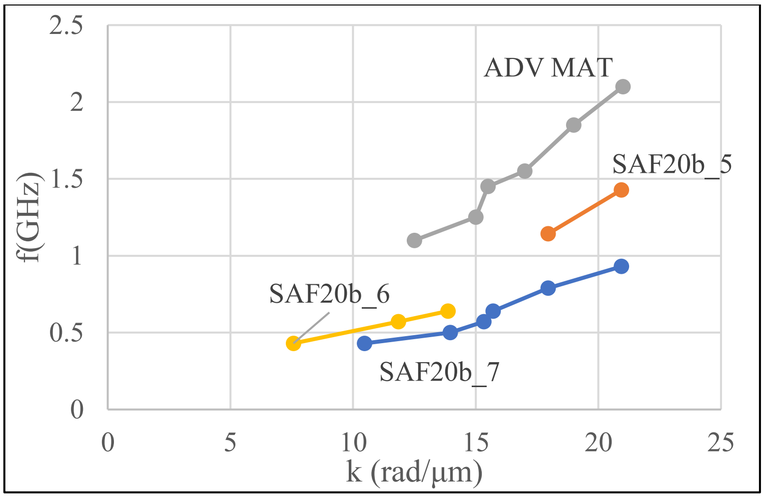

(a)

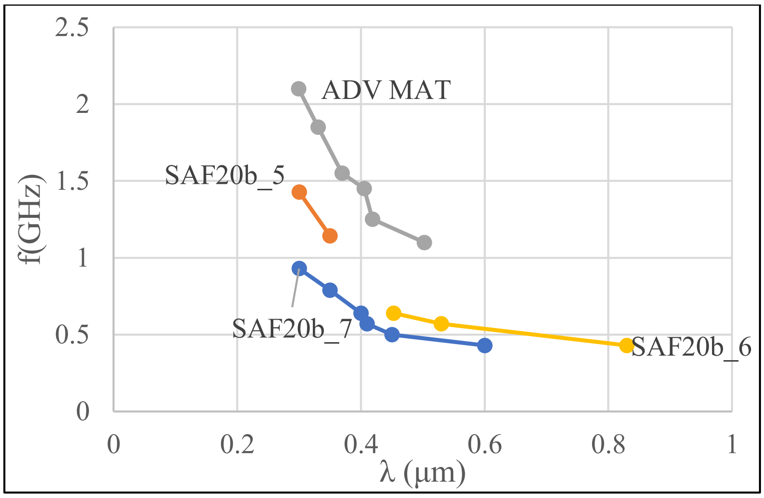

(b)

Figure 4.34: spin-wave dispersion relation (a) frequency vs wavevector and (b) frequency vs wavelength. A strong displacement towards lower frequencies with respect to the previously measured exchange biased SAF has been observed, with a larger shift for thicker samples.

4.6.2 Spin-wave modes inside nanostructures in a SAF

To try to improve the domain walls and spin-wave emitters stability over time, synthetic antiferromagnetic samples stabilized by shape anisotropy have been developed, as described in the paragraphs before. For the identification of emitted spin waves, similarly to the procedure employed for the exchange biased samples, static XMCD-STXM images were first taken to study the domain configuration of the patterned structures. An example for SAF21_5 is reported in Figure 4.35, where the patterned features have been investigated. Differently from what it was expected, no Landau domains were clearly visible during the measurements. Two possible sources for this issue were defined: first, some inhomogeneities in terms of deposition on the different features are recognizable, where more material is present in the middle and less on the borders, giving them a typical “swollen” structure. This could also explain the difference in contrast between the borders and the center of the structure. As a matter of fact, the variation of the thickness of the layers alters the interlayer exchange coupling established between the two ferromagnetic films, leading to an oscillating behavior of the magnetization, which periodically exhibits a tilting in the out-of-plane direction. Moreover, since the synthetic antiferromagnet was designed as perfectly compensated (equal thickness of the two ferromagnetic layers) the flux closure state has already been achieved, making the shape anisotropy term less influential on the stabilization of the equilibrium configuration. For these reasons, the emission and excitation of spin waves for these samples was more complicated, due to the lack of well-defined spin textures to be used as emitters of spin waves.

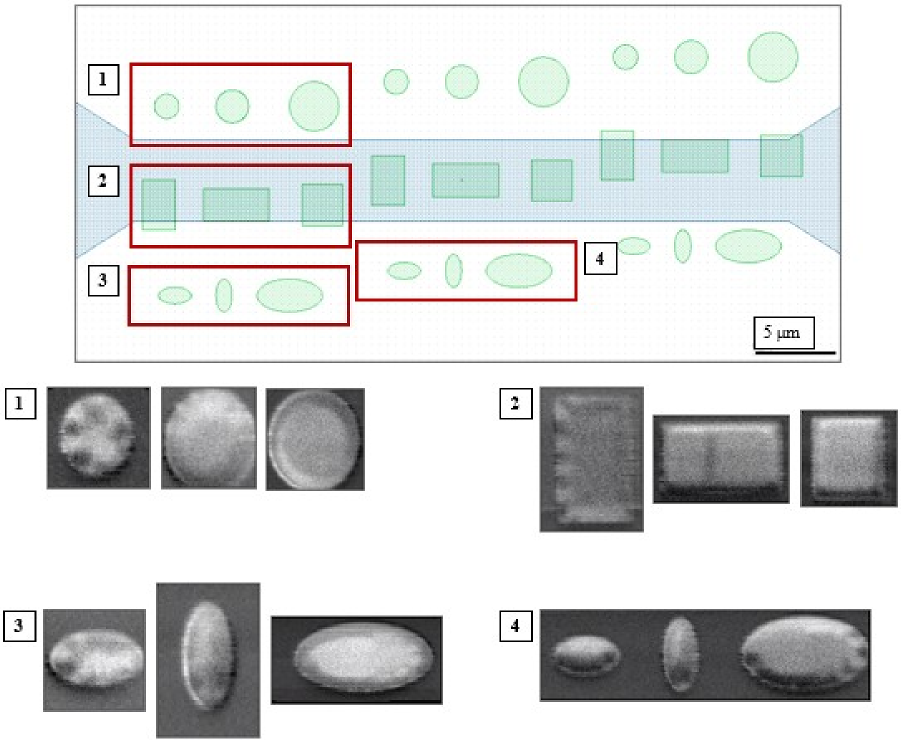

Figure 4.35: (a) schematic of the different geometric features patterned on the membrane of SAF21_5. The blue shaded area represents the stripline across the membrane. (b) XMCD-STXM images of the highlighted features taken at 30°. Size of the nanostructures, from left to right: (1) d = 1.5 µm, 2 µm, 3 µm; (2) size = 2 x 3, 3 x 2, 2.5 x 2.5 µm^2; (3)-(4) size = 2 x 1, 1 x 2, 4 x 2 µm^2.

Nevertheless, it was still possible to observe propagating spin waves emitted by non-homogeneous spin texture and by the borders of the structures, such as the larger circle shown in Figure 4.35(b) above. Despite the higher background noise and the lower contrast, it was possible to plot the profile of the z-component of the magnetization and extract the spin-wave wavelength. In Figure 4.36 the frames of a STXM movie showing the spin-waves propagation inside the circle are reported. For an excitation frequency $f = 0{,}57\ GHz$ the resulting wavelength is $\lambda \sim 600\ nm$, which can be confronted with the results presented before for the exchange biased SAF at the same frequency and with the same CoFeB layers' thickness. As presented in Figure 4.32(b), for SAF20b_7 the calculated wavelength along the red dashed line is $\lambda \sim 410\ nm$, considerably smaller respect to SAF21_5. There are several factors that come into play to explain this difference: first, while for the exchange-biased SAF sample the magnetization has a known direction, given the presence of EB, this is not true for SAF21_5. As a consequence of this, it is not clear which spin-wave modes arise from the structure. Moreover, since the non-uniform magnetization leads to non-planar wavefronts, establishing the spin-wave wavelength is more complicated. The effect of borders must also be considered, having a wavelength comparable to the dimension of the feature ($d = 3{,}5\ \mu m$). Finally, the absence of exchange bias may also partially influence the spin-wave dispersion relation.

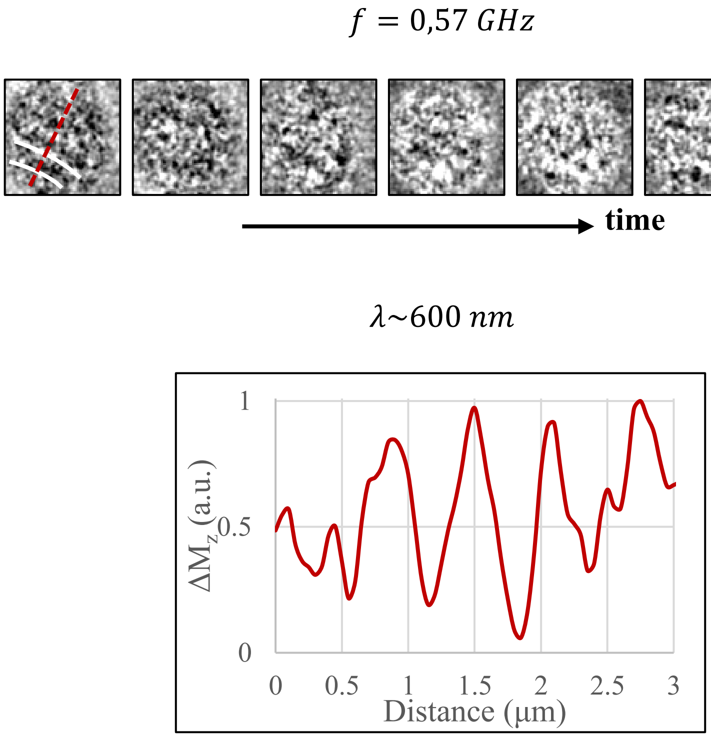

Figure 4.36: STXM frames highlighting the temporal evolution of emitted spin waves and intensity profile for the out-of-plane component of the magnetization as a function of the excitation frequency. Size 3,5x3,5 μm^2.

To summarize, static and time resolved Scanning Transmission X-ray Microscopy measurements have been carried out to assess the excitation and propagation of spin waves inside two types of synthetic antiferromagnetic structures (with and without an exchange bias coupling with an antiferromagnetic layer). Magnetization dynamics and propagation of spin waves have been observed extensively on the exchange-biased SAF samples at different frequency ranges, between 0.43 and 1.42 GHz depending on the thickness of the CoFeB layers, both with and without an external in-plane field applied to the system. The increase of the thickness of the ferromagnetic layers leads to a shift of the dispersion relation to lower frequencies, which is connected with the strengthening of strain effects on the system, consistently to what is present in literature [78]. The presence of strain can also modify the domain wall structures, making spin-wave emitters less stable to prolonged measurements. To have a higher control on the spin texture and domains structure, the development of synthetic antiferromagnetic multilayers without the presence of exchange bias have been proposed, aiming to stabilize via shape anisotropy Landau domains on small patterned geometric features. In this regard, some criticalities have been encountered: due to the very small dimensions of the patterned shapes, the deposition process led to an inhomogeneous thickness on their surface, while the equal thickness of the CoFeB layers (perfectly compensated SAF) reduces the influence of shape anisotropy for determining the magnetization equilibrium configuration, since the flux closure state has already been achieved. Despite these issues, it was still possible to observe propagating spin waves at $f = 0{,}57\ GHz$ and extract the corresponding spin-wave wavelength.

Chapter 5

X-ray Laminography: towards three-dimensional nanoscale time-resolved imaging of spin-wave modes

5.1 Overview

Until now, spin waves have only been measured with two-dimensional static and time-resolved imaging through the well-established Scanning Transmission X-ray Microscopy (STXM) technique, as reported in the previous chapter. A major challenge for the improvement on the understanding and controlling of spin waves is then related to the possibility of measuring the dynamical response of magnetic structures with a three-dimensional resolution, obtaining a direct experimental visualization of the complex spatial profile and its variation along the thickness of the film. This is important both from a physical and a technological point of view, for mapping the internal magnetic structure and dynamics of magnetic materials and for the three-dimensional control of the spin waves for the development of the next generation computing architectures, respectively [6]. In particular, harnessing the third dimension for the realization of innovative three-dimensional nanomagnonic devices would represent a revolutionary breakthrough, allowing the engineering of the spin-wave bandstructure [8], the long-range emission of short-wavelength spin waves [7] and the control of their propagation inside complex heterostructures [2], [3]. For these reasons, great effort has been focused for the development of a three-dimensional non-destructive time-resolved imaging technique with nanoscale resolution that allows to investigate the inner architecture of complex objects and their magnetic configurations [6], [63], [64], [79], [80]. Only recently, three-dimensional static magnetic imaging has been achieved using hard and soft X-rays, neutron and electron tomographies [11]–[14], [81]. Among these methods, synchrotron X-rays are the most interesting one due to their high spatial resolution imaging and their pulsed time structure that allows to perform time-resolved measurements with the pump-probe technique. Nevertheless, some problems arise with the conventional tomography measurements, in particular related to the geometry of the sample, giving the so-called ‘missing wedge’ artifacts due to high absorption at high angles. In this context, the newly developed Soft X-ray Laminography technique present at the PolLux beamline (X07DA) of the Swiss Synchrotron Light Source offers the unique opportunity of combining the already existing time-resolved Scanning Transmission X-ray Microscope setup with the alternative *Laminography* geometry [6], [15], [65], which allows to access all three components of the magnetization with just one axis of rotation, holding the promise of observing for the first time the three-dimensional emission and propagation of spin waves inside the spin texture of synthetic antiferromagnetic structures.

The last part of this thesis work is the result of the first set of experiments performed with the *Soft X-ray Laminography* (SoXL) technique at the PolLux beamline of the SLS synchrotron facility, aimed to obtain for the first time a three-dimensional reconstruction with nanoscale resolution of spin-waves emission and propagation from the synthetic antiferromagnetic structures described in the previous chapter. The final goal of the project is specifically to reconstruct the sequences of three-dimensional time-resolved images, to resolve separately the spatial profile along the thickness of the film and the spin-wave wavelength along the in-plane direction, to obtain the spin-wave dispersion relation and to study the variation of the localization in the z-direction respect to the excitation frequency. In this chapter, after the analysis of the micromagnetic simulations performed on the spin-waves profile of the out-of-plane component on the magnetization along the thickness of the film, I will describe the SoXL instrumentation setup, and the optimization procedures performed for finding the ideal conditions for studying the developed samples. After that, the results of the static measurements of the magnetic configuration of the samples will be presented, which aimed at identifying the domain walls and spin-waves emitters in the structure. Later, I will discuss the results of the first time-resolved Soft X-ray Laminography experiments on synthetic antiferromagnetic structures. Finally, the three-dimensional reconstruction strategy will be described, alongside with the reconstructed topographic three-dimensional image obtained.

5.2 Micromagnetic simulations: three-dimensional spin-wave mode profile in SAF

To simulate the three-dimensional localization of spin waves in a synthetic antiferromagnetic structure at different frequencies and thicknesses, the total simulated volume was discretized into 1024 x 128 x 8 number of cells, for a total size of 10.24 μm on the x-direction and 1.28 μm along the y-direction. Similarly to paragraph 4.2, the investigated system was a CoFeB / Ru / CoFeB / IrMn synthetic antiferromagnet (Table 4.2 summarized the parameters of the material), with varying thickness equal to 90, 140 and 200 nm, respectively, and the spin texture was excited with an external field of 1 mT applied in the z-direction with a frequency varying between 1 and 2,5 GHz. In Table 5.1 the dimensions of the cell (d) for the three values of thicknesses are reported.

Thickness	d_x	d_y	d_z
90 nm	10 nm	10 nm	11,25 nm
140 nm	10 nm	10 nm	17,5 nm
200 nm	10 nm	10 nm	25 nm

Table 5.1: dimension of the cells of the simulated system in each direction for the three values of thicknesses investigated.

The simulations were performed with the Mumax^3 software, and the resulting magnetic configuration was analyzed with MATLAB. To extract the raw information from the files generated from Mumax^3 the code in [82] was used, while I carried out their manipulation to acquire the quantitative profile of the out-of-plane component of the magnetization, obtaining also the value of the angle α of M within the dynamic mode with respect to the static magnetization (Figure 5.1).

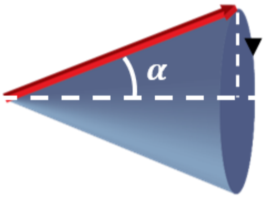

Figure 5.1: identification of the angle α of the propagating dynamic mode of the magnetization respect to the static component, corresponding to the semi-angle of the cone describing the precession of the magnetization.

Figure 5.2 shows the section of the simulated volume for which the (*x,z*)-profile was extracted, also highlighting the position of the domain wall with the blue dotted line and the direction of the propagation of the spin waves inside the film.

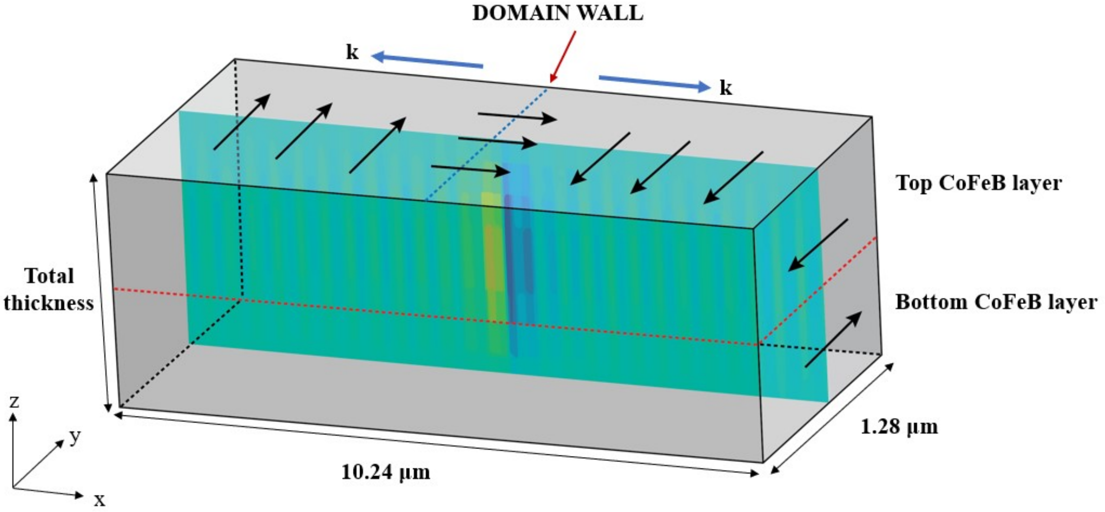

Figure 5.2: schematic representation of the simulated volume. The (x,z)-plane highlighted in red shown where the profile of the spin waves was extracted.

In what follows, the analysis of the results of the simulations are presented, comparing first the three-dimensional profiles of the domain walls for the three simulated systems, and then for each excitation frequency and total thickness of the layer the obtained values of the out-of-plane component of the magnetization normalized with the saturation magnetization and the values of the angle α of the dynamic part of M respect to its static component.

5.2.1 Three-dimensional domain walls profile in SAF

Before analyzing the localization of the spin waves inside the simulated systems, the attention was focused on the three-dimensional profile of the static component of the magnetization close to the domain wall. As already mentioned in detail in paragraph 4.2 (see also Figure 4.1), close to the domain wall the magnetization experiences an out-of-plane canting in the same direction for both the top and bottom layers, breaking the perfect compensation of the synthetic antiferromagnet in the z-direction, as a consequence of the magnetostatic energy minimization that favors the stabilization of a flux-closure state. For the three thicknesses, the obtained values of the out-of-plane component of the magnetization normalized with respect to the saturation magnetization, and the values of the angle θ describing the tilting of M close to the domain wall have been compared. Starting with $t_{tot} = 90\,nm$, Figure 5.3 shows the simulated profiles. The top left panel of (a) reports the (x,z)-profile of $m_z = M_z/M_s$, in which as an example the domain wall is indicated with the red line, while the position of the extracted 1D profile along the z-direction reported in the bottom panel is represented by the black dashed line. Similarly, in the top panel of (b) the (x,z)-profile of $\theta°$ is presented, with the corresponding 1D profile along z below it. For this system, the maximum value of the normalized component of the magnetization is equal to 0.1, localized in the center of the structure, while at $z = 0, 90\ nm$ the minimum of the profile is present, equal to 0.02. The corresponding maximum and minimum angles identified in these positions are 5.75° and 1.13°, respectively.

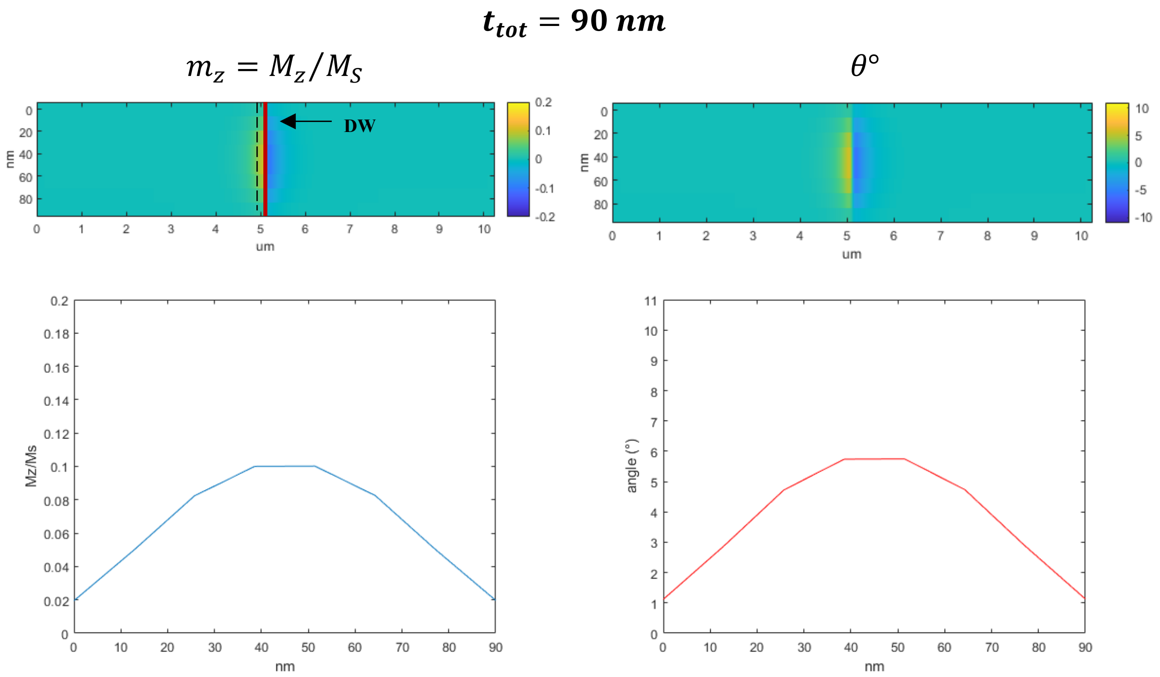

(a) (b)

Figure 5.3: simulated profiles for $t_{tot} = 90\ nm$ of (a) the normalized out-of-plane component of the magnetization and (b) of the value of the angle θ corresponding to the tilting of the static component of the magnetization in the z-direction. The top panels show the (x,z)-profiles, while the bottom panel the corresponding 1D profiles extracted along the black dotted line.

Considering now the sample with $t_{tot} = 140\ nm$, Figure 5.4 reports the obtained profiles for m_z and $\theta°$. In this case, the maximum value obtained for the normalized component of the magnetization is equal to 0.14, to which an angle of 8.13° is associated, while its minimum value is 0.022, with an angle of 1.28. As before, the maximum values are present in the middle of the structure, while the minima at $z = 0, 140\ nm$.

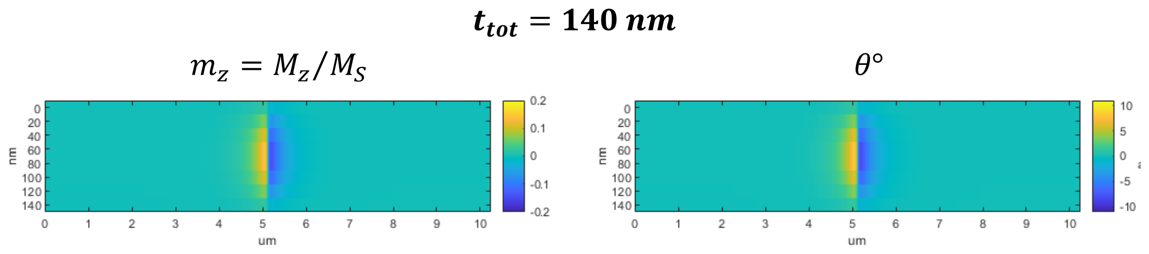

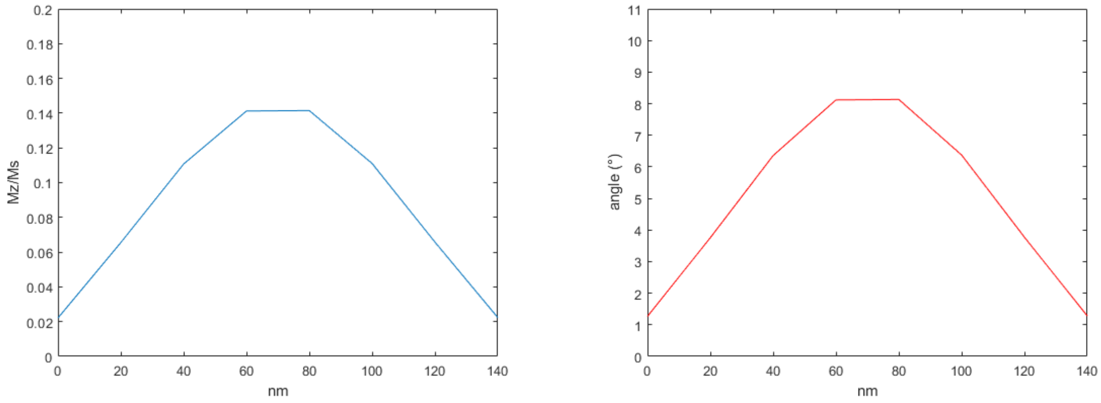

(a) (b)

Figure 5.4: simulated profiles for $t_{tot} = 140\ nm$ of (a) the normalized out-of-plane component of the magnetization and (b) of the value of the angle $\theta°$ corresponding to the tilting of the static component of the magnetization in the z-direction. The top panels show the (x,z)-profiles, while the bottom panel the corresponding 1D profiles extracted along the black dotted line.

Finally, Figure 5.5 presents the profiles for the thicker layer with $t_{tot} = 200\ nm$. In this case, the obtained maximum value of m_z ($\theta°$) found in the middle of the system is equal to 0.18 (10.28°), while the minima are equal to 0.025 (1.44°).

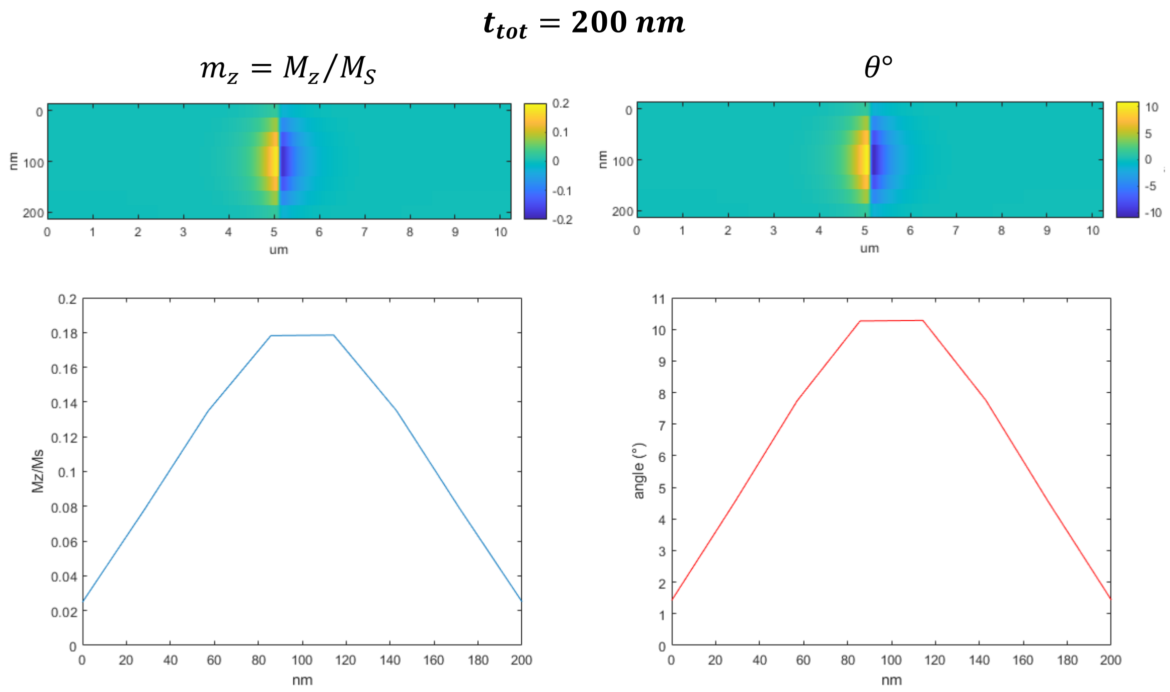

(a) (b)

Figure 5.5: simulated profiles for $t_{tot} = 200\ nm$ of (a) the normalized out-of-plane component of the magnetization and (b) of the value of the angle $\theta°$ corresponding to the

tilting of the static component of the magnetization in the z-direction. The top panels show the (x,z)-profiles, while the bottom panel the corresponding 1D profiles extracted along the black dotted line.

The results for the three thicknesses are summarized in Table 5.2 and show a visible tendency for both the amplitude of the out-of-plane component of the magnetization and the angle associated to the canting of the static component of M along the z-direction: the increase of the thickness of the multilayer leads to an overall increase of the tilting of the magnetization out-of-plane near the domain wall, which reaches its highest value in the middle of the structures at $z = t_{tot}/2$, close to the simulated interface between the two antiferromagnetically-coupled FM films (note that in the real system, the two FM layers are separated by a thin Ru film, which allows to establish the antiparallel IEC).

Thickness	$\boldsymbol{m_{z,max}}$	$\boldsymbol{m_{z,min}}$	$\boldsymbol{\theta_{max}}$	$\boldsymbol{\theta_{min}}$
90 nm	0.1	0.02	5.75°	1.13°
140 nm	0.14	0.022	8.13°	1.28°
200 nm	0.18	0.025	10.28°	1.44°

Table 5.2: maximum and minimum values for m_z and the angle $\theta°$ corresponding to the tilting of the static component of the magnetization in the z-direction for each thickness of the simulated system.

In addition to this, the spatial extension of the out-of-plane component of the magnetization along the x-direction for the three simulated systems has also been investigated. The black dashed line in Figure 5.6 shows the position of the extracted 1D profile, while the resulting profiles for $t_{tot} = 90, 140, 200\ nm$ are reported in Figure 5.7. For each thickness, the distance d between the domain wall (straight line) and the dashed line (positioned in the point where the angle reaches the value equal to zero) has been quantitatively estimated: for $t_{tot} = 90, 140, 200\ nm$ the resulting d is equal to 0.9, 1.1, 1.3 μm, respectively. Also along the x-direction then, the SAF with total thickness of 200 nm is characterized by a larger tilting of the magnetization in the out-of-plane direction, which extends further away from the domain wall respect to the other systems.

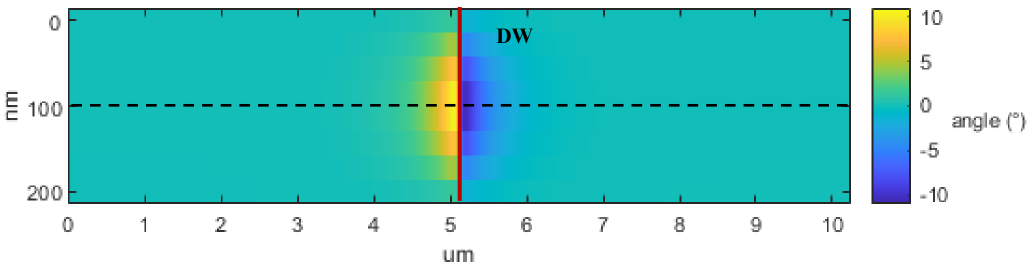

Figure 5.6: examples of the (x,z)-profile for the angle θ° for the simulated SAF with thickness of 200 nm. The red line represents the domain wall, while the black dashed line shows the position of the extracted 1D profile.

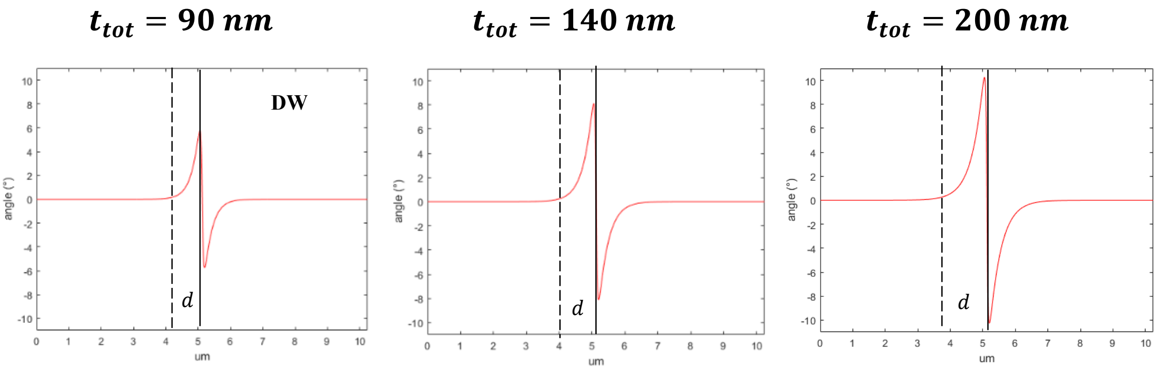
$t_{tot} = 90\ nm$ $t_{tot} = 140\ nm$ $t_{tot} = 200\ nm$

Figure 5.7: simulated profiles along the x-direction for $t_{tot} = 90, 140, 200\ nm$ of the angle θ° describing the canting of the static component of M along the z-direction.

In conclusion, the behavior of the static component of the magnetization close to the domain wall has been simulated. As expected, the magnetization of the two ferromagnetic layer presents an out-of-plane tilting in the same direction when moving towards the domain wall, breaking the antiferromagnetic coupling established in the rest of the film. The canting of M is more pronounced when increasing the thickness of the synthetic antiferromagnetic structure, both in terms of absolute value of $\mathrm{m_z}$ and in terms of the spatial extension along the x-direction, when moving away from the domain wall.

5.2.2 Three-dimensional spin-wave modes profile in SAF

After having analyzed the three-dimensional profile of the static component of the magnetization close to the domain wall, the synthetic antiferromagnetic structures with different thickness were investigated at different excitation frequencies. Specifically, the out-of-plane component of the magnetization normalized to the saturation magnetization and the values of the angle α of the dynamic part of M respect to its static component were quantitatively estimated far from the domain wall, in such a way that the measured contribution was only given by the dynamical part of the magnetization, and no influence of the static component coming from the DW was present. The angle α, in particular, is related to the spin-waves amplitude, and is needed to simulate the localization along the thickness of the film of the spin-wave modes.

Starting at $f = 1\,GHz$, Figure 5.8 shows the simulated profiles for $t_{tot} = 90, 140, 200\ nm$. For each thickness, the top panel reports the (*y*,*z*)-profile of $m_z = M_z/M_s$ and of α, while the black-dashed line highlights the position were the 1D profiles (shown in the bottom panels) have been measured. As an example, the m_z-profile of Figure 5.8(a) also shows the position of the domain wall with a red line. The maximum value of m_z, calculated in the middle of the structure for $z = t_{tot}/2$, corresponds to the thicker system and is equal to 0.021, with an angle of 1.2°. For the other two thicknesses, m_z (α) was equal to 0.019 (1.12°) and 0.006 (0.35°) for $t_{tot} = 140\ nm$ and $t_{tot} = 90\ nm$, respectively.

$$\boldsymbol{f = 1\ GHz}$$

$$t_{tot} = 90\ nm$$

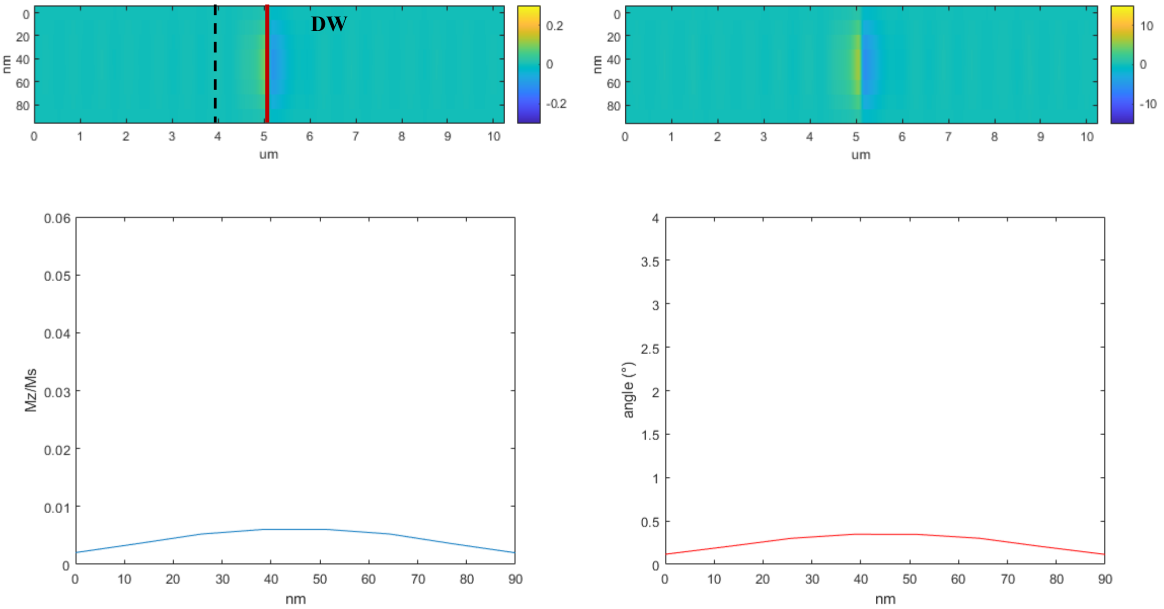

(a)

$$t_{tot} = 140\ nm$$

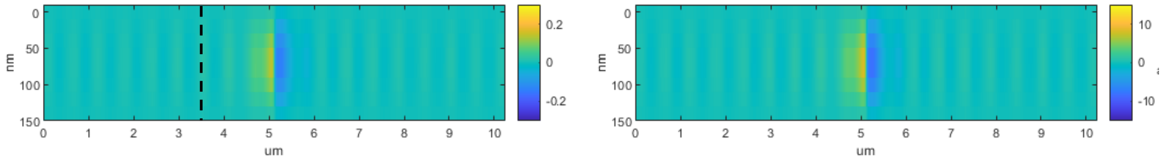

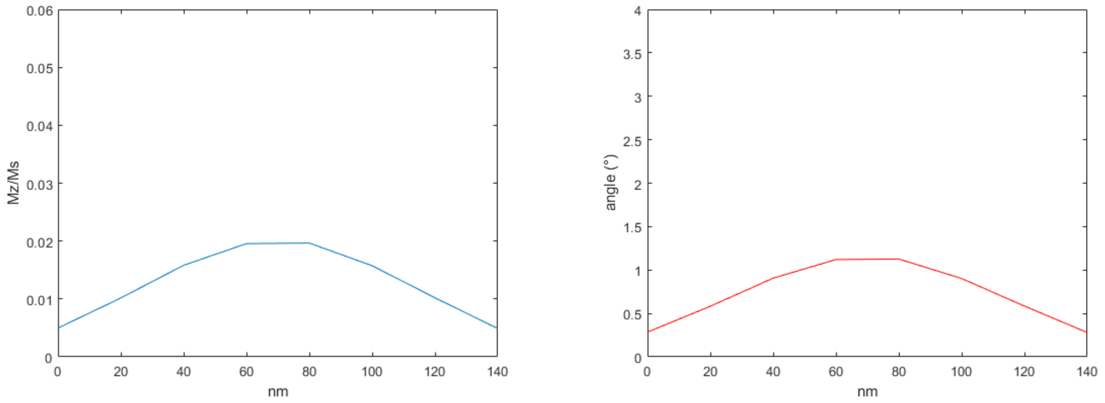

(b)

$t_{tot} = 200\ nm$

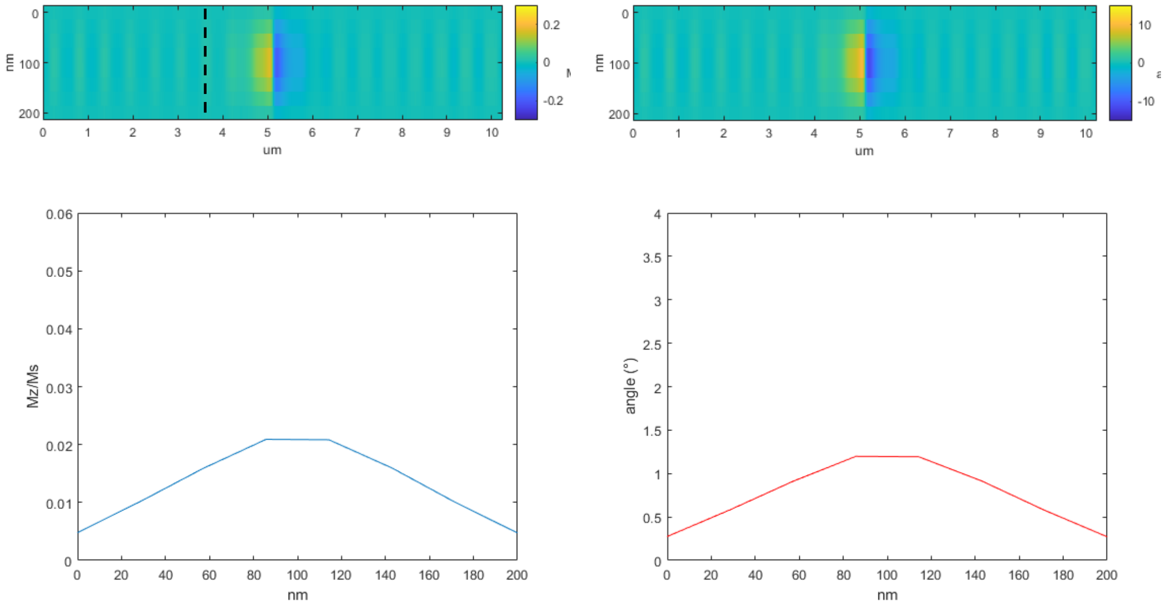

(c)

Figure 5.8: simulated profiles of the normalized out-of-plane component of the magnetization m_z and of the value of the angle α at $f = 1\ GHz$ for (a) $t_{tot} = 90\ nm$, (b) $t_{tot} = 140\ nm$ and (c) $t_{tot} = 200\ nm$. For each thickness on the top panel the (*y,z*)-profile of m_z and of its angle are presented, and the black-dashed line represents the slice for which the 1D profile shown on the bottom panel has been extracted.

The results are summarized in Table 5.3, were also the minimum values of m_z and α are shown. In addition to this, the $\alpha_{max}/\alpha_{min}$ ratio has been calculated since it is a particularly helpful parameter for determining the level of localization of the spin-wave modes along the thickness of the film. For the SAF with thickness of 200 nm, the $\alpha_{max}/\alpha_{min}$ ratio is equal to 4.3, while it is equal to 4 and 2.9 for the systems 140 nm and 90 nm thick, respectively.

Thickness	$\boldsymbol{m_{z,max}}$	$\boldsymbol{m_{z,min}}$	$\boldsymbol{\alpha_{max}}$	$\boldsymbol{\alpha_{min}}$	$\boldsymbol{\alpha_{max}/\alpha_{min}}$
90 nm	0.006	0.002	0.35°	0.12°	2.9
140 nm	0.019	0.005	1.12°	0.28°	4
200 nm	0.021	0.005	1.2°	0.28°	4.3

Table 5.3: maximum values for m_z and for its angle for each thickness at $f = 1\ GHz$. The calculated value of the $\alpha_{max}/\alpha_{min}$ ratio, used to estimate the level of localization of the spin-wave modes along the film thickness, is also reported.

Increasing the excitation frequency at $f = 1{,}5\ GHz$ the overall values of $\mathrm{m_z}$ and of the angle α increase for all thicknesses, and the results are reported in Figure 5.9. Also in this case, the maximum tilting of the magnetization in the z-direction is reached for the larger sample with total thickness of 200 nm, and the angle is equal to 2.67° corresponding to a value of the normalized out-of-plane magnetization of 0.047. In the case of the intermediate system, on the other hand, the maximum value of the angle describing the out-of-plane canting of the magnetization is slightly smaller and equal to 1.98°, which is related to a value of $\mathrm{m_z}$ of 0.034. Finally, for $t_{tot} = 90\ nm$ the value of m_z and of its angle are equal to 0.03 and 1.65°, respectively.

$$\boldsymbol{f = 1{,}5\ GHz}$$

$$t_{tot} = 90\ nm$$

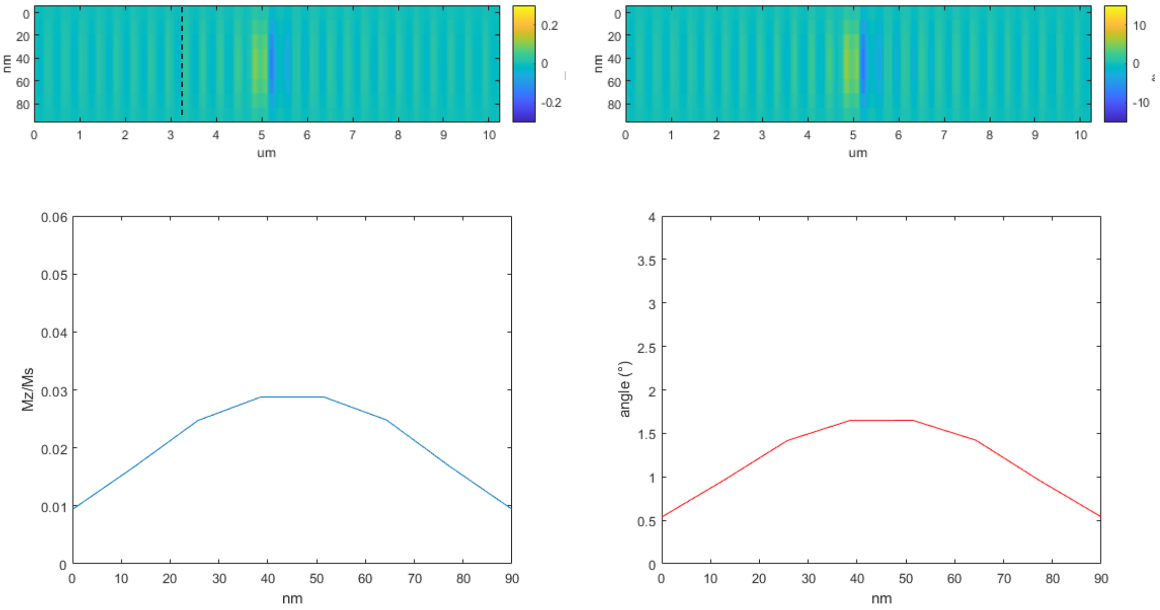

(a)

$t_{tot} = 140\ nm$

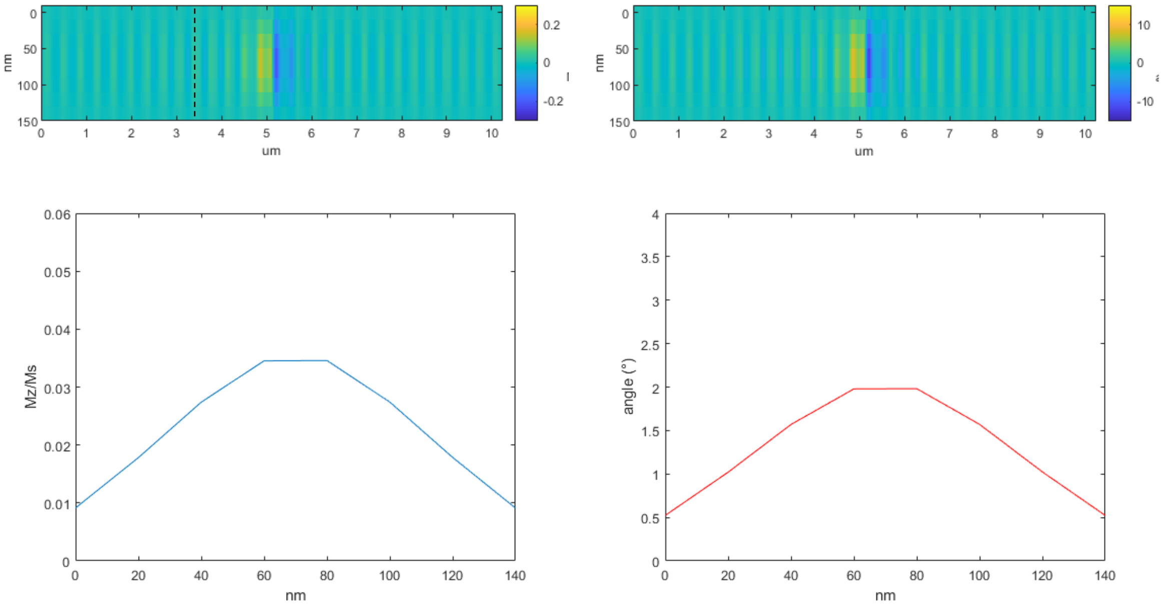

(b)

$t_{tot} = 200\ nm$

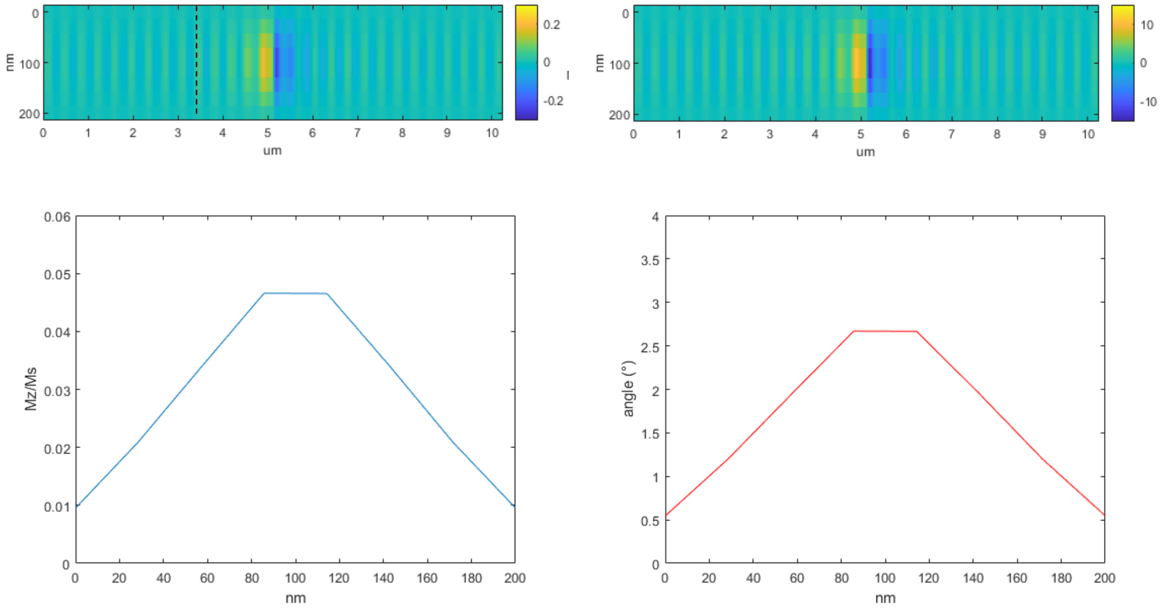

(c)

Figure 5.9: simulated profiles of the normalized out-of-plane component of the magnetization m_z and of the value of the angle α at $f = 1{,}5\ GHz$ for (a) $t_{tot} = 90\ nm$, (b) $t_{tot} = 140\ nm$ and (c) $t_{tot} = 200\ nm$. For each thickness on the top panel the (y,z)-profile of m_z and of its

angle are presented, and the black-dashed line represents the slice for which the 1D profile shown on the bottom panel has been extracted.

These measured values are recapped in Table 5.4, alongside with the minimum values for each thickness of both m_z and α, and the value of the $\alpha_{max}/\alpha_{min}$ ratio, the define the level of localization of each spin-wave mode. An overall increase of the ratio is observed respect to the previously analyzed frequency, and the highest value, equal to 5.04 is reached once again by the thicker simulated SAF.

Thickness	$\boldsymbol{m_{z,max}}$	$\boldsymbol{m_{z,min}}$	$\boldsymbol{\alpha_{max}}$	$\boldsymbol{\alpha_{min}}$	$\boldsymbol{\alpha_{max}/\alpha_{min}}$
90 nm	0.052	0.009	1.65°	0.54°	3.05
140 nm	0.078	0.009	1.98°	0.54°	3.67
200 nm	0.094	0.008	2.67°	0.53°	5.04

Table 5.4: maximum values for m_z and for its angle for each thickness at $f = 1{,}5\ GHz$. The calculated value of the $\alpha_{max}/\alpha_{min}$ ratio, used to estimate the level of localization of the spin-wave modes along the film thickness, is also reported.

Finally, for an excitation frequency of $f = 2{,}5\ GHz$ the results are reported in Figure 5.10. Consistently to the trend observed in the previous cases, the highest value of the normalized out-of-plane component of the magnetization is reached by the sample with total thickness equal to 200 nm, and is equal to 0.045, with an angle α of 2.56°. As before, decreasing the thickness leads to smaller values of m_z and of the angle α: for $t_{tot} = 140\ nm$ they are equal to 0.03 and 1.63°, while for $t_{tot} = 90\ nm$ they correspond to 0.01 and 0.62°, respectively.

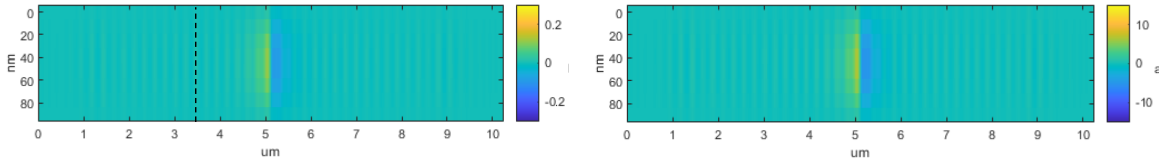

$$\boldsymbol{f = 2,5\ GHz}$$

$$t_{tot} = 90\ nm$$

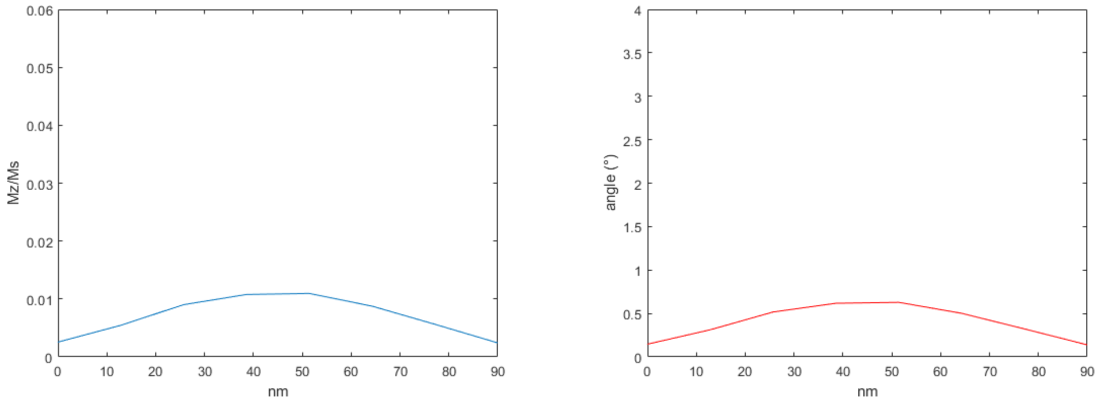

(a)

$t_{tot} = 140\ nm$

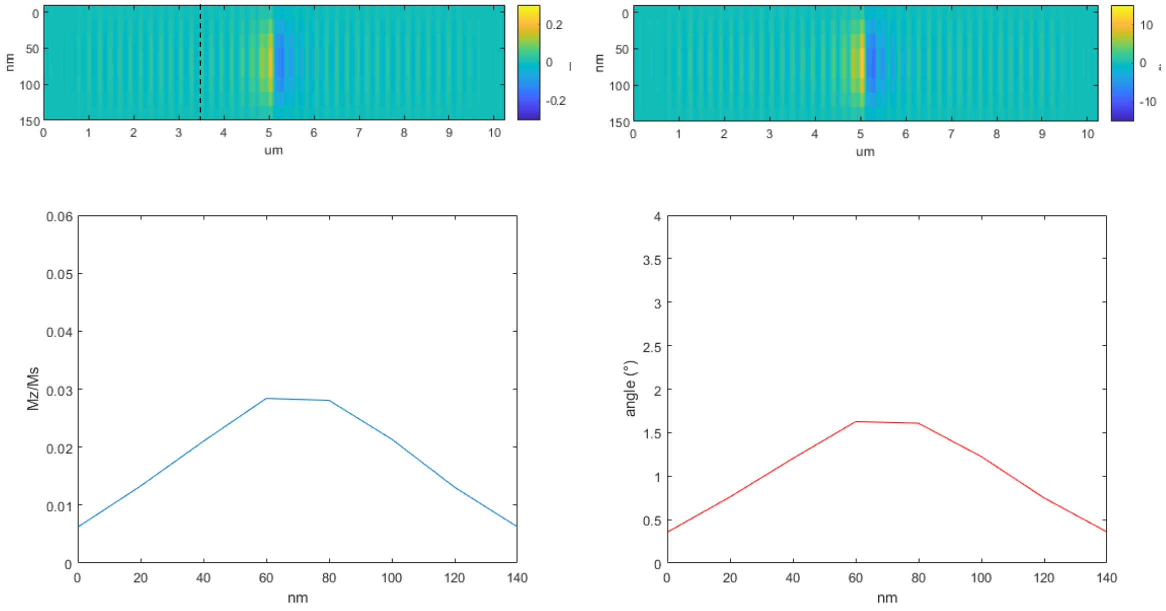

(b)

$t_{tot} = 200\ nm$

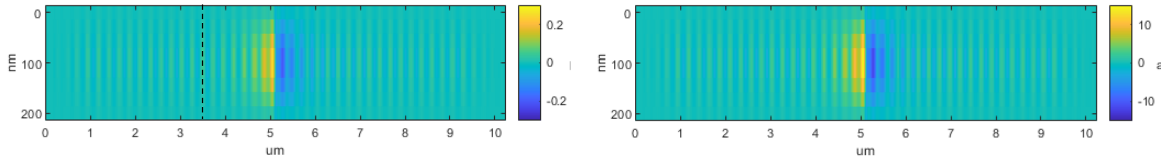

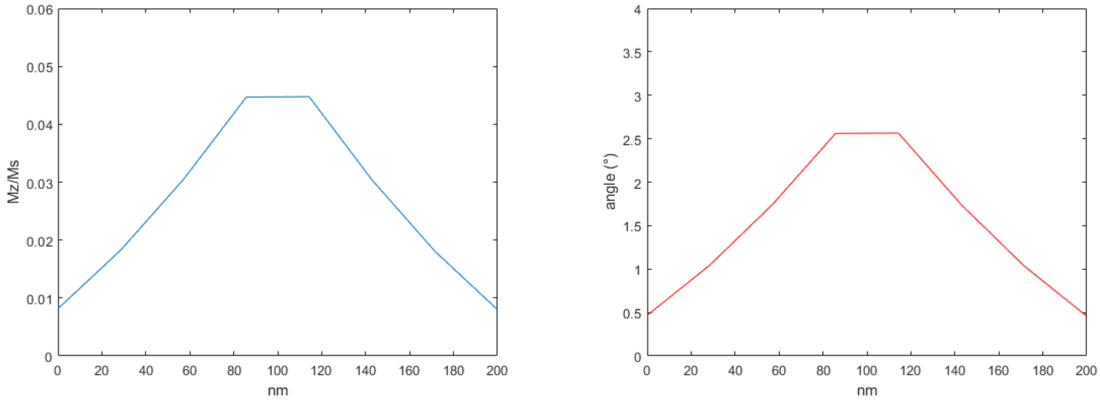

(c)

Figure 5.10: simulated profiles of the normalized out-of-plane component of the magnetization m_z and of the value of the angle α at $f = 2{,}5\ GHz$ for (a) $t_{tot} = 90\ nm$, (b) $t_{tot} = 140\ nm$ and (c) $t_{tot} = 200\ nm$. For each thickness on the top panel the (*y*,*z*)-profile of m_z and of its angle are presented, and the black-dashed line represents the slice for which the 1D profile shown on the bottom panel has been extracted.

Table 5.5 sums up the results of these simulations for f = 2,5 GHz, also adding the minimum values of m_z and α and the $\alpha_{max}/\alpha_{min}$ ratio, which has a value of 4.06, 4.53 and 5.45 for $t_{tot} = 90, 140, 200\ nm$, respectively.

Thickness	$m_{z,max}$	$m_{z,min}$	α_{max}	α_{min}	$\alpha_{max}/\alpha_{min}$
90 nm	0.01	0.003	0.61°	0.15°	4.06
140 nm	0.03	0.006	1.63°	0.36°	4.53
200 nm	0.045	0.008	2.56°	0.47°	5.45

Table 5.5: maximum values for m_z and for its angle for each thickness at $f = 2{,}5\ GHz$. The calculated value of the $\alpha_{max}/\alpha_{min}$ ratio, used to estimate the level of localization of the spin-wave modes along the film thickness, is also reported.

The results of the simulations performed show a clear trend for the amplitude of the out-of-plane component of the magnetization and for the angle α associated to the spin precession respect to the direction of the static magnetization: in all cases, the higher values are reached for the thicker sample with $t_{tot} = 200\ nm$, while the decrease of the thickness leads to a general decrease of the m_z and α. Moreover, the $\alpha_{max}/\alpha_{min}$ ratio, which describes the level of localization of the spin-wave modes along the thickness of the film, at all frequencies reaches its maximum for the thicker samples. For these reasons, the SAF with $t_{tot} = 200\ nm$ represents the optimal system for the three-dimensional investigation of the spin-wave modes localization with the Soft X-ray Laminography technique. Additionally, considering the three simulated thicknesses, the overall best response is reached for an excitation frequency of $f = 1{,}5\ GHz$, for which all the simulated synthetic antiferromagnetic structures ($t_{tot} = 90, 140, 200\ nm$) are characterized by a much higher value of m_z respect to the other frequencies. Note that for the simulated systems no strain contribution has been added. Moreover, during the STXM measurements (Chapter 4) the best conditions in terms of experimental constraints (i.e. stripline impedance) have been observed at low frequencies. For these reasons, the actual excitation frequencies expected to give the best results in terms of the amplitude of the out-of-plane component of the magnetization are shifted to lower values respect to the one investigated in the simulations.

5.3 Optimization of the Soft X-ray Laminography instrumentation at the PolLux beamline

After having identified the optimal conditions via simulations, we focused on the optimization of the newly developed S*oft X-ray Laminography* (SoXL) technique present at the PolLux beamline (X07DA) of the Swiss Synchrotron Light Source, Paul Scherrer Institut, Switzerland [15], and then on the static and time-resolved investigation of the magnetic configuration of the synthetic antiferromagnetic structures described in Chapter 4, as it will be presented in the next paragraph.

The PolLux beamline offers a synchrotron radiation in the soft x-ray range, with energy between 270 and 1600 eV and operates a Scanning Transmission X-ray Microscope (STXM). To install the new Laminography setup, the existing STXM setup has been modified adding a in vacuo rotation piezoelectric stage (SmarAct GmbH, SR-7021-S-HVK-TI) on top of the translational stage of the STXM. The schematic representation of the whole Laminography instrumentation is presented in Figure 5.11(a), while two insights on the Laminography rotational stage and on the sample positioning on the SoXL setup is shown in Figure 5.11(b) and Figure 5.11(c), respectively. The SoXL is characterized by a Fresnel Zone Plate (FZP) with a spot diameter of the order of tens of nanometers, towards which the x-ray beam is focused. Only the first diffraction order is selected by the Order Selecting Aperture (OSA), while the directly transmitted light (zero-order) and the higher diffraction orders are blocked. To study the sample, it is positioned in the focal point and raster-scanned by the incident beam, while the transmitted x-rays are analyzed by a point detector allowing spatial resolution usually of the order of 30-40 nm. Moreover, as it will be reported later, if the detector is properly chosen this setup also allows to perform time-resolved measurements. Several additional control systems have been added to the instrumentation, monitoring the stages movements during the image acquisition, and ensuring that the sample always remains in focus (for each movement along the *x'*-direction there is the corresponding movement on the *z'*-direction). Two configurations are possible for the angle θ_L between the rotation axis and the incident beam, that can be equal to either 45° or 60°; to obtain the images presented in this work, the configuration with $\theta_L = 45°$ has been chosen [15].

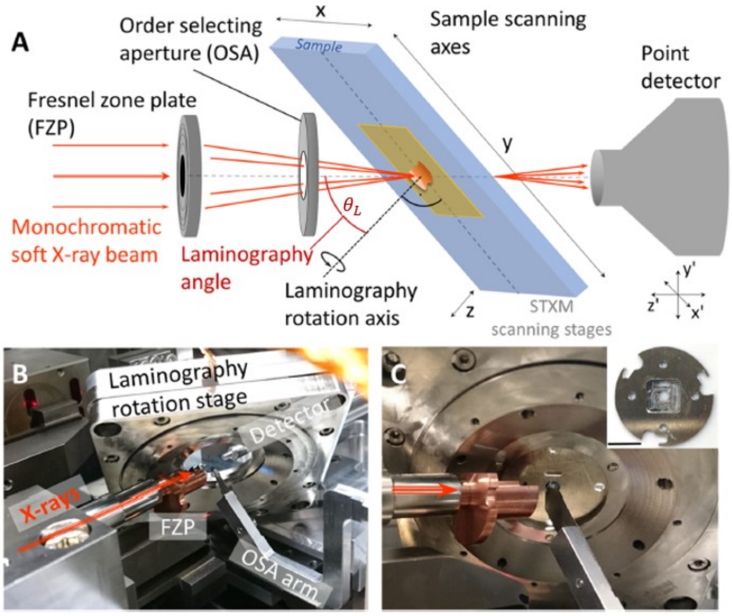

Figure 5.11: (a) schematic representation of the soft X-ray Laminography instrumentation, implemented on top of the already existing STXM setup. (xyz) denotes the sample coordinates while (xyz)' the STXM coordinates. (b) photography of the SoXL rotation stage without the sample; (c) zoomed photo of the sample plate (inset scale bar = 1 cm) [15].

Despite being more flexible than the tomography setup, it is still important to remember that the thickness of the sample is restricted by some critical factors when performing a SoXL experiment: dealing with soft X-rays limits the maximum amount of material that can be investigated, due to the maximum penetration depth of the incident beam (usually between hundreds of nm and tens of μm). Moreover, the depth of focus (DOF), which is a defined by the used FZP, imposes some limitations on the accessible information depth [15]. For this reason, the maximum sample thickness should *not* be larger than the DOF, which is of the order of few μm. Finally, since the Laminography setup works at a certain angle θ_L, the effective thickness of the sample d_{eff} is larger than its nominal thickness and defined by $d_{eff} = d/\cos(\theta_L)$, increasing its value by a factor of 1,4 or 2 for $\theta_L = 45°$ or $\theta_L = 60°$, respectively [15]. Another important consideration on the SoXL setup must be made regarding the achievable depth resolution along the z-direction: since the axis of rotation is tilted of an angle θ_L, the final resolution along the z-direction $\Delta z = \Delta x/\sin(\theta_L)$ will be always worse than the corresponding STXM in-plane resolution [15]. Moreover, to be able to reconstruct the topology of the sample and its magnetic configuration, the number of required projection *N* to take must be carefully assessed, since it represents a critical parameter and is strictly related to the desired in-plane resolution Δr. In general, it is possible to write:

$$N \geq \pi \frac{d}{\Delta r} \tan \theta_L \tag{5.1}$$

If the goal of the experiment is also to gain information about the magnetic configuration of the sample, for each projection three different measurements have to be taken, specifically with right-circularly polarized light (C_+), left-circularly polarized light (C_-) and linearly polarized light (L). The XMCD image can in principle be calculated as: $XMCD = -\ln(P_-) + \ln(P_+)$, where $P_{+/-}$ is the $C_{+/-}$ projection. In this case, however, due to some uncertainties on the intensity of the circularly polarized light, the obtained image is characterized by some offset. For this reason, a normalization process is generally employed using the linearly polarized light as a reference [15]. As previously described in Chapter 3, the magnetic contrast is proportional to the relative orientation of the magnetization with the direction of the x-ray beam, allowing to probe different components of the magnetization choosing the angle of incidence of the x-rays: if they are perpendicular to the surface, only the out-of-plane component of the magnetization is observed, while if they are tilted it is possible to gain information also on the in-plane components. The three-dimensional magnetic reconstruction strategy that takes the data given by the *N* projections and iteratively refines the non-accessible information due to the “missing-cone” described before has been presented in paragraph 3.2.5, while the results are shown in paragraph 5.6.

The first step of the series of experiments performed with the SoXL technique consisted in taking several static images at different angles respect to the laminography rotation axis. The goal of this measurement was to optimize the rotation stage of the Soft X-ray Laminography setup, with particular attention also on the focusing mechanism. Since the reconstruction algorithm needs a clearly distinguishable topographic feature to three-dimensionally reconstruct the object, the corner of the sample’s structure was selected and 46 XMCD images equally distributed over 360° were taken (for each projection, C_+, C_- and L measurements). In Figure 5.12 some of the resulting images are reported, and the rotation of the corner is easily recognizable. Note that as a consequence of the use laminography setup, whose rotation axis is inclined of 45° respect to the incoming x-ray beam, the images appear slightly distorted one respect to the other, while the small difference in contrast between the different projections may be caused by an imperfect overlap of the different frames.

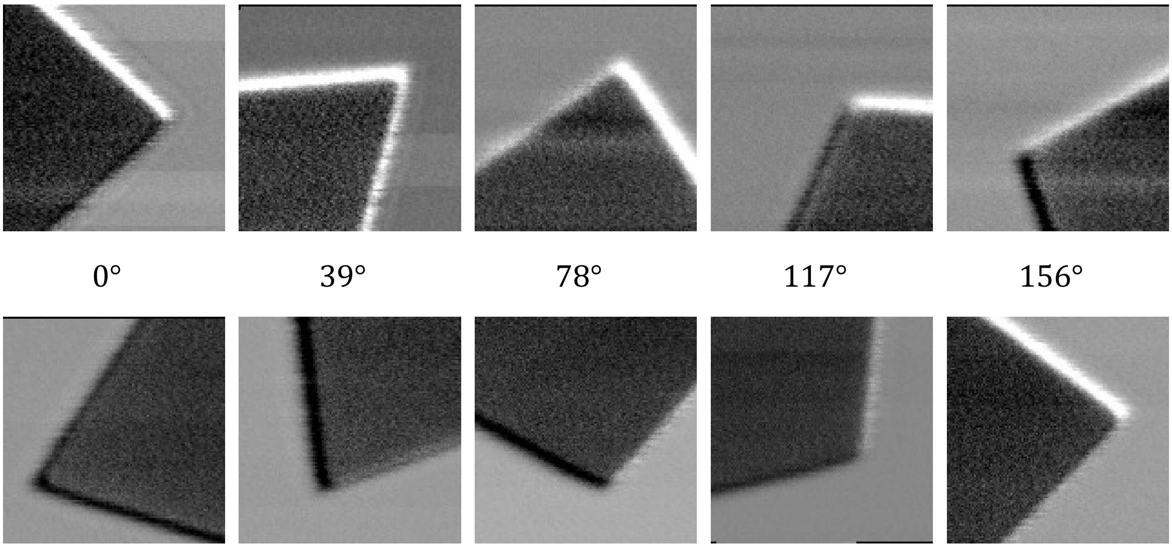

0° 39° 78° 117° 156°

195° 234° 273° 312° 351°

Figure 5.12: several static SoXL images taken at different angles at the corner of the structure.

These measurements allowed to confirm the correct functioning of the SoXL setup and to optimize the sample movements when changing the from one angle to the other. In particular, for each movement along the *x'*-direction, there must be a precise movement along the *z'*-direction, in order not to change the focus of the instrument.

5.4 Observation of static and magnetic topographic nanostructures in SAF

The magnetic configuration of the samples was studied with static SoXL after the optimization process, aiming at identifying the spin-wave emitters and domain walls recognized during the standard STXM experiments. In particular, SAF20b_6, SAF20b_7 and SAF21_5 have been selected as the optimal candidates among the developed samples for the three-dimensional investigation of their spin texture, given their larger thickness (more suitable for this kind of experiment aimed at resolving the magnetization in the z-direction) and their demonstrated excellent dynamic response (i.e. emission of spin waves at several frequencies) to the external excitation. Importantly, all the SoXL images presented in this chapter are rotated of 180° respect to the standard STXM setup.

The first sample investigated was the exchange-biased SAF20b_7: Figure 5.13(a) shows the optical microscopy image of the stripline above its membrane with the patterned squares and highlighted the orientation of the magnetization of the top-CoFeB layer and of the domain patterned via tam-SPL. In Figure 5.13(b) a μMOKE image of the central patterned square is reported before the striplines were fabricated, with the dotted white lines pointing towards the patterned domain walls. Similarly to the STXM experiments, the attention was focused on the bottom domain wall, which is the one that is expected to emit spin waves towards the center of the domain.

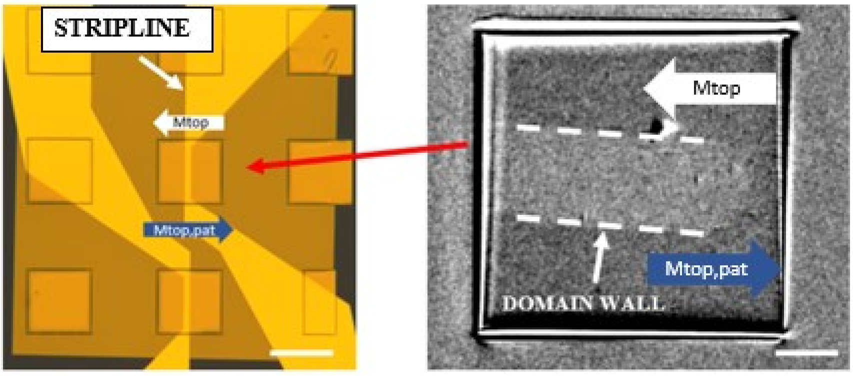

(a) (b)

Figure 5.13: (a) optical microscopy image of the SAF20b_7 membrane with the striplines for the excitation of the spin waves. With the white and blue arrows, the direction of the magnetization of the top CoFeB layer and of the patterned domain has been highlighted, respectively. Scale bar = 100 µm; (b) µMOKE image of the central patterned square of the membrane. The white dotted lines show the two patterned domain walls. Scale bar = 2 µm.

Several images sweeping the whole domain wall have been taken, and a few examples are presented below in Figure 5.14. Each static image was taken with size equal to 5 µm x 5 µm; on their right, a zoomed optical microscope image of the central patterned square is present (size 100 µm x 100 µm) and in blue it is shown the corresponding position of the SoXL image with respect to the stripline. On the SoXL images the blue dotted line is placed in correspondence to the border of the stripline, which is characterized by a higher level of noise, since the signal transmitted through that area is reduced by the presence of the stripline itself. Finally, as highlighted by the arrow in Figure 5.14(a) the domain wall is visible: the change of contrast on the two sides of the domain wall confirms the different orientation of the out-of-plane component of the magnetization. Noticeably, the domain walls are inclined of 45° degrees: this is a consequence of the laminography setup employed during these measurements, with $\theta_L = 45°$.

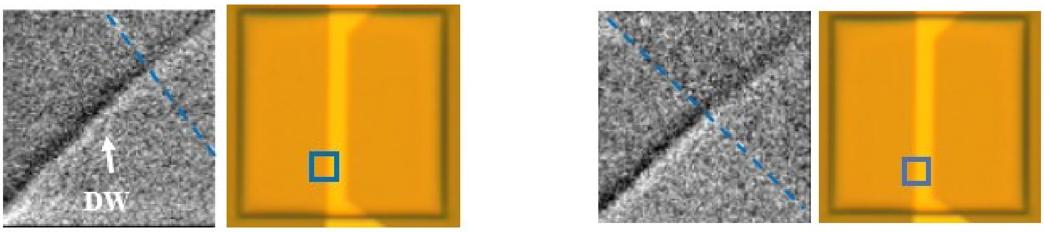

(a) (b)

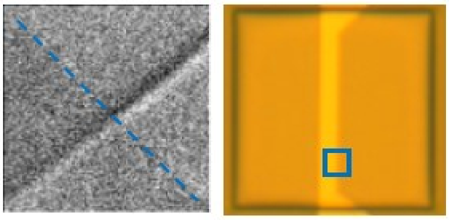

(c)

Figure 5.14: SoXL images (size 5 μm x 5 μm) of the domain wall in different positions with respect to the stripline, whose border is shown with the blue dotted line. The images on their right correspond to the patterned structure investigated (size 100 μm x 100 μm), and the blue square represents the corresponding analyzed region.

The second structure measured statically with the SoXL setup was the exchange-biased SAF20b_6, for which in Figure 5.15(a) the optical microscope image of its membrane with both the nanostructures and the striplines is reported. Specifically, as shown in Figure 5.15(b), the investigated patterned square was the central one, for which in the μMOKE the two domain walls have been highlighted by the white dotted lines. In this case, two striplines are present, allowing to excite a larger portion of the domain wall.

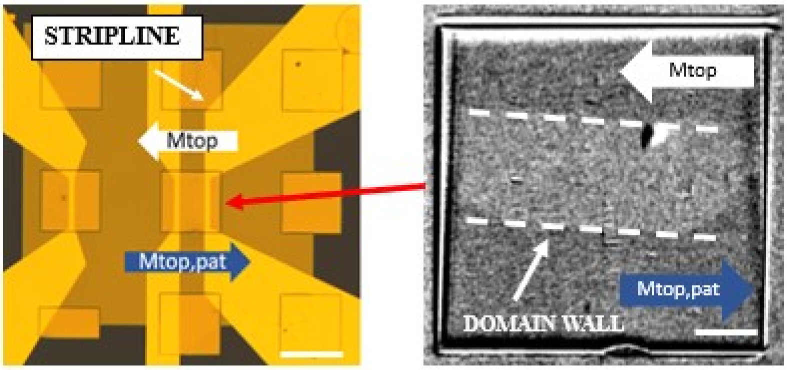

(a) (b)

Figure 5.15: (a) optical microscope image of the SAF20b_6 membrane with the striplines for the excitation of the spin waves. In this case, two striplines cross the central patterned square, allowing to excite a larger portion of the domain wall. With the white and blue arrows, the direction of the magnetization of the top CoFeB layer and of the patterned domain has been highlighted, respectively. Scale bar = 100 μm; (b) μMOKE image of the central patterned square of the membrane. The white dotted lines show the two patterned domain walls. Scale bar = 2 μm.

For this sample, multiple images were taken in different positions and at different angles, starting from the static image reported in Figure 5.16, where a large area across the whole left stripline (visible from the increased contrast pointed out by the white arrow) was scanned.

As in the previous case, the bottom domain wall is visible as a consequence of the change of contrast on the two sides, given by the opposite orientation of the out-of-plane component of the magnetization. Finally, the presence of a large topographic defect has been shown with the red circle.

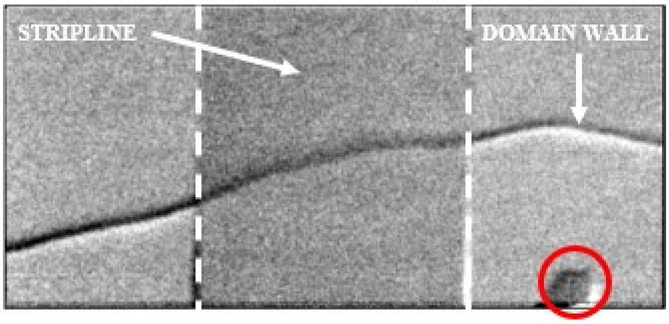

Figure 5.16: SoXL image (size 20 μm x 10 μm) of the domain wall across the whole stripline. The borders delimiting the stripline has been shown with the white dotted lines. The domain wall is recognizable thanks to the change of contrast across the DW, indicating the different orientation of the out-of-plane component of the magnetization. In the red circle a topographic defect is present.

For the same sample, the domain wall in proximity of the right stripline has also been investigated. In this case four static images at 0°, 60°, 120° and 180° with respect to the laminography rotation axis have been taken and are reported in Figure 5.17. For each image, the blue dotted line marks the border of the stripline, which is represented by the darker area, while for all angles the domain wall is visible given the contrast for the different orientation of the out-of-plane component of the magnetization. Noticeably, the domain wall shows good contrast at all angles, confirming the correct functioning of the SoXL setup. As a matter of fact, although the SoXL setup is tilted respect to the incident beam and should probe all the components of the magnetization, only the out-of-plane component of the sample is actually investigated, because the SAF is perfectly compensated in-plane. The magnetic contrast visible from the images is then defined only by M_z, which does not change when changing the angles around the Laminography rotation axis.

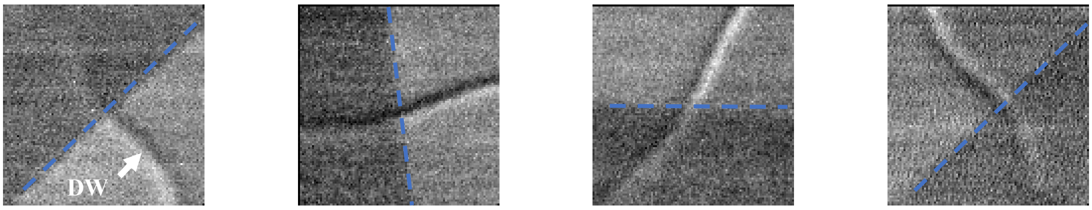

$\theta = 0°$ $\theta = 60°$ $\theta = 120°$ $\theta = 180°$

Figure 5.17: four SoXL static images (size 5 µm x 5 µm) taken at different angles respect to the laminography rotation axis. The blue dotted lines show the borders of the stripline, while the domain wall has been highlighted in the first image by the white arrow.

Finally, the last investigated sample was SAF21_5, characterized by the absence of the antiferromagnetic layer exchange coupled with the CoFeB film and whose patterned nanostructures have been stabilized by shape anisotropy. The resulting image for the larger patterned circle (diameter 3,5 µm) is shown in Figure 5.18: as a consequence of the laminography setup, characterized by a 45° angle between the normal to the surface of the sample (i.e. laminography rotation axis) and the incident x-ray beam, the circle appears deformed with an elliptical shape. Similarly to what has been observed with the conventional STXM technique no Landau domains are visible during the measurement, and it is possible to recognize the "swollen" structure described in paragraph 4.6, with variable thickness between the center and borders of the structure. As a consequence of this, the interlayer exchange coupling between the two ferromagnetic layers is modified, and the effect is visible from the change in the contrast highlighted by the red arrows.

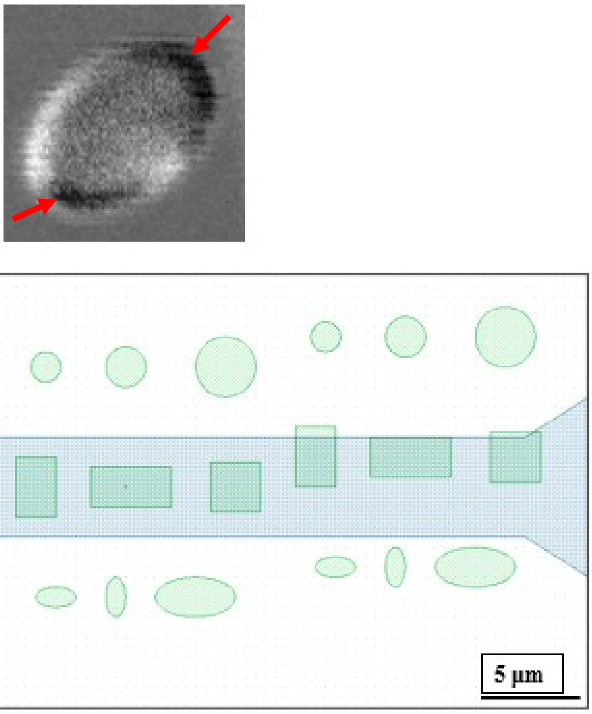

Figure 5.18: SoXL image (size 5 µm x 5 µm) of the nanopatterned circle on the membrane (top) and schematic representation of the whole patterned area on the membrane (bottom), with highlighted in red the measured circle.

5.5 Observation of spin waves using the time-resolved Soft X-ray Laminography setup

After having successfully visualized with the static SoXL setup the domain walls of the exchange-biased SAF samples, the detector was changed and substituted with a silicon avalanche photodiode (APD) detector which enables to perform time-resolved measurements (trading some efficiency for operations in the energy range between 270 and 500 eV) [6], [15]. Due to the fact that the time-resolved SoXL is a time-consuming technique (for each angle C_+, C_- and L measurements are taken) only a single sample was studied, and SAF20b_6 was chosen since it has two striplines crossing the central patterned membranes, allowing to search for spin-waves emission on a larger area. At first, a large time-resolved overview image was taken, to localize the spin-wave emitters. The result of the measurement is shown in Figure 5.19: on the left, a frame of video obtained with the laminography setup, while on the right a zoomed optical microscope image of the patterned square on the center of the membrane, with highlighted the area over which the image was taken. In Figure 5.19(a) the stripline is visible, while on the bottom left it is possible to recognize the magnetization dynamics, where the spin waves are emitted in a region close to the border of the stripline. The system was excited with a frequency of 0,64 GHz, while a voltage of 1,8 V peak-to-peak was applied to inject the current on the stripline.

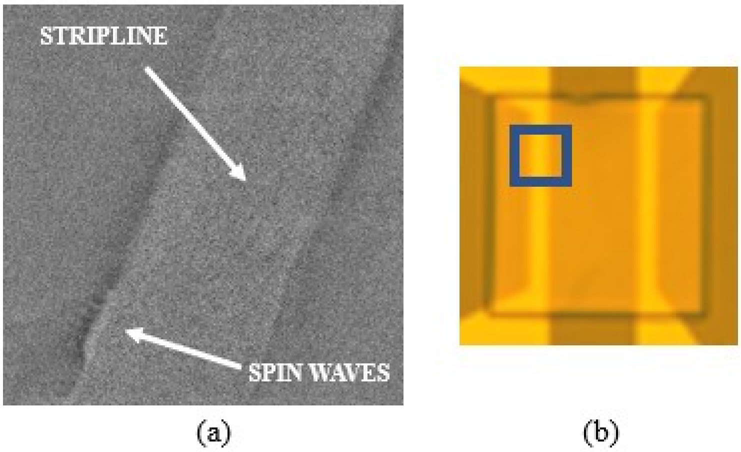

Figure 5.19: (a) frame of a time-resolved measurement over a larger area (size 20 µm x 20 µm) across the stripline. Two white arrows indicate the stripline and the emitted spin waves close to its borders, respectively. (b) zoomed optical microscope image of the central patterned square (size 100 µm x 100 µm) of the membrane of SAF20b_6. The two striplines are visible in yellow, while with the blue square the scanned area is shown.

After having identified the promising source for the spin-waves emission, time-resolved SoXL measurements at 0°, 60° and 120° have been performed, and the results are reported below in Figure 5.20(a), (b) and (c), respectively. The size of the investigated region is 5 µm x 5 µm, while the excitation frequency is $f = 0,64\, GHz$. For each frame, the spin-wave textures are shown with the red line, while the emitted spin waves have been highlighted with the orange one. The corresponding position at which these images have been taken is reported in Figure 5.20(d) with the blue square on the optical microscope image.

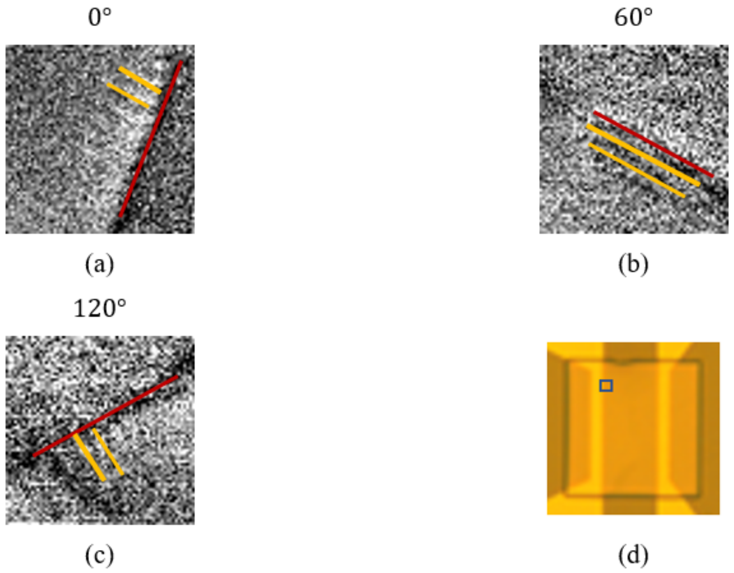

(a) (b)

(c) (d)

Figure 5.20: frames of time-resolved SoXL measurements with excitation frequency $f = 0,64\, GHz$ of a region with size 5 µm x 5 µm at an angle equal to (a) 0°, (b) 60° and (c) 120°. In (d) the corresponding position (blue square) is indicated on the optical microscope image of the patterned structure on the membrane (size 100 µm x 100 µm).

Two criticalities have been encountered during these first measurements: first, the position of spin-wave emitters appears to slightly change during long measurements. Second, the reconstruction algorithm (described in detail in paragraph 5.6) needs a clear topographic feature to track the rotation of the sample during the measurements (i.e. autocorrelation), and no recognizable defect was present in this case on the analyzed area. To solve the first problem, the sample was magnetized with an external in-plane field of 4000 Oe in the direction of the stripline, while heating the sample at 240°C, aiming at stabilizing the emission of the spin waves from the borders of the stripline itself. Figure 5.21 shows the orientation of the external applied field respect to the stripline.

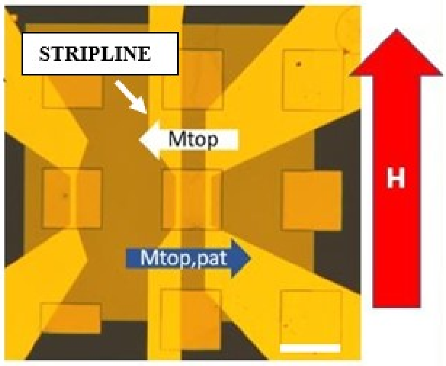

Figure 5.21: optical microscope image of the membrane of SAF20b_6 with the patterned structures. The external in-plane field (red arrow) is parallel to the stripline crossing the central square. Scale bar=100 µm.

After the sample magnetization, the same procedure applied before was followed: first, the whole region was scanned for the identification of a promising magnetic feature for the emission of spin waves. In addition to this, the attention was also focused on finding a clearly visible topographic defect to track during the sample rotation and allowing to reconstruct the three-dimensional image. Figure 5.22(a) shows the overview static image (size 25 µm x 25 µm) of the investigated area, with highlighted with the blue square the identified optimal region for performing the time-resolved SoXL measurement. The red arrows point to the defect that was used for tracking the rotation of the sample. Figure 5.22(b) reports the correspondent position of the scanned area on an optical microscope image of the whole membrane with the patterned structures.

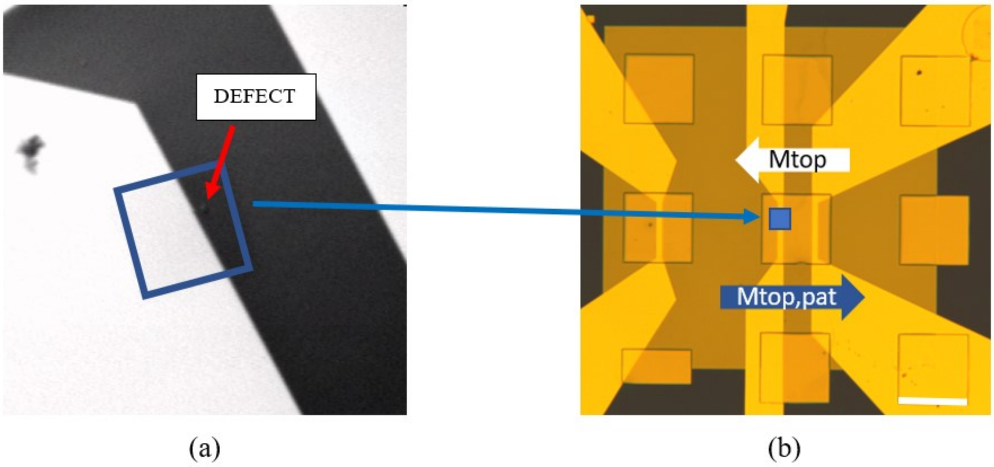

Figure 5.22: (a) static overview image (size 25 µm x 25 µm) of the scanned area across the stripline (darker zone) for the identification of the optimal region to perform the time-resolved SoXL measurement (blue square). A defect is also reported with the red arrow, needed for tracking the rotation of the sample during the experiment. (b) optical microscope

image of the membrane with the patterned squares. In blue, the correspondent investigated region. Scale bar = 100 µm.

The three-dimensional time-resolved SoXL measurement was performed taking 14 equally spaced projections over 360°, with the size of the scanned area equal to 7,5 µm x 7,5 µm. In Figure 5.23 the complete set of static images highlighting the rotation of the sample is reported. In each image, the darker region represents the stripline, while near its border the defect used for tracking the rotation is visible (and pointed out in the first image with the red arrow). To obtain the time-resolved images, the measurement was repeated three times, using right-circularly polarized soft x-rays (C_+), left-circularly polarized soft x-rays(C_-), and linearly circularly polarized soft x-rays (L), with energy tuned at the Co L_2 absorption edge (796 eV).

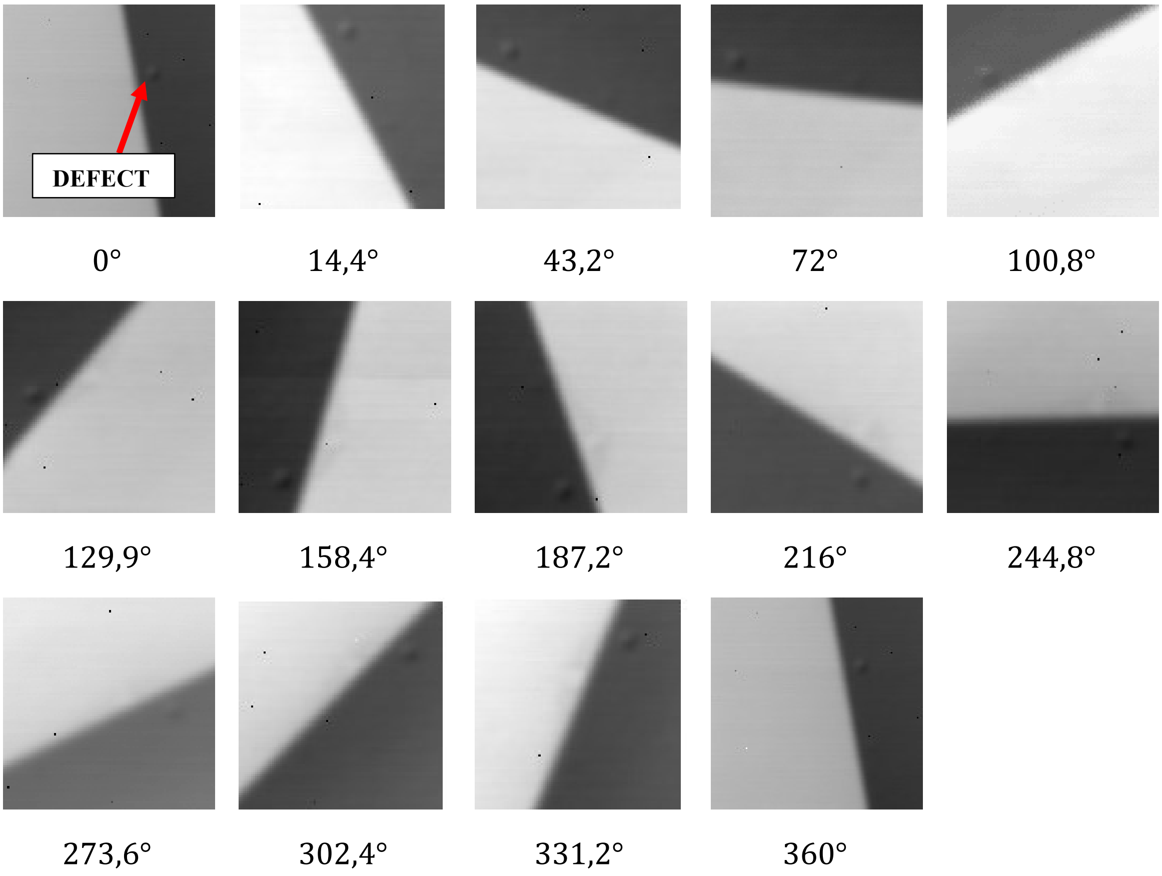

0° 14,4° 43,2° 72° 100,8°

129,9° 158,4° 187,2° 216° 244,8°

273,6° 302,4° 331,2° 360°

Figure 5.23: static images of the scanned area for each projection (size 7,5 µm x 7,5 µm). The darker region represents the stripline. In the first image, the defect used for tracking the rotation of the sample during the measurements is highlighted with a red arrow and can be recognized as it changes position in all the other images.

As an example, in Figure 5.24 two examples of the resulting time-resolved SoXL measurements are shown. In the first image on the left, taken at 0°, the border of the stripline is visible and it is shown with the red line. The image on the right, on the other hand, has been taken at 129,9° and in addition to the already mentioned visible border of the stripline, spin waves emitted from it are present on the bottom left of the image (orange lines). However, despite having magnetized the sample parallelly to the stripline to stabilize the magnetization dynamics, the emitted spin waves were recognizable intermittently in the different projections, due to the change in position of the emitters during the long measurements.


0°
129,9°

(a) (b)

Figure 5.24: example of two frames of time-resolved SoXL measurements at (a) 0° and (b) 129,9° with size 7,5 µm x 7,5 µm. The border of the stripline is shown with the red line, while the emitted spin waves on the bottom left with the orange lines.

5.6 Three-dimensional image reconstruction

The data obtained from the three-dimensional SoXL measurements were analyzed with the reconstruction algorithm described in detail in paragraph 3.2.5. At first, an estimate of the structure of the specimen must be made, and then iteratively with a gradient-based approach, using all the combined information contained in the projections, the error is reduced until convergence is reached. In order to correctly perform the magnetic reconstruction, the topographic reconstruction of the specimen is also needed in advance, and it is possible to derive it from the same set of data obtained during the time-resolved SoXL experiments. Importantly, to be able to reconstruct three-dimensionally the spin-waves localization, the spin-wave emitters must be stable in time during the different measurements. As already mentioned, since during the experiments performed the spin texture changed its structure, and because of the fact that the number of projections taken was not enough to have a complete set of data on the magnetic structure of the sample, it was not possible to obtain a good three-dimensional reconstruction of its magnetic configuration. For this reason, in the following only the results of the topographic reconstruction process of the samples investigated in this work is reported. A critical issue during the measurements is related to the identification of a topographic feature (for example, a defect on the surface of the sample, or a previously placed marker) that allows the algorithm to automatically track the rotation of the specimen: Figure 5.23 shows the position of the defect used during the SoXL experiments performed. Despite the low number of projections taken at the different angles, it was still possible to partially reconstruct topographically the structure, and the results are presented in Figure 5.25, where the three-dimensional reconstructed volume is shown at different angles. The red dashed line represents the border of the structure and delimits the region of the solid with higher contrast, corresponding to the stripline. Noticeably, since the film underneath the stripline is continuous, no contrast arises from it. In addition to this, in Figure 5.25(a), (b) and (e) the white circles show the position of the defect used for tracking the sample during its rotation. Finally, the consequence of the low number of projections taken during the measurements is shown by the black lines in Figure 5.25(a),(c),(d) and is recognizable in every image: since some angles are missing from the reconstructions, it was not possible to reconstruct entirely the volume of the sample. Particularly interesting are the lines highlighted in Figure 5.25(c) and (d), since they have the typical shape of the "missing-cone" described before in Figure 3.15.

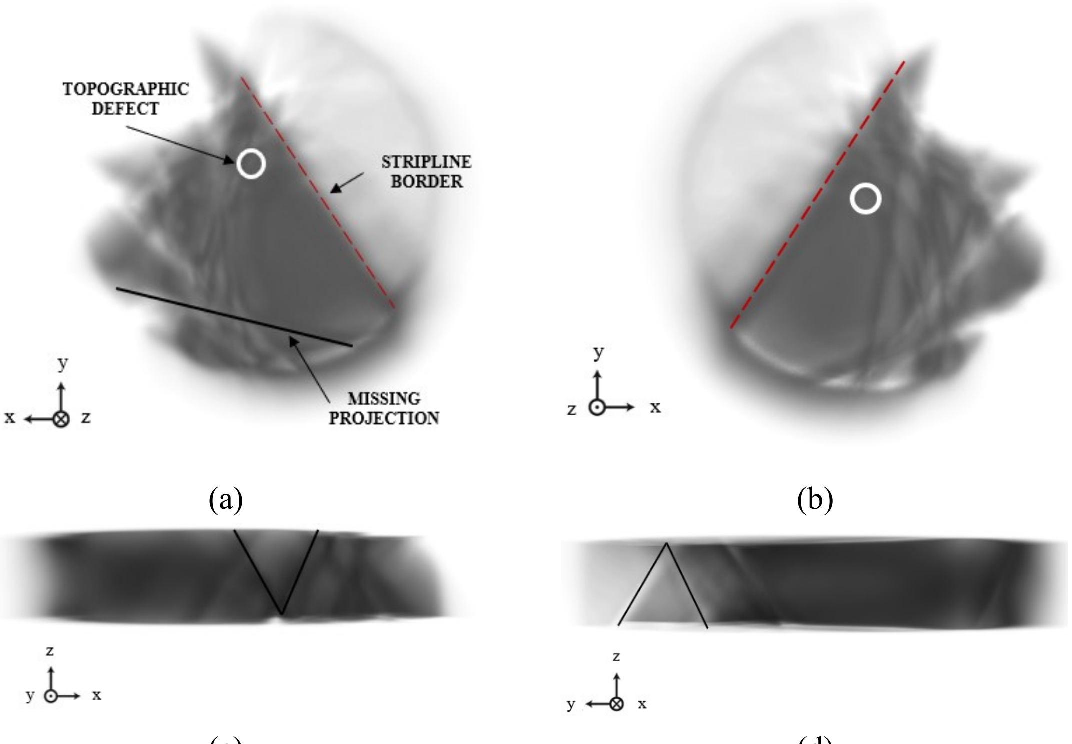

(a) (b)

(c) (d)

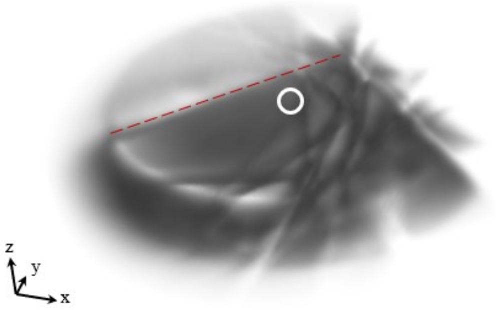

(e)

Figure 5.25: different views of the topographic partial reconstruction of the three-dimensional volume of the investigate sample (size 7,5 µm x 7,5 µm). (a)-(b) x,y-projections. The red dashed lines show the border of the stripline, which is represented by the region with the higher contrast. The white circle points to the defect used for tracking the rotation of the sample during the measurement, while the black lines show the missing information needed for the reconstruction of the whole volume, caused by the low number of projections taken; (c) x,z-projection with the black lines highlighting the missing cone artefact, similarly to (d) which shows the x,y-projection. (e) three-dimensional topographic reconstruction of the investigated volume, also showing the position of the tracked defect (white circle) and the border of the stripline (red dashed line).

To summarize, several static and time-resolved three-dimensional Soft X-ray Laminography measurements have been performed. The goal of the first part of these measurements was to optimize the laminography setup, focusing in particular on the newly installed piezoelectric rotation stage. For this reason, 46 static images equally distributed over 360° of the corner of the structure were taken. Later, the magnetic configuration of SAF20b_6 was investigated, aiming at finding the optimal position measuring the emission of spin waves, and the domain walls present on the structure were measured statically and at different angles. Finally, two separate set of time-resolved measurement with the laminography setup were performed. In the first one, the emission and propagation of spin waves from the domain wall has been demonstrated and observed at three different angles (0°, 60°, 120°). However, during the long measurements (more than 2 hours for each projection) the spin-wave emitters appeared to change their position. Moreover, the absence of a clear topographic feature on the surface of the analyzed area did not allow to reconstruct three-dimensionally the image. To solve these two problems, the measurements were repeated a second time. In this case, the sample was magnetized uniformly in-plane in the direction parallel to the stripline, aiming at stabilizing the emission of spin waves from its borders. After finding a topographic defect close to the border of the stripline, 14 time-resolved projection at different angles were taken. Despite the previously induced magnetization to stabilize the spin-wave emitters, they still appeared to be unstable, and spin waves have been observed intermittently, complicating the magnetization dynamics reconstruction procedure. A partial topological reconstruction of the three-dimensional volume of the sample was possible, despite the number of projections taken during the measurements was not enough to allow a full 3D reconstruction.

This first set of measurements represented a huge step towards the three-dimensional imaging of spin-wave modes in synthetic antiferromagnetic structures via the newly developed Soft X-ray Laminography technique at the PolLux beamline endstation of the Swiss Light Source. Spin waves have been extensively studied at different frequencies, and it was possible to observe their propagation at different angles with the time-resolved laminography setup. Due to the fact that SoXL is a time-consuming measurement and several optimization were needed to be made before starting the experiments, it was not possible to obtain enough projections for a full three-dimensional magnetic reconstruction, but this experience allowed to understand the optimal conditions for the spin-waves propagation and three-dimensional visualization, both in terms of the development of the samples and of the SoXL setup, that will be used in the next phases of the project to finally visualize three-dimensionally the spin-wave dynamics inside a synthetic antiferromagnet.

Chapter 6

Conclusions and perspectives

The present research thesis work aimed at obtaining for the first time a three-dimensional reconstruction with nanoscale resolution of spin-waves emission and propagation inside Synthetic Antiferromagnets (SAFs) via the newly developed Soft X-ray Laminography technique. These magnetic heterostructures have already been proven to be very efficient for the implementation of optically inspired nanomagnonic devices for the generation, control, and manipulation of spin waves inside their spin texture, with a high degree of tunability. This is a consequence of the peculiar properties of synthetic antiferromagnets: in particular, the nonreciprocal behavior of spin waves in SAFs arising from the dipolar coupling between the two ferromagnetic layers leads to a resilience from back-scattering at defects, allowing to maintain a high-quality spin-wave wavefronts. Spin waves in SAF are also characterized by sub-μm wavelengths at relatively low frequencies, which has two benefits: first, it holds the promise of developing highly efficient miniaturized devices. Second, it allows the investigation of the magnetization dynamics via time-resolved Scanning Transmission X-ray Microscopy (STXM) technique at the beamline PolLux-SLS, whose operational frequency is limited below 5 GHz. Finally, the propagating Demon-Eschbach spin-wave modes in SAF are extremely localized along the z-direction, which makes them the perfect candidates to demonstrate the feasibility of Soft X-ray Laminography for the three-dimensional visualization of the spin waves propagation. In this context, harnessing the third dimension not only would be a huge step forward for the understanding of the underlying physical principles governing the magnetization dynamics, but it would also represent a technological breakthrough for the development of innovative nanomagnonic devices.

In this thesis work two different types of heterostructures have been developed: an exchange-biased SAF based on CoFeB/Ru/CoFeB/IrMn/Ru and a SAF without the exchange bias, consisting of CoFeB/Ru/CoFeB/Ru. Multiple samples with different CoFeB thicknesses have been grown, with the goal of studying the spin-wave dispersion relation as a function of the thickness of the ferromagnetic layers. Regarding the stabilization of domain walls, which are used as spin-wave emitters, two different strategies have been employed. In the exchange-biased SAF, a magnetic patterning via the versatile thermally assisted magnetic –

Scanning Probe Lithography technique was performed, and magnetic domains were directly written on the structures. In the other samples, the stabilization of Landau domains through shape anisotropy in previously nanopatterned geometric features have been exploited. After the nanofabrication, through the use of MOKE microscopy, it has been possible to verify the correct presence of the patterned domains and the stabilization of the Landau domains in the exchange biased SAF and in the structures without exchange bias, respectively. Finally, the spin waves emission and propagation inside all the developed samples have been observed at multiple frequencies (ranging from 0.43 to 1.42 GHz) with the STXM method, allowing to calculate their dispersion relation as a function of the film thickness. Noticeably, a shift towards lower frequencies when increasing the thickness of the layer have been observed, as a consequence of the strengthening of strain effects on the systems.

After having confirmed the correct functioning of the developed samples as efficient platforms for the emission and propagation of spin waves, we focused on the optimization of the Soft X-ray Laminography (SoXL) instrumentation and on the consequent measurements both statically and dynamically of the proposed structures. The SoXL setup consists in a generalized geometry with respect to the conventional X-ray Tomography, with the Laminography rotational axis inclined (and not perpendicular anymore) to the incident x-rays beam, in such a way that it is possible to probe all the components of the magnetization, allowing also to strongly reduce the artefacts present during the reconstruction process of thin films. In the first set of measurements, whose goal was to optimize the SoXL rotational stage, 46 equally distributed over 360° XMCD projections of the corner of the structure of a selected sample were taken. Each projection consists in probing the sample with right circularly polarized light, left circularly polarized light and linearly polarized light. The static magnetic configuration of the sample was later investigated for the identification of the domain walls and spin-wave emitters, which were observed at multiple angles. This was possible thanks to the peculiar property of the developed synthetic antiferromagnetic structures, which present an in-plane perfect compensation given by the antiferromagnetic coupling between the two CoFeB layers, allowing to visualize with good magnetic contrast the out-of-plane component of the magnetization, with no notable changes for the different angles. Finally, the time-resolved SoXL measurements were performed exciting the system at 0.64 GHz. At first, three videos at 0°, 60° and 120° have been acquired and the emission of spin waves from the spin texture have been observed. However, during these measurements two criticalities have been recognized: first, the position of spin-wave emitters appears to slightly change during the long measurements. Second, the reconstruction algorithm requires the presence of a recognizable topographic feature to track during the sample rotation, and in this case no defect was visible in the analyzed area. To solve the first problem, the sample was uniformly magnetized in-plane parallelly to the direction of the striplines used to excite the magnetization dynamics, aiming at obtaining more stable spin waves emitted from the striplines borders. After the identification of a topographic defected close to the border of the stripline, time-resolved SoXL measurements were repeated a second time and 14 projections equally distributed over 360° have been taken. Also in this case the spin-wave emitters appeared to be unstable, and it was possible to observe spin waves only intermittently, hindering the correct three-dimensional reconstruction of the magnetization. A partial 3D topographic reconstruction has been obtained, despite the limited number of projections acquired, due to the long measurement time and the several optimization procedures performed before starting the experiments.

Nevertheless, our work represented an important step towards obtaining for the first time the nanoscale three-dimensional imaging of spin-wave modes, since it allowed us to understand the optimal conditions for visualizing the magnetization dynamics, both in terms of the development of the samples and of the SoXL setup. This innovative instrument offers significant advantages over the conventional X-ray Tomography approach for 3D imaging. Thanks to its inclined rotation axis with respect to the incident x-rays beam, it allows to directly probe all the components of the magnetization, reducing at the same time the artefacts present during the reconstruction procedure of thin films. Moreover, being installed on a STXM setup it allows to perform time-resolved measurements, visualizing with good magnetic contrast the propagating spin waves at all angles. The next steps of the project will focus on the stabilization of robust spin-wave emitters, and on the further optimization of the sample geometry specifically for solving the criticalities inherent to the SoXL measurements. Once obtained a sufficient degree of control and stability, it will be possible to obtain a full three-dimensional visualization with nanoscale resolution of spin-wave modes in synthetic antiferromagnetic structures. In the long term, this will allow to finally manipulate the spin-waves dynamics in three-dimensions for the development of the next generation computing architectures.

Bibliography

[1] E. Albisetti *et al.*, "Synthetic Antiferromagnets: Optically Inspired Nanomagnonics with Nonreciprocal Spin Waves in Synthetic Antiferromagnets, *Advanced Materials.* vol. 32, 2020.

[2] S. Wintz *et al.*, "Magnetic vortex cores as tunable spin-wave emitters," *Nature Nanotechnology*, vol. 11, 2016.

[3] V. Sluka *et al.*, "Emission and propagation of 1D and 2D spin waves with nanoscale wavelengths in anisotropic spin textures," *Nature Nanotechnology*, vol. 14, 2019.

[4] R. Nakane, G. Tanaka, and A. Hirose, "Reservoir Computing with Spin Waves Excited in a Garnet Film," *IEEE Access*, vol. 6, 2018.

[5] Á. Papp, W. Porod, and G. Csaba, "Nanoscale neural network using non-linear spin-wave interference," *arXivLabs,* 2020.

[6] C. Donnelly *et al.*, "Time-resolved imaging of three-dimensional nanoscale magnetization dynamics," *Nature Nanotechnology*, vol. 15, 2020.

[7] H. Yu *et al.*, "Omnidirectional spin-wave nanograting coupler," *Nature Communications*, vol. 4, 2013.

[8] P. A. Popov *et al.*, "Spin wave propagation in three-dimensional magnonic crystals and coupled structures," *Journal of Magnetism and Magnetic Materials*, vol. 476, pp. 423–427, Apr. 2019.

[9] N. Kardjilov *et al.*, "Three-dimensional imaging of magnetic fields with polarized neutrons," *Nature Physics*, vol. 4, no. 5, 2008.

[10] I. Manke *et al.*, "Three-dimensional imaging of magnetic domains," *Nature Communications*, vol. 1, no. 8, 2010.

[11] A. Hilger, I. Manke, N. Kardjilov, M. Osenberg, H. Markötter, and J. Banhart, "Tensorial neutron tomography of three-dimensional magnetic vector fields in bulk materials," *Nature Communications*, vol. 9, no. 1, 2018.

[12] T. Tanigaki *et al.*, "Three-dimensional observation of magnetic vortex cores in stacked ferromagnetic discs," *Nano Letters*, vol. 15, no. 2, 2015.

[13] C. Donnelly *et al.*, "Three-dimensional magnetization structures revealed with X-ray

vector nanotomography," *Nature*, vol. 547, no. 7663, 2017.

[14] M. Suzuki *et al.*, "Three-dimensional visualization of magnetic domain structure with strong uniaxial anisotropy via scanning hard X-ray microtomography," *Applied Phyics Express*, vol. 11, no. 3, 2018.

[15] K. Witte *et al.*, "From 2D STXM to 3D Imaging: Soft X-ray Laminography of Thin Specimens," *Nano Letters*, vol. 20, no. 2, 2020.

[16] S. Blundell and D. Thouless, "Magnetism in Condensed Matter," *Oxford University Press*, 2001.

[17] F. Bloch, "Zur Theorie des Ferromagnetismus," *Zeitschrift für Physics*, 1930.

[18] J. M. D. Coey, Magnetism and magnetic materials, *Cambridge University Press,* 2010.

[19] A. Aharoni and A. Arrott, "Introduction to the Theory of Ferromagnetism," *Physics Today*, vol. 50, no. 9, 1997.

[20] W. H. Meiklejohn and C. P. Bean, "New magnetic anisotropy," *Physical Review*, vol. 105, no. 3, 1957.

[21] W. F. Brown, "Theory of the approach to magnetic saturation," *Physical Review*, vol. 58, no. 8, 1940.

[22] T. L. Gilbert, "A Lagrangian formulation of the gyromagnetic equation of the magnetic field," *Physical Reviews,* vol. 100, 1955.

[23] L. Landau, "On the theory of the dispersion of magnetic permeability in ferromagnetic bodies," *Perspectives in Theoretical Physics*, 1992.

[24] P. Weiss, "The variation of ferromagnetism with temperature," *Comptes rendus hebdomadaires des séances de l'Académie des sciences*, vol. 143, 1906.

[25] A. E. Berkowitz and K. Takano, "Exchange anisotropy — a review," *Journal of Magnetism and Magnetic Materials*, vol. 200, no. 1–3. 1999.

[26] J. Nogués and I. K. Schuller, "Exchange bias," *Journal of Magnetism and Magnetic Materials*, vol. 192, no. 2, pp. 203–232, Feb. 1999.

[27] F. Radu and H. Zabel, "Exchange bias effect of ferro-/antiferromagnetic heterostructures," *Springer Tracts in Modern Physics*, vol. 227, 2007.

[28] K. O'Grady, L. E. Fernandez-Outon, and G. Vallejo-Fernandez, "A new paradigm for exchange bias in polycrystalline thin films," *Journal of Magnetism and Magnetic Materials*, vol. 322, no. 8. 2010.

[29] J. C. S. Kools, “Exchange-biased spin-valves for magnetic storage,” *IEEE Transactions on Magnetics*, vol. 32, no. 4 part 2, 1996.

[30] M. A. Kuznetsov, O. G. Udalov, and A. A. Fraerman, “Anisotropy of Neel ‘orange-peel’ coupling in magnetic multilayers,” *arXivLabs,* 2018.

[31] P. Grünberg, R. Schreiber, Y. Pang, U. Walz, M. B. Brodsky, and H. Sowers, “Layered magnetic structures: Evidence for antiferromagnetic coupling of Fe layers across Cr interlayers,” *Journal of Applied Physics*, vol. 61, no. 8, 1987.

[32] J. Unguris, R. J. Celotta, and D. T. Pierce, “Oscillatory exchange coupling in Fe/Au/Fe(100),” *Journal of Applied Physics*, vol. 75, no. 10, 1994.

[33] J. Unguris, R. J. Celotta, and D. T. Pierce, “Observation of two different oscillation periods in the exchange coupling of Fe/Cr/Fe(100),” *Physical Review Letters*, vol. 67, no. 1, 1991.

[34] R. Coehoorn, “Period of oscillatory exchange interactions in Co/Cu and Fe/Cu multilayer systems,” *Physical Review B*, vol. 44, no. 17, 1991.

[35] Y. Wang, P. M. Levy, and J. L. Fry, “Interlayer magnetic coupling in Fe/Cr multilayered structures,” *Physical Review Letters*, vol. 65, no. 21, 1990.

[36] S. S. P. Parkin, N. More, and K. P. Roche, “Oscillations in exchange coupling and magnetoresistance in metallic superlattice structures: Co/Ru, Co/Cr, and Fe/Cr,” *Physical Review Letters*, vol. 64, no. 19, 1990.

[37] P. Grünberg and D. E. Bürgler, “Metallic Multilayers: Discovery of Interlayer Exchange Coupling and GMR,” *Handbook of Spintronics*, 2015.

[38] M. D. Stiles, “Interlayer exchange coupling,” *Journal of Magnetism and Magnetic Materials*, vol. 200, no. 1–3, pp. 322–337, 1999.

[39] T. Kasuya, “A Theory of Metallic Ferro- and Antiferromagnetism on Zener’s Model,” *Progress of Theoretical and Experimental Physics*, vol. 16, no. 1, 1956.

[40] K. Yosida, “Magnetic properties of Cu-Mn alloys,” *Physical Review*, vol. 106, no. 5, 1957.

[41] M. A. Ruderman and C. Kittel, “Indirect exchange coupling of nuclear magnetic moments by conduction electrons,” *Physical Review*, vol. 96, no. 1, 1954.

[42] Y. Yafet, “Ruderman-Kittel-Kasuya-Yosida range function of a one-dimensional free-electron gas,” *Physical Review B*, vol. 36, no. 7, 1987.

[43] R. A. Duine, K. J. Lee, S. S. P. Parkin, and M. D. Stiles, “Synthetic antiferromagnetic

spintronics," *Nature Physics*, vol. 14, no. 3. 2018.

[44] A. Prabhakar and D. D. Stancil, Spin waves: Theory and applications, *Springer,* 2009.

[45] B. A. Kalinikos and A. N. Slavin, "Theory of dipole-exchange spin wave spectrum for ferromagnetic films with mixed exchange boundary conditions," *Journal of Physics C: Solid State Physics*, vol. 19, no. 35, 1986.

[46] R. W. Damon and J. R. Eshbach, "Magnetostatic modes of a ferromagnet slab," *Journal of Physics and Chemistry of Solids*, vol. 19, no. 3–4, 1961.

[47] J. R. Eshbach, "Spin-wave propagation and the magnetoelastic interaction in yttrium iron garnet," *Journal of Applied Physics*, vol. 34, no. 4, 1963.

[48] A. Barman and A. Haldar, "Time-Domain study of magnetization dynamics in magnetic thin films and micro- and nanostructures," *Solid State Physics - Advances in Research and Applications*, vol. 65, 2014.

[49] J. Förster *et al.*, "Nanoscale X-ray imaging of spin dynamics in yttrium iron garnet," *Journal of Applied Physics*, vol. 126, no. 17, 2019.

[50] J. T. Gudmundsson, "Physics and technology of magnetron sputtering discharges," *Plasma Sources Science and Technology*, vol. 29, no. 11. 2020.

[51] G. Rius Suné, "Electron Beam Lithography for Nanofabrication," *Thesis*, Universitat Autonoma de Barcelona, Barcelona, 2008.

[52] Giacomo Sala, "Magnetic patterning of exchange-biased systems for nanomagnonics,", *Thesis*, Politecnico di Milano, Milano, 2017.

[53] S. Kishimoto, "Electron Moiré method," *Theoretical and Applied Mechanical Letters*, vol. 2, no. 1, 2012.

[54] E. Albisetti *et al.*, "Nanopatterning reconfigurable magnetic landscapes via thermally assisted scanning probe lithography," *Nature Nanotechnology*, vol. 11, no. 6, 2016.

[55] F. J. Giessibl, "Advances in atomic force microscopy," *Reviews of Modern Physics*, vol. 75, no. 3. 2003.

[56] F. J. Giessibl, "Atomic resolution of the silicon (111)-(7x7) surface by atomic force microscopy," *Science.*, vol. 267, no. 5194, 1995.

[57] "https://www.keysight.com."

[58] J. Kerr, " XLIII. On rotation of the plane of polarization by reflection from the pole of a magnet ," *London, Edinburgh, Dublin Philosophical Magazine and Journal of Science*, vol. 3, no. 19, 1877.

[59] S. Yamamoto and I. Matsuda, “Measurement of the resonant magneto-optical Kerr effect using a free electron laser,” *Applied Sciences (Switzerland)*, vol. 7, no. 7. 2017.

[60] Mattia Stella, “Development of a Kerr Microscope for the study of magnetic micro and nanostructures,” , *Thesis*, Politecnico di Milano, Milano, 2017.

[61] “https://www.psi.ch/en/sls/pollux/endstation.”

[62] S. Finizio, “Time resolved Scanning Transmission X-ray Microscopy”, *private communication*, 2021.

[63] M. Holler *et al.*, “Three-dimensional imaging of integrated circuits with macro- to nanoscale zoom,” *Nature Electronics*, vol. 2, no. 10, 2019.

[64] L. Helfen *et al.*, “On the implementation of computed laminography using synchrotron radiation,” *Review of Scientific Instruments*, vol. 82, no. 6, 2011.

[65] C. Donnelly *et al.*, “Tomographic reconstruction of a three-dimensional magnetization vector field,” *New Journal of Physics*, vol. 20, no. 8, 2018.

[66] A. Vansteenkiste, J. Leliaert, M. Dvornik, M. Helsen, F. Garcia-Sanchez, and B. Van Waeyenberge, “The design and verification of MuMax3,” *AIP Advances*, vol. 4, no. 10, 2014.

[67] E. Albisetti *et al.*, “Nanopatterning spin-textures: A route to reconfigurable magnonics,” *AIP Advances*, vol. 7, no. 5, 2017.

[68] A. Bergman, B. Skubic, J. Hellsvik, L. Nordström, A. Delin, and O. Eriksson, “Ultrafast switching in a synthetic antiferromagnetic magnetic random-access memory device,” *Physical Review B - Condensed Matter and Materials Physics*, vol. 83, no. 22, 2011.

[69] E. Monteblanco, F. Garcia-Sanchez, D. Gusakova, L. D. Buda-Prejbeanu, and U. Ebels, “Spin transfer torque nano-oscillators based on synthetic ferrimagnets: Influence of the exchange bias field and interlayer exchange coupling,” *Journal of Applied Physics*, vol. 121, no. 1, 2017.

[70] R. Lavrijsen, J. H. Lee, A. Fernández-Pacheco, D. C. M. C. Petit, R. Mansell, and R. P. Cowburn, “Magnetic ratchet for three-dimensional spintronic memory and logic,” *Nature*, vol. 493, no. 7434, 2013.

[71] W. Legrand *et al.*, “Room-temperature stabilization of antiferromagnetic skyrmions in synthetic antiferromagnets,” *Nature Materials*, vol. 19, no. 1, 2020.

[72] K. Di *et al.*, “Enhancement of spin-wave nonreciprocity in magnonic crystals via

synthetic antiferromagnetic coupling," *Scientific Reports*, vol. 5, 2015.

[73] B. Lenk, H. Ulrichs, F. Garbs, and M. Münzenberg, "The building blocks of magnonics," *Physics Reports*, vol. 507, no. 4–5. 2011.

[74] N. Wiese, T. Dimopoulos, M. Rührig, J. Wecker, M. Brückl, and G. Reiss, "Antiferromagnetically coupled CoFeB/Ru/CoFeB trilayers," *Applied Physics Letters*, vol. 85, no. 11, 2004.

[75] Giuseppe Scaramuzzi, "Nanoscale spin-waves based platforms for magnon computing,", *Thesis*, Politecnico di Milano, Milano, 2018.

[76] G. Vallejo-Fernandez, B. Kaeswurm, L. E. Fernandez-Outon, and K. O'Grady, "Effect of the ferromagnetic layer thickness on the blocking temperature in IrMn/CoFe exchange couples," in *IEEE Transactions on Magnetics*, vol. 44, no. 11 part 2, , 2008.

[77] G. Malinowski, M. Hehn, S. Robert, O. Lenoble, and A. Schuhl, "Correlation between structural quality and magnetic properties of IrMn-based multilayers," *Journal of Applied Physics*, vol. 98, no. 11, 2005.

[78] S. Finizio *et al.*, "Unexpected field-induced dynamics in magnetostrictive microstructured elements under isotropic strain," *Journal of Physics: Condensed Matter*, vol. 30, no. 31, 2018.

[79] L. Helfen *et al.*, "High-resolution three-dimensional imaging of flat objects by synchrotron-radiation computed laminography," *Applied Physical Letters*, vol. 86, no. 7, 2005.

[80] L. Helfen *et al.*, "Synchrotron-radiation computed laminography for high-resolution three-dimensional imaging of flat devices," *Physica Status Solidi: Application and Materials*, vol. 204, no. 8, 2007.

[81] R. Streubel, F. Kronast, P. Fischer, D. Parkinson, O. G. Schmidt, and D. Makarov, "Retrieving spin textures on curved magnetic thin films with full-field soft X-ray microscopies," *Nature Communications*, vol. 6, 2015.

[82] H. Corte, "Oommf vector data file to Matlab array", *MATLAB Central File Exchange*, 2013.

Acknowledgments

A conclusione di questo lavoro di tesi desidero ringraziare in poche righe chi mi ha dato la possibilità di raggiungere questo traguardo. Ringrazio innanzitutto il Professor Riccardo Bertacco per avermi accolto nel suo gruppo, permettendomi di vivere l'esperienza più gratificante e interessante di questi anni universitari. Durante il suo corso ho maturato la passione verso la spintronica e il nano-magnetismo, la quale è cresciuta ulteriormente durante i mesi di lavoro trascorsi al PoliFAB. Un ringraziamento immenso va a Edoardo Albisetti, che durante questo periodo mi ha insegnato, sostenuto e stimolato con grande entusiasmo e pazienza. Mi ha sempre aiutato in qualsiasi momento con grandissima disponibilità, e non ha mai fatto mancare parole di incoraggiamento. Ha rappresentato per me il punto di riferimento e d'ispirazione, mostrandomi con la sua passione cosa vuol dire svolgere l'attività di ricerca e aiutandomi a capire cosa voglio fare in futuro. Lo ringrazio anche per la sua simpatia, il suo buonumore contagioso e per le chiacchierate fatte insieme durante le pause pranzo. Grazie allo staff di PoliFAB, Lorenzo Livetti, Alessia Romeo e Claudio Somaschini, per avermi aiutato a risolvere qualsiasi tipo di problema tecnico, sempre con grande disponibilità. Grazie anche a Christian Rinaldi, per avermi dato una mano con pazienza durante le misure al VSM. Ringrazio moltissimo anche Simone Finizio, che nonostante la distanza ha sempre dimostrato una grandissima disponibilità nel rispondere alle mie assillanti domande via e-mail o durante le videochiamate per gli esperimenti in remoto al sincrotrone.

Grazie agli amici di una vita Giovanni, Fabiano, Marco, Francesco, Davide, Filippo, Jacopo, Matteo, Lorenzo, Matteo, per le mille avventure passate insieme, per le interminabili aste del fantacalcio, per le ancora più interminabili polemiche giornaliere, per le cene a base di carne di struzzo e per le sempre immancabili risate: siete sempre stati la mia certezza. A voi dico, come da tradizione: in luto dederis, de luto removeat.

Un grazie anche a Elena, ormai diventata come una sorella adottiva con cui condivido mille risate, a Vincenzo, per il sostegno degli ultimi mesi e per tutte le puntate viste insieme (Sasageyo!), e a Meri, vera amica con cui scherzare e parlare di tutto.

Un sentito grazie a tutti i miei amici scout, con i quali sono cresciuto e maturato come persona, con cui ho condiviso meravigliose avventure e da cui ho imparato il senso di responsabilità e perseveranza nei momenti più difficili e impegnativi, e l'importanza di mettersi al servizio degli altri.

Un ringraziamento speciale va a Federica, per essere la persona più speciale e importante della mia vita, per dimostrarmi ogni giorno il suo amore tra mille risate, scherzi e faccini, per avermi dato la forza e sostenuto in ogni momento. Gran parte di questo è anche merito tuo.

Infine, la mia più profonda gratitudine va a tutta la mia famiglia. Grazie ai miei nonni Roberta e Renato, che sono sempre stati un esempio di vita, gentilezza e disponibilità. Grazie alle mie zie e i miei zii, in particolare a mia zia Barbara, per l'immancabile sostegno e affetto che mi ha sempre dimostrato. Grazie infinite a mia sorella Margherita, a cui sono profondamente legato, per essere stata il mio supporto silenzioso in qualsiasi momento. La ringrazio anche per l'aiuto che mi ha dato in questi intensi mesi di tesi, per tutti i disegni che mi ha aiutato a fare, anche con solo un braccio a disposizione! A mamma e a papà: non riesco a trovare le parole con cui esprimere quanto voi rappresentiate per me, siete sempre stati l'esempio da cui ho tratto ispirazione, e non mi avete mai fatto mancare la vostra vicinanza. Non potrò mai ringraziarvi abbastanza.

Davide Girardi

Aprile 2021